Elucidating Protein Stabilization with Fluorescence Techniques

Li Hung Chloe Chung

Photophysics Research Group

Department of Physics

University of Strathclyde,Glasgow, United Kingdom

'A thesis submitted to the University of Strathclyde, Glasgow, in part fulfillment of the requirements for the degree of Doctor of Philosophy.'

January, 2020

This thesis is the result of the author's original research. It has been composed by the author and has not been previously submitted for examination which has led to the award of a degree.

Signed:

Date:

For mum and dad

Abstract

Insulin is an important protein that controls blood glucose levels, but its function becomes ineffective during protein aggregation. Insulin readily undergoes protein aggregation and it contributes to hyperglycaemia. In long-term hyperglycaemia, glucose can alter the structure and stability of insulin via glycation.

In this thesis, fluorescence techniques have been used to monitor protein dynamics that are crucial to our understanding of protein aggregation and glycation. A synthetic protein that readily forms fibrous structures with homogenous growth kinetics is synthesized to simplify the interpretation of fluorescence kinetics. The conformational changes that both insulin and the protein model undergo throughout 700 hours have been monitored with a range of fluorescence techniques.

For the fibrillogenesis model, time-resolved emission spectra (TRES) measurements revealed two fluorescent species occurring around 33,000 and 31,500 cm^{-1} at 0.33 hours after preparation. After this time, the second component decreases to 30,500 cm^{-1} and continues to emit at this range throughout 700 hours. This suggests that fibril formation occurs within a few hours (confirmed by structured illumination microscopy (SIM)) and remains stable. Long term stability of the model provides a measurement-supported basis for its use as a reference material in fluorescence studies of protein aggregation.

For free hexameric insulin, TRES measurements show drastic conformational changes. Two fluorescent components are shown at 33,000 cm^{-1} and 32,000 cm^{-1}. The second component decreases to 31,000 cm^{-1} after 196 hours. This shows that the protein aggregates increase in size during this time. For free monomeric insulin, there

is a lack of fluorescence intensity or TRES spectral changes, which show a lack of conformational change throughout 700 hours. In ThT studies and dSTORM images, there was no evidence to show amyloid fibrils were formed in both hexameric and monomeric insulin.

Spectral similarities are shown in TRES measurements between free hexameric insulin and insulin with glucose until 196 hours after preparation. At least two fluorescent species were observed around 33,000 and 31,500 cm^{-1}. The second component decreases to 30,500 cm^{-1} at 196 hours and does not experience spectral shifts in 10 ns, which shows that glycation begin to cross link insulin aggregates, making them more rigid. In dSTORM images show there are an abundance of aggregates compared to free hexameric insulin which confirms cross linkage observed in the TRES measurements. For monomeric insulin with glucose, no significant changes were shown in the spectroscopy measurements and dSTORM images show smaller aggregates compared to free monomeric insulin. This demonstrates that glycation inhibits monomeric insulin aggregation.

The findings in this thesis hold promise for monitoring the storage of insulin and its application in the control of diabetes and may support the development of more effective therapeutics against amyloidosis.

Journal Publications

Li Hung C. Chung, David J. S. Birch, Vladislav Vyshemirsky, Maxim G. Ryadnov and Olaf J. Rolinski, "Tracking Insulin Glycation in Real Time by Time-Resolved Emission Spectroscopy", *J. Phys. Chem. B.*, **123**, 7812-7817, (2019)

Li Hung C. Chung, David J. S. Birch, Vladislav Vyshemirsky, Angelo Bella, Maxim G. Ryadnov and Olaf J. Rolinski, "Protein Fibrillogenesis Model Tracked by its Intrinsic Time-Resolved Emission Spectra", *Methods Appl. Fluoresc.*, **7**, 035003, (2019)

Li Hung C. Chung, David J. S. Birch, Vladislav Vyshemirsky, Maxim G. Ryadnov and Olaf J. Rolinski, "Insulin Aggregation Tracked by its Intrinsic TRES", *Appl. Phys. Lett.*, **111**, 263701, (2017)

Conference Contributions

L. H. C. Chung, O. J. Rolinski, A. Bella, V. Vyshermirsky, M. G. Ryadnov, and D. J. S. Birch, "Time-Resolved Emission Spectral Studies of Glycation Effects on Tyrosine Fluorescence in Protein Under Physiological Conditions", Poster Presentation: *Methods and Applications in Fluorescence Conference, San Diego, USA*, 21-23rd May 2019

L. H. C. Chung, O. J. Rolinski, A. Bella, V. Vyshermirsky, M. G. Ryadnov, and D. J. S. Birch, "Investigating Glycation Effects on Tyrosine Fluorescence in Protein Aggregation With Time-Resolved Emission Spectra", Oral Presentation: *Fluorofest, Texas, USA*, 21-23rd May 2019

L. H. C. Chung, Chair Policy and Package Session: *Postgraduate Institute Conference, Glasgow, UK*, 23-24th October 2018

L. H. C. Chung, A. Bella, V. Vyshermirsky, O. J. Rolinski, D. J. S. Birch, and M. G. Ryadnov, "Protein Aggregation and The Effects of Glycation Tracked by Intrinsic TRES", Poster Presentation: *Postgraduate Institute Conference, Glasgow, UK*, 23-24th October 2018

L. H. C. Chung, A. Bella, V. Vyshermirsky, O. J. Rolinski, D. J. S. Birch, and M. G. Ryadnov, "Tracking Protein Aggregation by Intrinsic TRES", Oral Presentation: *7th EuCheMS Chemistry Congress, Liverpool, UK*, 26-30th August 2018

L. H. C. Chung, A. Bella, V. Vyshermirsky, O. J. Rolinski, D. J. S. Birch, and M. G. Ryadnov, "Tracking Protein Aggregation by Intrinsic TRES", Poster Presentation: *7th*

EuCheMS Chemistry Congress, Liverpool, UK, 26-30th August 2018

L. H. C. Chung, O. J. Rolinski, D. J. S. Birch, A. Bella, M. Shaw, A. Knight, and M. G. Ryadnov, "Tracking De Novo Peptide Aggregates in Real Time Using Fluorescence", Poster Presentation: *SUPA Annual Meeting, Edinburgh, UK*, 6th June 2018

L. H. C. Chung, O. J. Rolinski, D. J. S. Birch, A. Bella, M. Shaw, A. Knight, and M. G. Ryadnov, "Tracking De Novo Peptide Aggregates in Real Time Using Fluorescence", Poster Presentation: *Engage at Strathclyde, Glasgow, UK*, 30th April 2018

L. H. C. Chung, O. J. Rolinski, D. J. S. Birch, A. Bella, M. Shaw, A. Knight, and M. G. Ryadnov, "Tracking De Novo Peptide Aggregates in Real Time Using Fluorescence", Poster Presentation: *IOP Medical Physics Group Early Career Symposium, London, UK*, 10th November 2017

L. H. C. Chung, O. J. Rolinski, D. J. S. Birch, A. Knight, and M. G. Ryadnov,"Elucidating Protein Fibrillogenesis Pathways", Oral Presentation: *University of Strathclyde - University of Tokyo 2017 Student Symposium, Glasgow, UK*, 23th September 2017

L. H. C. Chung, O. J. Rolinski, D. J. S. Birch, A. Bella, M. Shaw, A. Knight, and M. G. Ryadnov, "Tracking De Novo Peptide Aggregates in Real Time Using Fluorescence", Poster Presentation: *Methods and Applications in Fluorescence Conference, Brugges, Belgium*, 10-13th September 2017

L. H. C. Chung, O. J. Rolinski, D. J. S. Birch, A. Bella, M. Shaw, A. Knight, and M. G. Ryadnov, "Elucidating Protein Fibrillogenesis Pathways", Poster Presentation: *Physics Postgraduate Conference, Glasgow, UK*, 24th August 2017

L. H. C. Chung, O. J. Rolinski, D. J. S. Birch, A. Bella, M. Shaw, A. Knight, and M. G. Ryadnov, "Elucidating Protein Fibrillogenesis Pathways", Poster Presentation: *SUPA Annual Meeting, Edinburgh, UK*, 10th May 2017

L. H. C. Chung, O. J. Rolinski, D. J. S. Birch, A. Bella, M. Shaw, A. Knight, and M. G.

Ryadnov, "Elucidating Protein Fibrillogenesis Pathways", Poster Presentation: *Fluorofest, Glasgow, UK*, 24-26th April 2017

L. H. C. Chung, O. J. Rolinski, D. J. S. Birch, A. Bella, M. Shaw, A. Knight, and M. G. Ryadnov, "Elucidating Protein Fibrillogenesis Pathways", Oral Presentation: *Fluorofest, Glasgow, UK*, 24-26th April 2017

L. H. C. Chung, O. J. Rolinski, D. J. S. Birch, A. Bella, M. Shaw, A. Knight, and M. G. Ryadnov, "Elucidating Fibrillogenesis Pathways in Proteins", Poster Presentation: *Analytical Science Division Postgraduate Institute Meeting, London, UK*, 6th April 2017

L. H. C. Chung, A. Knight, and D. J. S. Birch, "Elucidating Self-Assembly Pathways in Silica and Peptides", Oral Presentation: *Physics Postgraduate Conference, Glasgow, UK*, 17th August 2016

Acknowledgements

I am extremely grateful to be given the opportunity to pursue a PhD. Without the constant support from amazing people in my life, the completion of my doctorate would not have been possible. Thank you for believing in me.

Firstly, I would like to express my gratitude to my supervisors David Birch and Olaf Rolinski for giving me the opportunity of a lifetime. Their doors have always been open to have long in depth discussions despite their busy schedules. Their encouragement and guidance has enabled me to develop a deep understanding of my project, I could not have completed my PhD without their support. A mention to Yu Chen for being a great role model and inspiring me to pursue a PhD.

I am also grateful for my supervisors Alex Knight for making me feel welcome at NPL and to Maxim Ryadnov for helpful advice and feedback throughout my PhD. Thank you to my colleagues Angelo Bella and Michael Shaw for expanding my knowledge within the areas of chemistry and microscopy by having the patience to train me and answer my questions. A special thanks to Jascindra Ravi and Nilofar Faruqui for making sure I was getting the most out of my NPL experience - I will never forget the advice and support you have given me. My experience at NPL has made me grow as a person.

I am lucky to have met some amazing people at NPL. Especially to Shaun Geaney, Mariam Akhtar, Elsje van Es, Paris Smith, and Maria Tsalenchuk for making London feel less lonely by mocking my Scottish accent 90% of the time.

I would like to thank Lucas Herdly for being a great lab partner, your laboratory tips and extensive science knowledge has been invaluable. I would also like to thank

Daniel Maclure for constantly quizzing me on my project, it forced me to know my project inside out. To the rest of my research group: Natakorn Sapermsap, Milan Adelt, and Alastair Davy, who have given me many fond memories.

To Hazel Stewart, Gillian Craig, Hajar Mousavi, Mollie McFarlane, Samantha Hume, Zoë Davidson, Aracelli Venegas-Gomez and Rachel Jones for being great support networks. I look up to every one of you and I am lucky to have such great women in my life who empower each other. Thanks for all the great advice and laughs you have given me.

我想特别感謝我的父母，感謝你們對這個家無私的貢獻和支持。你們作為父母的堅持意志讓我無比驕傲，以你們為榜樣。你們教會了我，凡事皆有可能，只要你刻苦努力。我非常非常的愛你們。

To my siblings who enforced their character building techniques to shape who I am today. To Bond who has always been forgiving and compassionate, even if I did ruin your drawing masterpieces. Especially to Ken and Vivien, I thank you for all the sacrifices you have made for me and I know I can always depend on you both. To my favourite cousin Gameboy, I look forward to living in London with you! To my favourite nephew, Ashton who has incredible wit and can always make me laugh. Also to Jun Jun, who is only 2 years old but your smile lights up the room and has brought a lot of joy into our lives.

A special mention to Barry McAuley who has been my rock throughout the years and encourages me to do the impossible. I wouldn't be the woman I am today without you. I am looking forward to exploring the world with you. Also to the McAuley family who bought me Pandemic which is the only thing that calms me down during stressful times.

Many thanks to my life long friends, Fiona Logan, Jennifer McKechnie, Fiona McKay, Fiona Paisley, Fiona Paterson, Kirstie Mulheron, Christine Langlands, Heather Mccance, Eilidh Heggie, and Greg Brown. Who are all as equally busy as I am but we have the best fun when we are together.

Finally, to the lacrosse team, I am proud to be part of a team who are extremely supportive of each other. The memories this team have given me are unforgettable. Special thanks to Nadia Morris, Freya McMeeken, Joanna Murray, Mhairi Burnett and Jade Ayd who make me feel old and young at the same time.

List of Figures

List of Tables

Abbreviations

Aβ	Amyloid Beta
AD	Alzheimer's Disease
AGEs	Advanced Glycation End Products
ANS	8-Anilinonaphthalene-1-sulfonic acid
BSA	Bovine Serum Albumin
CD	Circular Dichroism
CHCA	α-Cyano-4-hydroxycinnamic acid
DAS	Decay Associated Spectra
DCM	Dichloromethane
DHB	2,5-Dihydroxybenzoic acid
DIPEA	N,N-Diisopropylethylamine
DMF	Dimethylformamide
DMSO	Dimethyl Sulfoxide
dSTORM	Direct Stochastic Optical Reconstruction Microscopy
EM	Electron Microscopy
FRET	Fluorescence Resonance Energy Transfer
FT	Fourier Transform
FTIR	Fourier Transform Infrared Spectroscopy
FWHM	Full Width Half Maximum
Fmoc	Fluorenylmethyloxycarbonyl
H	Hydrophobic
HBTU	2-(1H-benzotriazol-1-yl)-1,1,3,3-tetramethyluronium hexafluorophosphate
HOBt	Hydroxybenzotriazole
HPLC	High Performance Liquid Chromatography
HSA	Human Serum Albumin
IR	Infrared

KIH	Knob Into Holes
KOH	Potassium Hydroxide
LED	Light Emitting Diode
MALDI	Matrix-Assisted Laser Desorption/Ionization
MCA	Multi-Channel Analyser
MEA	Monoethanolamine
MS	Mass Spectrometry
NA	Numerical Aperture
NDP	Nuclear Dependent Polymerization
NIR	Near Infrared
NMR	Nuclear Magnetic Resonance
NNLS	Non-linear Least Squares
OTF	Optical Transfer Function
P	Polar
PALM	Photoactivated Localization Microscopy
PBS	Phosphate Buffered Saline
PBST	Phosphate Buffered Saline with Tween
PD	Parkinson's Disease
PMT	Photomultiplier Tube
PSF	Point Spread Function
SAF	Self-Assembling Fibre
SIM	Structured Illumination Microscopy
SLM	Spatial Light Modulator
SMLM	Single Molecule Localisation Microscopy
SPPS	Solid Phase Peptide Synthesis
SSIM	Saturated Structured Illumination Microscopy
STED	Stimulated Emission Depletion Microscopy
TAC	Time to Amplitude Converter
TCSPC	Time-Correlated Single Photon Counting
tBu	Tert-Butyl
TFA	Trifluoroacetic Acid
TICT	Twisted Intramolecular Charge Transfer
TIRF	Total Internal Reflection Fluorescence
ToF	Time of Flight
TRES	Time-Resolved Emission Spectroscopy
ThT	Thioflavin T
UV	Ultraviolet

Amino Acid List

Amino Acid	Three Letter Code	One Letter Code
Alanine	Ala	A
Arginine	Arg	R
Asparagine	Asn	N
Aspartic Acid	Asp	D
Cysteine	Cys	C
Glutamic Acid	Glu	E
Glutamine	Gln	Q
Glycine	Gly	G
Histidine	His	H
Isoleucine	Ile	I
Leucine	Leu	L
Lysine	Lys	K
Methionine	Met	M
Phenylalanine	Phe	F
Proline	Pro	P
Serine	Ser	S
Threonine	Thr	T
Tryptophan	Trp	W
Tyrosine	Tyr	Y
Valine	Val	V

Contents

Chapter 1

Introduction

Protein amyloids are linked to many neurodegenerative diseases which are a threat to the world's ageing population. All proteins have a specific structure, which enables them to carry out their assigned function. Nonetheless, some proteins can unfold spontaneously and refold incorrectly (known as misfolding) which makes the function of the protein ineffective. It is believed that the fibril-type of protein aggregation shows follow three main steps: (1) misfolding of the monomeric form into a low oligomer, which (2) nucleates the formation of elongated proto-fibrils that (3) aggregate forming mature fibrils [1,2]. The formation of fibril-like structures are known as amyloid formation. Inside environments such as cellular and extracellular matrices, protein amyloids can accumulate due to macromolecular crowding [3,4]. The accumulation of amyloids can deposit within neuronal cells causing diseases such as Alzheimer's disease (AD) and Parkinson's disease (PD) [5, 6]. Most importantly, proteopathies (neurodegenerative disorders caused by protein misfolding and aggregation) are caused by different proteins [1], but all result from the same generic mechanism of fibrillogenesis. Yet, a capability to monitor this very process of persistent protein aggregation is lacking.

In 2019, The International Diabetes Federation estimated that 463 million adults have diabetes, it been responsible for over 4.2 million deaths worldwide, and $760 billion of global health expenditure has been spent on diabetes [7]. Due to its importance in the medicinal field, insulin is one of the most common proteins to study as it regulates glucose homeostasis. Diabetic patients most commonly receive insulin via

subcutaneous insulin injections. However, the protein provides complications as it as it readily aggregates into amyloid fibrils and deposits have been found in frequent injection sites [8]. Moreover, serum samples taken from PD patients displayed an autoimmune response to insulin fibrils, which may suggest that insulin aggregation may play a role in neurogenerative diseases [9]. In vitro, amyloid fibrils can form during purification and isolation steps, which requires low pH around 1-3. Aggregation is also prevalent in the production, delivery and long-term storage of insulin [10].

Since the overall structure determines the function of the protein, the ability for insulin to reduce blood glucose levels becomes non-existent when insulin is fibrillar. This provides more problems because hyperglycaemia (excessive glucose levels in the blood) contributes to a nonenzymatic process called glycation. Glycation alters protein structures by creating irreversible products after long periods of time, called advanced glycation end products (AGEs). It has been suggested that glycation plays an important role in amyloidosis as glycated proteins are often found in amyloid deposits [11, 12].

Insulin has been studied under different conditions in order to understand the mechanism of its fibrillation. The fibrillation rate is heavily dependent upon factors such as pH, temperature, protein and salt concentrations. Under low pH conditions and at room temperature, insulin has been shown to predominantly consist of α-helical structures through circular dichroism (CD) [13], fourier transform infrared spectroscopy (FTIR) [13], nuclear magnetic resonance (NMR) [14], and mass spectroscopy (MS) [15]. With the combination of acidic conditions and high temperatures (70 °C), insulin starts to partially unfold and β-sheets start to become the dominant structure after a few hours [13]. Neutral pH and under high agitative conditions have also been studied [16, 17]. It has been shown that altering insulin environmental conditions produce different structural properties and morphologies.

As mentioned above, there have been extensive studies upon characterizing fibrillar structures. However, the photophysical properties of amyloids are largely unknown. Fluorescence techniques are a powerful method to investigate dynamics,

interactions, self-assembly, and protein folding due to its high sensitivity towards surrounding fluorophore environments. In particular, it has been commonly used to study amyloid formation with extrinsic fluorophores such as Thioflavin T, Congo Red, and 8-Anilinonaphthalene-1-sulfonic acid (ANS). The use of extrinsic probes has given us a wealth of information relating to the aggregation process. However, it may perturb the self-assembly of protein kinetics which contributes to misleading interpretations.

To overcome this problem, while still having the advantages of time and spatial resolutions in the nanoscale, intrinsic fluorophores are used. Insulin has seven intrinsic fluorophores (3 phenylalanine (Phe) and 4 tyrosine (Tyr) residues) and with the absence of tryptophan (Trp) residues, monitoring the local environments of tyrosine during aggregation is possible. A few disadvantages intrinsic fluorophores have are that all three residues are excited by UV light which are harmful to live cells and do not have large quantum yields compared to extrinsic fluorophores. There is more control when labelling the protein with an extrinsic fluorophore, whereas, intrinsic fluorophores are in many locations which gives multi-exponential intensity decays in proteins. However, there are a few proteins such as amyloid beta [18] and human serum albumin [19] which are easier to examine as they have only one intrinsic fluorophore in their structures. There are many dyes which are synthesised with specific properties to study solvent polarity, pH changes, etc. Dyes have an emission range from UV to near infrared (NIR), with short to long lifetimes (ns-μs). Extrinsic fluorophores also have been developed to have high photostability, which are capable for maintaining high quantum yields for an extended period of time, this is important for fluorescent microscopy.

It is known that there is a mixture of monomers and higher oligomeric forms (such as dimers and hexamers) in insulin solution [20]. The mixture of these oligomeric states is one complicating factor for studying insulin aggregation. However, they can be separated because they are heavily dependent upon pH. Monomeric insulin is commonly known as the active form as the conformation allows binding to insulin receptors. Hexameric insulin has been found to be more stable than monomers and dimers since they take longer to aggregate [21–23]. The hexameric form is stabilized

by zinc ions; it is found in the pancreas and is the preferred form for long term insulin storage for therapeutic purposes. In vitro, hexameric insulin is stable at pH 7.4 but dissociates and becomes monomeric at pH 2.0 in acetic acid [24].

Polymorphism due to alternative aggregation pathways with different fibrillation rates is another complication that amyloid formation brings [25]. To truly understand fibril formation, the protein model needs to be simplified and it would be advantageous if the protein model self-assembled from the monomer up to long fibrous structures. In order to do this, de novo proteins are designed from well-established rules where every residue and their interactions are understood to enable reliable protein engineering to occur. The α-helical coiled coil has been studied in considerable depth and it is the most understood protein structure. It is also one of the simplest self-assembling protein models, and therefore in the past few decades there have been a large number of experimental and theoretical studies that have established sequence to structure rules in the coiled-coil domain [26]. Protein design enables the possibility to include any desired intrinsic fluorophores into the model, which is advantageous as it allows the self-assembly of the de novo peptide to be probed non-invasively. Synthetic protein models can offer the possibility of studying conformational changes, stability of proteins, their interactions and functions without complex environments in nature. The α-helical coiled-coil systems would offer valuable comparisons with amyloid structures found in nature.

Other than having a fundamental understanding of protein misfolding and stability for medicinal reasons, the development of synthetic biomaterials relies heavily upon sequence to structure rules to enable better control over the polypeptide sequence. For example, extended fibrillar networks can be used as a scaffold to support cell growth [27]. Amyloids existing in nature such as α-synuclein and insulin fibrils have also been exploited for applications such as creating hydrogels for entrapment of enzymes [28] and in nanowires for optical applications [29].

There are more than 20 proteins with different amino acid sequences and native states that can form amyloid fibrils, which means that they all share a common core

β-sheet structure. Glycation has also been shown to occur in various proteins that are in contact with blood such as albumin [30] and haemoglobin [31]. Therefore, gaining knowledge on the mechanism of protein aggregation and its stability is important for the enhancement of therapeutics in order to prevent, reverse or halt amyloid formation for numerous cases of amyloidoses. However, the fundamental process of protein aggregation is still largely unknown.

Protein aggregation has been studied directly and indirectly with the use of a range of techniques. Electron microscopy (EM) has provided structural information with nanometer to subnanometer resolution, which revealed that insulin changes from a predominantly α-helical structure to β-sheets when fibril assembly occurs [32]. EM microscopy comes with a few disadvantages being, the electron beam can produce temperatures up to 150 °C which is high enough to denature the protein. Furthermore, the very high vacuum will destroy the sample if it is not completely dry, the lack of aqueous solution eliminates the ability to observe the protein dynamics in real time. Moreover, insulin has been shown to denature and accelerate its aggregation when it comes into contact with hydrophobic surfaces, therefore, monitoring them in bulk solution would minimize these effects [33, 34]. With the use of indirect spectroscopy techniques such as circular dichroism (CD) also observe the same conformational changes in protein aggregation [13]. Since peptide bonds absorb in the far UV region, the α-helical structure have distinct negative bands occurring at 222 and 208 nm, whereas, the β-sheet structure has a negative band around 218 nm. There is a major disadvantage for measuring in the far UV region because most buffers also strongly absorb in this region, which can lead to misleading results.

Fluorescence spectroscopy is widely used to study fibril formation due to its high sensitivity to local environments and its ability to monitor protein structure, dynamics, and interactions with low protein concentration. In steady state-based fluorescence experiments, Thioflavin T (ThT) is commonly used as a probe to monitor β-sheet formation in amyloid fibrils. The ThT fluorescence intensity typically shows a sigmoidal function when mixed with a protein undergoing fibril formation. The fluorescence intensity is negligible in the early stages and as time increases there is a gradual in-

crease until a plateau is reached in the final stage. As the ThT quantum yield increases from nearly 0 to a higher value on binding to the β- sheets of probed fibrils, this result indicates that fibril formation by insulin undergoes three stages: an initial lag phase, a growth phase, and a final equilibrium phase [2]. ANS fluorescence is sensitive to polarity and viscosity where their quantum yield increases and the fluorescence maximum experiences a blue shift when bound to solvent exposed hydrophobic surfaces. Therefore, ANS has been commonly used to determine partially folded intermediates of proteins [21]. In steady-state spectroscopy, the sample is illuminated by a continuous light source and the fluorescence is averaged over time.

Since fluorescence occurs in a nanosecond timescale, the molecular information gained from a fluorescence measurement is lost due to the time averaging process. The time-resolved fluorescence measurement can determine the how much time the fluorophores spends in the excited state how much time the fluorophore spends in the excited state. This provides information such as different types of quenching, the molecule's reaction to different environments, and the distances between fluorophores. In steady state measurements, ThT provides no information during early fibril formation as its intensity remains at zero until the growth stage. However, since ThT becomes rigid when it binds to β-sheets, ThT would experience different micro-environments during early fibril formation. Therefore, in time-resolved fluorescence measurements can extract dynamic changes in the photophsyics of ThT. The fluorescence lifetime of ThT unbound to β-sheets is around a few ps [35]. Whereas, ThT bound to β-sheets shows a bi-exponential decay function, where the contribution and lifetime value of the slower component increases with incubation time [36].

There are many proteins that undergo spectral relaxation due to processes such as solvent relaxation, fluorophore conformational changes, and/or dielectric relaxation which can occur in the same timescale as the decay rate of the fluorophore. When spectral relaxation occurs in the nanosecond timescale, the emitted spectrum measured using steady-state fluorescence techniques will not be detected as it is the intensity averaged over time. In time resolved emission spectra (TRES), it is possible to obtain information upon time-dependent processes that occur in the excited states. TRES

has been used to study dynamics of proteins, solvent relaxation, and detect different fluorescent species present in the sample [37].

Fluorescence microscopy have been used abundantly to study protein dynamics and visualise protein aggregates. However, due to the diffraction of light the optical microscope is unable to image objects distances smaller than 250 nm apart. New microscopy techniques have been developed to break the diffraction barrier, and this is known as super-resolution microscopy. In particular, structured illumination microscopy (SIM) uses patterned light to illuminate the sample which enhances the spatial resolution by a factor of 2. SIM also has fast imaging rates which allows protein fibril formation to be filmed in real time [38]. Another super-resolution technique that has a higher resolution than SIM, is direct stochastic optical reconstruction microscopy (dSTORM) where its spatial resolution is less than 50 nm. dSTORM enables the localisation of single molecules and the fluorophores tagged onto the protein are switched on and off in order to break the diffraction barrier. Pinotsi et al. [39] have shown to track fibril growth at the single molecular level with the use of dSTORM, which offers in-depth information upon the self-assembly process.

Insulin aggregation have been well studied under acidic conditions, at high temperatures and probed with extrinsic dyes. However, there is a lack of information of insulin's long-term stability in physiological conditions. This thesis aims to monitor the stability of both hexameric and monomeric forms of insulin as their conformations are essential to control blood glucose levels. Due to hyperglycaemia and the complications it brings, interactions between glucose and both forms of insulin are studied as well. Since polymorphism complicates the fluorescence kinetics, a synthetic protein model has been designed to self-assemble from the monomer up to compare its aggregation kinetics with bigger and more complex proteins such as insulin. With the use of time-resolved spectroscopy, the aggregation and stability is studied for a few weeks (up to 700 hours) non-invasively by taking advantage of the intrinsic probes (Tyr) in insulin and the synthetic protein model. Extrinsic dyes have also been used to gain an insight upon the end point assembly of the natural and synthetic proteins with the use of super resolution microscopy such as SIM and dSTORM.

1.1 Principles of Protein Structure

In 1952, Linderstrom-Lang first described how proteins have different levels of protein structures [40], the simplest one is known as the primary structure. The function of protein is determined by the sequence of amino acids. There are 20 different building blocks that are used to make proteins called amino acids. Amino acids have a configuration of a central carbon called an α-carbon which is attached to a side chain (R), an amine group (-NH2), and carboxyl group (-COOH) (shown in figure 1.1).

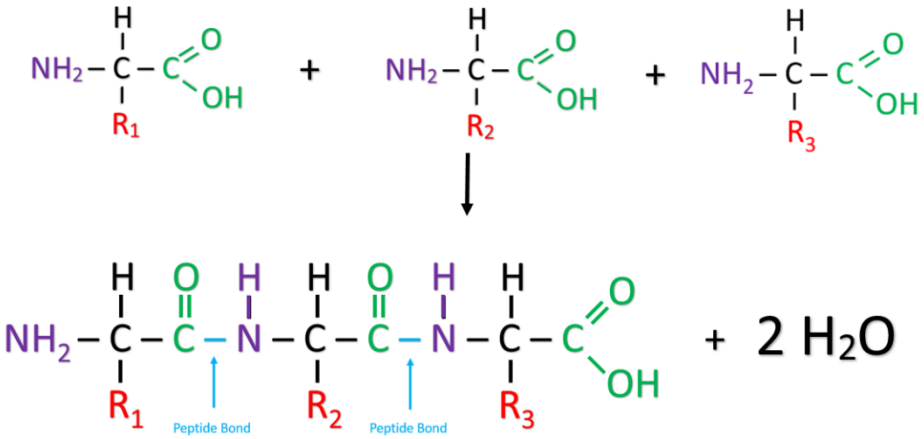

Figure 1.1: Three amino acids undergo a condensation reaction to form a peptide chain and water.

A peptide is formed when two or more amino acids are joined together through a condensation reaction. In a condensation reaction, the carboxyl group of one amino acid loses an OH and the amino group of another amino acid loses hydrogen, and in turn peptide bonds will form between these two groups. As a result, a peptide is formed with water molecules. When many amino acids join together, it creates a polypeptide chain of particular sequence. At one end of the polypeptide chain it would contain an amino group and the other would have a carboxyl group, known as N and C terminus, respectively. Each amino acid is characterized by their different side chains.

It is important to understand the side chain characteristics of amino acids as they will determine how the protein folds. The amino acid sequence contains spatial information, which dictates the final structure of the protein. The structure is also

associated to the function of the protein, therefore a small change in the sequence can influence the effectiveness of the protein.

Once the primary structure has formed, the polypeptide chain will begin to turn and fold into patterns that plays an important role in the overall protein conformation. The sequence of the amino acid will dictate how the protein folds into the next level of a protein structure, known as the secondary structure. Secondary structures are formed via hydrogen bonding along the polypeptide backbone, creating two common patterns called the α-helix and the β-sheet. In the 1960s, X-ray crystallography experiments [41,42] were carried out and supported the protein structure theory that Linderstrom-Lang proposed.

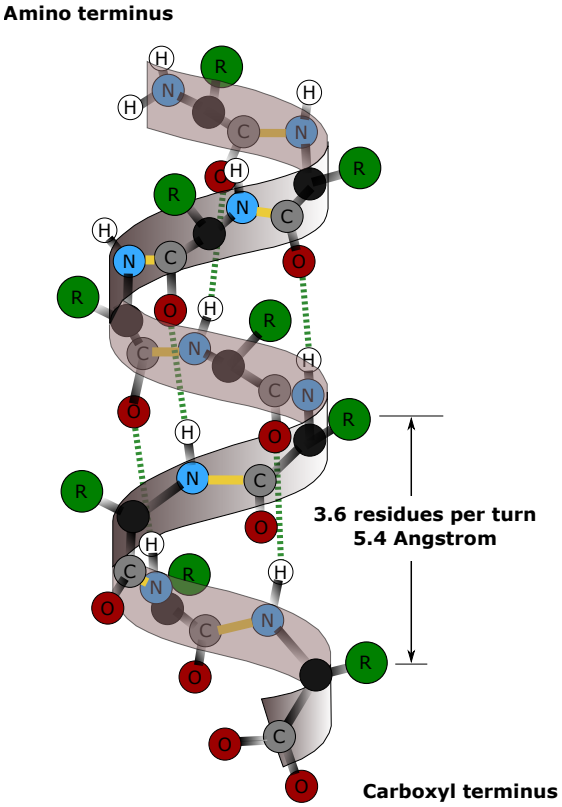

Figure 1.2: Structure of an α-helix. Yellow lines and green dotted lines represent peptide bonds and hydrogen bonds, respectively. The green, black, white, red, blue, and grey circles represent side chains, α-carbon, hydrogen, oxygen, nitrogen, and carbon atoms.

The helical structure is formed by hydrophobic and electrostatic interactions and more importantly, by hydrogen bonds between the amine hydrogen of one amino acid and the carboxyl oxygen of another (figure 1.2). Helices have different pitches, which is the distance between each consecutive turn of the helix which is 5.4 Å which consists of 3.6 per turn. The polypeptide begins to twist forming a helical structure, where the peptide backbone is on the inside and the side chains are on the outside.

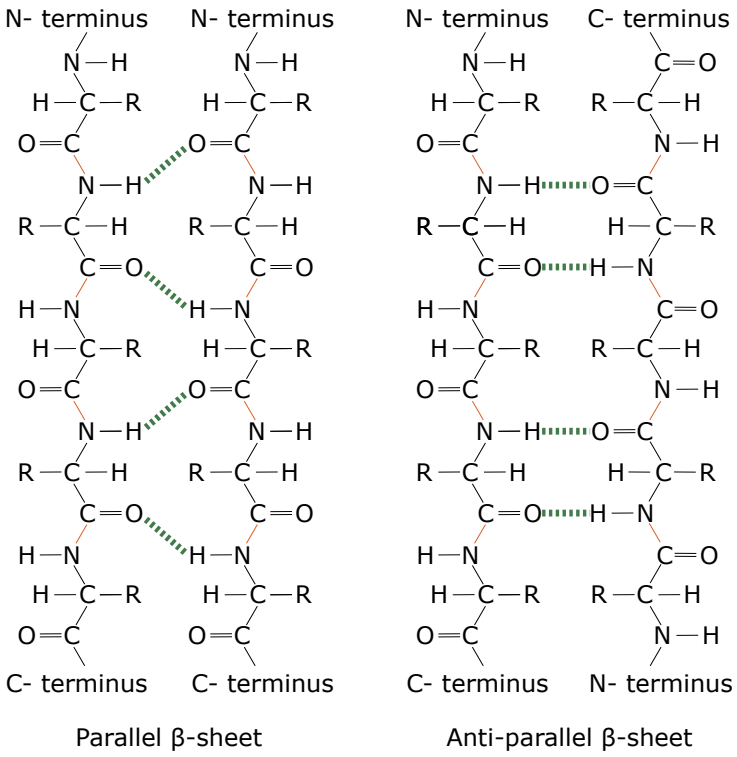

Figure 1.3: Parallel and anti-parallel β-sheets. The green dashed lines represent hydrogen bonds and the red bonds are peptide bonds.

Another common structure that exists in proteins are β-sheets. In α-helices, the polypeptide backbone is coiled. Whereas within β-sheets the polypeptide backbones are planar and are stacked side by side. There are two types of β-sheet arrangements and both are shown in figure 1.3. In anti-parallel β-sheets, the polypeptides point in opposite directions. In this arrangement, the α-carbons on both strands are aligned. Therefore, NH group of one strand can interact with the C=O group on the opposite strand are stabilized by hydrogen bonds. However, when the β-sheets are parallel, both

strands point in the same direction. As shown on the left of figure 1.3, the α-carbons on both strands are not aligned.

There are two common types of proteins; globular and fibrous proteins. In globular proteins, they predominately consist of α-helices and they are tightly folded and coiled compared to fibrous proteins which predominately consist of β-sheets [43]. The tertiary structure of a protein is the secondary structure of a polypeptide folded into a three-dimensional structure. This three-dimension structure gives the protein its functional properties and this is dependent upon the characterization of amino acid side chains. Side chains can also determine whether amino acids are hydrophilic or hydrophobic. Hydrophilic amino acids are found on the surface of proteins and will interact with water through hydrogen bonds. Hydrophobic amino acids, which repel water would likely bury themselves at the centre of the protein to avoid having contact with water. Furthermore, hydrogen, ionic, disulphide bonding between side chains can assist in the stabilization of the tertiary structure.

The quaternary structure of a protein is defined by the interaction between two or more polypeptide chains. The polypeptide chains experience various interactions such as van der Walls interactions, ionic, disulphide and hydrogen bonding to create a quaternary structure. Not all proteins have a quaternary structure, however, a good example of a protein associating into multiple polypeptide subunits is insulin. Insulin can form dimers and hexamers that contains 2 and 6 subunits, respectively. The final structure of the protein plays an important role in its function. However, when proteins are misfolded, their functions change and could become toxic to cells and are known to be the main cause of neurodegenerative diseases.

1.2 Intrinsic Amino Acids

Amino acids that have aromatic side chains are important for fluorescence studies as they are able to absorb UV light and can fluoresce. There are only 3 amino acids that are intrinsically fluorescent which are: phenylalanine (Phe), tyrosine (Tyr) and tryptophan (Trp) shown in figure 1.4.

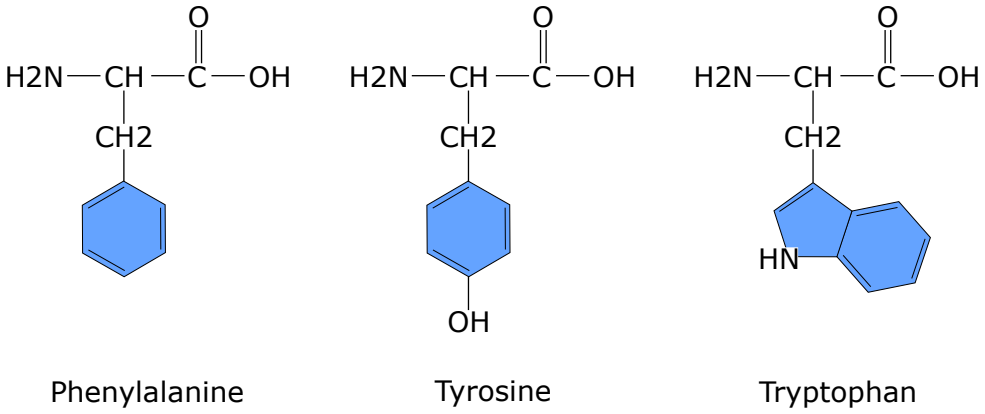

Figure 1.4: Chemical structures of fluorescent amino acids.

Phe has the lowest quantum yield (ratio of the number of photons emitted by the fluorophore to the number absorbed) of 0.04 and displays the shortest absorbance (257 nm) and emission (282 nm) peak wavelengths. The excitation wavelength used for protein studies is typically around 280 nm and therefore, Phe is rarely excited and with such a low quantum yield the fluorescence is barely observed. Tyr has a quantum yield of 0.14 and its peak absorption and emission are around 280 and 303 nm, respectively. Trp has the highest quantum yield of 0.20 and displays an absorbance peak similar to tyrosine's absorbance. However, it exhibits the longest emission peak wavelength around 350 nm. Since the absorbance spectra of Trp is broad, it is typically excited at 295 nm to avoid exciting tyrosine. When Phe, Tyr and Trp are in close proximity to one another, Trp is usually the dominant fluorophore because Phe and Tyr tend to transfer their energy to Trp. Thus, the quantum yield of Phe and Tyr decreases when Trp is present. However, Tyr has been deemed to be a relatively simple fluorophore and is a useful fluorescent probe for protein aggregation in absence of Trp residues. Trp is the most commonly used intrinsic probe due its sensitivity to polar environments, where the emission spectra blue shifts when Trp is buried. Not only is it sensitive to polarity, it is also susceptible to quenchers such as acrylamide, amide, histidine and disulphide groups. Studying protein aggregation with the use of intrinsic amino acids are advantageous as they do not disrupt the aggregation pathway, like extrinsic fluorophores would.

1.3 α-Helical Coiled Coils

An α-helical coiled coil is one of the most common structural motifs in nature, according to primary sequence analysis, it was found that 2-3% of amino acids in all proteins form coiled-coil structures [44]. Our understanding between sequence and structure of coiled coils is in sufficient depth that it is widely exploited for the design of peptides and proteins.

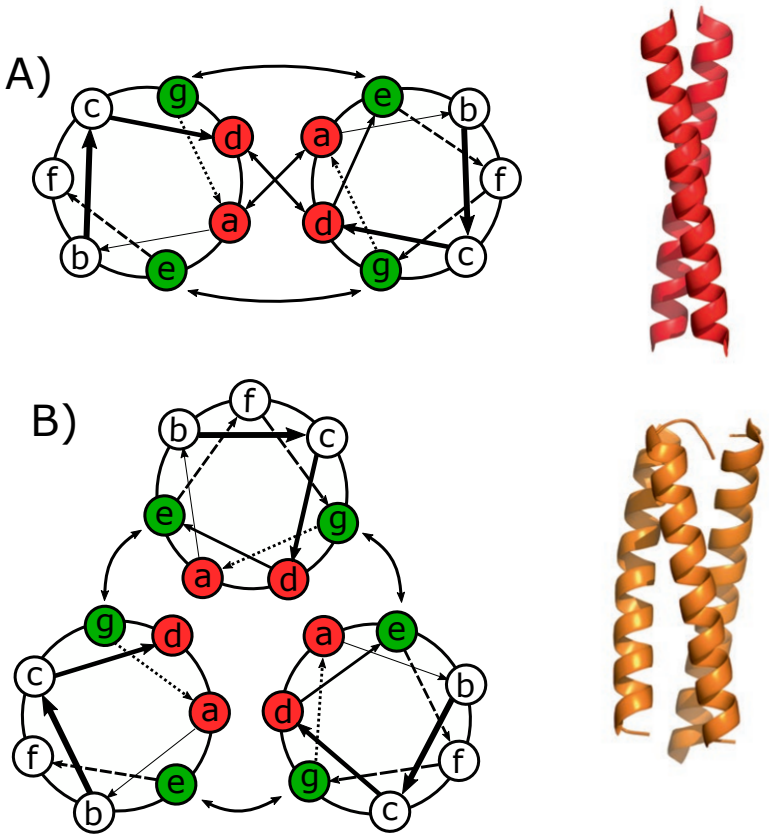

Figure 1.5: Helical wheel diagrams and ribbon structure of A) dimeric and B) trimeric coiled-coil assemblies.

The α-helical coiled-coil primary sequence is often characterized by a heptad repeat of hydrophobic *(H)* and polar *(P)* residues, *HPPHPPP*, which is usually referred to as ***(abcdefg)***$_n$. Where n is the number of repeats, and most coiled coils have four or more heptad repeats. The α-helices are amphipathic, and the hydrophobic residues usually preoccupy the a and d positions. The a and d sites need to be three and

four residues apart because α-helix is 3.6 residues per turn to make an amphipathic structure. However, the heptad repeat has a spacing average of 3.5 residues and therefore, the α- helix in a coiled coil has a different helical pitch and forms a left handed helix. When two or more helices join together to form a coiled-coil, the hydrophobic residues between helices tightly wrap around each other via knobs into holes (KIH) interactions [45] to form a hydrophobic core. Specifically, in coiled coils, the positions *a* and *d* on one helix is referred to as a knob and will go into a hole created by *dgad* residues on the other helix. This results in tight helical packing called supercoiling shown in figure 1.5 C and D. The hydrophobic core is further stabilized by interhelix salt bridges, this is possible when charged side chains are located on positions *e* and *g*.

Since the coiled-coil structures are heavily reliant upon hydrophobic interactions, the residues on the *a* and *d* positions will determine the oligomeric state of coiled-coils. A region of the yeast transcriptional activator GCN4-p1 is a natural coiled-coil that has been mutated and studied to provide straight forward sequence to structure rules [46, 47]. It was shown that isoleucine (Ile) in position *a* and leucine (Leu) in position *d* would yield parallel dimers and only one kind of residue *d* (Ile or Leu) in positions *a* and would lead to trimers. The trimeric state tends to form in peptides and proteins when there is an absence of strong sequence elements [48].

In nature, coiled-coil motifs are blunt ended which means that the α-helical strands are flush with one another. Pandya et al. used the established rules from the leucine zipper to design a self-assembling fibre (SAF) [49]. The leucine zipper was shown to be blunt ended [50], however, SAF peptides were able to form long fibrous structures (several hundred μm long) by creating sticky ended dimers. To promote sticky-ended dimers and trimers, the sequence is split in half. The N-terminal half is positively charged where the Lys occupy the *e* and *g* positions and the C-terminal half is negatively charged, where Glu residues are in positions *e* and *g*.

1.4 Insulin Structure and its Self-Assembly

There are vast amount of proteins that are responsible for different roles in the body of animals and humans. Insulin was discovered in 1921 and due to its significance, it quickly became the most studied protein in biochemistry. Insulin was the first protein to have its chemical sequence established in 1955. Insulin is a hormone that ensures blood glucose levels are stable by enabling glucose cellular uptake. If insulin production is deficient or insulin becomes dysfunctional, it causes diabetes. There are two main types of diabetes, called type 1 and 2. Type 1 diabetes is an autoimmune disease where antibodies attack the pancreas, which is the organ that is responsible for producing insulin. Type 2 diabetes is the most common form for diabetes and it typically develops during adulthood. With this kind of diabetes, the pancreas is unable to produce enough insulin when the body becomes resistant or ignores insulin signals. If there is not enough glucose cellular uptake, it can cause high blood glucose levels called hyperglycaemia. After long periods of time, hyperglycaemia can cause irreversible damage to kidneys, eyes, blood vessels and nerves.

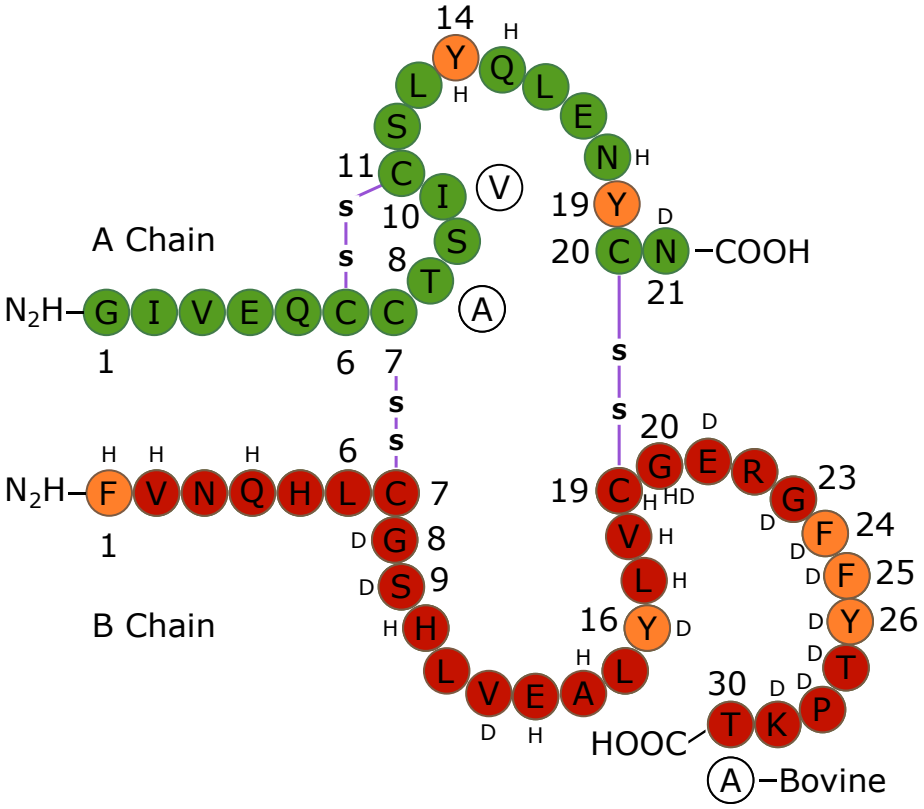

Figure 1.6: The primary sequence of human insulin with substitutions of amino acids shown for bovine insulin (white circles). The A and B chains are depicted with green and red circles, respectively. The disulphide bonds are represented by purple lines and the intrinsic fluorophores phenylalanine (F) and tyrosine (Y) have orange circles. The D and H letters indicate which residues are involved in the dimer and hexamer formation, respectively.

Insulin has two polypeptide chains A and B, which contain 21 and 30 amino acids, respectively. Both chains are helical and linked together with two disulphide bonds between A7 and B7, also with A20 and B19. With another intramolecular disulphide bond in chain A between A6 and A11. In chains A and B there are 4 Tyr (in positions A14, A19, B16, and B26) and Phe (in positions B1, B24, and B25) residues. There are slight amino acid differences in the primary sequence between human and bovine insulin, shown on figure 1.6. The amino acids threonine (Thr), isoleucine (Ile) and Thr on positions A8, A10 and B30 are replaced by alanine (Ala), valine (Val), and Ala, respectively. Even with slight differences, it has been shown that bovine insulin aggregates more readily, which makes it a stronger model to looking at protein aggregation [51].

In nature, insulin contains a mixture of monomers, dimers, and hexamers, which are heavily dependent upon numerous factors such as pH, temperature, agitation, and concentration.

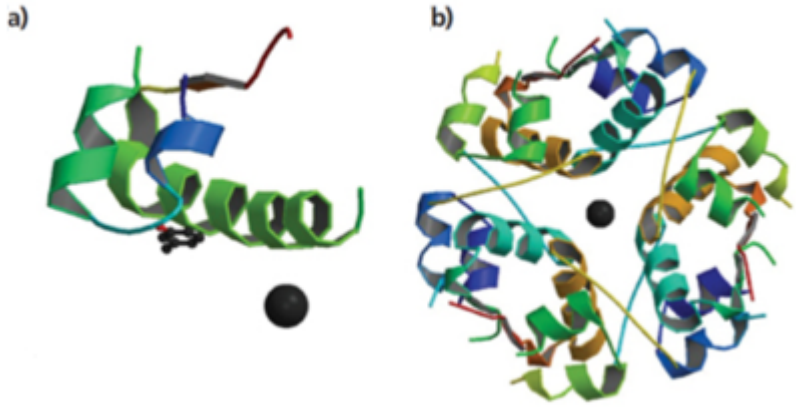

Figure 1.7: Crystal structure of A) monomeric and B) hexameric insulin in the presence of zinc measured by X-ray diffraction, PDB: 1ZEH.

In 1969, X-ray crystallography determined the 3D structure of insulin monomeric and hexameric forms are shown on figure 1.7. The A chain has two helical components which lies in A1-A7 and A14-A20, both α-helices are anti-parallel and are stabilized with disulphide bonds and van der Waals interactions. The A7-B7 disulphide bond is positioned at the surface, however, A20-B19 bond is buried in the hydrophobic core. The first 7 amino acids in the B chain have an extended conformation and is followed by a turn at B8, and the residues B9-B19 have a well-defined α-helix. The amino acids at positions B20-B23 create another turn and a β-strand from B24-B30 lies anti-parallel to the B9-B19 helix. The disulphide chain is responsible for burying A6-A11 and the non-polar side chains A2, A16, B11, B15, and B24 are also buried in the hydrophobic core.

Insulin monomers only exist at low concentrations (<0.2 μM) when the pH is neutral [52]. At higher concentrations at neutral pH, the monomers self-associates to a dimeric formation. Dimer formation is due to the burial of hydrophobic residues with B8, B9, B12, B13, B16, and B24-B28 of two monomers. The burial of aromatic residues

(Tyr B16, Phe B24, and Tyr B26) and the hydrogen bonding between two anti-parallel β-strands (between B24-B26 of both monomers) create a closely packed structure.

It is important for the pancreas to store large amounts of insulin to enable the gradual release of insulin when it is needed. In nature, the hexameric form is the most efficient method of packing as it forms close-packed arrays. This form also ensures proficient conversion of proinsulin to insulin and reduces degradation of the protein [53]. When zinc ions are present, the B10 His side chain from 3 dimers will coordinate around zinc ions (figure 1.7B). The hydrophobic surfaces of the dimers will come into contact with each other (B14 and B17). Due to the non-polar side chain residues, A13 and A14 form a non-polar cavity, which leads to the burial of the B10 side chain from another dimer.

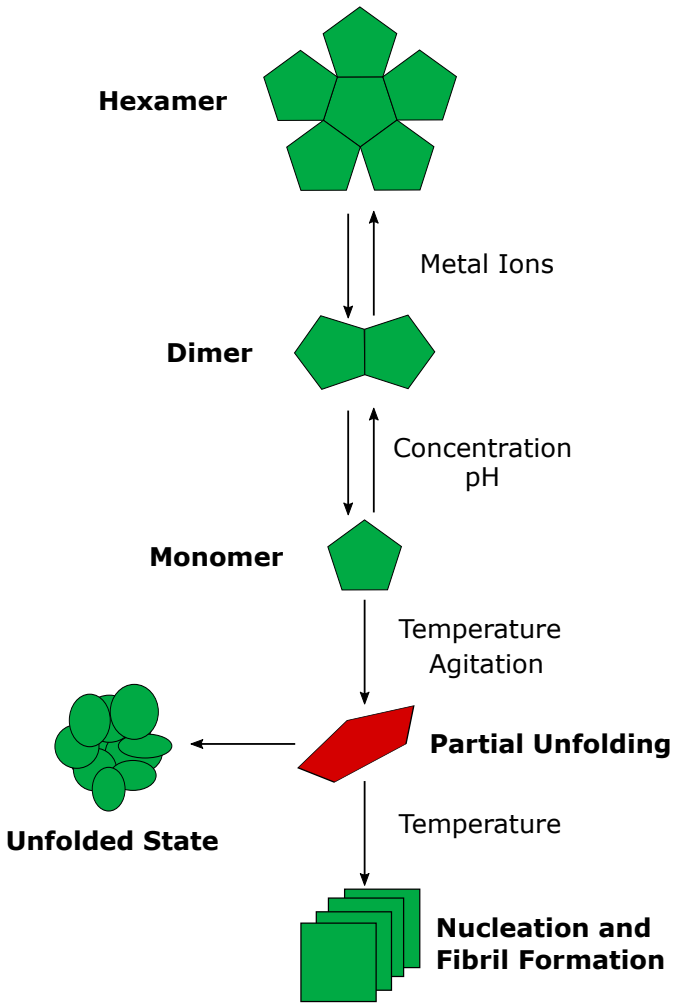

Figure 1.8: Schematic of different conditions create various pathways for insulin.

Monomers and dimers readily form amyloid fibrils compared to hexamers as they are known to be less stable. Amyloid fibrils all share a common cross β-pattern, where the β-sheet strands are perpendicular to the long fibril axis [32]. Amyloid formation is a multi-step process normally defined as the nucleation-dependent polymerization (NDP) that have 3 distinct phases; called the lag, growth and saturation phase. The lag phase comprises of soluble monomeric species forming into a stable nuclei, which acts as a precursor for fibril formation. In the growth phase, the monomers interact with the nuclei to elongate into fibrils. The growth phase grows exponentially compared to the lag phase but they both rates are heavily dependent upon the initial concentration

of monomers. There is a critical concentration of monomers needed to form a nucleus. It has been shown that the elongation of fibrils are due to the addition of monomers instead of oligomers, thus, the growth phase is directly linked to the concentration of soluble monomers. Large distribution of fibrillar lengths are formed during fibril formation because both lag and growth phases occur simultaneously. This means that fibrils with longer lag times, will form nuclei at longer rates, whereas, the process of elongation has already begun for shorter lag times. The heterogeneous kinetics exhibited by natural proteins are more difficult to study. The lag phase has shown to be significantly reduced with the use of agitation or seeds (pre-formed nuclei) [2, 54]. When there are no more soluble monomers left to attach onto the end of the fibril, the fibril is known to be mature. This stage is known as the saturation phase.

Hexamers stabilized with zinc can misfold and dissociate into monomers in acidic pHs and high temperatures (figure 1.8). The monomer then undergoes partial unfolding and changes from a predominantly α-helical to rich in β-sheets [32]. It has been observed that there are specific segments of insulin that are responsible for fibril formation. Ivanova et al. [55] has revealed that the sequence LVEALYL in the B chain (B11-B17) is able to inhibit or accelerate fibril formation of full-length insulin, which is dependent upon its concentration. This shows that the small sequence in the B chain is important for the amylogenic core of the insulin fibril. The amylogenic core are formed by two anti-parallel strands of LVEALYL form a steric zipper. A segment in the A chain (A13-19) LYQLENY has also been observed to contribute to insulin fibrillation. The A chain forms β-sheets and both sheets lie outside of the β-sheets formed by LVEALYL. The A chain stabilizes the β-sheets formed by LVEALYL because hydrogen bonds are created between the tyrosine-tyrosine interactions present in both LYQLENY and LVEALYL β-sheets. It has been found from mass spectroscopy that the disulphide bonds of the native protein are still intact when amyloid formation is complete [20]. The disulphide bonds between two parts of the A chain gives the β-strand a curved shape which tightly compacts the protofilament. The protofilament was found to have a cross section of 30 x 40 Å [32]. The twist of the protofilaments are dictated by the twist of the β-strands in β-sheets, and the protofilaments that wrap together to create a

fibril. With the use of electron microscopy, insulin fibrils have been observed to have widths of 5-8 nm and lengths of a few micrometres. Widths increased to ranges around 10-20 nm when a few fibrils wrapped together [56, 57].

1.5 Insulin Glycation

When hyperglycaemia occurs for long periods of time due to insulin resistance and diminished insulin secretion, insulin is vulnerable to non-enzymatic glycation [58, 59]. Glucose levels around 33.3 mM in animal studies has been shown to have higher levels of glycated insulin compared to normal glucose levels of 5.6 mM [60]. Glycation is well known to play a major role in the development of diabetes as it results in the inability for insulin to regulate glucose homeostasis [58, 59]. Glycation can also decrease the clearance of insulin on its receptor, which leads to the increase of insulin resistance [61]. Glucose has been shown to react with lysine (Lys) on B29 and with the N-terminus on both chains A and B [60, 62]. In animal models, it has been shown that 8-11% of insulin is glycated inside the pancreas [58,59]. However, it also affects the structure and stability of many plasma proteins including as haemoglobin and serum albumin, which may suggest that glycation can also happen in the bloodstream. Depending upon the conditions that glycation is in, it has been shown either to accelerate or inhibit amyloid formation [63]. Under reducing conditions, a reducing agent $NaBH_3CN$ is used and the chemical is able to unfold the protein, and thus, accelerate fibril formation whilst being able to glycate most site within insulin. Whereas, in non-reducing conditions, Phe (B1) or Lys (B29) sites are modified with glucose and has been shown to inhibit amyloid formation [62]. Using mass spectroscopy, glucose binding sites have been found at Lys (B29) in chain B and in the N-terminus of both chains A and B [60, 62]. From nuclear magnetic resonance nuclear Overhauser effect spectroscopy experiments, it was found that valine (Val) (B2) and leucine (Leu) (B17) were the best residues for glucose interactions [64], and molecular dynamics simulations showed that glucose had a large affinity toward the hydrophobic pocket between Val (B2) and Leu (B17) [65].

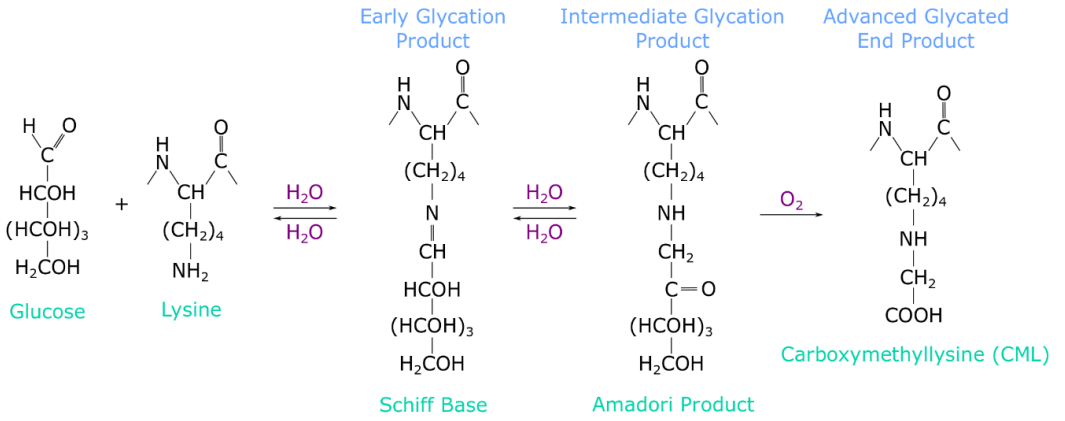

Figure 1.9: The pathway for the production of advanced glycated end products (AGEs).

Protein glycation is a post translation modification where free amino group such as the side chains of arginine (Arg), Lys, N-terminus of proteins, and thiol groups of cysteine residues react with a carbonyl group of a reducing sugar (shown on figure 1.9). Through a condensation reaction, the early Maillard reaction forms a Schiff base. The Schiff base rearranges itself into a more stable Amadori product. In the late stage of glycation, advanced glycated end (AGEs) products are produced through oxidation and dehydration reactions. AGEs are tightly bound to the protein and it effects long-lived proteins as this process is occurs over a course of several weeks. AGEs are able to cross link between proteins and protein aggregates, through the bonding of lysine and arginine residues [66]. When cross-linking occurs, proteins become rigid and cross-linking is accelerated in diabetic patients due to the high levels of glucose.

Chapter 2

Principles of Photophysics

2.1 Basic Principles of Fluorescence

Molecules are excited when they absorb photons at a specific wavelength and they discard their excess energy through non-radiative and radiative processes. A Jablonski energy level diagram is typically used to illustrate the relaxation pathways involved after the excitation of a fluorophore, shown in figure 2.1.

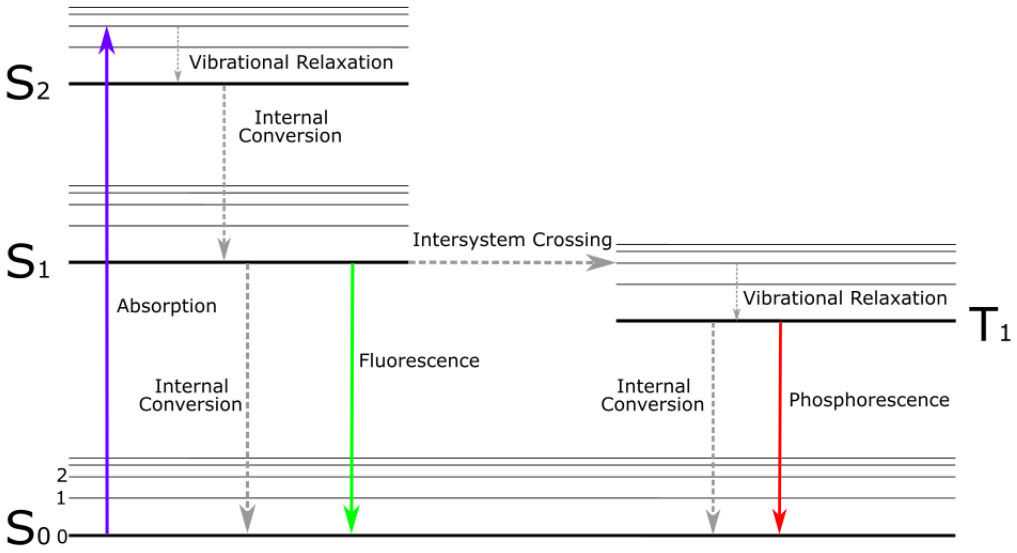

Figure 2.1: Jablonski diagram which illustrates the pathway of photon absorption (purple line), emission (green and red line), and non-radiative pathways (grey dashed lines).

The Jablonski diagram shows two groups of excited states determined by spin multi-

plicity called singlet and triplet states. Singlet electronic states split into ground (S_0), first (S_1) and second (S_2) electronic states. In singlet states, the electron in S_1 or S_2 has the same spin as the electron residing in the ground state. Whereas, (T_1) represents the excited electronic level within the triplet state and the electron in the excited orbital has a different spin to when the electron is in the ground state. Each electronic state consists of vibrational energy levels 0, 1, 2, etc. and rotational levels (not shown). Wavenumbers are directly proportional to the energy of a photon and therefore, transitional differences are often expressed in cm^{-1}. The wavenumber difference between electronic, vibrational, and rotational energy levels are around 30,000, 1,000 and 10 cm^{-1}, respectively. The wavelength is defined by the length of a single wave (the distance between one peak to the next), whereas the wavenumber is the number of waves per unit distance. Typically, at room temperature, the fluorophores populate the ground state at the lowest vibrational energy level. The absorption of photons by molecules occur at specific energies and as a result, the fluorophore transitions from (S_0) to a higher vibrational energy level of (S_1) or (S_2) in a timescale of $\sim 10^{-15}$ s. The energy of the photon is proportional to the wavenumber but inversely proportional to the wavelength, shown in equation (2.1).

$$E = \frac{hc}{\lambda} = h\nu c \tag{2.1}$$

where E is the photon energy, h is Planck's constant, ν is the wavenumber, λ is wavelength, and c is the speed of light. The energy of a state is the sum of vibrational E^{vib}, electronic E^{el}, and rotational E^{rot} energies:

$$E_{Snm} = E^{el}_{Sn} + E^{vib}_{Snm} + E^{rot}_{Snmo} \tag{2.2}$$

where n, m, and o are the number of electronic, vibrational, and rotational states, respectively. Rotational energies are considerably smaller compared to electronic and vibrational states and therefore, they are normally neglected to simplify calculations.

After the absorption of a photon, the fluorophore can undergo many pathways to relax back to the ground state. One of the pathways is internal conversion which

dissipates energy non-radiatively between two excited singlet states ($S_{2,m}$) to the lowest vibrational mode in ($S_{1,0}$) over a timescale of ~10^{-12} s. The energy of a photon emitted between two electronic states is equal to the energy gap $E_{Sn'm'} - E_{Snm}$:

$$hc\upsilon_{SnmSn'm'} = (E^{el}_{Sn'm'} - E^{el}_{Snm}) + (E^{vib}_{Sn'm'} - E^{vib}_{Snm}) \tag{2.3}$$

Due to internal conversion and vibrational relaxation from intermolecular collisions, the emission of a photon occurs from the lowest excited state ($S_{1,0}$) to ($S_{0,m}$). Therefore, in general the emission spectrum is independent of the excitation wavelength, described by Kasha's Rule [67]. The emission spectrum $G(\nu)$ is given by:

$$G(\nu) = \sum_m \frac{64\pi^4\nu^3}{3h}|\mu_{S0mS10}|^2\delta(\nu - \nu_{S0mS10}) \tag{2.4}$$

where $\delta(\nu - \nu_{S0mS10})$ is the delta function of a photon position after absorption and radiative decay and $|\mu_{S0mS10}|^2$ is the probability of electric dipole radiation. For fixed-nuclei, the electronic transition dipole is equal to $|\mu_{SnSn'}|^2 FCF_{SnmSn'm'}$ where $FCF_{SnmSn'm'}$ is the Franck-Condon factor and equation (2.4) can be simplified to:

$$G(\nu) = a\nu^3 S_{vib}(\nu - \nu_{S01})|\mu_{01}|^2 \tag{2.5}$$

where the constant $a = (64\pi^4)/3h$ and $S_{vib}(\nu)$ is the function which represents all the vibrational modes:

$$S_{vib}(\nu) = \sum_m FCF_{S0mS10}\delta\left(\nu - \frac{E^{vib}_{S10} - E^{vib}_{S0m}}{hc}\right) \tag{2.6}$$

where $\nu_{S01} = \frac{1}{hc}(E^{el}_{S1} - E^{el}_{S0})$.

Generally, the emission and absorption spectrum are mirror images because the vibrational levels in the ground and excited states have similar spacing. Also, the emission spectrum will be shifted to longer wavelengths since the absorption of a photon occurs at higher energies than the emission. This is known as the Stokes shift. The Stokes shift of a fluorophore can increase through the increase in temperature, collisions in the excited state, energy transfer, and solvent effects.

The radiative process is known as luminescence and is split into two categories called fluorescence and phosphorescence which are dependent on their electronic spin. Fluorescence occurs within the singlet state and as the spin multiplicity obeys the Pauli Exclusion Principle, the relaxation upon the ground state occurs within a few nanoseconds ($\sim 10^{-9}$ s). Phosphorescence occurs within the triplet state, where the excited electron changes its spin from (S_1) to the excited triplet state (T_1) via intersystem crossing. The triplet transition is "forbidden" since the electron in the triplet state has the same spin as the electron in the ground state which violates the Pauli Exclusion Principle. Therefore, the probability of the electron transitioning from (T_1) to (S_0) is finite and as a result, the process is long lived $\sim 10^{-6}$ to 10^{-3} s. Phosphorescence occurs at longer wavelengths compared to fluorescence because the energy level of the triplet state is lower than the singlet state.

2.2 Quantum Yield

The fluorophores can return to the ground state either radiatively (k_r) or non-radiatively (k_{nr}), and the brightness of a fluorophore depends on the number of emitted photons compared to the number absorbed. The ratio between emitted and absorbed photons is called the quantum yield (ϕ) and can be calculated in terms of (k_r) and (k_{nr}).

$$\phi = \frac{k_r}{k_r + k_{nr}} \tag{2.7}$$

If the radiative decay rate is much larger than the non-radiative rate, the quantum yield could be close to 1. However, it can never be higher than 1 since not all absorbed photons are emitted. Quantum yield measurements are useful as it provides information on how the fluorophore reacts to different temperatures, pH, and viscosity as they can alter the contribution of non-radiative decay rates.

2.3 Fluorescence Lifetime

The fluorescence lifetime of a fluorophore is the average time that the fluorophore remains in the excited state before de-populating to the ground state. The average time is taken because the emission of a photon is a random process and the time it takes for each fluorophore to reach the ground state does not equal the fluorescence lifetime. The fluorescence lifetime is given by:

$$\tau_f = \frac{1}{k_r + k_{nr}} \tag{2.8}$$

where τ_f is the fluorescence lifetime. The natural lifetime (τ_n) of a fluorophore occurs when there are no extrinsic factors affecting the time spent on the excited state. Therefore, the non-radiative decay rate is 0 and the quantum yield is 1. The natural fluorescence lifetime is described by the equation below:

$$\tau_n = \frac{1}{k_r} \tag{2.9}$$

In time resolved fluorescence measurement, it measures the fluorescence intensity decay of a fluorophore following a short excitation pulse (δ-function). The diagram below shows a simplified version of the Jablonski diagram:

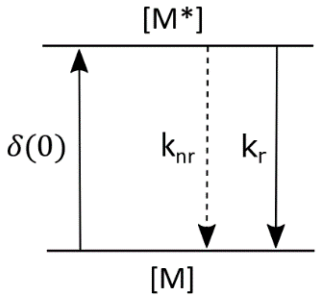

Figure 2.2: Simplified Jablonski diagram to explain the kinetics of fluorescence lifetime. Where $\delta(0)$ (solid line), k_{nr} (dashed line) and k_r (solid line), represents a short excitation pulse, non-radiative decay rate and radiative decay rate, respectively.

The kinetics of the fluorescence lifetime in the simplest case can be fitted using a mono-exponential decay:

$$\frac{d[M^*]}{dt} = -(k_r + k_{nr})[M^*] \tag{2.10}$$

where $[M^*]$ is the population of the excited state at time t in the Birks notation. Equation (2.10) is substituted with equation (2.8) and integrated to give:

$$[M^*] = [M^*]_0 \exp\left(-\frac{t}{\tau_f}\right) \tag{2.11}$$

where $[M^*]_0$ represents the initial population of the excited state at time $t = 0$. The fluorescence intensity is proportional to $[M^*]$, therefore equation (2.11) becomes:

$$I(t) = I_0 \exp\left(-\frac{t}{\tau_f}\right) \tag{2.12}$$

Since the fluorescence intensity is proportional to excited state population, the fluorescence lifetime can be calculated by measuring the time it takes for the fluorescence intensity to fall to $1/e$ or 36.8% of its initial value at time = 0. Most fluorophores in dilute solution have a single exponential decay.

2.4 Solvent Relaxation

The emission spectra of polar fluorophores are extremely dependent on solvent polarity which creates an increased red shift in the Stokes' shift. Solvent effects occur between the fluorophore and the surrounding solvent molecules, and the effect is depicted in figure 2.3:

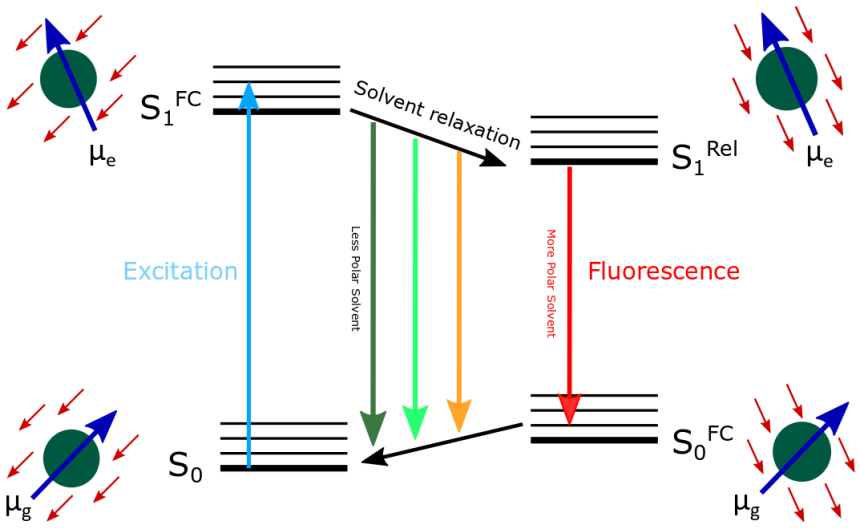

Figure 2.3: Solvent relaxation diagram. Where the solvent dipoles (small red arrows) surrounding the fluorophore dipoles (dark blue arrow) shows different orientation in the ground state (S_0), unstable Franck-Condon energy state (S_1^{FC}), lower excited state energy levels (S_1^{Rel}) or the ground Franck-Condon energy state (S_0^{FC}).

Generally, the fluorophore in the ground state has a smaller dipole moment (μ_g) than in the excited state (μ_e). In the ground state, the fluorophore and solvent dipoles align with each other which minimizes the total potential energy of the system. From the Franck-Condon principle, upon excitation the transition from the ground to the excited state is too fast for the nuclei to change their configuration. Since the electrons are smaller than the nuclei, the fluorophore's dipole moment can reorient after excitation and create an unstable Franck-Condon energy state S_1^{FC}. After some time, the solvent dipole moments can reorient or relax to lower excited state energy levels S_1^{Rel}. The emission of a photon changes the dipole moment back to μ_g orientation and the solvent envelope eventually relaxes back to the ground state. Relaxation of the solvent dipole is greater when solvent polarity and dipole moment of the fluorophore is large. Therefore, the emission of photons will occur at longer wavelengths. In contrast, non-polar fluorophores are less responsive to solvent effects.

2.5 Dielectric Relaxation

Heterogeneous models like protein produce complex dielectric properties compared to simple fluorophores in bulk solvents. By studying the dielectric properties within protein, we can study protein stability and its structural characteristics. Protein stability and structure is governed by hydrogen bonds, covalent bonds, van der Waals forces and hydrophobic interactions [68]. These bonds and interactions play an important role in the dielectric properties of protein as well as its stability. There are two types of dielectric materials: polar and non-polar. A polar dielectric material has a dipole moment with or without an external electric field present. A non-polar dielectric is when the material only has a dipole moment in the presence of an electric field. Once an electric field is applied to the non-polar dielectric material, the centre of positive and negative charge will separate in the direction of electric field. After applying the external electric field, the dipole moments remain polarized for a finite amount of time before they return to their randomized orientations. Protein are known to have polarized dielectric characteristics because they are made up of repeating polar amino acid units, (-CO-CR-NH-) [69].

2.6 Fluorescence Quenching

The fluorescence quantum yield can be reduced by a number of processes, known as quenching. Static and dynamic quenching are two forms of fluorescence quenching which involves close interactions between external molecules (or quencher) and the fluorophore.

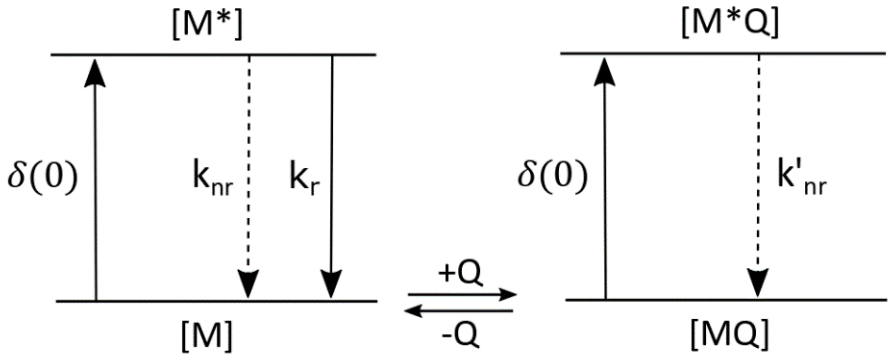

Figure 2.4: Static quenching diagram. Where $\delta(0)$ (solid line), k_{nr} (dashed line) and k_r (solid line), represents a short excitation pulse, non-radiative decay rate and radiative decay rate, respectively. When a quencher (Q) is added, it usually creates non-fluorescent complexes [MQ] and produces a non-radiative decay rate k'_{nr} (dashed line).

In static quenching, the quencher (Q) forms non-fluorescent complexes with the fluorophore in the ground state. As shown in figure 2.4, the non-fluorescent complex is able to absorb a photon but the non-radiative constant k'_{nr} is much larger than the radiative decay rate k_r, which becomes negligible. Static quenching can be described mathematically by the Stern-Volmer equation:

$$\frac{I_0}{I} = \frac{[M]_0}{[M]} = 1 + K_s[Q] \tag{2.13}$$

where $[M]_0$ and I_0 is the fluorophore concentration and fluorescence intensity in the absence of a quencher, respectively. $[M]$ and I is the fluorophore concentration and fluorescence intensity in the presence of a quencher, respectively. $[Q]$ is the concentration of the ground state quencher and K_s is the association constant of the complex that determines how sensitive the fluorophore is towards the quencher, which is described by:

$$K_s = \frac{[MQ]}{[M][Q]} = \frac{[M]_0 - [M]}{[M][Q]} \tag{2.14}$$

where [MQ] is the concentration of the non-fluorescent complex. To observe static quenching, the absorption spectrum for the fluorophore in the presence of quencher and without must be compared as there is an effect on the ground state kinetics. As the quencher does not affect the excited-state kinetics, it only decreases the rate of radiative decay but there is no change in the fluorescence lifetime. There are some well-known examples of static quenchers such as, carbon nanotubes [70] and graphene oxide [71].

Dynamic quenching differs from static quenching because the molecules collide with the fluorophore in the excited state [M^*]. After this interaction, the fluorophore returns to the ground state without the emission of a photon and the excitation energy is dissipated as heat. Since dynamic quenching occurs in the excited state, the quantum yield as well as the fluorescence lifetime are both reduced.

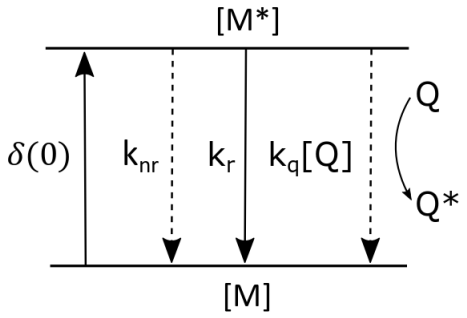

Figure 2.5: Schematic of dynamic or collisional quenching. Where $\delta(0)$ (solid line), k_{nr} (dashed line) and k_r (solid line), represents a short excitation pulse, non-radiative decay rate and radiative decay rate, respectively. When the quencher collides with the fluorophore in the excited state [M^*], the quenched radiative decay is represented by $k_q[Q]$ (dashed line).

For dynamic quenching, the concentration of the excited fluorophore [M^*] depopulates the excited state at a rate of:

$$\frac{d[M^*]}{dt} = -\left(k_r + k_{nr} + k_q[Q]\right)[M^*] \tag{2.15}$$

where k_q is the quenching constant. By substituting equation (2.8) into equation (2.15), the equation becomes:

$$\frac{d[M^*]}{dt} = -\left(\tau_0^{-1} + k_q[Q]\right)[M^*] \tag{2.16}$$

where τ_0 is the unquenched lifetime. The ratio of the fluorescence intensity is equal to the ratio of fluorescence lifetime with and without quencher. Therefore, the fluorescence lifetimes can be included in the Stern-Volmer equation:

$$\frac{\tau_0}{\tau} = \frac{I_0}{I} = \frac{\tau_0^{-1} + k_q[Q]}{\tau_0^{-1}} = 1 + \tau_0 k_q[Q] \tag{2.17}$$

where τ is the lifetime in the presence of a quencher. To analyse the quenching process, it is common to plot the Stern-Volmer plot (I_0/I or τ_0/τ against quencher concentration). A linear plot represents one fluorescent species present and the nonlinear plot gives an indication of multiple fluorophores present in the quenching process. The Stern-Volmer quenching constant K_s is equal to the gradient found in the plot where a high K_s value represents fluorophores that are more accessible to quenchers than low K_s values. A wide range of heavy atoms such as molecular oxygen [72] and iodide ions [73] can be used as dynamic quenchers because they promote intersystem crossing to the triplet state.

The easiest method to determine whether the dominant quenching process is static or dynamic is to plot a Stern-Volmer graph at various temperatures. An increase in temperature leads to an increase in collisional rates in the dynamic quenching process, however, it also dissociates the ground complexes created in static quenching. Therefore, when the temperature increases, the Stern-Volmer quenching constant will increase and decrease in the dynamic and static quenching processes, respectively.

2.7 Fluorescence Resonance Energy Transfer

Fluorescence resonance energy transfer (FRET) is a widely used technique to investigate molecular interactions in vivo. Due to its sensitivity towards distances ranging

from 1 to 10 nm, FRET enables the investigation of protein-protein interactions [74], ligand binding to a receptor [75], and protein aggregation [76]. FRET is a non-radiative transfer between nearby donor and acceptor fluorophores through dipole-dipole interactions. In FRET, energy transfer occurs between the excited state the donor and the ground state of the acceptor fluorophore without the emittance (donor) or absorption (acceptor) of a photon.

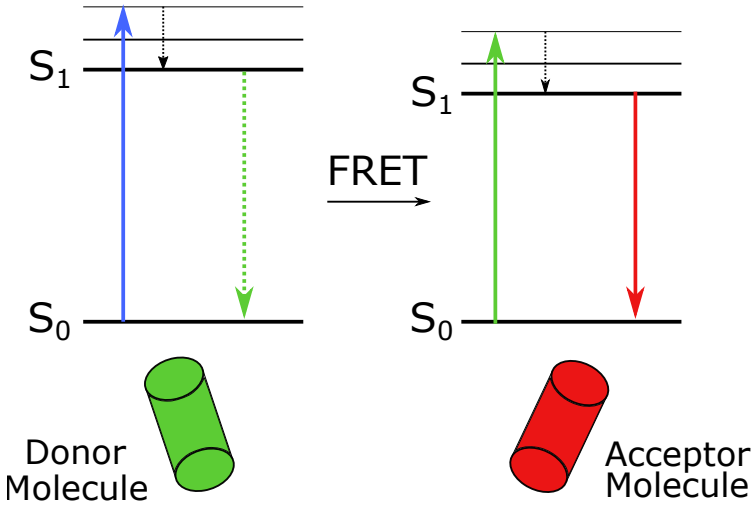

Figure 2.6: Jablonski diagram of energy transfer between a donor and acceptor molecule.

The donor is promoted to the excited state (S_1) at a specific wavelength and quickly relaxes to the lowest vibrational level of the excited state via interconversion (shown on figure 2.6). In the case of FRET, the fluorophore can either decay back to the ground state (through non-radiative decay or emit a photon) or energy transfer to the acceptor can occur. Where the excited fluorophore has a similar resonance frequency as the nearby acceptor dipole (< 10 nm). The energy transfer depends upon the spectral overlap of the emission spectrum of the donor and the absorption spectrum of the acceptor (shown on figure 2.7).

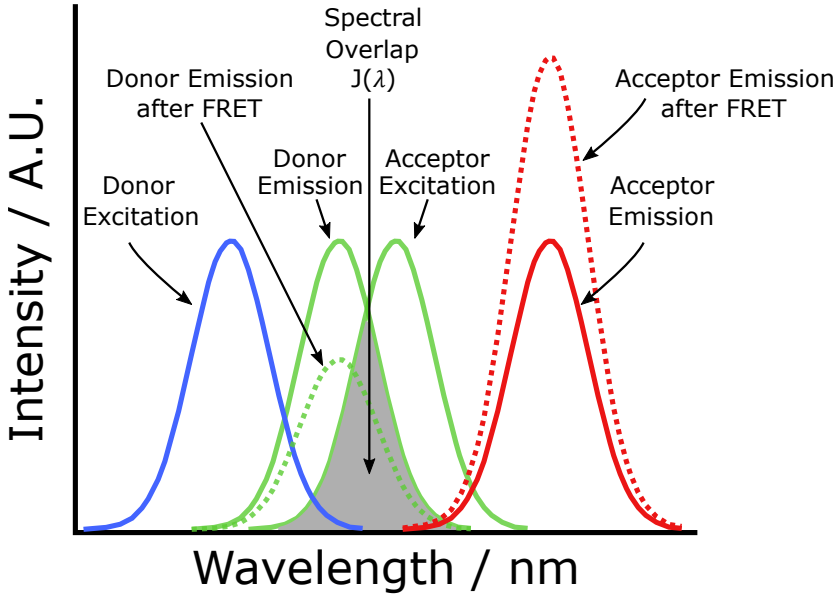

Figure 2.7: The absorption and emission spectra of an ideal donor and accepter pair.

When the donor transfers energy to the acceptor, the fluorescence of the donor will be quenched, however, the fluorescence of the acceptor will be enhanced. The efficiency of energy transfer E is the number of excited donors that transfer the energy to the acceptor over the number of photons absorbed by the donor, which is given by:

$$E = \frac{k_T}{k_T + \tau_D^{-1}} \tag{2.18}$$

where τ_D is the fluorescence lifetime decay of the donor without an acceptor and k_T is the energy transfer rate from the donor to acceptor which is given by:

$$k_T = \frac{1}{\tau_D}\left(\frac{R_0}{r}\right)^6 \tag{2.19}$$

where R_0 is the Förster distance which is the distance at which the efficiency is 50%, where half of the donor molecules transfer energy to the acceptor, and r is the distance between donor and acceptor. Energy transfer also depends upon the distances between the donor and acceptor and equation (2.18) and equation (2.19) can be rearranged to give:

$$E = \frac{R_0^6}{R_0^6 + r^6} \tag{2.20}$$

The energy transfer dependence upon distance is shown in figure 2.8.

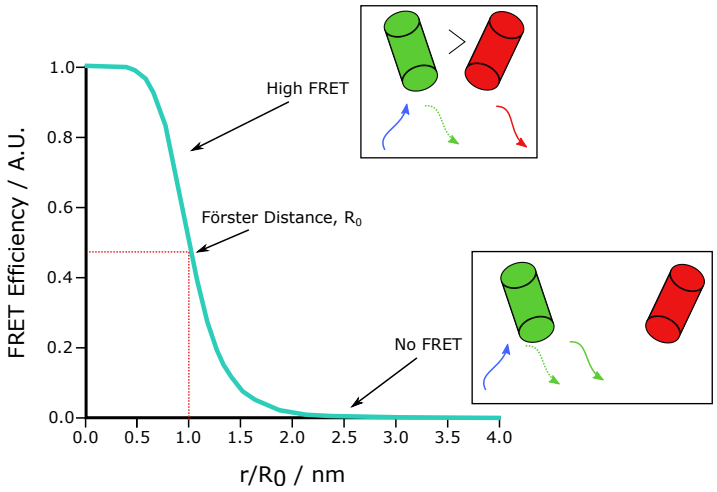

Figure 2.8: The FRET efficiency as a function of distance between the donor and acceptor.

When the donor and acceptor distance is smaller than the Förster distance, the FRET efficiency is above 50% and dramatically increases to 100% at 0.5 R_0. Whereas, when r is double the distance of R_0, the transfer efficiency decreases to 0%. The Förster distance is dependent upon many factors which is given by:

$$R_0 = 0.211(\kappa^2 n^{-4} Q_D J(\lambda))^{1/6} \tag{2.21}$$

where κ is the orientation between donor and acceptor dipoles, n is the refractive index of the medium, Q_D is the quantum yield of the donor in absence of the acceptor, and $J(\lambda)$ is the spectral overlap between the emission spectra of the donor and the absorption spectra of the acceptor, shown in figure 2.7.

2.8 Fluorescence Anisotropy

When the fluorophore is excited with polarized light, the fluorescence emitted by the fluorophore will also be polarized and exhibit different intensities depending upon the

axis of polarization. Fluorescence anisotropy r, measures the extent of polarization of fluorescence, and samples showing anisotropies not equal to zero, display polarized emission. In solution, the dipole moments of the fluorophores in the ground state are randomly orientated. When dipole moments of the fluorophore aligns with the direction of polarized light, the fluorophore is promoted to the excited state. Therefore, the fluorophores in the excited state are polarized. The fluorophore can be depolarized through processes such as Brownian rotational diffusion and FRET. In experiments, the fluorophores are excited with vertically polarized light and the emission is measured at vertical and horizontal polarization planes with polarizers. The time-resolved anisotropy is given by:

$$r(t) = \frac{I_{\parallel}(t) - GI_{\perp}(t)}{I_{\parallel}(t) + 2GI_{\perp}(t)} \tag{2.22}$$

where $I_{\parallel}(t)$ is the intensity measured when the excitation and emission polarizers are both vertically orientated, and $I_{\perp}(t)$ is the intensity measured when the polarizers are vertically and horizontally polarized, respectively. The denominator in equation (2.22) is equal to the total intensity, I_T because all fluorophores have an x, y and z axis. Suppose that the x axis = vertically polarized light and y axis is horizontally polarized, the z axis cannot be measured but still needs to be accounted for. The z axis is perpendicular to the x axis, which means the z axis intensity will be equal to $I_{\perp}(t)$. Therefore, all planes of polarization are considered in I_T. The instrument may have a sensitivity bias towards one polarization orientation and therefore, the differences need to be corrected, this can be performed with the G factor, given by:

$$G = \frac{I'_{\perp}(t)}{I'_{\parallel}(t)} \tag{2.23}$$

where $I'_{\parallel}(t)$ and $I'_{\perp}(t)$ the excitation light is horizontally polarised and the emission are horizontally and vertically polarized, respectively. The anisotropy decays as a function of:

$$r(t) = r_0 \exp\left(-\frac{t}{\tau_r}\right) \tag{2.24}$$

where τ_r is the rotational correlation time for the fluorophore and r_0 is the anisotropy at $t = 0$, where r_0 is given by:

$$r_0 = \frac{2}{5}\left(\frac{3cos^2\beta - 1}{2}\right) \tag{2.25}$$

where β is the angle between the excitation and emission dipoles when the dipoles are both parallel, the maximum value of $r_0 = 0.4$ and when they are in perpendicular orientation, $r_0 = -0.2$. The anisotropy value is zero when $\beta = 54.7°$ and this is known as the magic angle. Therefore, when collecting fluorescence lifetime decay data, the emission polarizer is set to the magic angle to eliminate depolarization effects such as FRET which can alter the decay of the fluorescence and which results in false fluorescence decay values.

2.9 Blinking Fluorophores

In optical microscopy, the spatial resolution is limited to around 250 nm due to the diffraction barrier. Objects closer than 250 nm becomes blurred due to the overlapping of the point spread function (PSF) of the fluorophores. In order to break the diffraction barrier, innovative methods need to be used to circumvent the overlay of PSFs. Single molecules can be localised with the use of photoswitchable fluorophores. Photoswitchable fluorophores are able to transition between the singlet and triplet states a number of times before completely photobleaching. The triplet state is known as the non-fluorescent or "OFF" state where the fluorophore has a lifetime of a few μs to s. Photoswitching buffers are used to extend the lifetime of the fluorophores in the triplet state, minimize photobleaching, and quenches the triplet state to the singlet state. When the majority of fluorophores are in their OFF states, the fluorophores in the singlet state emit stochastically and the probability of PSFs overlapping is limited. Therefore, it is possible to locate each fluorophore with high precision by fitting a 2D Gaussian model. This technique is known as single-molecule localisation microscopy (SMLM).

Chapter 3

Experimental Methods

3.1 Fluorescence Spectroscopy

There are experimental methods that we can use to yield information from the fluorophores which are discussed in the previous chapter. The absorption spectrum is sensitive to the solvent molecules near the absorbing molecules but insensitive to molecular dynamics. However, the emission measurement can detect interactions between other molecules because the fluorescent molecules remain in the excited state for a longer period. The absorption and emission spectra are known as steady-state measurements where the sample is irradiated by a continuous light source and the spectrum is averaged over time. Due to the time-averaging procedure, processes that are time-dependent is lost. Time-resolved fluorescence measurements are able to extract more in depth information about the local environment of the fluorophore. These measurements use pulsed light to illuminate the sample and intensity decays are recorded. The time-resolved measurement can detect the time the fluorophore spent in the excited state, known as the lifetime. This, in turn, can determine conformational changes of the fluorophore, inter- and intra-molecular distances and binding interactions.

3.1.1 Steady-State Absorbance

UV-Vis Spectroscopy can measure transitions from the ground state to the excited state across the ultraviolet to visible spectrum. The UV-Vis spectrometer uses two radiation

sources to excite a large range: a deuterium lamp (190-350 nm) and halogen lamp (300-1100 nm). When operating in the visible range, the mirror reflects the halogen light through the filter wheel whilst simultaneously blocking the radiation of the deuterium lamp. In the ultraviolet range, the mirror is raised to allow the radiation through the filter wheel. Switching of the sources and the movement of the filter wheel are both in synchronization with the grating monochromator. The monochromator disperses the incident light to produce a spectrum and the monochromator is able to rotate, which selects a narrow band of wavelengths through slit 2 towards a mirror. The mirror reflects the beam and it gets split into two different paths by a beamsplitter. One beam goes through the sample in the cuvette and the other beam goes through an identical cuvette and contains only the solvent. Both beams are detected and compared. The intensity detected from the reference compartment is defined by $I_0(\lambda)$ as little absorbance occurs, which produces a baseline and the intensity detected after sample absorption is $I(\lambda)$.

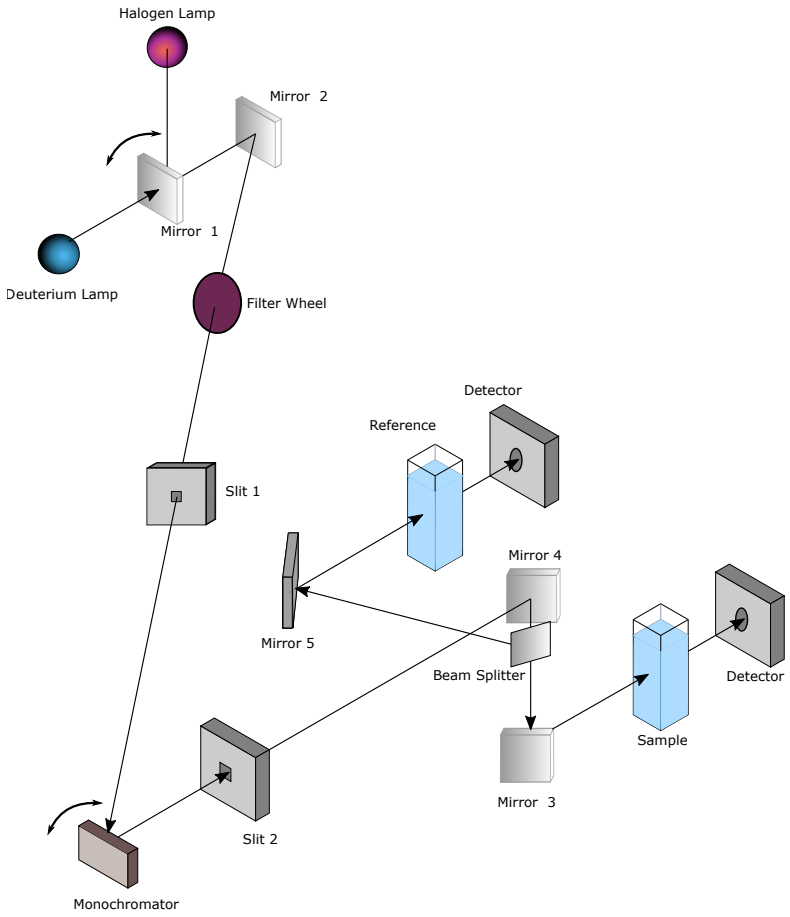

Figure 3.1: Schematic of UV-Vis spectrometer apparatus.

The absorbance $A(\lambda)$ is given by:

$$A(\lambda) = log\frac{I_0(\lambda)}{I(\lambda)} = -logT(\lambda) \tag{3.1}$$

where $T(\lambda)$ is the transmission after passing through the sample. The intensity of the sample is subtracted from the baseline to ensure that the absorbance of the sample is not influenced by the cuvette or solvent. Since the sample and reference chambers are illuminated simultaneously, the fluctuations in intensity from the output source are cancelled out.

Many physical parameters can be extracted from the absorbance via the Beer-Lambert law:

$$I(\lambda) = I_0(\lambda) \exp -\epsilon(\lambda)cl \tag{3.2}$$

thus the absorbance can be expressed as:

$$A(\lambda) = \epsilon(\lambda)cl \tag{3.3}$$

where the absorbance $A(\lambda)$ is directly proportional to the path length l, the molar extinction coefficient $\epsilon(\lambda)$, and the molar concentration c. The extinction coefficient is defined by how efficient the material is at absorbing light at a specific wavelength, per molar concentration. As the Beer-Lambert law gives a linear dependence, absorbance measurements are often used to calculate the concentration of the sample. However, there are a few exceptions where the Beer-Lambert law is not obeyed. For instance, molecules at high concentrations can change the extinction coefficient of the sample due to electrostatic interactions between molecules [77], particles that highly scatter [78,79], and the formation of aggregates [80–82]. Biological samples are good examples of this as they create large aggregates which scatter light resulting in Rayleigh scattering. As the absorption spectrometer will not differentiate scattered light, but merely detect light attenuation, the scatter could be interpreted as absorbed light. The intensity of Rayleigh scattering is proportional to $1/\lambda^4$.

3.1.2 Steady-State Fluorescence

There are key differences between the spectrophotometer and the spectrofluorimeter, where the latter uses a xenon lamp instead of the halogen and deuterium lamp. The excitation and emission monochromators are positioned perpendicular to each other to reduce the amount of excitation light being recorded by the detector. The xenon lamp with a large range of wavelengths (UV to IR) irradiates the excitation monochromator which chooses the desired wavelength to excite the fluorescent sample. The excited sample will emit a range of wavelengths which will pass through the emission monochromator onto the detector.

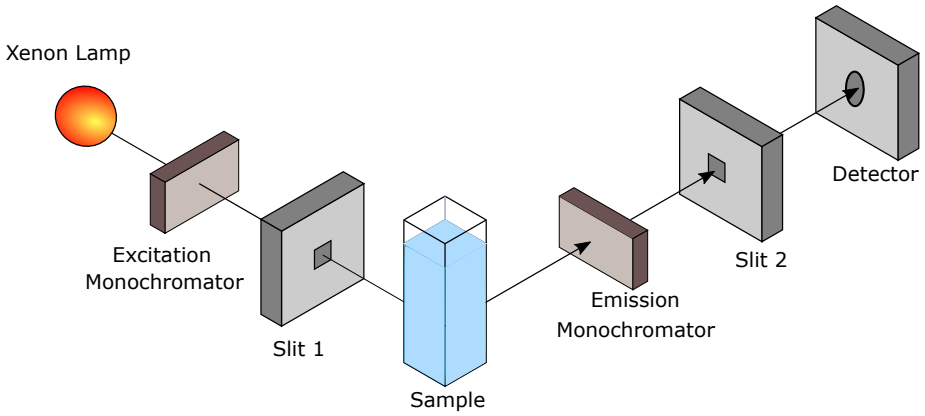

Figure 3.2: Schematic of the spectrofluorimeter apparatus.

In comparison to absorbance measurements, which are relative, fluorescence emission measurements are dependent upon the intensity of the light source. As the output of the light source can fluctuate with wavelength, it is important to record the intensity throughout the measurement and correct for fluctuations. The fluctuations $R(\lambda)$ are recorded by a light source detector placed in the sample chamber (not shown on diagram), and the overall fluorescence spectra $S(\lambda)$ is measured by a detector placed at the end of the emission monochromator. The corrected fluorescence spectrum is given by $S(\lambda)/R(\lambda)$.

3.1.3 Time-Resolved Fluorescence

There are two main methods for measuring time-resolved fluorescence; time-domain or frequency-domain, also known as pulse or phase fluorometry respectively. Pulse fluorometry offers many advantages such as, high sensitivity of photon counting (even with low levels of light) and well-established Poisson statistics from which the goodness-of-fit and data weights can all be determined mathematically. Most pulse

fluorometers are based on the time-correlated single counting (TCSPC) technique and used to determine fluorescence lifetime in this thesis. The TCSPC apparatus is shown below:

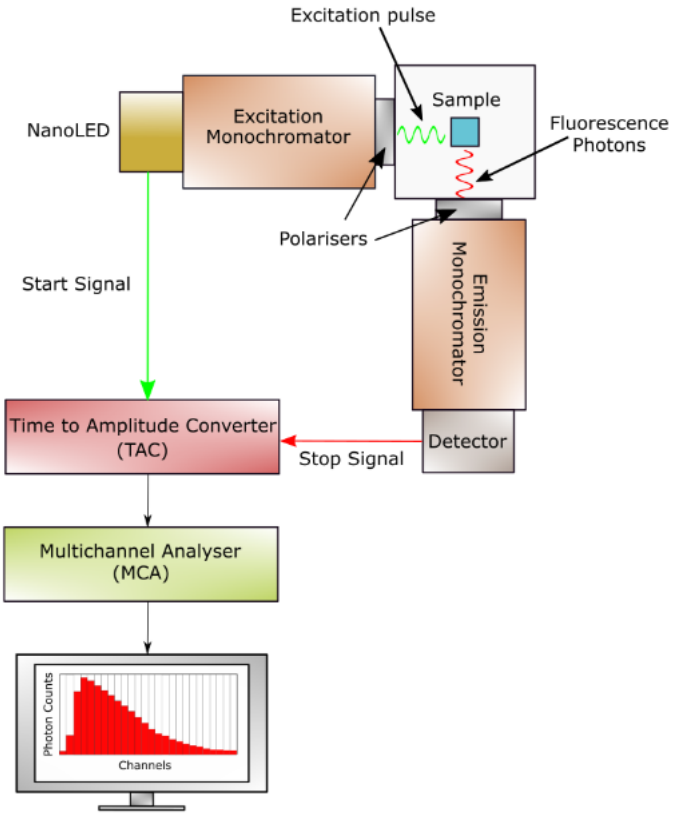

Figure 3.3: Time correlated single photon counting schematic.

The laser diode or LED produces a pulse of light, it simultaneously excites the sample and sends out a "start" signal to the time-to-amplitude converter (TAC). The TAC will start to generate a voltage that increases with time. During this time, the excitation light also goes through the monochromator and into the sample of interest. The fluorophore in the sample will absorb the photon and after a few ns, the fluorophore emits a photon. The emitted photon hits the photomultiplier (PMT) detector, which in turn, produces a "stop" signal that goes into the TAC. The signal will stop the voltage ramp that the TAC is producing and the amplitude of the voltage is proportional to the time delay between the "start" and "stop" signals. The amplitudes are converted to a digital value and stored in a histogram via the multi-channel analyser (MCA).

This process is iterated millions of times until typically one bin is populated to 10,000 counts and the histogram represents the fluorescence decay curve.

The monochromator in the excitation arm is optional as light sources in these experiments are monochromatic. Polarizers were used in fluorescence lifetime and time-resolved emission spectral (TRES) measurements to eliminate the influence of rotational effects on the fluorescence decay. The polarizer in the excitation channel was vertically orientated, whereas the polarizer in the detection channel was set to the magic angle (54.7°). Rotational effects can occur in processes such as FRET where it can accelerate fluorescence decay, resulting in incorrect values.

The TCSPC conditions are tuned with the intention of the PMT only detecting 1-2 photons per 100 excitation pulses to restrict data pile up. If the detection rate was above 2%, there is a possibility of two photons hitting the detector but only the first photon will be recorded. As the first photon will always be the fastest and the second will be discarded due to the dead time of electronics, there will be a bias towards shorter fluorescence lifetimes.

If the dead time of the timing electronics are longer than the fluorescence decay, this can be solved by performing the measurement in reverse mode. In reverse mode the emission signal will start the TAC and excitation light will stop the TAC. This configuration will increase the speed of the measurement because every emission photon be detected and stops the timing electronics from measuring dead time caused by the excitation pulse.

3.1.4 Fluorescence Lifetime Data Analysis

The fluorescence intensity decay collected from TCSPC are fitted to the multi-exponential model:

$$I(t) = \sum_{i}^{N} \alpha_i \exp\left(\frac{-t}{\tau_i}\right) \tag{3.4}$$

where α_i is the pre-exponential factor, t is the time after excitation and τ_i is fluorescence

lifetime. The impulse response function $I(t)$ can be fitted to the multi-exponential function and lifetimes can be extracted even if the instrumental response is not a δ-function. The instrumental response function $P(t)$ represents the convolution of the excitation pulse and the impulse response of the instrument and the measurement is carried out by recording a sample with no fluorescence lifetime, typically with scatter from a colloidal silica solution. From figure 3.4, $P(t)$ is broadened by the excitation pulse profile, photomultiplier, and timing electronics. Therefore, the measured fluorescence decay $F(t)$ differs greatly from $I(t)$.

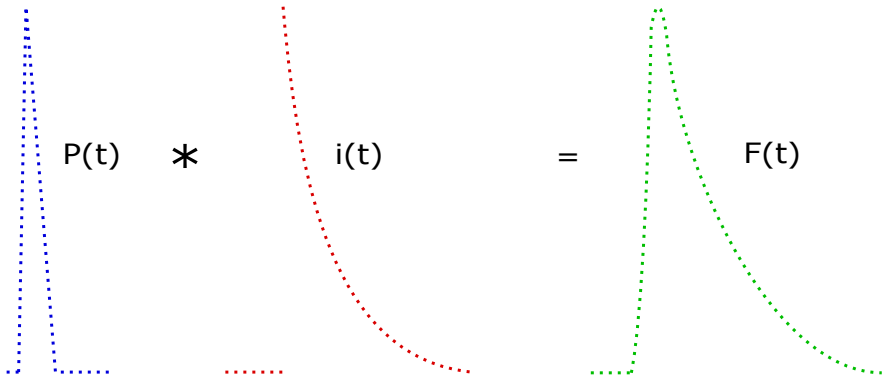

Figure 3.4: The convolution of the instrumental (blue dotted curve) and impulse response (red dotted curve).

To overcome the problem of broadening, the instrumental response is treated as a series of δ-functions and $F(t)$ as a series of exponentials from each δ-function. Therefore, the measured fluorescence decay $F(t)$ is the convolution $*$ of both the instrumental response $P(t)$ and impulse response $i(t)$, illustrated in figure 3.4.

$$F(t) = \int_0^t P(t')i(t-t')dt' = P(t) * i(t) \tag{3.5}$$

The variable t' is the instant where the δ-function generates a pulse to start the fluorescence response, $i(t-t')$. The parameters of $i(t)$ are recovered by reconvolution of a theoretical model such as single or multi-exponential model with the $P(t)$ which provides the theoretical fluorescence decay function, $F'(t)$. The nonlinear least squares (NLLS) method and χ^2 goodness of fit criterion are used to compare $F'(t)$ with $F(t)$. The NLLS method uses an algorithm to minimize the mismatch between $F'(t)$ and $F(t)$

by searching for parameters that give the best fit.

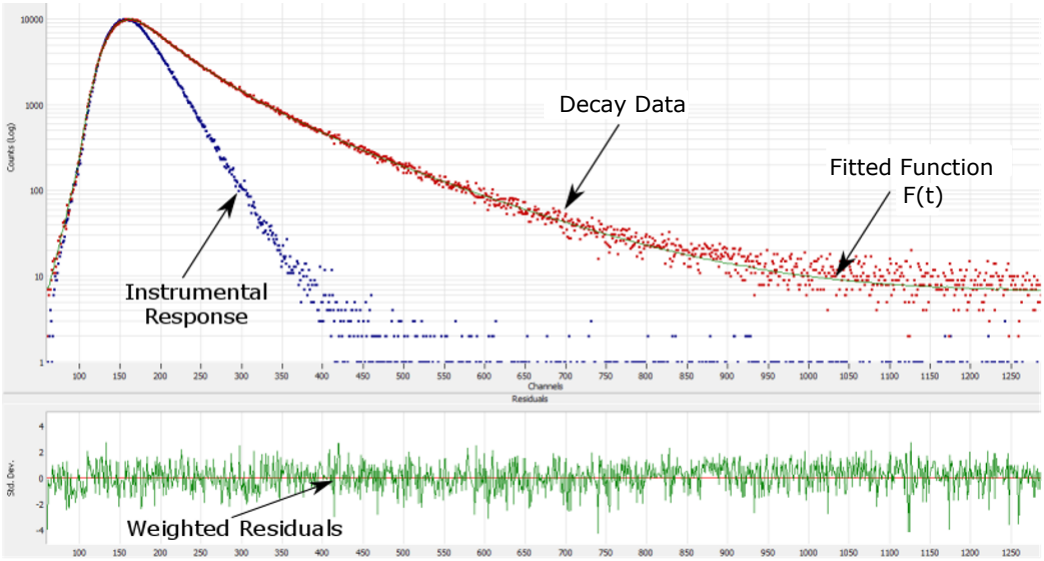

Figure 3.5: Fluorescence decay analysis. Where the instrumental response (blue dotted curve), decay data (red dotted curve), fitted function (green curve), and weighted residuals (green curve) are shown.

$$\chi^2 = \sum_{DataChannels} \left[\frac{D_t - F(t)}{\sqrt{D_t}} \right]^2 \tag{3.6}$$

where $D_t - F(t)$ is the deviation between the measured and fitted function and from Poisson statistics, $\sqrt{D_t} = \sigma(i)$ is the standard deviation of each data point. As χ^2 is dependent upon the number of data points, therefore, χ^2 would be large for an increasing number of data. To correct for this, the reduced χ^2 is used to examine a good fit.

$$\chi^2_R = \frac{\chi^2}{N - p} = \frac{\chi^2}{v} \tag{3.7}$$

where N is the number of data points, p is the number of parameters and v is the number of degrees of freedom. The number of data points would be much larger than the number of parameters, which means that v would be close to χ^2. Therefore, χ^2_R in the range of $0.9 \leq \chi^2_R \leq 1.2$ is considered a good fit and a value close to unity (equal to 1) is a perfect fit. Along with the χ^2_R value, the weighted residuals W_t are also examined

to determine the goodness of fit.

$$W_t = \frac{D_t - F(t)}{\sqrt{D_t}} \tag{3.8}$$

Weighted residuals give a visual representation of a fit as they should be randomly distributed around zero (shown in figure 3.5). If residuals express a pattern, this may indicate the wrong model has been used to fit the decay curve.

3.1.5 Time-Resolved Emission Spectra (TRES)

There are many processes that occur in the excited state which can induce solvent reorientation, conformational changes or changes in charge separation. Before, we assumed that these processes are considerably faster than the fluorescence lifetime decay, which can be true for small molecules such as dyes. However, dielectric relaxation in proteins or molecules in viscous solutions will relax around the solvent in a similar timeframe to the fluorescence decay. Due to the time averaging procedure in the steady state emission measurement, a great deal of the kinetics on the excited state (which is time dependent) cannot be resolved. Time-resolved emission spectra has an advantage over steady state measurement as it can generate emission spectra in time slices after excitation.

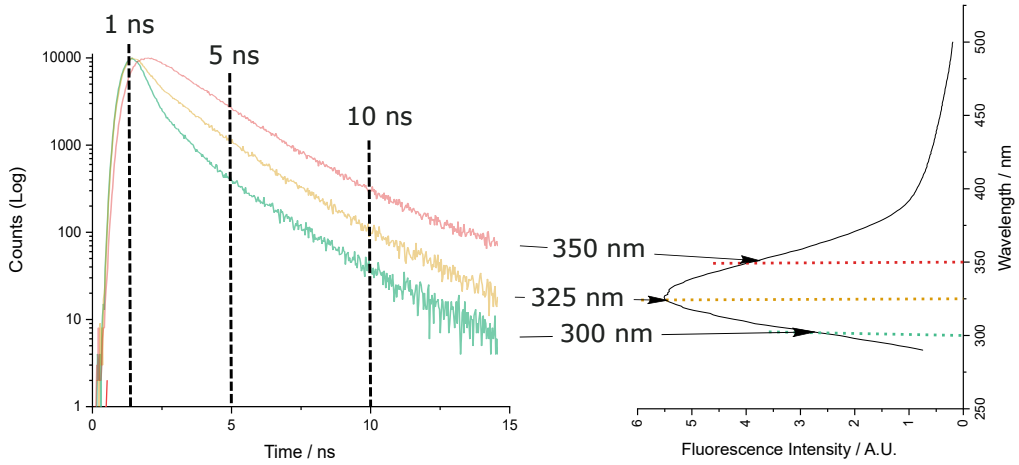

Figure 3.6: Schematic of how to measure time resolved emission spectra (TRES). The emission spectrum is first measured to determine the appropriate detection wavelength range for fluorescence lifetime decay measurements.

TRES is usually measured indirectly with the use of TCSPC technique as it removes distortion caused by the instrumental response via deconvolution. The fluorescence decays are wavelength dependent $I_\lambda(t)$, therefore, a range of emission wavelengths are measured across the spectrum (as shown on figure 3.6). The fluorescence decays are fitted using the multi-exponential model:

$$I_\lambda(t) = \sum_{i=1}^{N} \alpha_i(\lambda) \exp\left(\frac{-t}{\tau_i(\lambda)}\right) \tag{3.9}$$

where $\alpha_i(\lambda)$ are the pre-exponential factors and $\tau_i(\lambda)$ are the fluorescence lifetime decays for each wavelength. The parameters taken from the multi-exponential model have no physical significance and are used to enable an accurate representation of the intensity decays to create TRES. The rise time in the fluorescence decay is typically observed in longer wavelengths because fluorophores are populating the relaxed state. Negative pre-exponential factors from multi-exponential fitting often represents the rise time. The fluorescence decays are normalised $H(\lambda)$ so that the area of decays $\int_0^\infty I_\lambda(t)\, dt$ are equal to the steady-state intensity $S(\lambda)$:

$$H(\lambda) = \frac{S(\lambda)}{\int_0^\infty I_\lambda(t)dt} \tag{3.10}$$

for multi-exponential decay, the expression becomes:

$$H(\lambda) = \frac{S(\lambda)}{\sum_i \alpha_i(\lambda)\tau_i(\lambda)} \tag{3.11}$$

The normalised intensity decays can be used to generate TRES which is given by:

$$I_t(\lambda) = I_\lambda(t)H(\lambda) = \frac{I_\lambda(t)S(\lambda)}{\sum_i \alpha_i(\lambda)\tau_i(\lambda)} \tag{3.12}$$

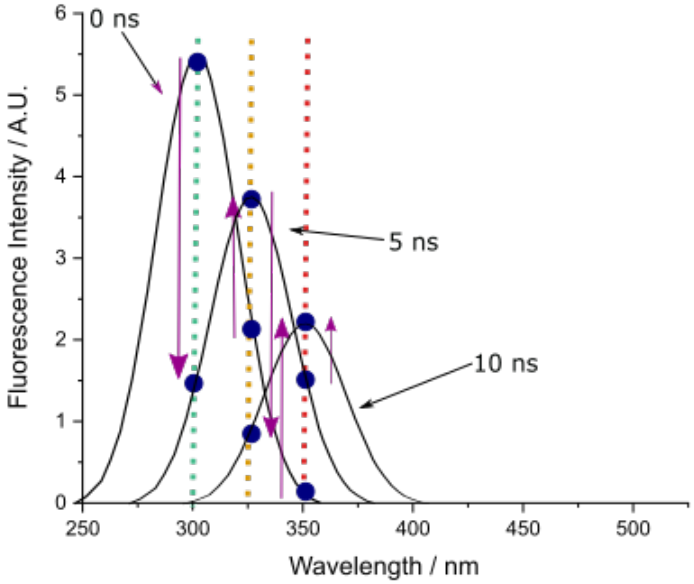

Figure 3.7: Schematic of time-resolved emission spectra after 0, 5, and 10 ns after excitation demonstrates the wavelength-lifetime dependence. During relaxation, the decay decreases and the spectrum undergoes a red shift with respect to time. Due to both processes, the intensity detected at 300 nm undergoes a large decrease from 0-5 ns (shown by the purple arrow). However, the intensity increases from 0-10 ns at 350 nm detection wavelength.

Figure 3.7 shows time slices of the emission spectra 0, 5, and 10 ns after excitation with detection wavelengths of 300, 325, and 350 nm. It can be shown that due to the depopulation of the excited state coupled with the shift from dielectric relaxation, the fluorophore will decay at shorter detection wavelengths. The dielectric relaxation also

may play a role in the rise time at longer wavelengths, as there is a growth in intensity from 0 – 5 ns before fluorescence decay occurs.

TRES spectra can be presented in the wavelength scale (shown on figure 3.7), but it is normally converted into wavenumbers because the model spectra is given as $I(\nu, t)$ by taking the reciprocal. Recorded decays are set to a specific wavelength λ with a constant bandpass $\Delta\lambda$ in the nm scale but when performing the conversion into cm^{-1}, the bandpass is no longer linear.

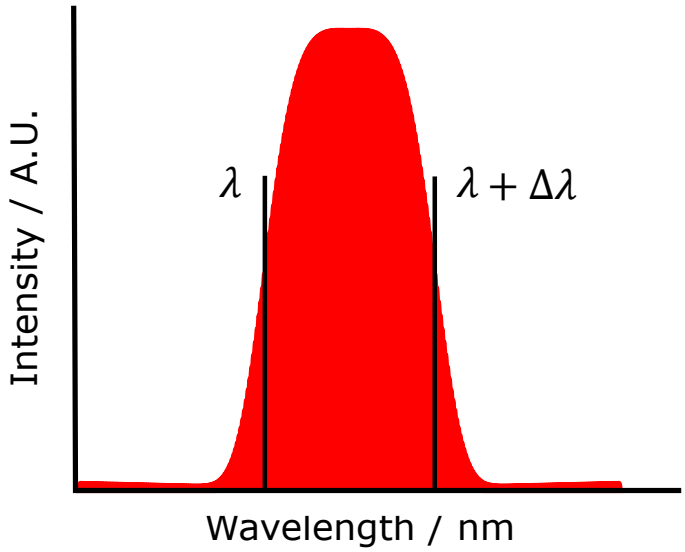

Figure 3.8: Intensity profile of photons passing through the emission monochromator.

Therefore, corrections must be taken into account and the relationship between wavelength and wavenumber. The bandpass in wavenumbers $\Delta\bar{\nu}$ is given by:

$$\Delta\bar{\nu} = \bar{\nu} - (\bar{\nu} + \Delta\bar{\nu}) \tag{3.13}$$

where $\bar{\nu}$ is the chosen emission wavenumber and the bandpass also can be represented by wavelengths:

$$\Delta\bar{\nu} = \frac{1}{\lambda} - \frac{1}{(\lambda + \Delta\lambda)} = \frac{\Delta\lambda}{\lambda(\lambda + \Delta\lambda)} \tag{3.14}$$

As seen in figure 3.8, the intensity is proportional to the wavelength range from λ to $\lambda + \Delta\lambda$ and the intensity decays can be written in terms of wavenumbers:

$$I_t(\lambda)\Delta\lambda = I_t(\bar{\nu})\Delta\bar{\nu} \tag{3.15}$$

where equation (3.14) can be substituted into equation (3.15), which gives:

$$I_t(\lambda) = I_t(\bar{\nu})\frac{1}{\lambda(\lambda + \Delta\lambda)} \tag{3.16}$$

Since $\Delta\lambda << \lambda$, the bandpass can be considered as negligible and the equation becomes:

$$I_t(\bar{\nu}) = \lambda^2 I_t(\lambda) \tag{3.17}$$

After the conversion into wavelengths, TRES was modelled with multiple modified Gaussian distributions to represent the spectral shapes of the fluorescent components. The Gaussian or normal distribution is a probability distribution that is often used in statistics as it represents a range of natural phenomena. The function describes how random variables are distributed where the centre of the curve is known as the mean, ν_i and the standard deviation, σ is the width of the distribution (depicted in figure 3.9).

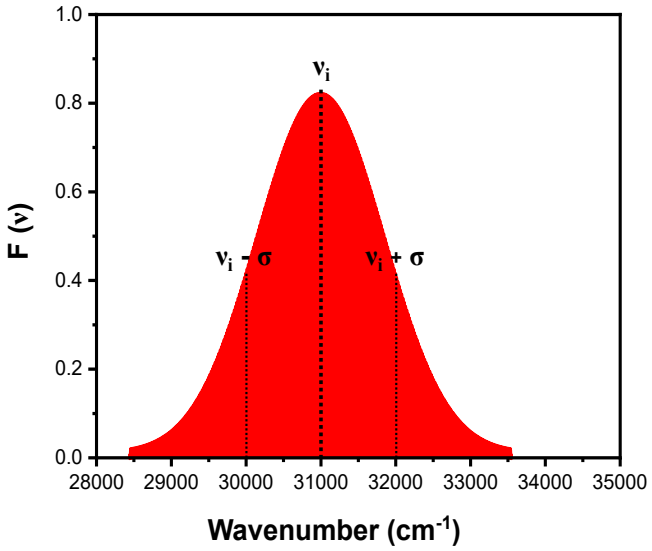

Figure 3.9: Illustration of Gaussian distribution where the peak position, ν_i and the standard deviation σ_i are shown.

Mathematically, the Gaussian plot is given by:

$$G(\nu) = \frac{1}{\sqrt{2\pi\sigma_i^2}} exp\left(-\frac{(\nu-\nu_i)^2}{2\sigma_i^2}\right) \tag{3.18}$$

where σ_i is the standard deviation, ν is the wavenumber and ν_i is the peak position. Time-resolved emission intensity is given by the emission spectrum shown in equation (2.5) multiplied by the population of fluorescent molecules in the excited state at time t, $N(t)$.

$$I_t(\nu) = a\nu^3 S_{vib}[\nu - \nu_{01}(t)]|\mu_{S01}|^2 N(t) \tag{3.19}$$

based on the Toptygin-type approach [83] the ν^3 parameter was included in the Gaussian model which was used to fit TRES.

$$F(\nu) = \sum_i^3 \frac{C_i}{\sqrt{2\pi}\nu_i\sigma_i(\nu_i^2 + 3\sigma_i^2)} \nu^3 \exp\left(\frac{-(\nu-\nu_i)^2}{2\sigma_i^2}\right) \tag{3.20}$$

the expression ($\sqrt{2\pi}\nu_i\sigma_i(\nu_i^2+3\sigma_i^2))^{-1}$ for each component i is the normalisation factor of the $\nu^3 exp\left[-\frac{(\nu-\nu_i)^2}{2\sigma_i^2}\right]$ function. Thus, C_i coefficient represents fluorescence contribution of the i^{th} component. According to Toptygin et al. distortions at the tail end of the spectrum is caused by inadequate spectral resolution, uncertainties in spectral correction, etc. and the wavenumbers can be corrected by plotting $\nu^{-3}I_t(\nu)$.

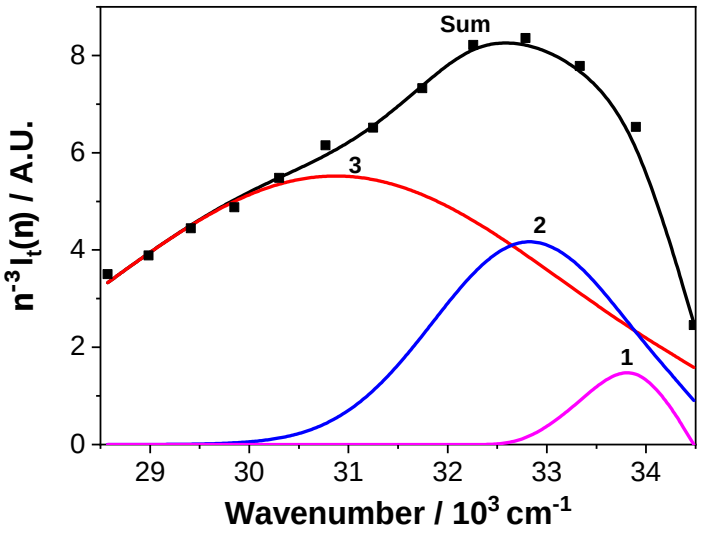

Figure 3.10: The experimental TRES data (square) fitted to 3 Toptygin-type models for an example sample measured at x ns after excitation. The 3 Toptygin-type curves labelled 1, 2, and 3 represent individual fluorophores emitting at 34000, 33000, and 31000 cm^{-1}, respectively.

To obtain a fuller and quantitative information on the observed spectral changes, the $\nu^{-3}I_t(\nu)$ spectra were modelled by the sum of 3 normalised Toptygin-type models given by equation (3.20). Figure 3.10 enables us to visualize where fluorescence species are emitting and how broad their spectra are. We are also able to monitor the total fluorescence emitted, peak positions and the widths of the spectra for each individual species from 0 – 10 ns after excitation. These parameters cannot be resolved in steady state emission spectra.

3.2 Fundamentals of a Microscope

Microscopes are a tool which assists researchers in studying building blocks that are essential in life and physical sciences. Objects that cannot be seen by the naked eye on the scale of ~100 μm, however, with the support of light and electron microscopes, structures can be magnified by several orders of magnitudes which allow us to visualise down to the sub-nanometre range. Figure 3.11 illustrates some structures which can be revealed with the use of microscopy.

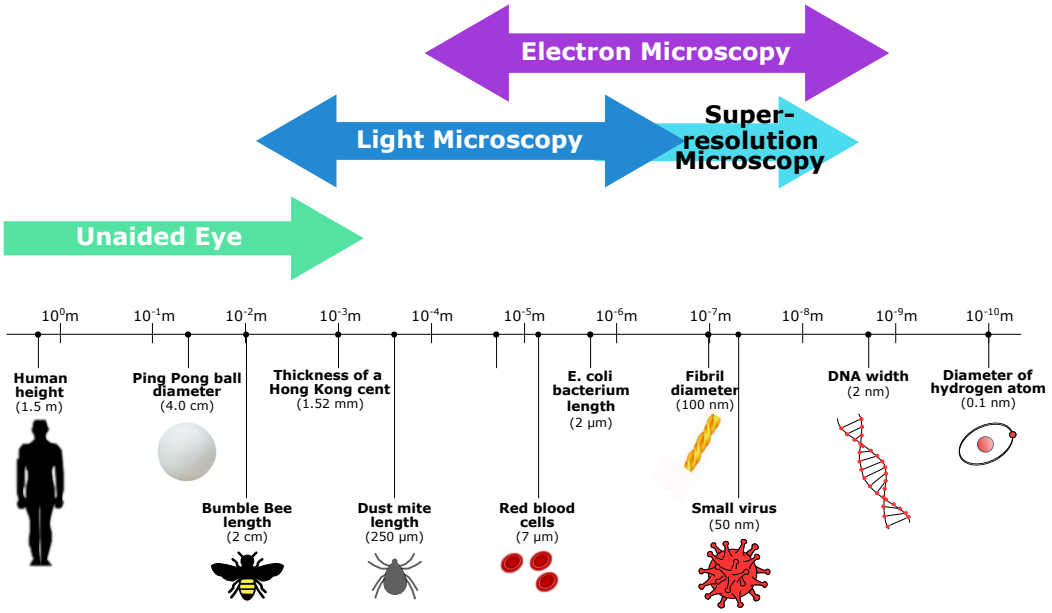

Figure 3.11: Spatial resolution of a microscope compared to the human eye.

The resolution of a microscope is defined by the smallest distance the microscope can resolve between two objects. This is given by Abbe's law:

$$d = \frac{\lambda}{2nsin\alpha} = \frac{\lambda}{2NA} \tag{3.21}$$

where λ the wavelength of excitation light, n is the refractive index of the medium, and α is the half angle of the light collection cone and NA is the numerical aperture of the objective lens. Therefore, microscopes are limited by approximately half the wavelength of light illuminating the sample. In light microscopes, the resolution is

around 200-350 nm because visible light is used. Whereas, electron microscopes use electrons and their wavelengths are significantly shorter than the wavelength of a photon. Therefore, electron microscopes have a sub-nanometre resolution.

The numerical aperture of an objective lens is its capability of capturing light to resolve details within the sample. Light below the microscope slide passes through the specimen and into the objective in a cone shape. Objective lenses have a *NA* limit of 0.95 as $sin\alpha$ can only be ≤1. However, NA can surpass 1 by increasing the refractive index between the objective front lens and the specimen cover glass (known as imaging medium). The angle α is limited by the physical diameter of the objective lens.

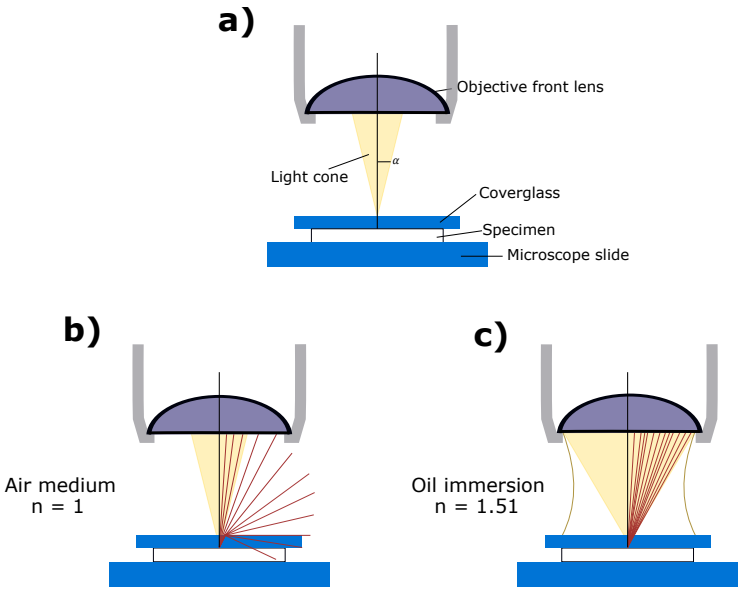

Figure 3.12: Schematic of the objective lens collecting light where a) illustrates the light cone and α. Down below, there is a comparison of how b) air and c) oil immersion affect the light rays coming from the sample.

Refractive index in the imaging medium can be increased from 1 to 1.51 through oil immersion. In figure 3.12, only a few light rays from the sample are being captured by the objective lens. Most of the rays are scattered into the air outside of the objective or reflected back into the cover glass. When the objective lens is immersed in oil with a refractive index similar to glass coverslips, the light rays that pass through the homogenous medium and do not undergo refraction. This enables light to have a

narrower distribution and therefore the objective lens can collect more light from the sample.

Spatial resolution is limited by light passing the through the aperture which causes diffraction patterns on the image, this is known as the diffraction limit. When imaging a single point source, the objective lens performs like a circular aperture and causes light from a bright point emitter to spread out. This is often known as the point spread function (PSF). The PSF often consists of a series of dark and bright rings surrounding a bright central region. This pattern is commonly known as the Airy pattern and the central region is often referred to as the Airy Disk (figure 3.13). When two point sources are close to one another (<200 nm) their Airy disks will overlap and will not be resolved. The Rayleigh criterion is an extension of the Abbe's law, where it describes the minimum separation needed between two point sources in order for the microscope to resolve them into two distinctive objects. According to the criterion, their Airy disks are distinct when the principal maximum of the first Airy disk coincides with the first diffraction minimum of its neighbouring disk.

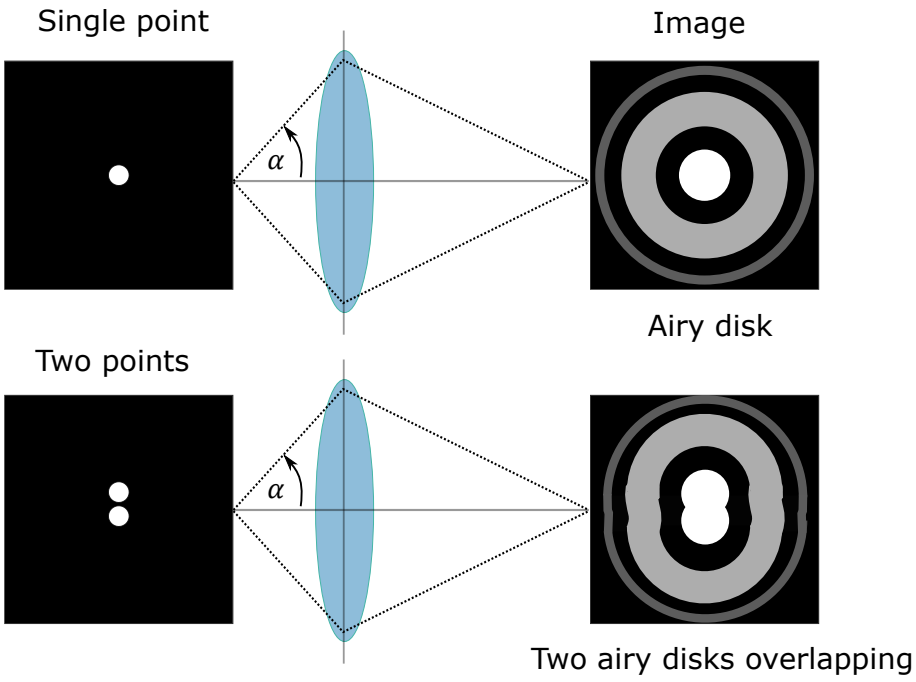

Figure 3.13: Illustration of the production of Airy disks once light from point sources passes through the objective aperture.

The Rayleigh criterion (R) lateral resolution (x, y) is described by:

$$R = \frac{0.61\lambda}{NA} \tag{3.22}$$

The axial resolution (along the z axis) is more complex as the diffraction pattern has the shape of an hourglass rather than a disk shape. However, they have similar properties to the Airy disk as they contain a principle maximum in the middle of the hourglass. Therefore, the Rayleigh criterion described in the axial direction is defined by the central maximum to the first diffraction minimum along the z axis. This can be calculated by:

$$R = \frac{2\lambda}{(NA)^2} \tag{3.23}$$

3.2.1 Fluorescence Microscopy

Fluorescence microscopy is an integral tool used in life sciences as it provides the ability to study dynamic biomolecular processes in aqueous solution. Therefore, processes such as protein interactions in buffer solutions and/or interactions of molecules inside living cells can be imaged.

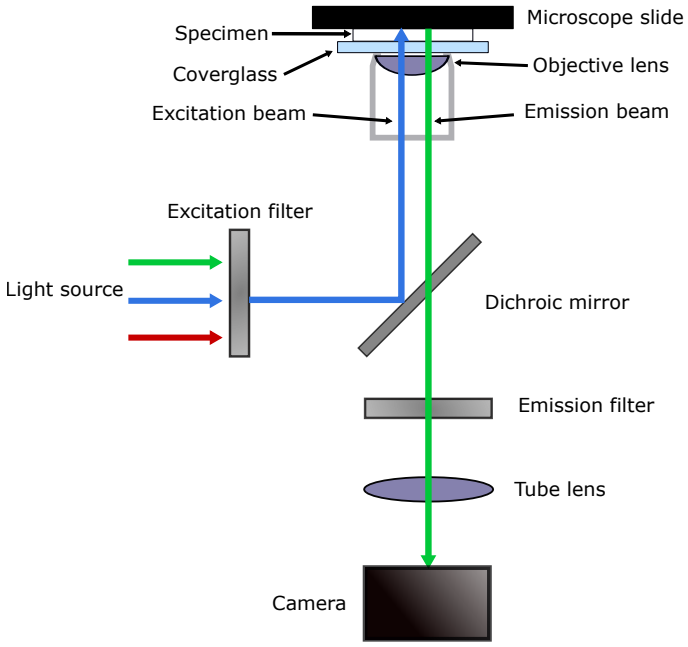

Figure 3.14: Schematic of the fluorescence microscope set up.

Fluorescence microscopy uses the concept of fluorescence where the excitation light passes through the excitation filter, reflects off the dichroic mirror and excites the fluorophores within the sample. The fluorophore emits at a higher wavelength due to Stokes' shift and its fluorescence is collected by the objective lens, passes through the dichroic mirror, emission filter and is imaged by the camera.

Fluorescence microscopy is relatively cheap, easy to operate, has fast acquisition times, and uses low light illumination compared to other microscopy methods [84]. Despite its major advantages, it is limited by its spatial resolution and therefore, processes such as early stages of protein self-assembly cannot be imaged.

Overcoming the diffraction limit in microscopy has been the prime target for many scientists and for the past two decades innovative techniques have been used to image below 200 nm. Microscopy methods that have surpassed the classical diffraction limit is known as super resolution microscopy. Techniques such as stimulated emission depletion (STED) microscopy [85,86] and photoactivated localization microscopy (PALM) [87] are super resolution microscopy methods commonly used to image biological systems. However, in this thesis there will be a more in depth discussion of techniques such as structured illumination microscopy (SIM) [88, 89] and direct stochastic optical reconstruction microscopy (dSTORM) [90–92].

3.2.2 Structured Illumination Microscopy (SIM)

Structured illumination microscopy (SIM) breaks the diffraction barrier by illuminating the sample with patterned light instead of a uniform field of light in a wide field microscope. SIM is able to extend the resolution of conventional microscopy because the interference between the sample and patterned light create Moiré fringes (figure 3.15A). Moiré fringes are the sum of different frequencies and their superposition of the sample and illumination light produce patterns of lower frequencies. Therefore, the microscope is able to observe high resolution information. The information about the structure stored in the Moiré fringes can be extracted if the illumination pattern is defined.

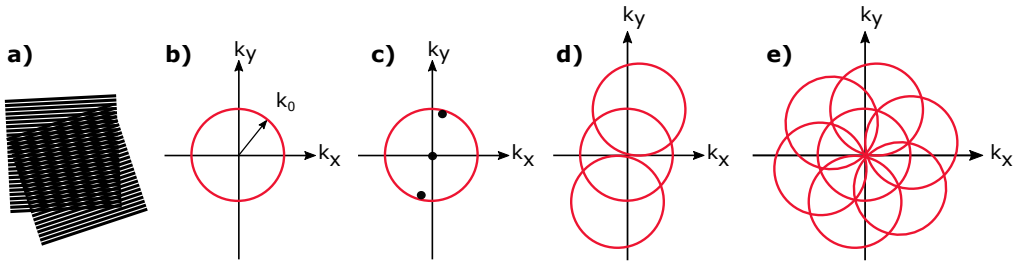

Figure 3.15: Schematic describing how structured illumination improves resolution by a factor of two. a) Two patterns with fine lines will superimpose to create Moiré fringes. b) The observable region of a microscope in reciprocal space where k_0 is the maximum spatial frequency. c) Only 3 Fourier transform modes are non-zero for a sinusoidal pattern. d) Information can be gathered beyond the observable region due to the low frequency Moiré fringe. e) It is possible to double the resolution by changing the orientation of the diffraction pattern. The figure was adapted from [89].

To understand SIM in more detail, it is essential to transform the image from real to reciprocal space by taking its Fourier transform. Optical transfer function (OTF) is the PSF in reciprocal space and it describes how frequency passes through the optical system. In Fourier space, a lens of a microscope acts as an aperture and is represented by a circle where the radius, r is given by:

$$r = k_0 = \frac{2NA}{\lambda_{em}} \tag{3.24}$$

where λ_{em} is the wavelength of emitted light and k_0 is the maximum observable spatial frequency. Conventional microscopes cannot resolve structures with lines finer than the diffraction limit, $d_0 \sim 200$ nm. In reciprocal space, the microscope can only detect information inside the observable region where is the radius is also equal to $1/d_0$ (figure 3.15B). Low frequency information is located close to the centre of the OTF and high frequency information resides on the edge of the Fourier image. As high frequency components carry high spatial resolution, it is desirable to virtually extend the observable region to enable access to fine structural information. The sinusoidal pattern in reciprocal space presents a non-zero point in the centre of the observable region and two displayed away from the origin (figure 3.15C). The distance and direction of the points are governed by line spacing and direction of the pattern, respectively. In addition to the information given by the conventional image, Moiré fringes enable the microscope to gather information displaced by the two points outside the observable region (figure 3.15D). As all the information from 3 points are in one observable image, there is a need to separate out the signals. This can be achieved by recording three different phases of the sample and through mathematical procedures, the information can be moved to its correct location. The illumination pattern is often chosen to be as fine as possible in order for the two points to extend out towards the edge of the observable region. It is possible to double the resolution of the conventional microscope by rotating the pattern in two different directions (figure 3.15E). Therefore, nine images is the minimum needed to reconstruct a super resolution image.

An inverted microscope (IX71, Olympus) was modified to collect SIM images,

shown in (figure 3.16). Light from the excitation source was collimated by a parabolic mirror into Pockels cell (M350-80, Conoptics Inc.). A Pockels cell is a voltage controlled tuneable wave plate which changes the direction of polarization at high switching rates. With the combination of Pockels cell and a quarter wave plate (AQWPO5M-600, Thorlabs Inc.) enables linearly polarized light to align with the orientating grating on the spatial light modulator (SLM) (SXGA-3DM, Forth Dimension Displays). The SLM is used to generate different grating patterns controlled by a computer. The spatial filter only allows the ± first order diffraction beams in the Fourier transform to pass through the back of the objective lens and onto the sample. Nine images are recorded with a CMOS camera (ORCA Flash 4.0, Hamamatsu Photonics).

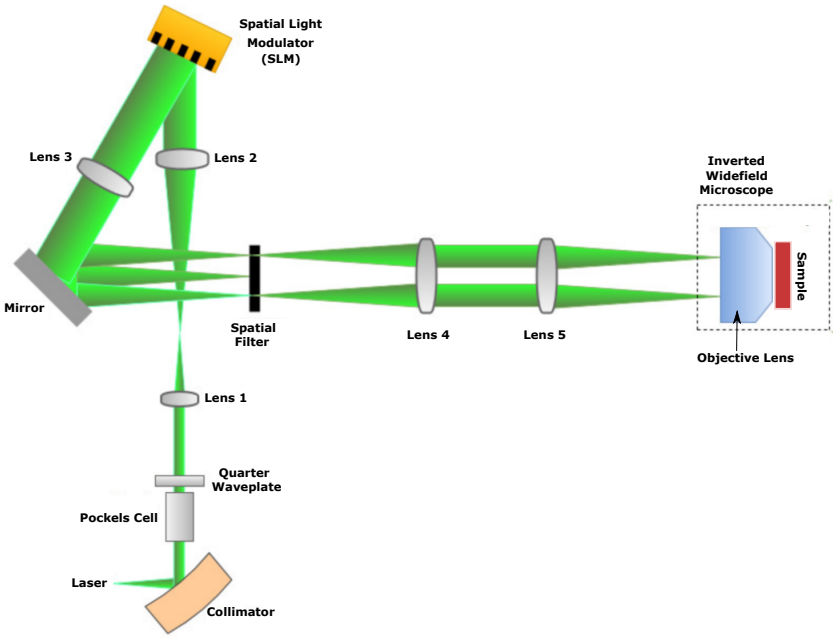

Figure 3.16: Schematic of modified inverted wide field microscope to provide structured illumination. The figure was adapted from [93].

In the linear theory (as discussed above) it states that the first diffracted order in Fourier transform can only be observed within the OTF, where k_0 is the maximum spatial frequency. Therefore, the resolution of SIM is limited by the sinusoidal illumination pattern that can only double the area of the observable region. However, the limitation has been broken by changing the pattern from sinusoidal to trapezoidal [94]. A

trapezoidal pattern has access to higher order frequency harmonics which are generated by nonlinearity. One method to achieve a nonlinear response from fluorophores is to increase the laser intensity in order to saturate the population of the excitation state. This is known as saturated SIM (SSIM). SSIM is able to enhance the resolution by a factor of two and in theory, the resolution is unlimited. However, in spite of its resolution enhancement, SSIM has disadvantages such as photobleaching and poor temporal resolution [95].

3.2.3 Direct Stochastic Optical Reconstruction Microscopy (dSTORM)

Direct stochastic optical reconstruction microscopy (dSTORM) breaks the diffraction barrier by temporally separating the emission of neighbouring fluorophores. As discussed previously, two fluorophores separated by a distance below 200 nm cannot be resolved. However, by isolating the PSF of the emitter, their exact location can be found by fitting the PSF with a 2D Gaussian function (figure 3.17). This can be achieved by switching the majority of the fluorophores to the dark state and only allowing less than 1% of fluorophores to emit light. Therefore, the probability of two point sources (<200 nm apart) emitting at the same time would be infinitesimally small and they can be filtered out during data analysis. The emitters would be switched back to the dark state and a new set of fluorophores would fluoresce stochastically. The process is repeated and new fluorophores are localised within the structure, giving a <50 nm resolution and provides insight to the structure and conformational changes of biomolecular processes such as protein aggregation [96, 97].

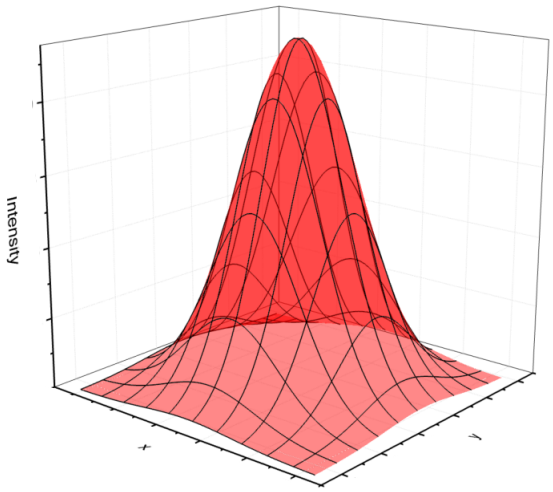

Figure 3.17: 2D Gaussian plot for localization of fluorophore PSF.

The 2D Gaussian function to approximate the intensity distribution of a PSF is given by:

$$f(x,y) = Aexp\left(-\left(\frac{(x-x_c)^2}{2\sigma_x^2} + \frac{(y-y_c)^2}{2\sigma_y^2}\right)\right) \tag{3.25}$$

where A is the amplitude, σ_x and σ_y are the standard deviations in x and y, x_c and y_c are the peak positions of each Gaussian. The position of the fluorophore has an error called the localisation precision and it is given by [98]:

$$\mu_x = \frac{\sigma_a^2}{N}\left(\frac{16}{9} + \frac{8\pi\sigma_a^2 b^2}{Na^2}\right) \tag{3.26}$$

where $\sigma_a^2 = \sigma^2 + \frac{a^2}{12}$, σ is the standard deviation of the PSF, a is the pixel size of the camera, N is the number of photons detected on the camera, b is the standard deviation of the background. If the background is negligible then the equation can be simplified to:

$$\sqrt{\mu_x} \approx \frac{\sigma}{\sqrt{N}} \tag{3.27}$$

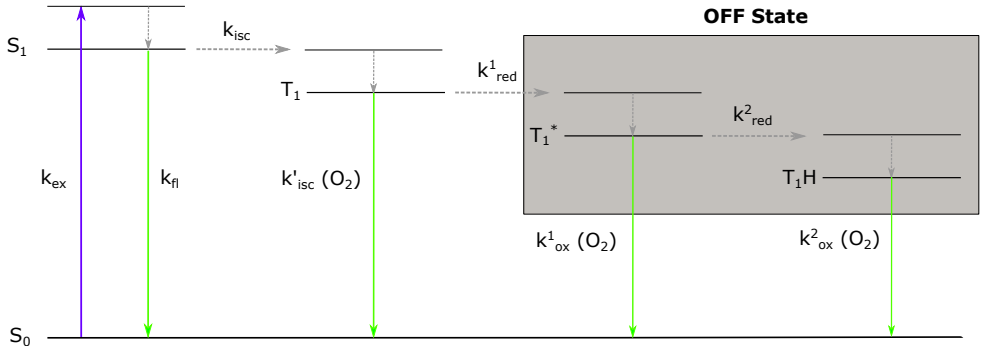

Figure 3.18: Illustration of Jablonski diagram with the inclusion of dark states for dSTORM. The figure was adapted from [92] where k_{ex} is the rate excitation and k_{fl} is the rate of fluorescence. Through intersystem crossing with rate k_{isc}, the fluorophore can go into the triplet state. Interactions with a molecular oxygen in the triplet state can produce a singlet oxygen with a rate of $k'_{isc}(O_2)$. Other interactions between thiols can occur at a rate of k^1_{red} to produce an OFF state radical anion T^*_1 and when oxidized, it can return to the ON state at a rate of $k^1_{ox}(O_2)$. The thiol radical can accept another electron in the OFF state to form a fully reduced form T_1 H and returns to the ON state through oxidation $k^2_{ox}(O_2)$.

Advanced photochemistry has to be applied to generate long lived fluorophores in the dark state required for dSTORM (figure 3.18). In general, the fluorophore absorbs the excitation light and fluoresces between the singlet ground (S_0) and excited state (S_1). However, on occasions, the fluorophore changes the spin of one electron and transitions into the triplet state (T_1). With high illumination power, the number of ON and OFF cycles increases and so the fluorophore transition from singlet to triplet state also increases and resides in the triplet state for a few microseconds. The fluorophore is subjected to collisional quenching with oxygen which is present in the triplet state. The collision effectively quenches the fluorophore back to S_0 and produces a singlet oxygen which is known to be a reactive oxygen species (ROS). To ensure the fluorophores live longer in the triplet state, molecular oxygen is removed with the use of an oxygen scavenger. The oxygen scavenger consists of glucose oxidase, catalase and β-D-glucose. In the imaging buffer solution, thiols such as β-mercaptoethylamine (MEA) react with the fluorophore in the triplet state to form a radical anion (T_1*) dark state and a thiyl radical. Some thiyl radicals create another dark state by accepting two electrons from thiols which produce a leuco fluorophore (T_1H). Both fluorophores in the dark states can return to the ground state through oxidation by molecular oxygen. The dark states

are long lived due to their thermal stability of a few seconds because of the removal of molecular oxygen.

3.3 Peptide Synthesis

As protein and peptides play a significant role in a many biological and physiological process, such as transportation of molecules through membranes, structural support in our connective tissue, and regulating gene expression. Since proteins play such an important role in medicinal and pharmaceutical fields, research has been targeted towards understanding structural characteristics of proteins and their mechanism to functionalize. Proteins and peptides are often chemically synthesized to study them in their purest form and isolated from nature's influence from its biological system.

3.3.1 Solid Phase Peptide Synthesis (SPPS)

A well-established method for producing synthetic peptides is known as solid-phase peptide synthesis (SPPS). The first SPPS experiment was carried out by Merrifield which uses a solid support resin to assemble a polypeptide chain from the C- to the N-terminus are carried out sequentially. Large improvements have been made to this process include automation which makes SPPS a simple approach and is preferred over other solution phase methods [99].

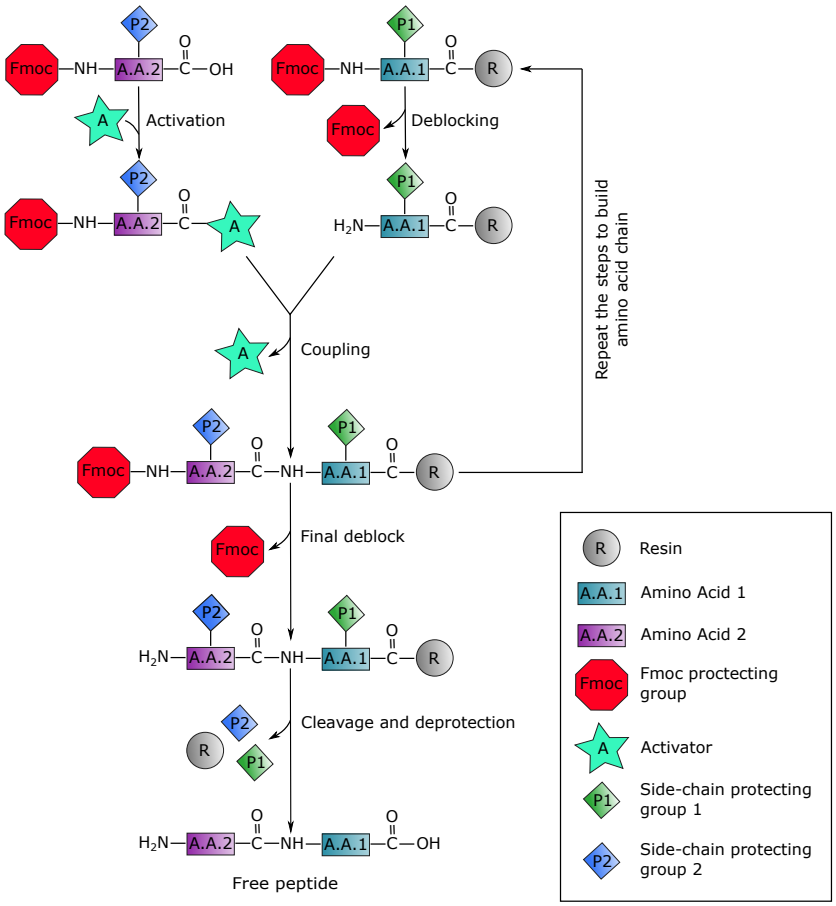

Figure 3.19: A simple solid-phase peptide synthesis diagram. Where the de-protection of Fmoc and coupling steps were repeated until the desired polypeptide chain is complete. Afterwards, resin cleavage and side chain deprotection steps were carried out to create a free peptide.

In the solid-phase peptide synthesis, the first amino acid is protected by side-chain and Fmoc protection groups to prevent undesirable side chain reactions and polymerization of activated amino acids [100]. The first amino acid is also attached to an insoluble solid support resin which allows any unbound by-products to be washed away whilst maintaining the polypeptide chain. This enables the use of large amounts of reagents, which speeds up reaction times. The Fmoc group must be removed before the addition of the second amino acid can take place. This is known as the deprotection step. Piperidine is used in the deprotection reaction because it is a base and the Fmoc group is stable in acidic conditions. The free amine in the first amino acid can now undergo a coupling reaction. In the second amino acid, the side chains and amine

function groups are protected. However, the free carboxylic group is unreactive and needs to be activated before undergoing a coupling reaction. The coupling reagent 2-(1H-benzotriazol-1-yl)-1,1,3,3-tetramethyluronium hexafluorophosphate (HBTU) activates the carboxylic acid by changing the anionic oxygen into a Hydroxybenzotriazole (HOBt) active ester. Through condensation reactions with the amino group in the first amino acid and the activated ester, peptide bonds are formed between the first and second amino acids. The soluble side products of the coupling reactions are washed away, and the amino acid chain is left covalently attached to the resin. These steps are repeated until the desired peptide sequence is complete. The final N-terminus deprotection step is accomplished with the use of piperidine. In the Fmoc SPPS, it is important that the side chain protection groups are not reactive to bases because they need to remain on the side chains during coupling and piperidine deprotection steps. Therefore, t-butyl (tBu) protecting groups are typically used with Fmoc protection groups which is an orthogonal Fmoc/tBu protection scheme. To remove the peptide from the resin and side chain protection groups, acids is used in the cleavage and deprotection step. Side chain protecting groups and the linker of the resin is acid labile, therefore, a cleavage cocktail of 95% trifluoroacetic acid (TFA) is used. This will yield the free peptide, without protecting groups nor the solid support resin.

The solution will contain the free peptide with other by-products from the side chain deprotection. Therefore, recrystallization and chromatography need to be used to separate the free peptide from the unwanted by-products.

3.3.2 Mass Spectrometry (MS)

Mass spectrometry (MS) is a powerful analytical technique that measures the mass of different molecules within the sample from their mass-to-charge ratios of their ions. It is used to study the content of purified protein, determine impurities and different molecules in a sample.

Traditional ionization techniques required molecules in the gas phase which limits the study of large biomolecules (such as peptides, lipids, and nucleotides) because they

would undergo fragmentation from electron impact. In the late 1980s, matrix-assisted laser desorption ionization (MALDI) [101] is known as a soft ionization technique that allows large molecules to remain intact during ionization. MALDI MS offers advantages over other MS techniques because singly charged ions are produced [102] which makes data interpretation more straightforward.

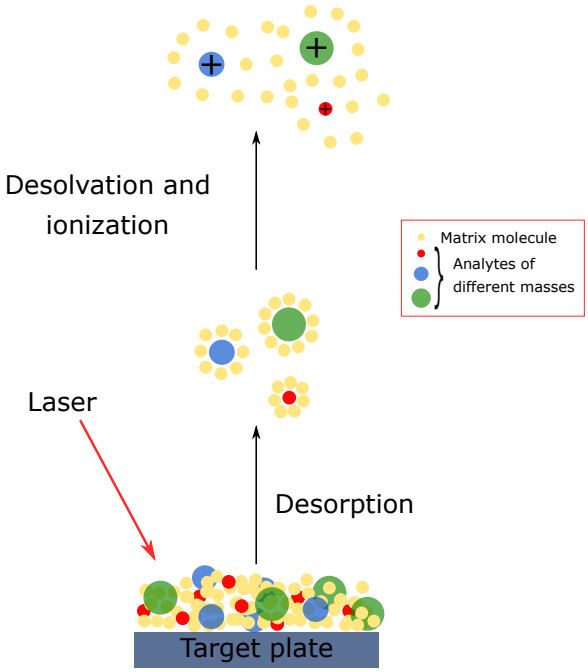

Figure 3.20: Schematic of MALDI ionizing analytes through desorption, de-solvation and ionization.

The sample is prepared by mixing the analyte with an excess amount of matrix and dried, leaving a crystallized sample on the target plate. Some common examples used as the matrix are α-Cyano-4-hydroxycinnamic acid (CHCA) [103] and 2,5-Dihydroxybenzoic acid (DHB) [104]. The matrix prevents the sample from decomposing. More importantly, all matrix molecules used have a benzene ring with attached function groups that absorbs the excitation light and converts it into heat energy. This causes the matrix and analytes to desorb from the target plate and ablate into the gas phase figure 3.20. In the gas phase, the analyte molecules form single positive charged ions through the process of proton transfer with the surrounding matrix molecules.

After the analyte ions have been created in the gas phase, the mass of the ions are

analysed by using the time of flight (ToF) mass spectrometer.

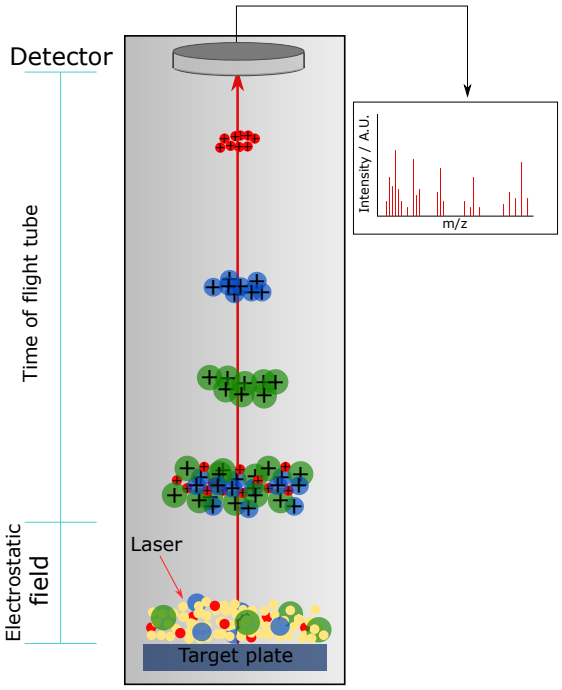

Figure 3.21: MALDI-ToF mass spectrometer schematic. Where the crystallized sample get ionised by the matrix, get accelerated by the electrostatic field and into the time of flight analyser.

The time of flight process accelerates the ions in the gas phase with a high voltage electric field. The ions are given the same initial kinetic energy E_k and after being accelerated, the ions can drift freely in the ToF tube (in the absence of an electric field). Due to the constant kinetic energy applied to the ions, the lighter ions will have a higher velocity and therefore, will be detected earlier than the heavier ions. Since the molecules usually have only one single positive charge, and the ToF analyser detects the time t taken to travel a finite distance, the mass spectrometer can generate a mass-to-charge ratio of each ion plotted against signal intensity according to $m/z \propto t^2$. The mass spectrum is compared with a library of well-characterized molecules and individual species are determined using bioinformatics.

3.3.3 High Performance Liquid Chromatography (HPLC)

High performance liquid chromatography (HPLC) is an important analytical technique that is used to separate, identify, and quantify various components in solution. This technique is used in a variety of industries such as pharmaceutical, food production, environmental, and in forensics. HPLC is known as high performance chromatography because it uses high pressures to separate out the components. In column chromatography, the solvents drip through the column by relying solely on gravity. By using high pressures, the time of separation dramatically decreases, and smaller particles can be used to pack the column. More interactions between the particles in the column and the components passing through the column will occur due to the increased surface area these particles provide. Therefore, having smaller particles in the column will enable better separation of the components in solution.

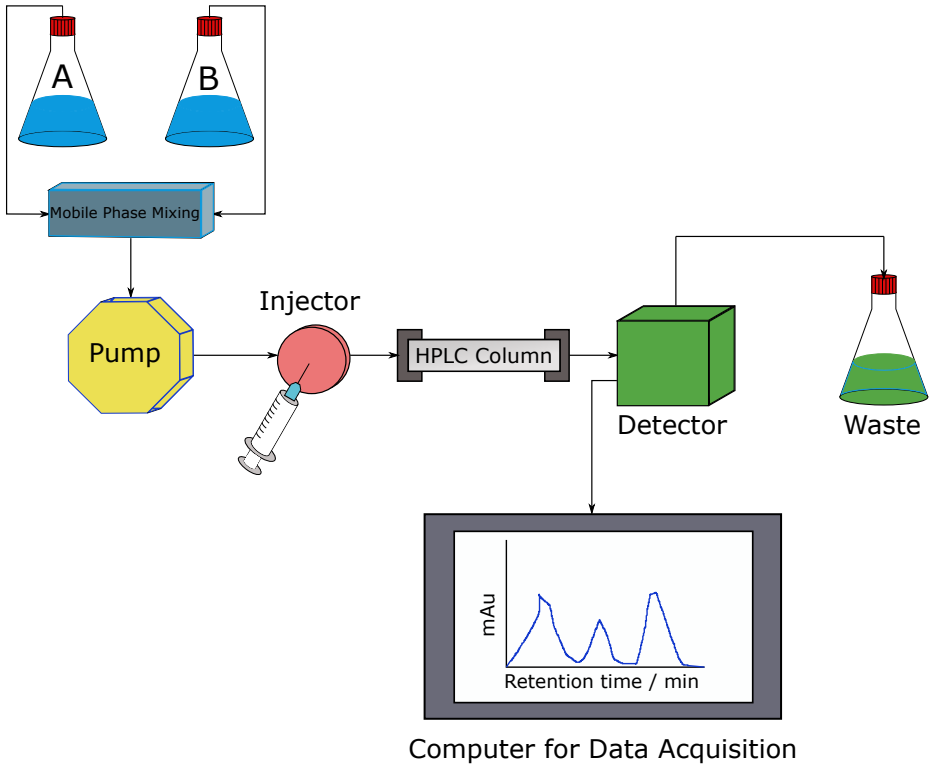

Figure 3.22: Simple schematic of HPLC, where different solvent gradients are created by mixing buffers A and B together. The sample is injected and pumped into the HPLC column at high pressures and into the detector. Wanted samples are collected and unwanted samples are discarded. The chromatography is collected using data acquisition software.

In gradient HPLC analysis, the mobile phase composition of polarity changes during elution with the use of polar and non-polar solvents (buffers A and B). This enables a large range of analyte polarities to be optimally resolved and retention times are reasonable. The mobile phase composition is controlled by the computer and it allows different ratios of buffers A and B to be mixed by the mobile phase mixer. In the mobile phase, the pump ensures that the solvents are under high pressure and controls the flow rate of solvents. The mobile phase is continuously passing through the column and into the waste. The HPLC column is packed with small particles from ~1.5-10 μm and this is known as the stationary phase. In reverse phase HPLC, the column is packed with silica particles which are attached to long chains of carbon, (typically 8 or 18 carbon atoms) which makes the stationary phase non-polar. Once the sample is injected through the injector, the mixture of analytes have different polarities and are separated by the column. The polar analytes will pass through the column at a faster rate than non-polar analytes. When the non-polar components pass through the column, they interact with the long hydrocarbon chains via van der Waals forces. Therefore, it takes time for the solvents passing through to break the hydrogen bonds and the non-polar analytes stay in the column for longer. The analytes pass through the column and back into the mobile phase. The detector passes UV light through the path of the mobile phase which measures the absorbance of the components. The chromatography data system translates the signal from the detector and plot the separated peaks, which is known as a chromatogram. The chromatogram provides qualitative and quantitative information about the sample. In the graph, mAu indicates the absorption of analytes and it can be used to determine analyte concentration.

Chapter 4

Investigation of Self-Assembly and Stability of the Fibrillogenesis Protein Model

4.1 Introduction

There is significant interest in improving the understanding of protein fibrillogenesis. The process is fundamentally important for normal and pathological phenomena including those that underpin the onset of neurodegenerative diseases such as Alzheimer's disease (AD), Parkinson's disease (PD) and diabetes mellitus type II [5,6]. These are proteopathic disorders, in which precursor protein undergoes abnormal development via a chain of conformational changes resulting in the formation of amyloid fibrils. Amyloid aggregation is structurally polymorphic due to the different assembly pathways monomeric units are involved in [105]. As a result, the units can assemble into different populations of oligomeric forms characterised by varied growth kinetics. In contrast, natural fibrillogenesis processes, such as those supporting the assembly of actin filaments or collagen and fibrin fibrils, exhibit more homogenous growth rates. To understand the rate of fibrillogenesis, it is advantageous if the complexity of natural proteins is reduced and fibrillogenesis studies performed using simplistic and reproducible models first. Such models can be based on well-established rules of

sequence-to-structure relationships and offer necessary predictability in control over fibrillogenesis at the molecular level. To achieve this, the approach requires a well-characterised protein folding element.

One of such elements is an α-helical coiled coil, which is characteristic of about 5-10% of all amino acids in proteins. The sequence-to-structure relationships for this motif are well understood and have been validated in many designs [26]. The hallmark of canonical α-helical coiled coils is a heptad repeat of hydrophobic *(H)* and polar *(P)* residues, *HPPHPPP*, which is usually designated as *abcdefg*. This arrangement gives rise to a rope-like bundle of two or more helices interdigitated with the formation of a contiguous hydrophobic interface, with each helix having 3.5 amino-acid residues per turn. Charged residues in *e* and *g* sites stabilise the bundle further via bridging electrostatic interactions [45].

Using these principles a coiled-coil sequence was designed to assemble into filamentous structures from the monomer up [38]. The sequence KLAALKQKLAALKKELAALEQELAALEQ was synthesized with Alexa Fluor 488 covalently labelled to lysyl residue in position 14. By labelling the peptide with the fluorophore, it was possible to monitor the fibrillogenesis by structured illumination microscopy. It is important to study the rate of fibrillogenesis of the protein model not only under static conditions but also in dynamic environments. In cellular environments, a high concentration of protein is found and hydrodynamic forces present in cells are responsible for the acceleration of protein fibrillogenesis. To mimic dynamic conditions in physiological conditions, we take advantage of the capillary forces that occur within a drying droplet [106].

The peptide sequence was also modified by replacing lysyl residue in position 14 with an intrinsic fluorophore, Tyr (see figure 4.1). A single Tyr residue in each monomer and the lack of tryptophan allows for selective excitation without the complication of energy transfer. Tyr is known to be sensitive to local microenvironments in evolving insulin [107], during glycation and in the aggregation of beta amyloid [108]. Therefore, the fluorescence response of tyrosine in both steady state and time resolved

measurements can be used to monitor fibrillogenesis. In addition, complementary information can be obtained using the same approach with regard to complexation with sugar molecules (glycation).

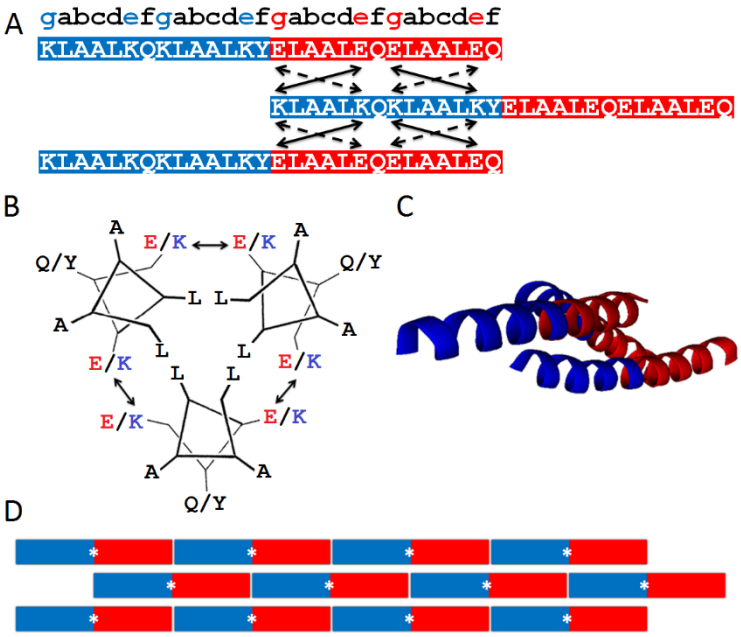

Figure 4.1: Fibrillogenesis model design. A) The linear amino-acid sequence of the protein model, three copies of which form a staggered coiled-coil unit with cationic and anionic overhangs, each having two heptads. B) The unit configured into coiled-coil helical wheels with 3.5 residues per turn. C) A ribbon diagram of the staggered unit (PDB 3L4F entry rendered with PyMol.) D) A schematic representation of the longitudinal propagation of the unit into a contiguous coiled coil. For clarity, only one coiled coil is shown: resulting fibrils are bundles of individual coiled coils. Key: cationic and anionic heptads and residues are shown in blue and red, respectively. Double-headed arrows indicate electrostatic interactions between lysines and glutamates. One of the two combinations of interactions, highlighted by bold and dashed arrows, can be formed within one coiled coil unit. Asterisks indicate the Tyr residue.

Protein glycation is a non-enzymatic process, which occurs as a post folding modification affecting protein stability, structure and function. In amyloid deposits, protein is often glycated which suggests a correlation between fibrillogenesis and glycation [11]. Both the self-assembly of the peptide into fibres and their potential complexation with glucose were studied using time-resolved emission spectra (TRES).

In addition to monitoring Tyr intrinsic fluorescence, Thioflavin T (ThT) is one of the most commonly used extrinsic probe to detect β-sheet formation [1, 2, 109, 110].

The dramatic enhancement of fluorescence and the spectral shift are often studied which makes ThT an extremely powerful structural probe. For ThT in solution, the benzothiozene and benzothiozole rings are free to rapidly rotate to form a twisted intramolecular charge transfer (TICT) state which quenches the excited state, resulting in low fluorescence quantum yield. However, when ThT is incubated with amyloid fibrils β-sheets provide steric and electronic stability to the excited state of the probe. Through immobilization of ThT, non-radiative decay TICT pathways are limited which causes a dramatic fluorescence enhancement. In addition, labelling the protein model enables the ability to seek out information about the formation of β-sheets and the effect it has on tyrosine residues. Although ThT has been commonly used, it is important to note that Tyr is a non-invasive probe and will not influence the self-assembly process as it is an intrinsic fluorophore. ThT also lacks the reporting of early stages of aggregation as its fluorescence intensity is dependent on the formation of β-sheets.

4.2 Methodology

4.2.1 Protein Synthesis of Protein Model with Intrinsic Fluorophore

The peptide was assembled on a Fmoc-Gln(Trt)-Wang resin using a PTI Tribute peptide synthesizer. HBTU/DIPEA and piperidine were used as coupling and deprotection reagents, respectively. After the synthesis the peptide was cleaved from the resin following a 2-hour treatment with the cleavage cocktail of 95% TFA, 2.5% TIS, 2.5% H_2O. Diethyl ether was added to the mixture to precipitate and wash the peptide, which was followed by centrifugation at 6500 rpm (20 min, 3 times). The pellet was then purified by a Dionex UltiMate 3000 HPLC system using a semi-preparative column (ACE 5C18-300 250 x 10 mm) at a flow rate of 3.5 ml/min. The purity of the peptide was confirmed by analytical HPLC (ACE 5C18-300 250 x 4.6 mm column; at a flow rate of 1 ml/min) (shown in figure C.1) and the identity was confirmed by MALDI-ToF mass spectrometry: MS [M + H]+: m/z 3068.61 (calculated), 3070.55 (observed in figure B.1).

4.2.2 Protein Synthesis of Protein Model with Alexa Fluor-488 Fluorophore

The peptide was assembled on a Fmoc-Gln(Trt)-Wang resin using a Liberty microwave peptide synthesizer (CEM Corp). HBTU/DIPEA and piperidine for coupling and deprotection reagents, respectively. Alexa Fluor-488 fluorophore was labelled orthogonally to Fmoc-Lys(Alloc)-OH. Peptides were cleaved and deprotected using the cleavage cocktail. The peptide was then purified using RP-HPLC with a semi-preparative (VydacC18 5 μm) column. The purity was analysed with the use of analytical RP-HPLC (shown in figure C.2 and figure C.3 for the unlabelled and labelled protein model, respectively) with an analytical (VydacC18 5 μm) column and MALDI-ToF. The gradient of buffer B increased from 10-70% over 50 minutes at a flow rate of 1 ml/min and 4.7 ml/min for analytical and semi-preparative, respectively. Buffer A was made up of 94.9% water, 5% acetonitrile, 0.1% TFA and buffer B had 94.9% acetonitrile, 5% water, 0.1% TFA. Protein model with no fluorophore: m/z 3033.65 (calculated), 3033.70 (observed in figure B.2) and protein model with Alexa Fluor-488: m/z 3555.65 (calculated), 3557.15 (observed in figure B.3).

4.2.3 Sample Preparation of Protein Model with Intrinsic Fluorophore

Aqueous peptide solutions (50 μM) were prepared in filtered (0.22 μm) 10 mM MOPS, pH 7.4. The fluorescence of the peptide was measured at 37.5 °C, pH 7.4 to mimic physiological conditions. A stock solution of D-(+)-Glucose (Sigma-Aldrich) in distilled water was added to the peptide where the final concentration of glucose was 50 mM.

4.2.4 Fluorescence Measurements of Protein Model with Intrinsic Fluorophore

Absorption and fluorescence intensity measurements were performed using Lambda 25 (Perkin Elmer) and Fluorolog (Horiba Scientific), respectively. Time-resolved fluorescence decays were taken on the DeltaFlex fluorescence lifetime system (Horiba Jobin Yvon IBH Ltd, Glasgow) using time correlated single photon counting. A NanoLED

with a wavelength of 279 nm and producing pulses of ~600 ps was used for excitation [111]. Fluorescence decays were measured with varying detection wavelengths from 290 to 340 nm in 5 nm increments. Each decay takes ~30 minutes to measure. The decays were fitted to a three-exponential model function for each detection wavelength. The parameters were recovered to generate time-resolved emission spectra and the Toptygin-based models [83] was used to represent time-resolved emission spectra (TRES). In turn, we were able to extract parameters such as peak position ν_i, half-width of the distribution σ_i and fluorescence contribution C_i of each component.

4.2.5 Fluorescence Measurements of Protein Model with Thioflavin T

Thioflavin T (ThT) (25 μM) was added to the peptide solution (50 μM) in MOPS buffer. The fluorescence intensity of tyrosine was measured with an excitation wavelength of 279 nm and an emission range of 290-500 nm. The intensity of ThT was measured with an excitation wavelength and emission range of 440 nm and 450-700 nm, respectively.

4.2.6 Structured Illumination Microscopy of the Protein Model with Alexa Fluor-488 Fluorophore

Protein model with no dye (300 μM) was mixed with protein labelled with Alexa Fluor-488 at a molar ratio of $1{:}10^{-3}$ prepared in filtered 10 mM MOPS at pH 7.4. The solutions were prepared at 200 μL and droplets of 2.5 μL were pipetted onto the Lab-Tek II Chamber (Thermo Fisher Scientific, New York). Images of mature fibrils were taken after the droplets dried completely and were rehydrated with MOPs buffer.

Structured illumination microscopy images were performed with a modified inverted microscope (IX71, Olympus). The light path was set to total internal reflection fluorescence (TIRF) mode using a 488 nm laser (Sapphire LP, Coherent Inc.) and the 100x/1.49 objective lens (UPLSAPO 60XS, Olympus) collected the fluorescence emitted from the fibrils. Nine raw images were captured with a CMOS camera (Orca Flash 4.0 v1, Hamamastu Photonics) and the images were processed through a Matlab programme to reconstruct a SIM image.

4.3 Results and Discussion

4.3.1 Monitoring Long-Term Stability for Protein Fibrillogenesis Model Through Intrinsic Fluorescence

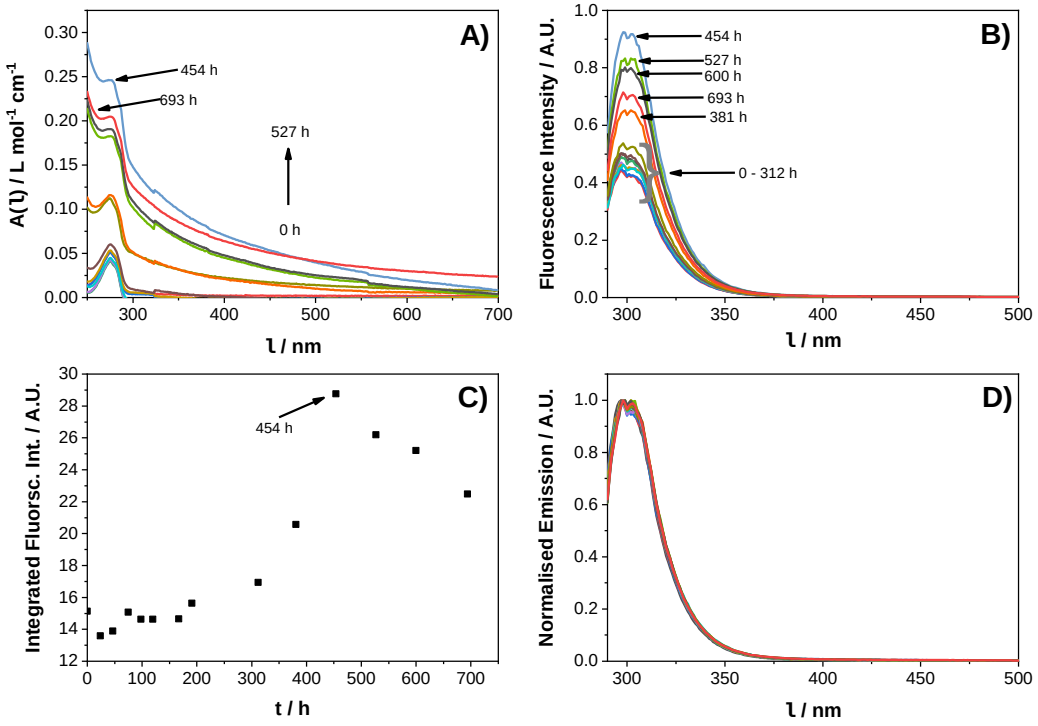

Figure 4.2: Steady state measurements A) absorbance and B) emission of the protein fibrillogenesis model for 0, 22, 43, 68, 95, 201, 312, 381, 454, 527, 600 and 693 hours after sample preparation. The integrated fluorescence intensity C) and normalised emission spectra D) were also plotted.

The steady state absorption spectra was measured for fibrillogenesis model at different times after preparation over 700 hours are shown in figure 4.2A. There is a dominant tyrosine absorbance peak around 279 nm and show an increasing effect of Rayleigh scattering with the sample ageing up to about 450 hours and then a gradual drop in absorbance. Simultaneously, the peak fluorescence and integrated intensities (shown in figure 4.2B and C, respectively) increased up to 450 hours and then starts to decrease. The growing contributions of scattered light in the absorption spectra are indictive of oligomeric forms increasing in size [112], while increases in fluorescence intensity are attributed to a higher quantum yield of tyrosine caused by its gradually decreasing

quenching by water [113]. Both observations are consistent with the fibrillogenesis process over the studied period. The potential cause of the decreased intensities observed in both spectra is likely to be caused by precipitation of the larger fibrils and, consequently, decreasing concentration of the fluorescent material in solution. This is consistent with experiments carried out by Bouchard et al., where precipitation was also found when insulin fibrils were formed [13]. The shape of the spectra (depicted in figure 4.2D) does not change which suggests that there are no new complex fluorescence species formed throughout 700 hours.

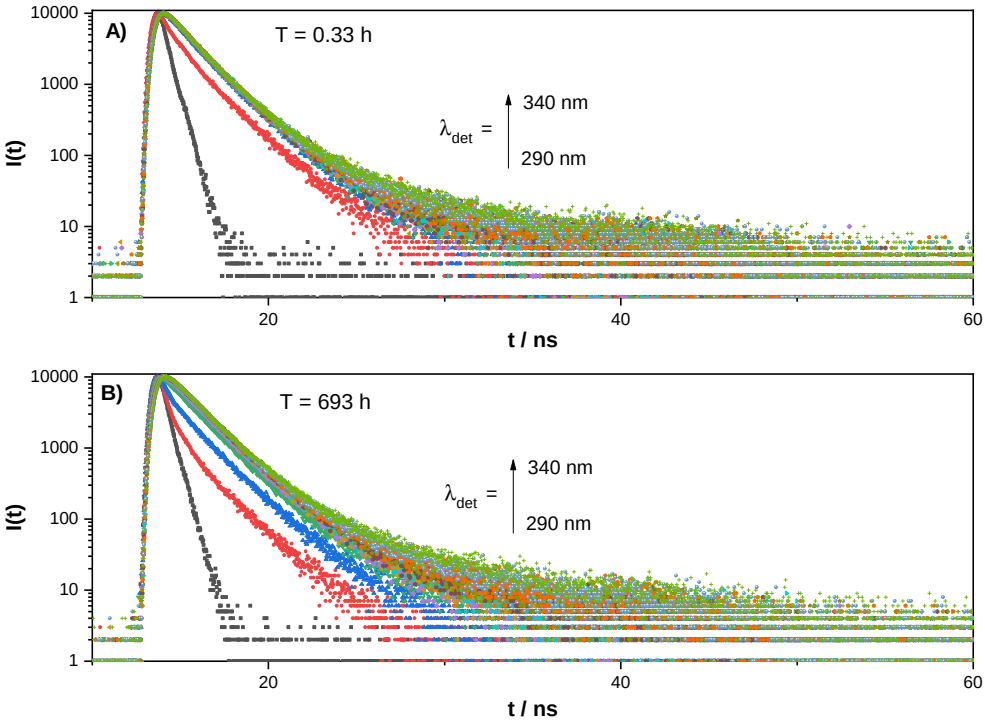

Figure 4.3: The instrumental pulse profile (grey) and fluorescence intensity decays for detection wavelengths of 290, 295, 300, 305, 310, 315, 320, 325, 330, 335 and 340 nm for A) 0.33 and B) 693 hours after sample preparation of fibrillogenesis model.

In the next stage, fibrillogenesis was monitored by means of the potential changes in the fluorescence intensity decay of Tyr residues. The full set of fluorescence intensity decays for the fibrillating sample was measured at wavelengths from 290 nm to 340 nm with 5 nm increments. The series of measurements started at a seeding phase in the first 0.33 hours of sample preparation, with subsequent measurements recorded at

22, 43, 68, 95, 201, 312, 381, 454, 527, 600 and 693 hours. Figure 4.3 presents examples of fluorescence intensity decays recorded at different time points and wavelengths. Fluorescence intensity decays recorded at longer wavelengths show the progressive emergence of a longer decay component, as illustrated in figure 4.3A and B for the earliest (0.33 h) and latest (693 h) samples, respectively. This observation is consistent with protein wavelength-lifetime dependence [107,114] which can be explained by the dielectric relaxation of the fluorophores occurring on the same timescale as the decay time, or by the presence of multiple components of different emission spectra and fluorescence lifetimes increasing with emission wavelengths. However, a substantial contribution of the scattered excitation light in the decay signal can also preferentially distort the decay at shorter wavelengths. In order to separate the scattered light from the actual fluorescence decays, we used the data fitting model decays consisting of both multi-exponential part and the scattered light component [115]. TableA.1-E in Appendix A show parameters recovered from fitting the 3-exponential model to the data measured for the 0.33, 43, 312, 454, and 693 hours old sample respectively, together with the percentage contribution of the scattered light $S_c(\lambda)$ at each detection wavelength λ. Increased contributions of the scattered light were detected in the decays measured at 290 nm due to the closeness of the excitation and detection wavelength, thus, picking up the excitation light by the detector even at low scatter from the sample. We note that due to structural complexity of the sample during fibrillogenesis (distribution in fibrillar size and structure) and potential effects of dielectric relaxation, the individual fluorescence decays cannot be resolved by means of any specific model of kinetics. Instead, the 3-exponential representations of these decays were used to produce TRES.

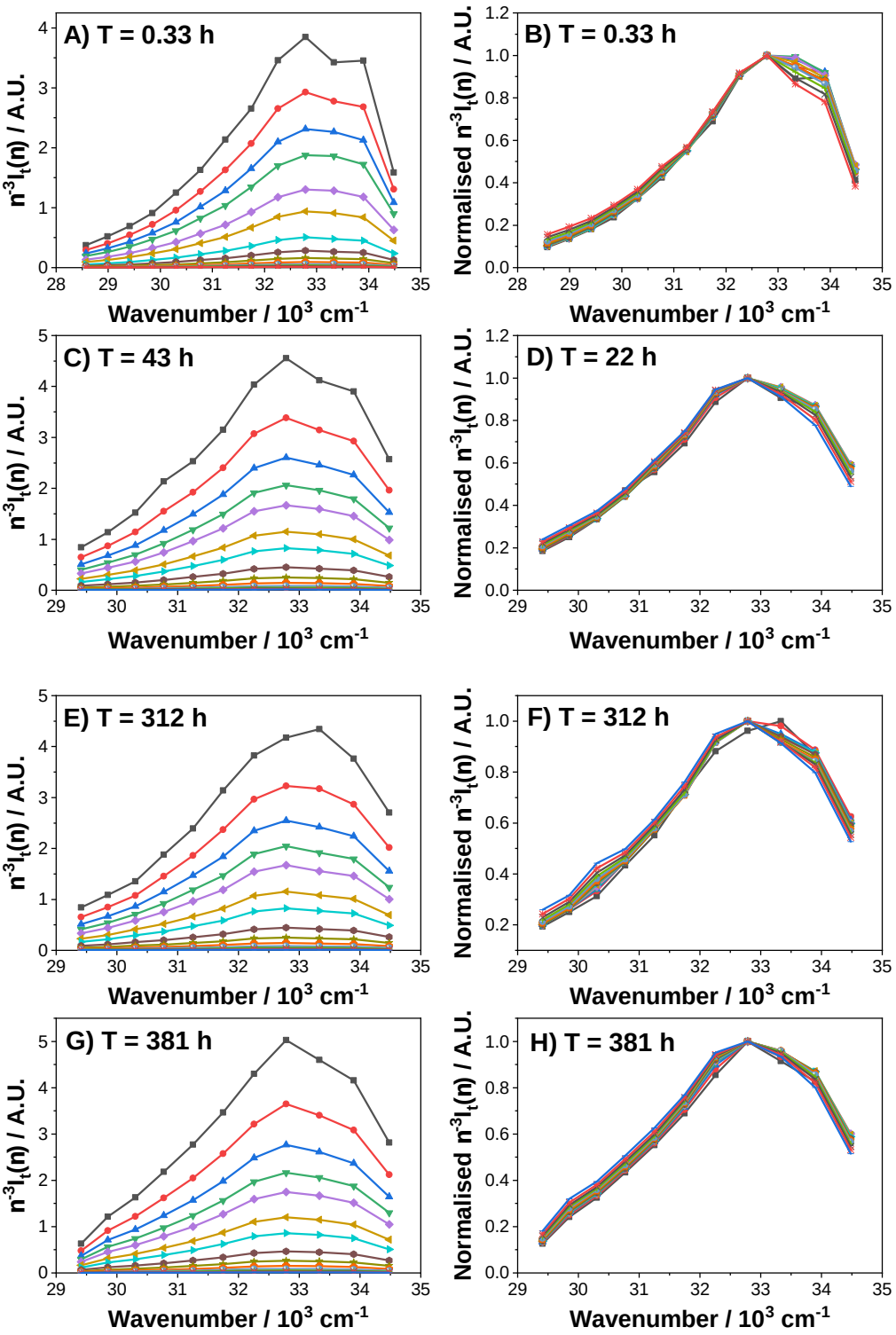
A) T = 0.33 h
B) T = 0.33 h
C) T = 43 h
D) T = 22 h
E) T = 312 h
F) T = 312 h
G) T = 381 h
H) T = 381 h
n-3It(n) / A.U.
Normalised n-3It(n) / A.U.
Wavenumber / 10³ cm-1

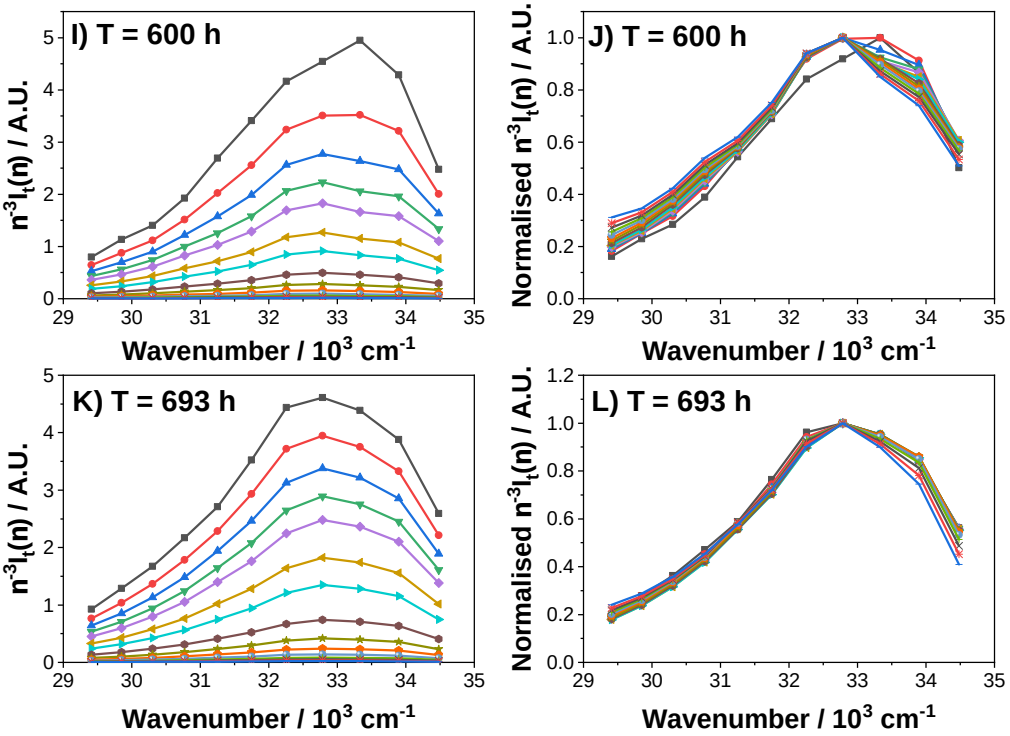

Figure 4.4: The left hand panel show the TRES spectra of the peptide model A), C), E), G), I), and K) for 0.33, 43, 312, 381, 600, and 693 hours, respectively. The right hand panel shows the same TRES data normalised for the peptide model B), D), F), H), J), and L). The plots were determined at 0, 0.25, 0.5, 0.75, 1, 1.5, 2, 3, 4, 5, 6, 7, 8, 9, and 10 ns after excitation. 0 ns is excluded from 0.33 hours due to high scatter.

For the protein model, the TRES representation $\nu^{-3}I_t(\nu)$ (using equation (3.12)) and normalised $\nu^{-3}I_t(\nu)$ were plotted for different times after preparation. A few samples of age 0.33, 43, 312, 381, 600, and 693 hours are shown in figure 4.4A, C, E, G, I, and K. The fluorescence spectra measured at all stages of fibrillization decay gradually and there is a faster decay at longer wavenumbers compared to lower wavenumbers, (which is better shown in the normalised spectra figure 4.4B, D, F, H, J, and L). The detailed analysis of spectra indicates two fluorescent forms with emission peaks at ~33,000 and 31,500 cm^{-1} and the effects of dielectric relaxation in both forms. However, the effect of dielectric relaxation is relatively small (~500 cm^{-1}). Overall the spectral shape changes are minimal.

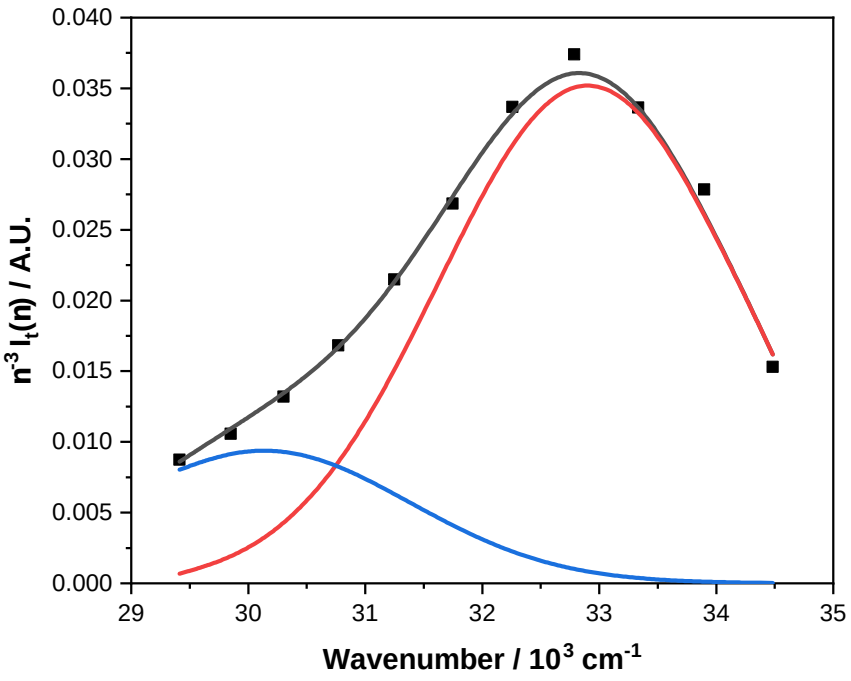

Figure 4.5: Experimental TRES data (■) fitted to 2 Toptygin-type models, where the first (red curve) and second component (blue curve) was emitting around 33000 and 30000 cm^{-1}), respectively and the sum of two components are represented by a grey curve.

To gather more information on the spectral changes for the peptide, all TRES were fitted by the distribution function (shown in figure 4.5). From equation (3.20) it was necessary to assume $N = 2$ to obtain a good fit, which implies the existence of two fluorescent forms with emission maxima ~33,000 and ~31,500 cm^{-1} (for freshly prepared sample) evolving differently over the studied period.

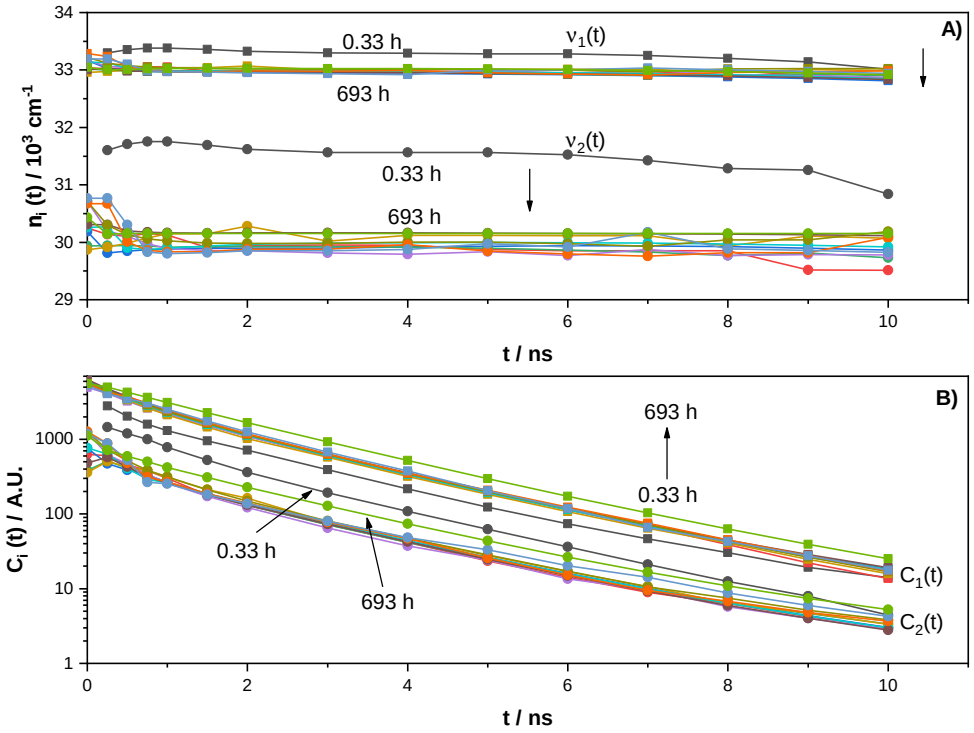

Figure 4.6: TRES parameters taken from the 2 Toptygin-type models of peak positions ν_i and the corrected fluorescence contributions C_i fitted to two exponential models. Fluorescent species 1 and 2 (■) and (●) where measured at 0.33, 22, 43, 68, 95, 201, 312, 381, 454, 527, 600, and 693 hours after sample preparation.

Figure 4.6A shows the shifts of spectral peak positions following the moment of excitation for the samples measured at different times after preparation, while the fluorescence contributions $C_i(t)$ of each component are shown on figure 4.6B. The curved shapes of all plots $LogI(t)$ versus time shows that the kinetics is more complex than exponential and both forms decay at similar rates. Combined analysis of the TRES and the steady-state data seem to suggest three stages of the model fibrillogenesis: During the first 22 hours the 33,000 cm^{-1} form shifts towards shorter wavenumbers by ~500 cm^{-1} (figure 4.6A) while 31,500 cm^{-1} form shows a much larger shift by ~1,500 cm^{-1}. Moreover, the percentage fluorescence contribution of the 33,000 cm^{-1} form increases from 63 to 90% (estimated from the initial values of $C_i(t)$ - figure 4.6B), while the other decreases from 37 to 10%. During this time the initial oligomers are formed, and Tyr residues experience significant changes in their local environments.

The second stage covers the period from ~24 to 450 hours. At this time, the positions of the spectral peaks $\nu_i(t)$ and the fluorescence intensity decays $C_i(t)$ do not change significantly. The increasing intensity of the steady-state fluorescence observed during this period (figure 4.2B) and no changes recorded in lifetimes can be explained by initial oligomers showing low quantum yield of fluorescence (due to static quenching by water), but become more fluorescent once incorporated into fibres.

The third stage begins after ~450 hours, when the TRES parameters remain stable and the rates of the decays $C_i(t)$ do not change substantially, but the peak intensities of the absorption and fluorescence spectra start to drop (figure 4.2A and B). This effect is consistent with the formation of larger forms that precipitate, which effectively reduces the concentration of fluorescent material in the sample. The process does not affect the detected fluorescence decays, which are independent of fluorophore concentration and because precipitation applies to larger fibrils, the local environments of tyrosine residues under measurement are unaffected. This suggestion is consistent with the increasing number of monomers in the growing fibrils. In the previous studies of the model prepared under similar conditions [38], the calculated number of monomers in a fibril was 225 x 10^3. Clearly the fibrillogenesis of the structures of this size is not reflected in changes of intrinsic fluorescence.

4.3.2 Monitoring Glycation of Protein Fibrillogenesis Model by its Intrinsic Fluorescence

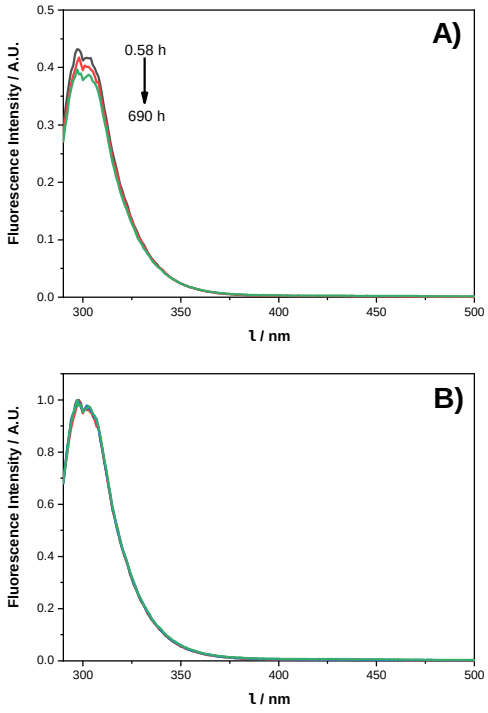

Figure 4.7: Steady state emission A) and normalised emission B) of fibrillogenesis model with glucose measured at times 5, 48, and 690 hours after sample preparation.

To further examine the stability features of the fibrillogenesis model, glucose was added to the sample to investigate potential glycation effects. The protein model was also incubated for nearly 700 hours and the steady state spectra was taken for 5, 48, and 690 hours are shown on figure 4.7A and the normalised spectra is shown on figure 4.7B. In contrast to the fibrillogenesis model without glucose, the intensity slightly decreases when glucose is added. This may show that glucose inhibits the fibrillization in the protein model because glucose disrupts the process of elongation and therefore tyrosine residues are unable to shield away from quenchers. As there are no glucose binding sites, the normalised spectra are similar to fibrillogenesis model without glucose and there is no evidence of new fluorescent species being formed. It has been reported that glycation can either inhibit or accelerate fibril formation.

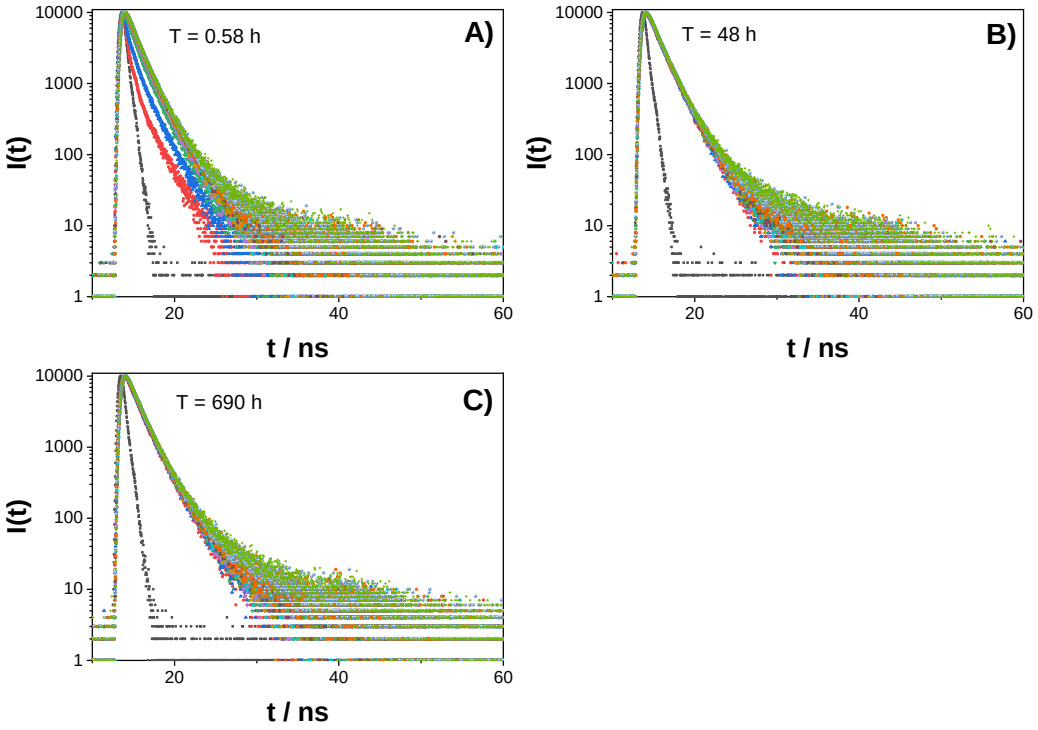

Figure 4.8: Fluorescence lifetime decays for fibrillogenesis model incubated with glucose for A) 0.58, B) 48 and C) 690 hours.

Figure 4.8 presents the fluorescence intensity decays for fibrillogenesis model with glucose incubated for 0.58, 48, and 690 hours. The intensity decay also shows protein wavelength-lifetime dependence, where 290 and 295 nm are heavily affected by scattered light in 5 hours after sample preparation. However, the fluorescence intensity decay shows that it is not influenced by scattered light, which is further evidence that glucose inhibits large aggregate formation.

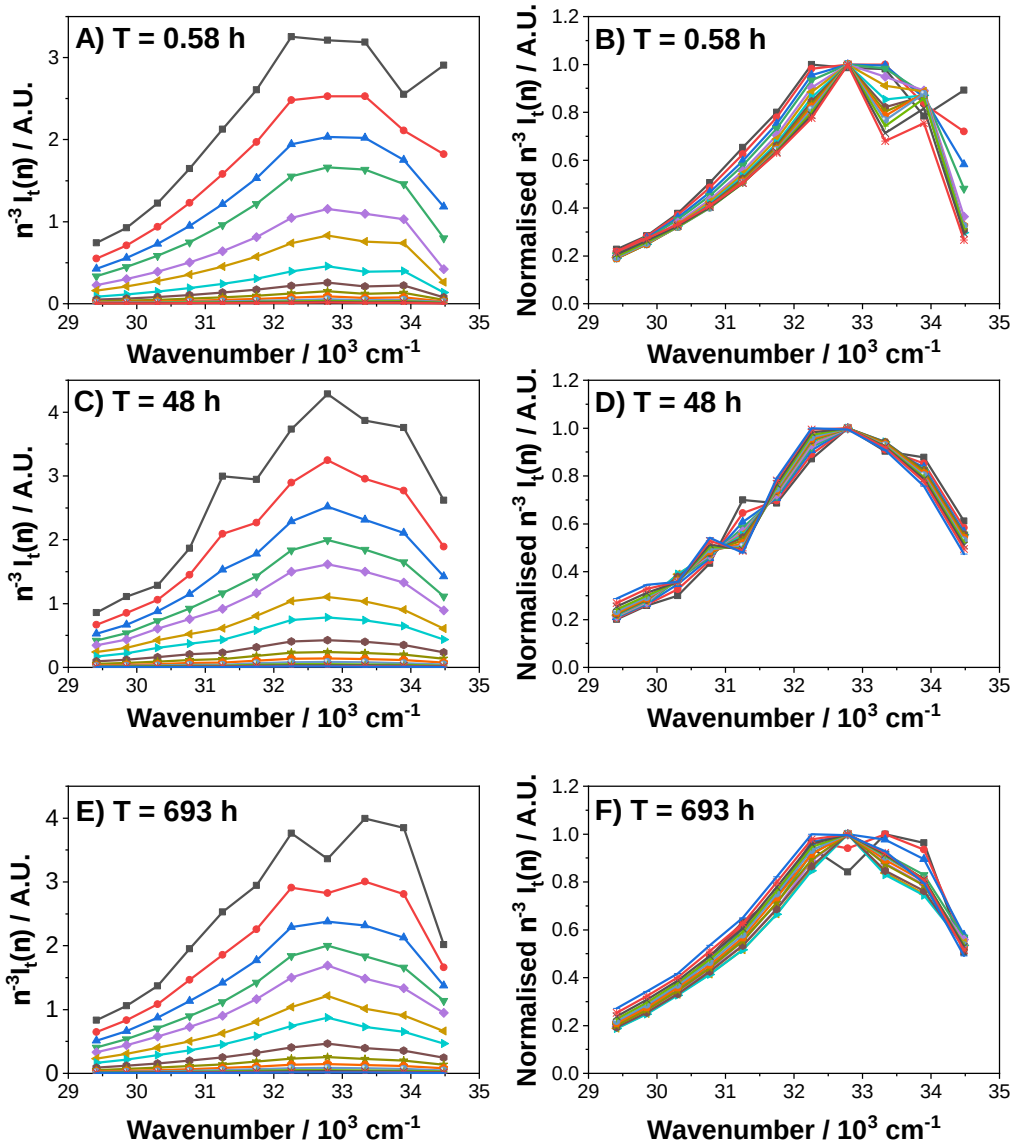

Figure 4.9: The left hand panel show the TRES spectra of the peptide model with glucose A), C), and E) for 0.58, 48, and 693 hours, respectively. The right hand panel shows the normalised TRES plots for the peptide model with glucose B), D), and F). The plots were determined at 0, 0.25, 0.5, 0.75, 1, 1.5, 2, 3, 4, 5, 6, 7, 8, 9, and 10 ns after excitation.

The examples of TRES for 0.58, 48, and 693 hours are shown in figure 4.9A, C, and E, respectively. For the sample 0.58 hours old, at 34500 cm^{-1} the points are outliers after each moment of excitation which may be heavily influenced from light scattering as it is close to the excitation wavelength (279 nm). The normalised TRES shown in figure 4.9B, D, and F show again small change within the TRES when glucose is present at 48 and 693 hours of incubation. As expected, (the peptide has no binding sites for glucose) no evidence of TRES changes were observed over time, demonstrating that the protein model is not prone to glycation.

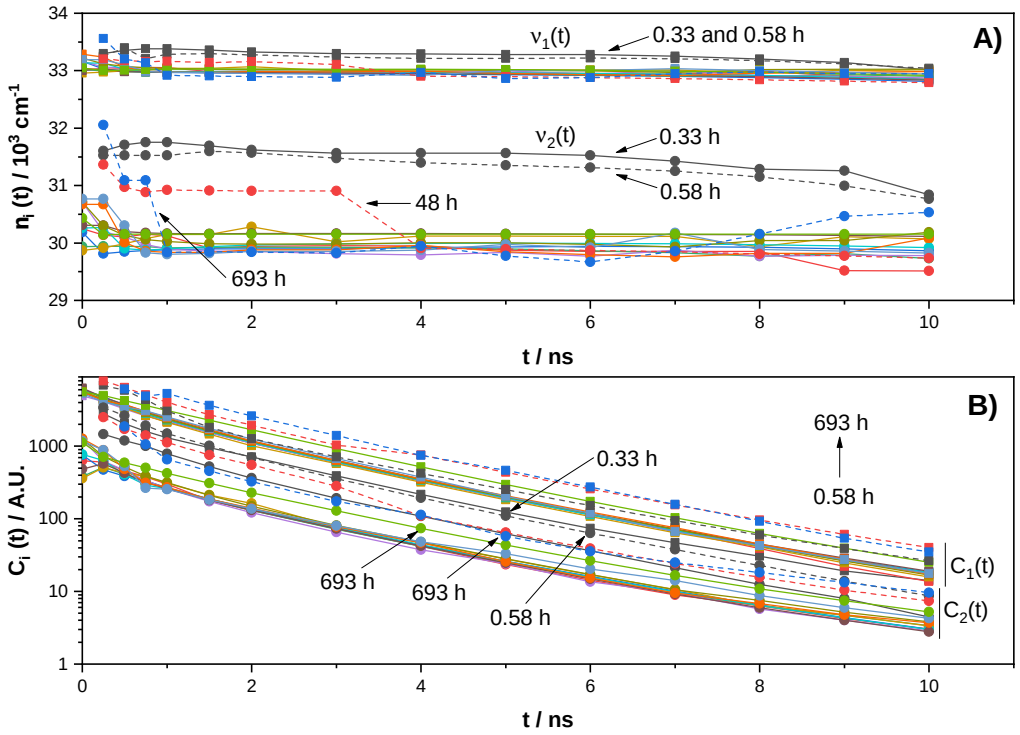

Figure 4.10: TRES parameters taken from the 2 Toptygin-type models of A) peak positions ν_i and B) the corrected fluorescence in log scale contributions C_i fitted to three exponential models. Fluorescent species 1 and 2 (■) and (●) fibrillogenesis model (solid curve) were measured at 0.33, 22, 43, 68, 95, 201, 312, 381, 454, 527, 600, and 693 hours after sample preparation. Fibrillogenesis model with glucose (dashed curve) were measured at 0.58, 48 and 693 hours.

For further investigation of the influence glucose has on the fibrillogenesis model, the spectral shifts were compared with the fibrillogenesis model. As shown on figure 4.10, the first component with the initial peak intensity of 33,500 cm^{-1} at 0.58 hours shifts ~500 cm^{-1} within 48 and 693 hours which shows a similar trend to fibrillogenesis model

without glucose. For 0.58 hours, the initial spectral shift in second component (32,000 cm^{-1}) is similar to the protein model without glucose at 0.33 hours after preparation. However, there was no large initial shift (at 0.25 ns) shown in the second component when the peptide was incubated with glucose for ~48 and 693 hours. Instead the second component started to shift to 30,000 cm^{-1} after 3 and 1 ns after excitation for 48 and 693 hours after sample preparation, respectively. The lack of initial shift confirms that there are no large aggregates formed when the protein model has been incubated with glucose. However, there may be fast dielectric relaxation because glucose is colliding with the protein model causing the spectral shift to lower energy levels. Furthermore, the percentage fluorescence contribution of both forms (33,500 and 32,000 cm^{-1}) do not change significantly from 68 to 65% and 32 to 35%, respectively. During this time the Tyr residues do not experience change in their local environments.

4.3.3 Binding Thioflavin T to Protein Fibrillogenesis Model and its Influence on Tyrosine Fluorescence

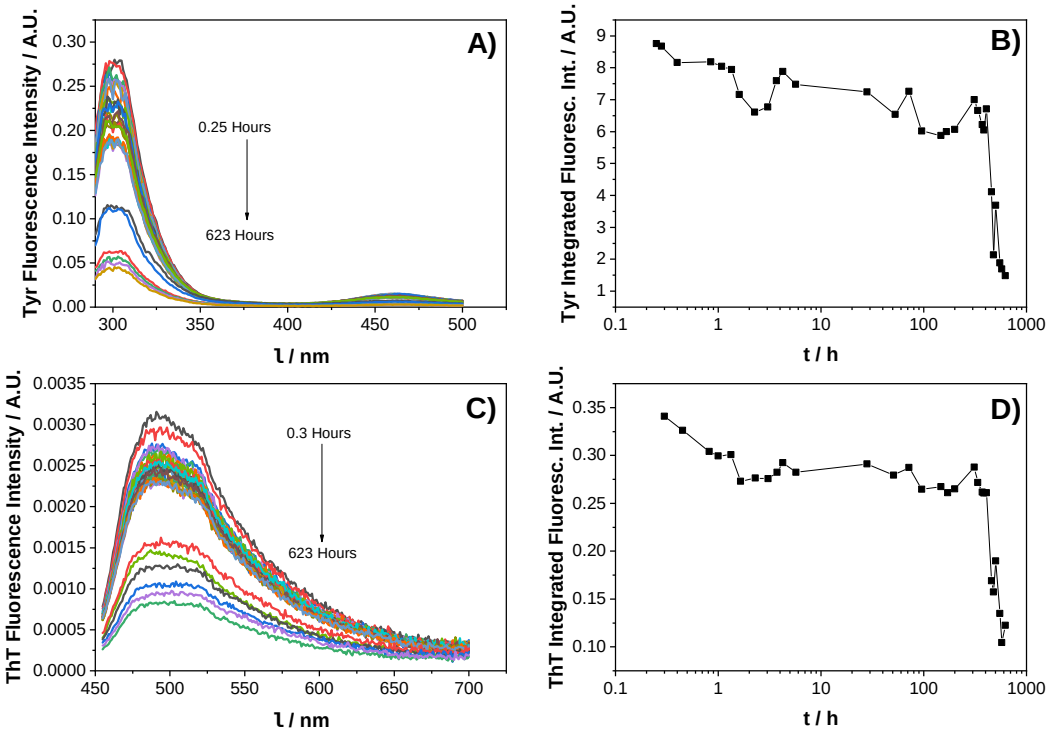

Figure 4.11: Steady state emission measurement of protein fibrillogenesis model labelled with Thioflavin T. A) Tyrosine was excited at 279 nm and fluorescence was collected at 290-500 nm and its B) integrated fluorescence intensity was plotted for 0.25, 0.28, 0.40, 0.85, 1.08, 1.35, 1.60, 2.27, 3.05, 3.68, 4.25, 5.67, 28, 53, 72, 96, 147, 167, 200, 311, 336, 372, 384, 407, 457, 479, 504, 552, 576, and 690 hours after sample preparation. C) Thioflavin T was excited at 440 nm and fluorescence was collected at 450-700 nm and its D) integrated fluorescence intensity was plotted 0.30, 0.45, 0.82, 1, 1.33, 1.65, 2.30, 3.07, 3.73, 4.25, 5.70, 28, 51, 72, 96, 147, 171, 200, 311, 336, 371, 384, 407, 457, 479, 504, 552, 576, and 690 hours after sample preparation.

To gather more information on the aggregation kinetics of the fibrillogenesis model, ThT was used to examine β-sheet formation. Steady state emission measurements were carried out where of both the tyrosine and ThT fluorescence were monitored at excitation wavelength of 279 and 440 nm in figure 4.11A and C, respectively. The range of emission wavelengths also differ, where tyrosine and ThT fluorescence is measured at 290-500 nm and 450-700 nm, respectively. The integrated fluorescence intensity was taken to show the total emitted photons for each sample, shown in figure 4.11B and D. In contrast to the unlabelled fibrillogenesis model (shown in figure 4.2C), the tyrosine

fluorescence exhibited a gradual decrease up to 457 hours of incubation. Figure 4.11A shows that there is another fluorescence peak around 460 nm which is not seen in the unlabelled fibrillogenesis model. These observations may indicate that tyrosine fluorescence is transferring energy non-radiatively to ThT.

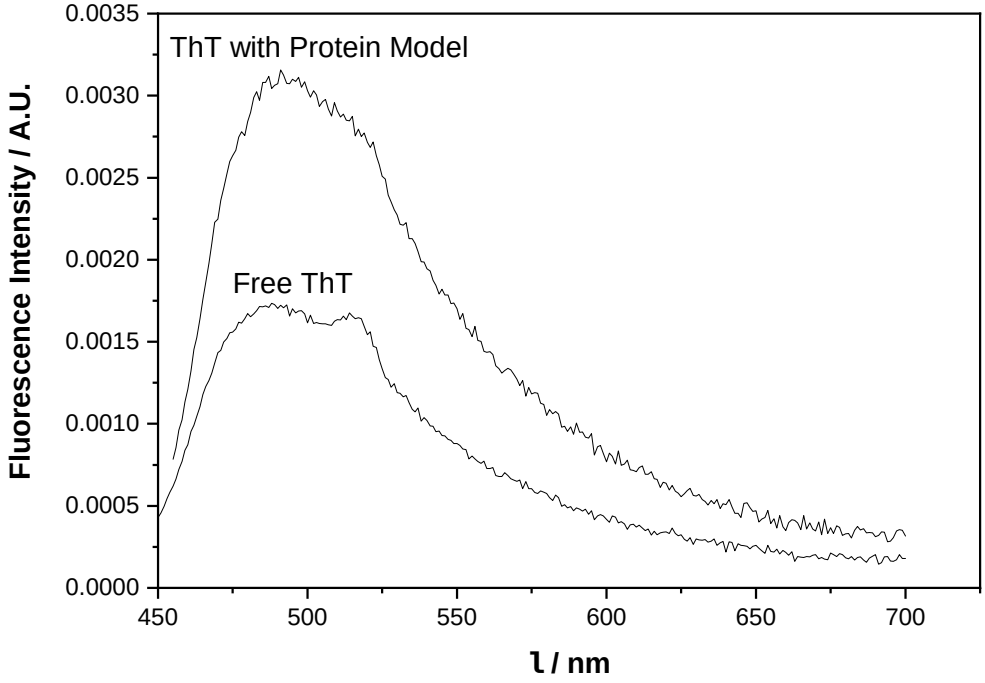

Figure 4.12: Comparison of steady state emission measurement of unlabelled protein fibrillogenesis model and protein model labelled with Thioflavin T. Thioflavin T was excited at 440 nm and fluorescence was collected at 450-700 nm.

There is a dramatic decrease shown in both tyrosine and ThT fluorescence shown in 457 hours (figure 4.11B and D, respectively), which coincides with the large decrease shown in the emission spectra after 454 hours after preparation of the unlabelled fibrillogenesis model (figure 4.2C). The steep decline of intensity confirms that large aggregates do precipitate out of the solution around 450 hours and therefore, their fluorescence cannot be detected. Since the intensity of ThT decreases dramatically after precipitation and ThT is in close proximity to Tyr to enable energy transfer, this shows that ThT does bind to the protein model. However, it can be observed that there is no significant increase in fluorescence intensity between ThT in water)

and ThT incubated with the fibrillogenesis model (shown in figure 4.12). Typically, when ThT binds to β-sheets, ThT has a fluorescence enhancement factor of 1000 [36]. Since the large enhancement is not shown, demonstrates that there is a lack of β-sheet conformation within the protein model. This is expected as the model was designed to primarily consists of α-coiled-coil motifs. Therefore, when ThT is bound to the protein, the benzothiozene and benzothiozole rings are still free to rapidly rotate in solution. This experiment indicates that ThT has an influence upon the local environment of tyrosine as it binds to the protein model, however, fibrils are still able to cluster and form large precipitates.

4.3.4 End Point Assembly For Fibrillogenesis Model Labelled with Alexa-Fluor 488

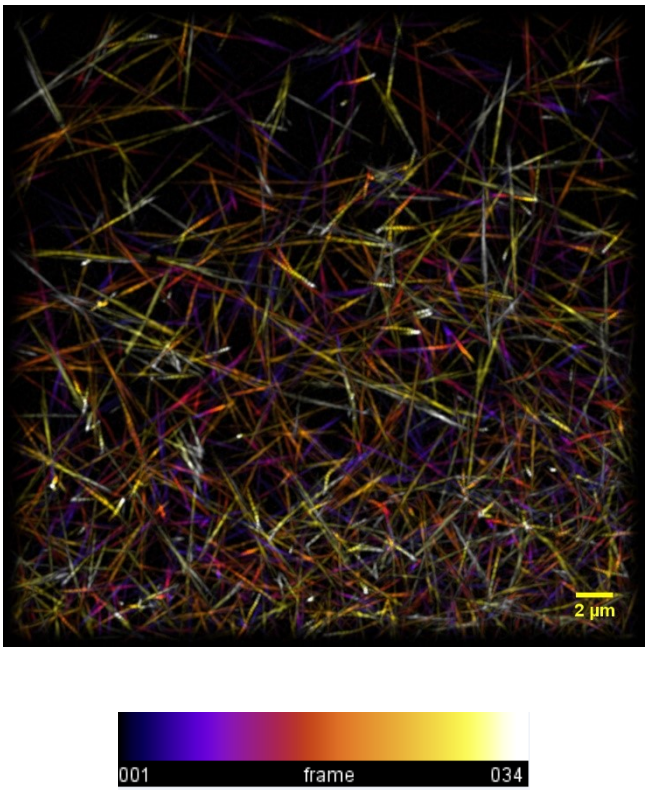

Figure 4.13: Structured illumination microscopy image of fibrillogenesis model from a droplet volume of 2.5 μL.

Structured illumination microscopy was used in conjunction with spectroscopy techniques to further the understanding of fibrillogenesis model (shown in figure 4.13). In this experiment, a volume of 2.5 μL was pipetted onto the centre of the cover slip and after 30 minutes the droplet completely dried. To image the droplet MOPS buffer was used to rehydrate the sample and an excitation wavelength of 488 nm was used. The images taken in the z direction have been stacked and colour coded and it shows a dense amount of fibrils. Fibrils produced under static conditions the crowding throughout the image is uniform and maturation of fibrils (~2.5 μm) takes several hours [38]. However, the fibrils created under dynamic conditions experience less crowding at the top of figure 4.13 and fibrils appear longer (~4 to 9 μm). Whereas, the bottom of the image is more densely packed and are shorter (~2 to 6 μm) and/or more intertwined with other fibrils. The fibrils get more densely packed near the bottom of the image because it is close to the edge of the droplet. According to Deegan et al. [116], a drying droplet does not shrink but instead the capillary forces from the top of the droplet migrate to the outer edge of the droplet. Therefore, most of the peptide material is deposited at the edge of the droplet. Since the area closer to the centre of the droplet has more space and there is also a limited number of fibrils that monomers can bind onto, fibrils are able to elongate, producing large fibrils.

4.4 Conclusion

To gain a deeper understanding of protein fibrillogenesis, simple synthetic models self-assembled from the monomer up is a fundamental step to our progress. The fibrillogenesis model which has been designed obeys well-established sequence to structure rules that create homogeneous fibrils. The synthetic protein has an α-coil-coiled structure which elongates into mature fibrils and has shown to have homogeneous growth kinetics. This will enable simpler fluorescence interpretation which is advantageous as natural proteins often create amyloid fibrils which have complex structures due to polymorphism.

To examine the model without perturbation, an intrinsic fluorophore (Tyr) was

used as a sensor of the protein and its evolution was monitored for ~700 hours. The increased scatter in absorbance and change in fluorescence intensity observed during the whole period suggest an equilibrated fibrillogenesis of the model peptide. The photophysics of the Tyr residue is not affected directly during most of the process except for the initial stage, i.e. formation of initial oligomers during around 24 h. The stability of the fibrillogenesis model has been demonstrated and can be used as a useful reference tool to allow us to compare tyrosine residues found in other peptides and protein in similar TRES experiments. Indeed, in this thesis we have used the fibrillogenesis model to compare with a natural protein such as insulin in chapters 5 and 6.

Since protein is often glycated in amyloid deposits, it is important to monitor the interaction between glucose and the fibrillogenesis model. In contrast to the free fibrillogenesis model, there is no significant change to the fluorescence intensity and there is no evidence that the aggregates precipitate with the incubation of glucose over 700 hours. This may suggest that glucose inhibits fibril formation.

ThT is one of the most commonly used to probe β-sheet formation however, the results show in the fibrillogenesis model that it inhibits the increase of tyrosine fluorescence. This is due to ThT interacting and quenching the tyrosine residue. There is a possibility that the probe inhibits the growth of fibrils altogether, however, the fluorescence intensity of ThT and tyrosine significantly decreases around 454 hours after sample preparation. This fluorescence decrease is also shown in the unlabelled fibrillogenesis model around 457 hours. Therefore, we believe that ThT does perturb the kinetics but does not inhibit protein aggregation. Furthermore, the fluorescence intensity of ThT shows no signs of β-sheet formation within the fibrillogenesis model which is expected and confirms that the de novo peptide follows the sequence to structure rules.

In addition to studying fibrillogenesis in static conditions, dynamic environments increase the rate of fibrillogenesis and show that isolated fibrils are able to grow longer as they have less competition with other fibrils. On the contrary, Shaw et al [106]. has

shown that fibrils grown in dynamic conditions does not affect their morphology and the fibrils are homogeneous. This may be because the images taken from Shaw were taken at the very edge of the droplet where the fibril deposition would be uniformly distributed. However, it was not possible to image the edge of the droplet in figure 4.13 due to the high fluoresce intensity of fibrils labelled with Alexa-Fluor 488 dye which saturated the camera. Despite where the droplet was imaged, we can conclude that the fibrillogenesis model has an end point assembly of long fibrous structures. This agrees with the steady state and TRES measurements found in static conditions with the fibrillogenesis model.

Chapter 5

Investigation of Intrinsic Fluorescence of Insulin in Physiological Conditions

5.1 Introduction

As said in the previous chapter, protein aggregation has attracted significant interest due to its role in neurodegenerative diseases including Alzheimer's disease (AD), Parkinson's disease (PD), and diabetes type II [5,6].

One protein that is prone to fibrillation is insulin, a hormone which regulates blood glucose levels within the body. Patients with diabetes do not produce enough insulin to stabilize blood glucose levels and thus need additional injections of this hormone. Insulin is an extensively studied protein because of complications caused by its aggregation. For example, at frequent injection sites, long fibrous insulin structures have been found [8,117,118]. Also, the long term storage of insulin has been shown to lead to aggregation, thus impacting the efficacy and cost of diabetes treatment [54]. Specifically, the transportation and storage at higher temperatures increase the likelihood of instability since fibril and covalent polymer formation are temperature-dependent. The devices used in insulin infusion therapy are particularly susceptible because wear-

ing at body heat, shaking the reservoir with bubble formation, and interaction with hydrophobic surfaces of the infusion cannula all encourage monomer formation and partial monomer unfolding, the prerequisites for fibril formation. Moreover, serum samples taken from patients suffering from Parkinson's disease (PD) displayed an autoimmune response to insulin fibrils, which suggests that insulin aggregation plays a role in neurodegenerative disease [9].

Insulin [119] consists of 51 residues with two polypeptide chains, A and B. Chain A has 21 amino acid residues and a disulphide bridge between two cysteine amino acids, while chain B is composed of 30 amino acids. Both chains are covalently linked together by two cysteine bridges. There are seven intrinsic fluorophores in an insulin particle: two Tyr residues on chain A and two Tyr and three Phe residues on chain B. The protein can exist in many different states which is dependent upon many external factors such as pH and concentration. Insulin is predominantly stored as a hexamer stabilized by zinc ions and favours hexamer conformations at pH 7.4 shown in figure 5.1A. Whereas, insulin dissociates at pH 2 in 20% acetic acid and produces native monomers shown in figure 5.1B. In the body, zinc hexameric insulin is stored in the pancreas and when it is released in the blood stream, the protein dissociates and is predominately in its monomeric form. The monomeric insulin state is known to be the more biologically active compared to hexameric insulin [53]. In certain conditions, the monomeric state has a propensity to form amyloid fibrils compared to the hexametric state because of their low stability.

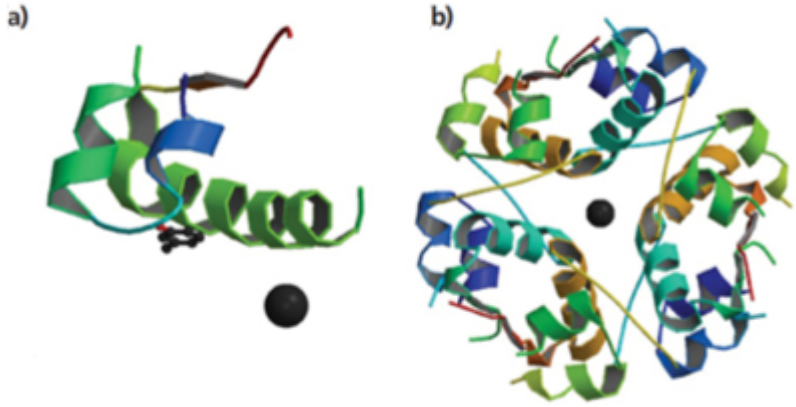

Figure 5.1: Crystal structure of A) monomeric and B) hexameric insulin in the presence of zinc measured by X-ray diffraction, PDB: 1ZEH.

Several techniques have been employed to study fibril formation including circular dichroism (CD) [21, 120], transmission electron microscopy (TEM) [121], atomic force microscopy [122], X-ray diffraction [43], and others [13, 20, 123].

Fluorescence spectroscopy is one of the most informative techniques to study protein folding and self-assembly and to monitor conformational changes. It offers an excellent combination of speed, ease of use, and nanometre-level molecular information [124]. Fluorescence benefits from labelling the protein assembly of interest with extrinsic fluorophores such as Thioflavin T (ThT), Auramine O, ANS, and Congo red [119, 125–127], to probe secondary structure alterations as a function of fluorescence responses. The use of these dyes has given a deeper understanding of protein fibrillation. The approaches used include conventional fluorescence spectra [128], fluorescence decay [36], and fluorescence correlation spectroscopy [129].

However, the use of extrinsic fluorophores is associated with some limitations as they can perturb protein kinetics, which leads to ambiguities in interpretation and lacks the sensitivity required for studying prefibrillar structures [130], and different probes used on the same system can yield different signals [131]. In this study, we attempt to overcome these limitations with the use of intrinsic fluorophores to detect conformational changes during insulin fibrillation. Our premise is that since insulin

has four tyrosine residues which are sensitive to local microenvironments, their fluorescence response carries information relevant to the insulin aggregation and fibrillation. Moreover, insulin contains no tryptophan residues which could complicate the kinetics with energy transfer from tyrosine. In previous studies of tyrosine response to insulin fibrillation, e.g. [119] its fluorescence was monitored at a fixed wavelength only and insulin fibril formation was accelerated by elevating temperatures and/or decrease pH of the aqueous solution, which is consistent with physiological conditions.

In this chapter, we report insulin's tyrosine fluorescence intensity decay and time-resolved emission spectra (TRES) to extract in-depth information on insulin aggregation kinetics under physiological conditions. Using time-resolved techniques carries significant advantages over the time-integrated approaches [124], the latter offering limited information on the dynamics of molecules in the excited-states.

In conjunction with spectroscopy measurements, dSTORM has been used to image the insulin at the nanometre scale. dSTORM is a powerful super-resolution technique that is able to break the diffraction barrier by using photoswitching buffers and high-powered lasers. The combination of them both encourages the majority of the fluorophores to reside in the dark state and only a small population of fluorophores returns to the ground state of the ON state. Once in the ON state, they undergo several hundred fluorescence cycles where a photon is emitted at each cycle before switching back to the OFF state. The switching buffers enable each fluorophore to undergo several ON-OFF cycles and emit a few thousand photons before photobleaching. With this method, the fluorophores are separated temporally, and thousands of images were captured. The images were all analysed and the position of each object was precisely determined by fitting a 2D Gaussian profile on the PSF of the emitter. The centre of each 2D Gaussian fitting is used to reconstruct an image with an improved resolution. dSTORM is able to visualize structures down to approximately <50 nm.

5.2 Methodology

5.2.1 Sample Preparation of Hexameric and Monomeric Insulin

Bovine insulin and phosphate-buffered saline pH 7.4 (PBS) were purchased from Sigma-Aldrich and were used without further purification. 50 μM solution of bovine insulin was prepared in PBS buffer (0.01 M) and sonicated until completely dissolved. Monomeric bovine insulin (50 μM) were prepared in acetic acid (20%) at pH 2.5. Both samples were kept and measured at 22 °C.

5.2.2 Fluorescence Measurements of Hexameric and Monomeric Insulin

The steady state fluorescence spectra measurements were recorded using Fluorolog (Horiba Scientific), respectively. For TRES measurements, the fluorescence decays were recorded on a DeltaFlex fluorescence lifetime system (Horiba Jobin Yvon IBH Ltd, Glasgow) using time correlated single photon counting (TCSPC). A NanoLED producing ~600 ps pulses at 279 nm [111] was used to excite the intrinsic tyrosine fluorescence at detection wavelengths λ ranging from 290 to 350 nm at 5 nm intervals. Each decay takes ~30 minutes to measure. To avoid the influence of rotational effects on fluorescence decays, a vertically oriented polariser in the excitation channel and a polarizer at the magic angle (54.7 °) in the detection channel were added in the optical path. Fluorescence decays recorded at the series of λ values were fitted to a multi-exponential model function. The recovered parameters from the multi-exponential decay function were used to create time-resolved emission spectra described in subsection 3.1.5.

5.2.3 Modelling TRES

In the next stage, modelling TRES was based on the Toptygin-type approach [83] and were used to represent the spectral shapes of fluorescent components. 2 and 3 normalised Toptygin-type distributions were used to model $\nu^{-3}I_t(\nu)$ and their output parameters were compared.

5.2.4 Fluorescence Measurements of Hexameric and Monomeric Insulin with Thioflavin T

Thioflavin T (25 μM) was added to hexameric (50 μM) and monomeric insulin (50 μM) samples in PBS prepared and measured at 25 °C. The fluorescence intensity of tyrosine was measured with an excitation wavelength of 279 nm and an emission range of 290-500 nm. The intensity of ThT was measured with an excitation and emission range of 440 nm and 450-700 nm, respectively.

5.2.5 Direct Stochastic Optical Reconstruction Microscopy of Hexameric and Monomeric Insulin with Alexa- Fluor 647

Stock solution of Tween (Sigma Aldrich) in PBS (0.1%) (PBST) were made and Bovine Serum Albumin (BSA) (5%) was added to create a blocking buffer. The blocking buffer (200 μL) was added to each imaging well in the Lab-Tek II Chamber (Thermo Fisher Scientific, New York) and was incubated at room temperature for 1 hour. The buffer was removed then 200 μL of the prepared hexameric and monomeric insulin samples to each well and incubated for 1 hour at room temperature. After incubation, 20 μL of formaldehyde (37%) was added to each well and was incubated for 10 minutes. After incubation, the wells were washed 3 times with PBS. PBS was then discarded and 200 μL of blocking buffer was added and incubated for 1 hour. The blocking buffer was then discarded and 100 μL of Anti-Insulin antibody (6.67 nM in blocking buffer) (Abcam, UK) was added to each well and incubated overnight at 4 °C. The wells were washed 3 times with blocking buffer in 10 minute intervals. The buffer was discarded and 100 μL of Goat Anti-Mouse IgG H&L with Alexa Fluor 647 (6.67 nM) (Abcam, UK) was added to each well and incubated in the dark for 1 hour at room temperature. The secondary antibody was washed 3 times with PBS in 10 minute intervals. The switching buffer (1 mL) was prepared with 500 μL glucose (10%), 5 μL enzyme stock solution (potassium chloride (KCl) (25 mM), tris hydrochloride (Tris-HCl) (25 mM), glucose oxidase (50 kU), catalase (1 MU), tris(2-carboxyethyl)phosphine (TCEP) (2 mM), glycerol (50%)), 10 μL of monoethanolamine (MEA) (5 M), 2 μL of potassium

hydroxide (KOH) (5 M), and 483 μL of sterile PBS. The pH of the switching buffer was checked before adding to each well before imaging.

dSTORM images were taken using a home built system based around an Olympus IX73 (Olympus) inverted microscope body. The objective lens used in the experiments was an oil immersion (N.A = 1.49) APON 60XOTIRF (Olympus) and Type F immersion liquid was used (1.518) (Leica). The 200 mW laser iBeam-Smart-640-S-HP (Toptica Photonics) with an excitation wavelength of 641 nm was focused at the back of the focal plane of the objective lens. A mirror could be adjusted to control the angle of incidence and ZT532/640rpc-UFI dichroic mirror (Chroma) was used to split the excitation light from the fluorescence emitted from the fluorophore. Band pass filters ZET532/640m (Chroma) were also used as an extra filter to reduce scattered light and/or reflected at glass sample interface. The camera Ixon Life 888 (Andor) was cooled down to -60 °C and it has 1024x1024 pixels with a pixel size of 13 μm x 13 μm, which corresponds to 122 nm x 122 nm in the sample as measured by the L42O2 micrometre ruler (Agar Scientific). The laser power and camera were controlled with the use of iBeam Smart and Andor SOLIS for Imaging Software, respectively. The data analysis was performed using an open source program called rapidSTORM [132].

5.3 Results and Discussion

5.3.1 Monitoring Long-Term Stability of Hexameric Insulin Through its Intrinsic Fluorescence

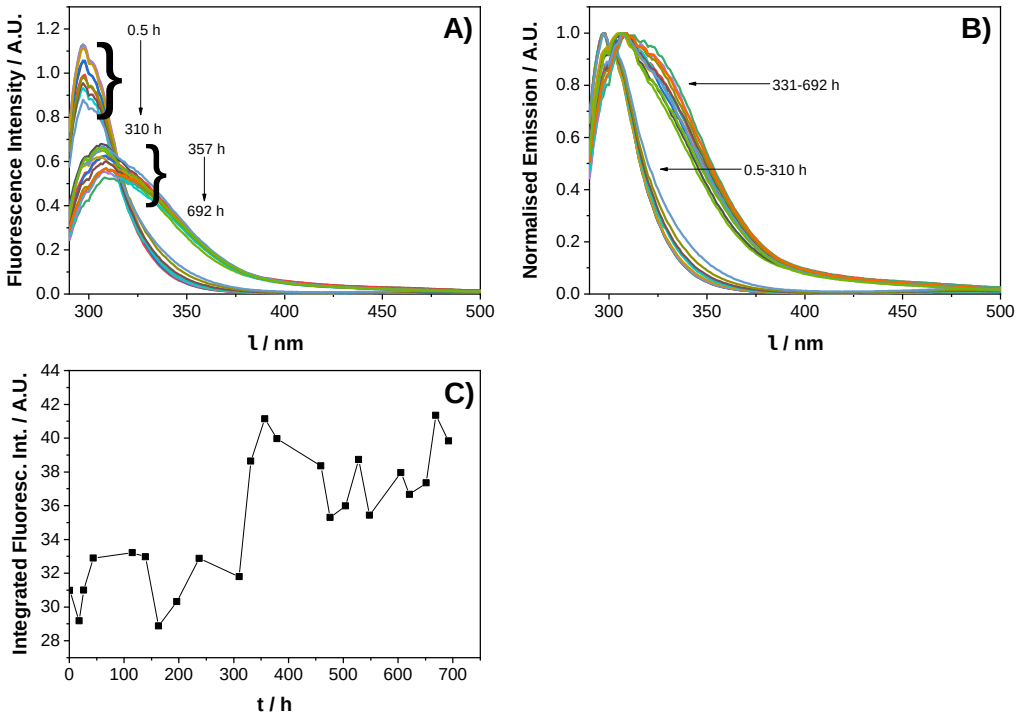

Figure 5.2: Fluorescence spectra of 50 μM hexameric insulin in PBS buffer at times 0.5, 18, 26, 44, 115, 139, 163, 196, 237, 310, 331, 357, 379, 459, 476, 504, 528, 548, 605, 621, 651, 669, and 692 hours after sample preparation A) and the normalised spectra B).The integrated intensity was calculated for each emission spectra C).

The steady state fluorescence spectra were measured for hexameric insulin at different times after preparation from 20 minutes (0.3 hours) up to over 600 hours are shown in figure 5.2. The freshly prepared sample (0^{th} hour) shows a dominant tyrosine intensity peak around 300 nm. After some time, the initial peak gradually decreases, and the spectrum becomes broader and shifts towards longer wavelengths. The normalised spectra on figure 5.2B demonstrates the shift and broadness. Furthermore, the total fluorescence intensity (shown on figure 5.2C) increases with aggregation time, which indicates fluorescence from the products of complex conformational changes. This

cannot be explained on the basis of the steady-state studies only. The drop in Tyr fluorescence intensity is consistent with the result reported by Bekard and Dunstan [119]. However, with the conditions of their experiment, (pH 1.9 and temperature 60°C) aggregation occurred within 10 hours, while in this experiment it takes around 30 days. This result confirms that at physiological pH and in the presence of zinc ions, the insulin hexamer formation is stable. The stable properties that hexameric insulin in pH 7 provides are exploited in drug product formulations.

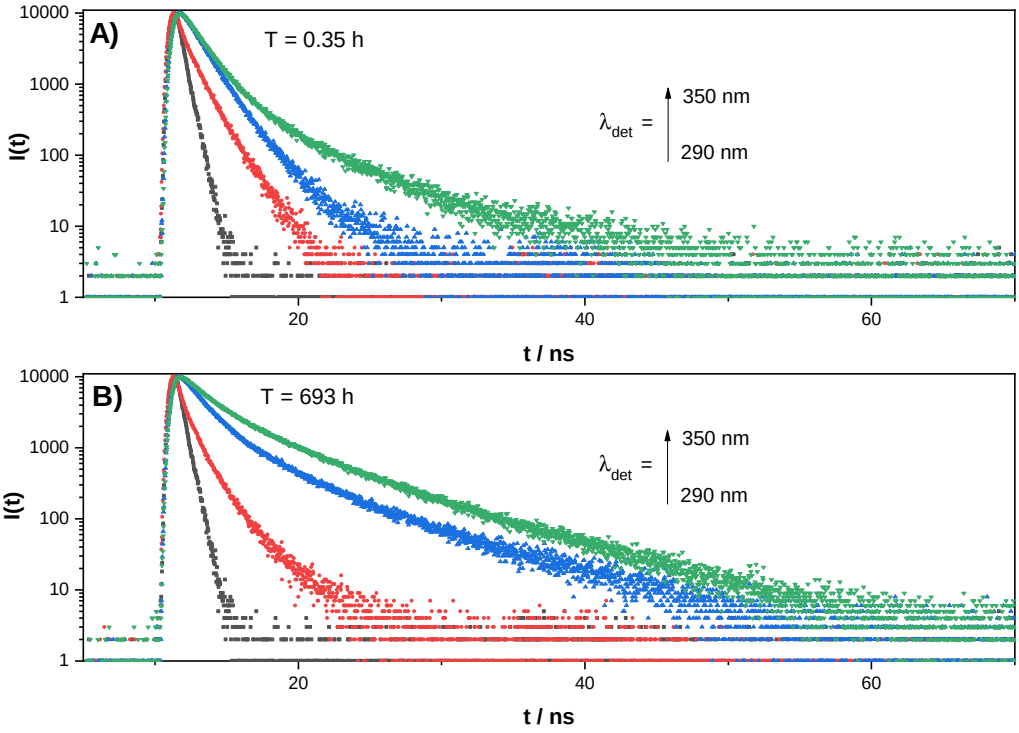

Figure 5.3: The instrumental pulse profile (black) and fluorescence intensity decays for detection wavelengths of 290 (red), 320 (blue), and 350 nm (green) for A) 0.33 and B) 693 hours after sample preparation of hexameric insulin.

The fluorescence decays of the insulin sample were recorded at different wavelengths and at different points of aggregation. Figure 5.3 demonstrates strong lifetime-wavelength dependence where the fluorescence intensity decays measured at the short-wavelength side of the spectrum (290 nm) decay more rapidly than the decays measured at the longer wavelength side (350 nm). This is consistent with the lifetime-wavelength correlation observed in proteins [114,133]. The effect can be explained by the fluorescence

intensity decay measured at the short-wavelength side of the spectrum being accelerated by the peak of the transient emission spectrum shifting away from the detection wavelength towards the red, due to dielectric relaxation, thus, causing a further decrease in intensity. For the same reason, the decay detected at the long-wavelength side of the spectrum decreases at a slower rate, as the peak of the shifting transient emission spectrum moves towards the detection wavelength. However, the detailed analysis of the recovered fluorescence lifetimes $\tau_i(\lambda)$ (see tables D.1-D.5 in Appendix D) shows that although the non-significant increase in two shorter lifetimes $\tau_i(\lambda)$ is typical for the lifetime-wavelength dependence, the strong increase in the longest lifetime has to be a consequence of significant structural change. The comparison of figure 5.3A and B and the differences in the $\tau_i(\lambda)$ in tables D.1 and D.5 show that the lifetime components of insulin after 690 hours of aggregation have increased compared to the lifetimes observed at 0.35 hours (21 minutes). This is likely to be due to numerous effects related to the complexity of insulin photophysics. Indeed, insulin has four tyrosine residues and three of them are buried in the protein [134] and therefore can be simultaneously involved in both hydrophobic and hydrophilic interactions. Therefore, the alterations in the local environments of the tyrosines at different stages of insulin aggregation are likely to result in more complex fluorescence kinetics. Nevertheless, because the fluorescence lifetime components $\tau_i(\lambda)$ are dependent on λ, the decay associated spectra (DAS) technique (assuming the spectrum to be the sum of the stationary spectra of few different forms) is not applicable and the TRES approach is needed.

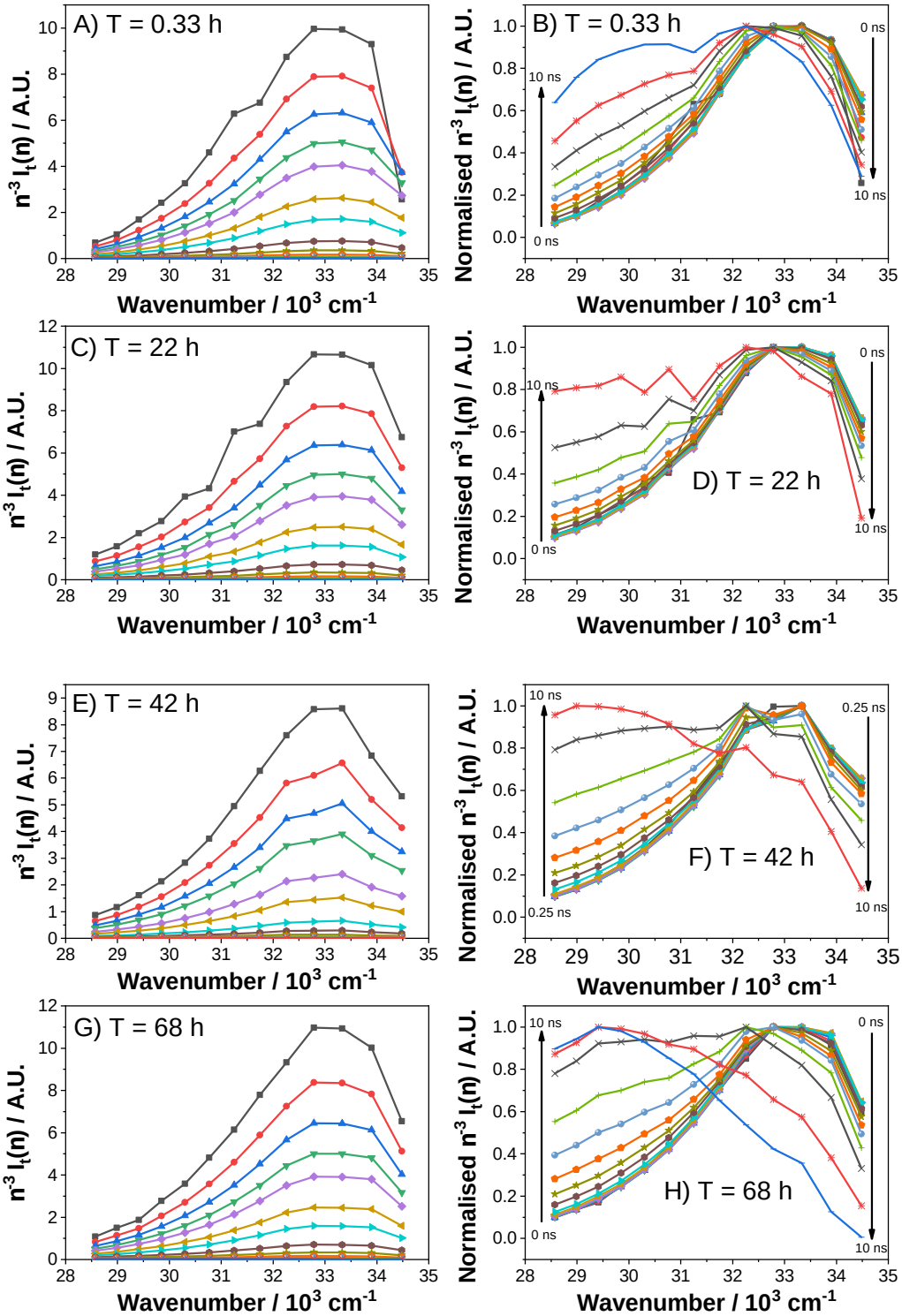
A) T = 0.33 h
B) T = 0.33 h
C) T = 22 h
D) T = 22 h
E) T = 42 h
F) T = 42 h
G) T = 68 h
H) T = 68 h
n-3 It(n) / A.U.
Normalised n-3 It(n) / A.U.
Wavenumber / 10^3 cm-1
0 ns
10 ns
0.25 ns

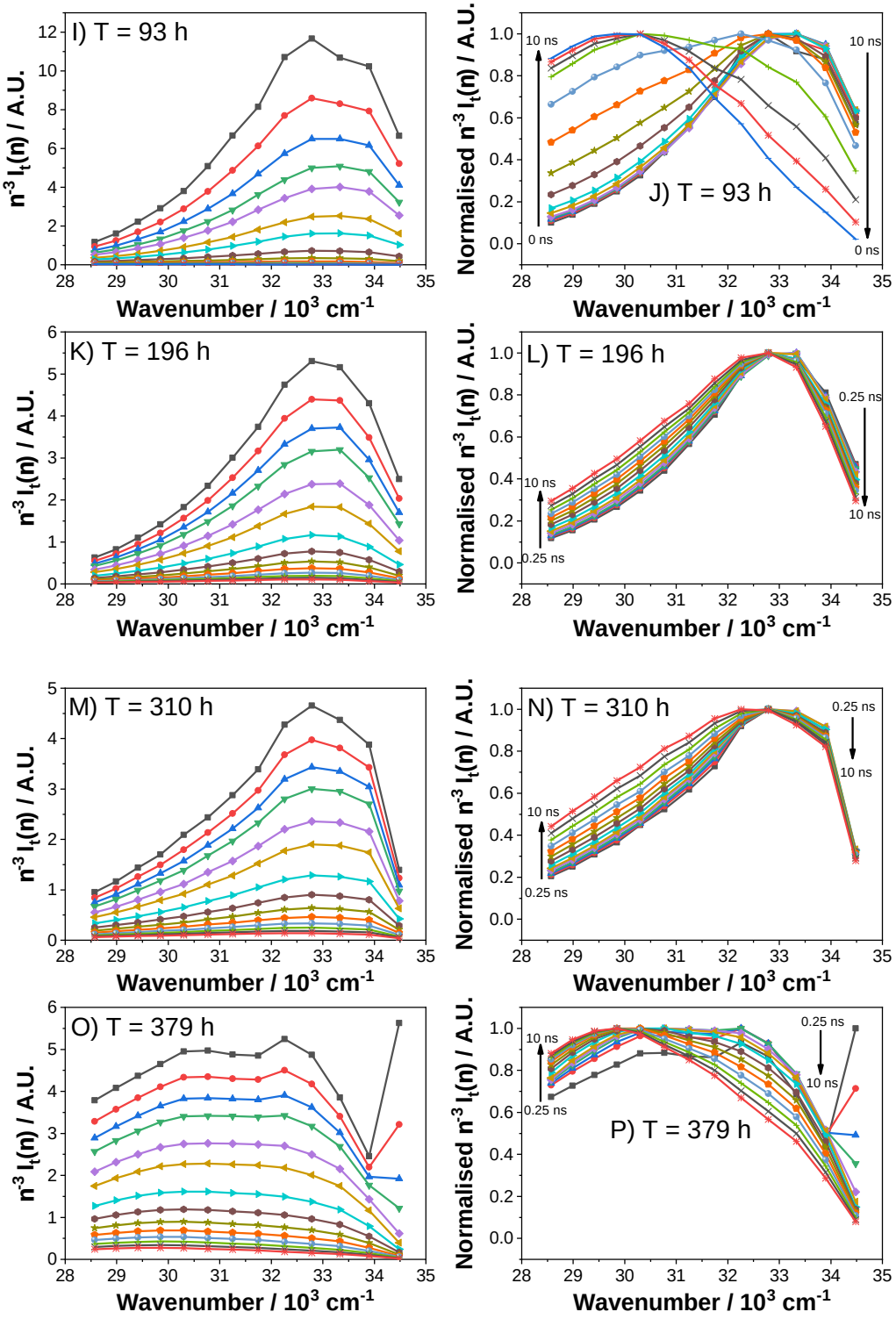
I) T = 93 h
J) T = 93 h
K) T = 196 h
L) T = 196 h
M) T = 310 h
N) T = 310 h
O) T = 379 h
P) T = 379 h
n-3 It(n) / A.U.
Normalised n-3 It(n) / A.U.
Wavenumber / 10^3 cm-1
10 ns
0 ns
0.25 ns

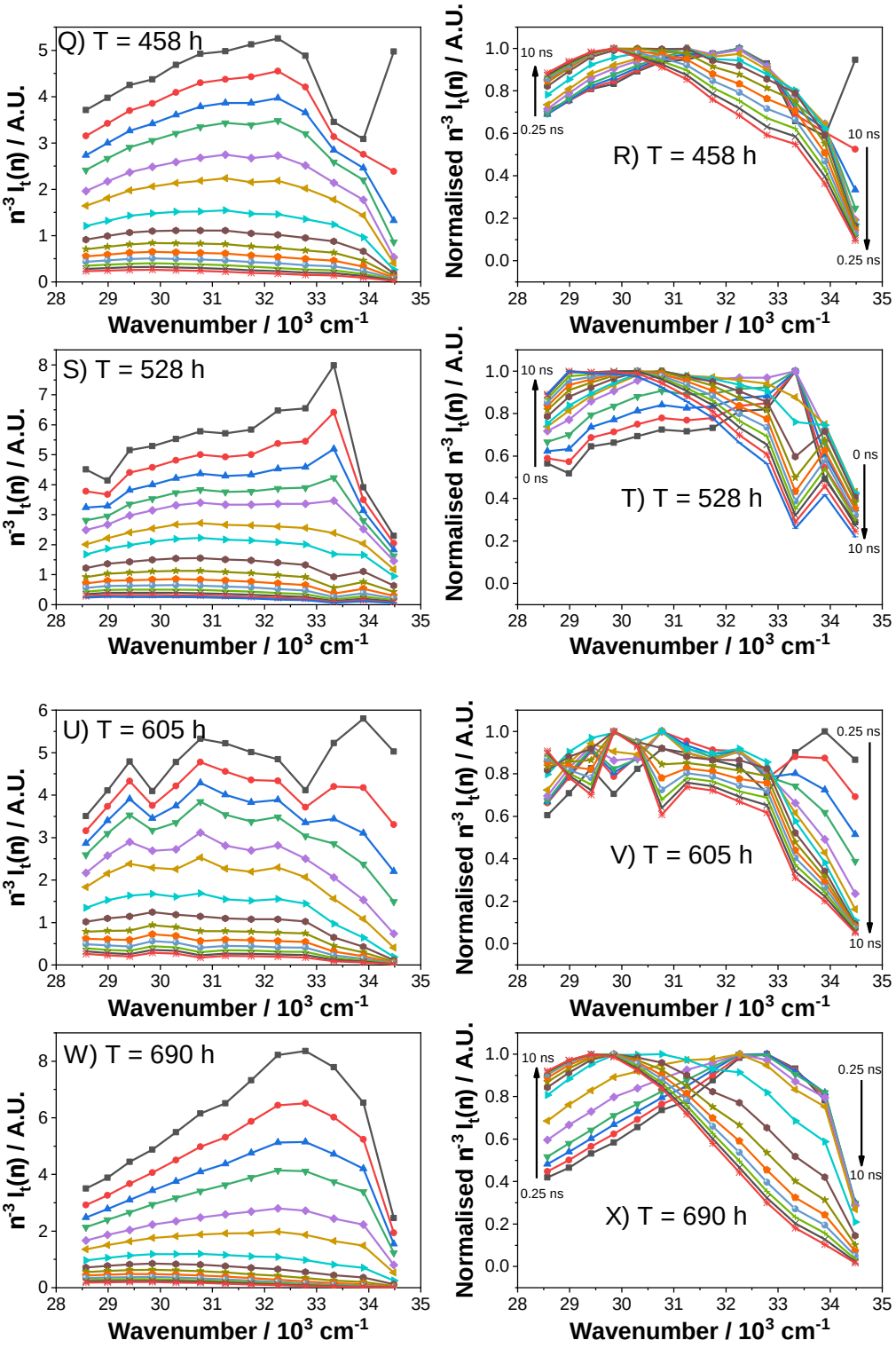

Figure 5.4: The left hand panel show the TRES spectra of hexameric insulin A), C), E), G), I), K), M), O), Q), S), U), and W) for 0.33, 22, 42, 68, 93, 196, 310, 379, 458, 528, 605, and 690 hours respectively. The right hand panel shows the normalised TRES plots for insulin. The plots were determined at 0, 0.25, 0.5, 0.75, 1, 1.5, 2, 3, 4, 5, 6, 7, 8, 9, and 10 ns after excitation. 0 ns is removed from 0.33, 42, 196, 310, 379, 458, 605, and 690 hours due to high scatter.

With the use of equation (3.12) TRES $I_t(\nu)$ were determined for the insulin sample at different times after its preparation. The $\nu^{-3}I_t(\nu)$ plots vs. time for 0.33, 22, 42, 68, 93, 196, 310, 379, 458, 528, 605, and 690 hours are shown in the left hand panel of figure 5.4. For all the plots $\nu^{-3}I_t(\nu)$ display peaks around 33,000 cm^{-1} (with the exception of 379, 458, and 605 hours due to high scatter near the excitation wavelength) whose intensities gradually decrease with time after excitation. The main difference between the TRES plots from 0.33-310 and 379-690 hours is the emergence of a broader structure at shorter wavenumbers observed in the older samples. This is better demonstrated in the normalised plots in the right-hand panel of figure 5.4. From 0.33- 42 hours after sample preparation there is little intensity decrease in 33,000 cm^{-1} compared to the measured samples at 68-93 hours. For 196-310 hours the normalised plots have little change at longer wavenumbers but the intensity slightly increases at shorter wavenumbers. For samples measured at 379-605 hour, the shorter wavenumbers (30,000) are more dominant than the 33,000 cm^{-1} peak throughout 0-10 ns after excitation.

5.3.2 Comparison of 2 and 3 Toptygin-Type Models to Fit TRES of Hexameric Insulin

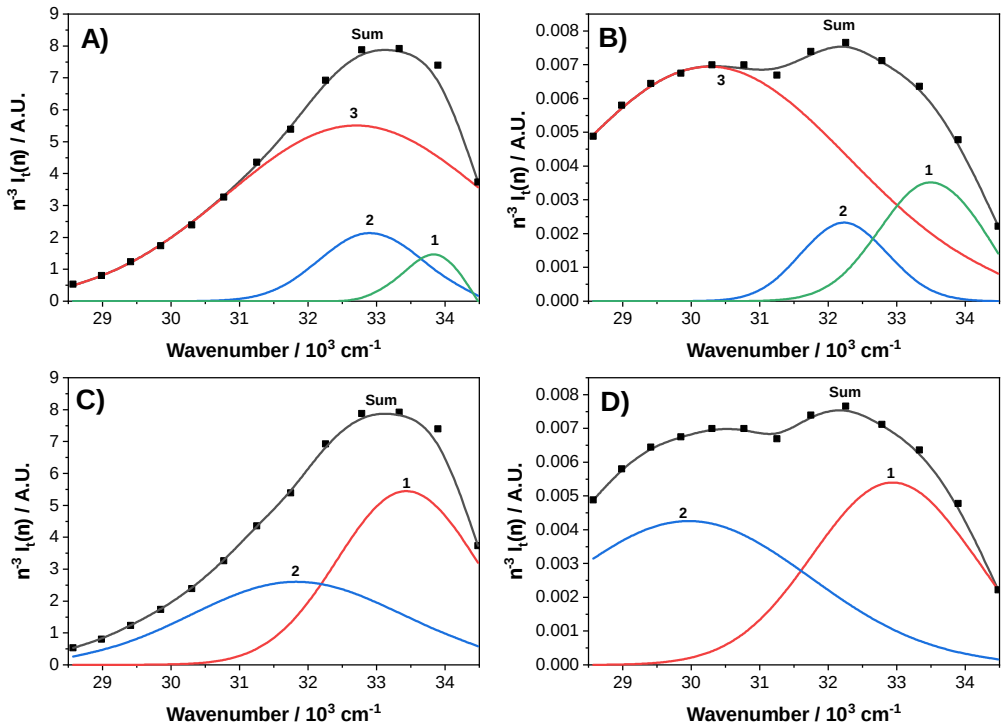

Figure 5.5: Experimental TRES data (■) fitted to 3 (A,B) and 2 (C,D) Toptygin-type models for the hexameric sample measured at 0.35 hours after preparation. The left (A,C) and right (B,D) panels are TRES determined at 0.25 ns and 10 ns after excitation, respectively. The 3 Toptygin-type curves labelled 1, 2, and 3 represent the individual fluorophores emitting at 34,000, 33,000, and 30,000 cm^{-1} respectively. The 2 Toptygin-type curves labelled 1, and 2 represent the individual fluorophores emitting at 33,500 and 31,500 cm^{-1} respectively.

To obtain fuller and quantitative information on the observed spectral changes, all $\nu^{-3}I_t(\nu)$ spectra were modelled by the sum of 3 normalised Toptygin-type profiles (equation (3.20)), where the χ^2 values obtained for the triple-Toptygin-type fitting were in the acceptable range of 1.00-1.19. Figure 5.5A and B show examples of fitting the triple Toptygin-type function to the data obtained for times 0.25 and 10 ns after excitation for 0.35 hours after sample preparation. The sample shows initially (at 0.25 ns after excitation) two emitting species with the maxima around 34,000 and 33,000 cm^{-1} (as recovered from the Toptygin-type fitting). After 10 ns, the first component around 34,000 remains the same, however, the second and third undergo spectral shifts

of ~500 and 2,000 cm^{-1}, respectively.

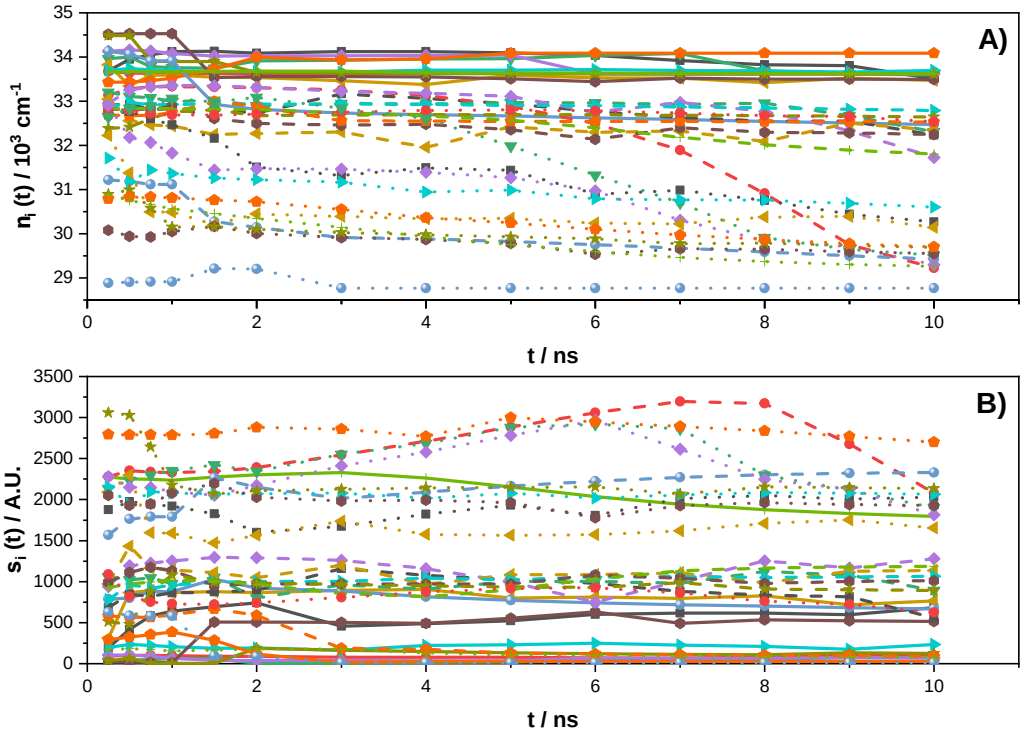

Figure 5.6: Three Toptygin-based models were used to fit TRES spectra for hexameric insulin and the A) peak positions ν_i and B) the width σ_i were extracted and plotted for 0.35 (■), 22 (●), 68 (▼), 93 (◆), 196 (◄), 310 (►), 379 (⬡), 458 (★), 528 (⬠), 605 (◕), and 690 (|) hours The components 1, 2, and 3 are represented with dotted, dashed, and solid lines, respectively.

In figure 5.6A, the first component remains around 34,000 cm^{-1} in the nanosecond time-scale and in time of aggregation ranging from a few hours to weeks. The second and third component have large peak position ranges from 33,000 to 33,500 cm^{-1} and 33,000 to 29,000 cm^{-1}, respectively. All their peaks gradually shift from to lower energy levels throughout 10 ns. The width of each component for 0.35, 22, 68, 93, 196, 310, 379, 458, 528, 605, and 690 hours after sample preparation were also plotted (figure 5.6B). The first component has a width around 0 throughout the measured samples, with the exception of 0.35, 196, 379, 605, and 690 hours. The above observations show that fitting TRES with 3 Toptygin-type parameters causes over parameterization. The peak positions of components 1 and 2 are close to one another and their Toptygin-type profiles shown in figure 5.5A and B largely overlap with each other. Furthermore, the

width of component 1 is around 0 for the majority of measured samples.

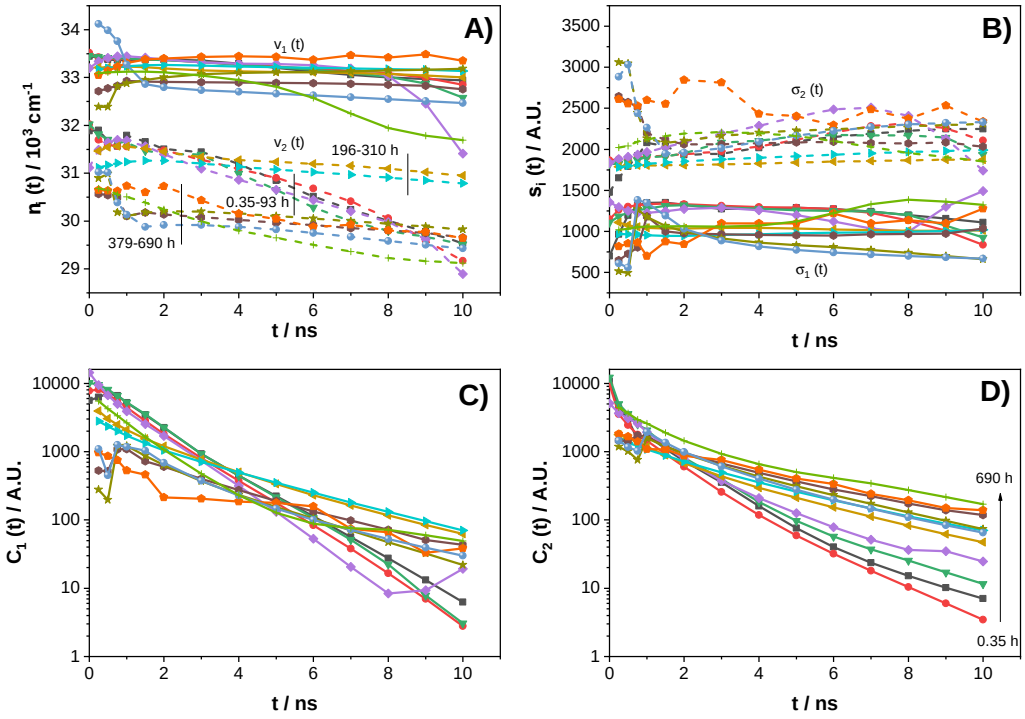

Figure 5.7: TRES parameters taken from 2 Toptygin-type Models of A) peak positions ν_i and B) the half-width of the distribution σ_i, and C) the corrected fluorescence contributions C_i fitted to 3 exponential functions. Fluorescence species 1 (straight line) and 2 (dashed line) for hexameric insulin were measured at 0.35 (■), 22 (●), 68 (▼), 93 (◆), 196 (◄), 310 (►), 379 (⬡), 458 (★), 528 (⬠), 605 (◕), and 690 (|) hours after sample preparation.

The $\nu^{-3}I_t(\nu)$ spectra were re-modelled by the sum of 2 normalised Toptygin-type profiles (equation (3.20)), the χ^2 values obtained for the double-Toptygin-type fitting were still in the acceptable range of 1.00-1.19. Figure 5.5C and D shows examples of fitting the double Toptygin-type function to the data obtained for times 0.25 and 10 ns after excitation for 0.35 hours after sample preparation. The 2 Toptygin-type fitting shows that it also fits well to the TRES plots. The sample shows at 0.25 ns after excitation, there are two emitting species with the maxima around 33,500 and 32,000 cm^{-1}. After 10 ns there is a slight shift in component 1 to 33,000 cm^{-1}, however, component 2 undergoes a large spectral shift of 2,000 cm^{-1}. The peaks of the Toptygin-type profiles fitted to the experimental $\nu^{-3}I_t(\nu)$ curves are plotted in figure 5.7A. The locations of peaks emitting around 33,000 cm^{-1} seem to be weakly dependent on the age of the sample where 0.35-

605 hours show a non-significant spectral shift towards longer wavelengths which is consistent of dielectric relaxation. Indeed, contrary to most of the fluorophores for which dielectric relaxation is much faster than fluorescence decay, the dielectric relaxation of intrinsic fluorophores like tyrosine and tryptophan in proteins usually occurs on the same nanosecond timescale as fluorescence which leads to more complex photophysics.

However, the sample aged of 690 hours in the first component experiences a large spectral shift of 1,000 cm^{-1} in the nanosecond timescale. Moreover, for the second component there is a larger shift of 2,000 cm^{-1} which occurs around 0.33 to 93 hours of sample preparation. The spectral shifts are unlikely to be due to dielectric relaxation because their values are significant. Instead, we currently interpret the large shifts as a result of the excitation triggered conformational changes of insulin aggregates. The initial value of the second component generally decreases with time and because the energy gap decreases when protein aggregates get larger. At later times (e.g. 196-310 and 379-690 hours) the second component does not undergo large spectral shifts; this may be because larger aggregates do not change conformation as quickly as smaller aggregates. It has been observed that the widths of the first component are much smaller than the second, which indicates that the fluorescence species in the second component is more complex. Note that none of the components have widths equal to zero and therefore, we believe that using two Toptygin-type functions to fit the $\nu^{-3} I_t(\nu)$ spectra is better than three.

Since our model of the insulin fluorescence spectra (equation (3.20)) uses the normalised Toptygin-type distribution functions, the fluorescence contributions $C_i(t)$ represent the contributions of fluorescence from two components. Consequently, the time decays of $C_i(t)$ can be regarded as the fluorescence decay of these components. The first fluorescence contribution from 0.35-68 hours after sample preparation has a steep decline and the line is linear in the logarithmic scale, which indicates that there is one fluorescent species present. 93 hours also has a steep decline, however, after 8 ns there is an increase in intensity. After 93 hours, the fluorescence decays start to gradually decrease because the fluorescence lifetime decay increases with the age of the sample.

From 379-690 hours after preparation, the initial fluorescence intensity is lower than fresher samples (0.35-68 hours) because at 0 ns after excitation the fluorescence decay is heavily influenced by scattered light and therefore omitted from figure 5.7C, this can also be seen in figure 5.7D. Similar trends can be seen for the second component, however, it undergoes a fast fluorescence decay within 1 ns. The curves exhibit non-linearity in the logarithmic scale which indicates complex fluorescence kinetics due to conformational changes and/or emission from more than one fluorescent species. The combined analysis of figure 5.2 and figure 5.7 suggests that hexameric insulin does not undergo drastic conformational change up to 310 hours of aggregation because the steady state emission spectra does not change significantly and the tyrosine fluorescence (~290 nm) is dominant and the peak positions for component 2 are around 32,000 cm^{-1}. However, after 379 hours after sample preparation, the initial peak positions decrease to 31,000 cm^{-1}, the fluorescence lifetime decays increase, the total fluorescence intensity increases, and the fluorescence intensity grows broader. The decrease in tyrosine fluorescence could be explained by new fluorescent complexes could be quenching the fluorophore. However, the total fluorescence intensity and fluorescence lifetime increases with aggregation time may be because the new fluorescent species are be shielded by quenchers and/or energy transfer from tyrosine is taking place.

5.3.3 Monitoring Long-Term Stability of Monomeric Insulin Through its Intrinsic Fluorescence

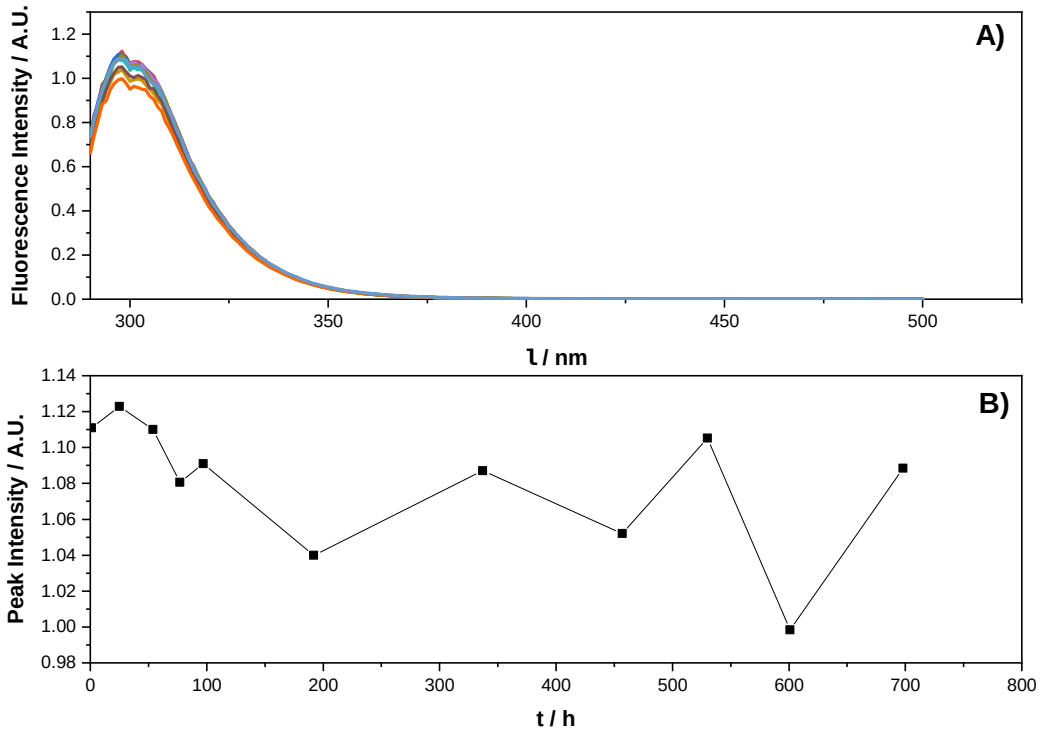

Figure 5.8: A) Steady state emission spectra intensity of monomeric insulin measured in 1 (grey curve), 25 (red curve), 54 (blue curve), 77 (green curve), 97 (pink curve), 192 (yellow curve), 337 (cyan curve), 457 (brown curve), 530 (olive curve), 601 (orange curve), and 698 (light blue curve) hours after sample preparation and its B) peak intensity (298 nm) over 700 hours.

To monitor the stability of monomeric insulin compared to the hexameric form, the fluorescence spectrum was taken at similar times from 0-700 hours (shown in figure 5.8). In contrast to hexameric insulin, there is no significant change to the fluorescence intensity (peak intensity value differs from 1 - 1.12) and it has maintained its shape throughout 700 hours. The experimental conditions are similar to Bekard and Dunstan [119], however, in this experiment the temperature was measured at room temperature (23 °C). As there is a lack of conformational change, which indicates that the native insulin monomer form is does not undergo fibril formation. Therefore, the monomeric form may be more stable than hexameric insulin typically used in medicine.

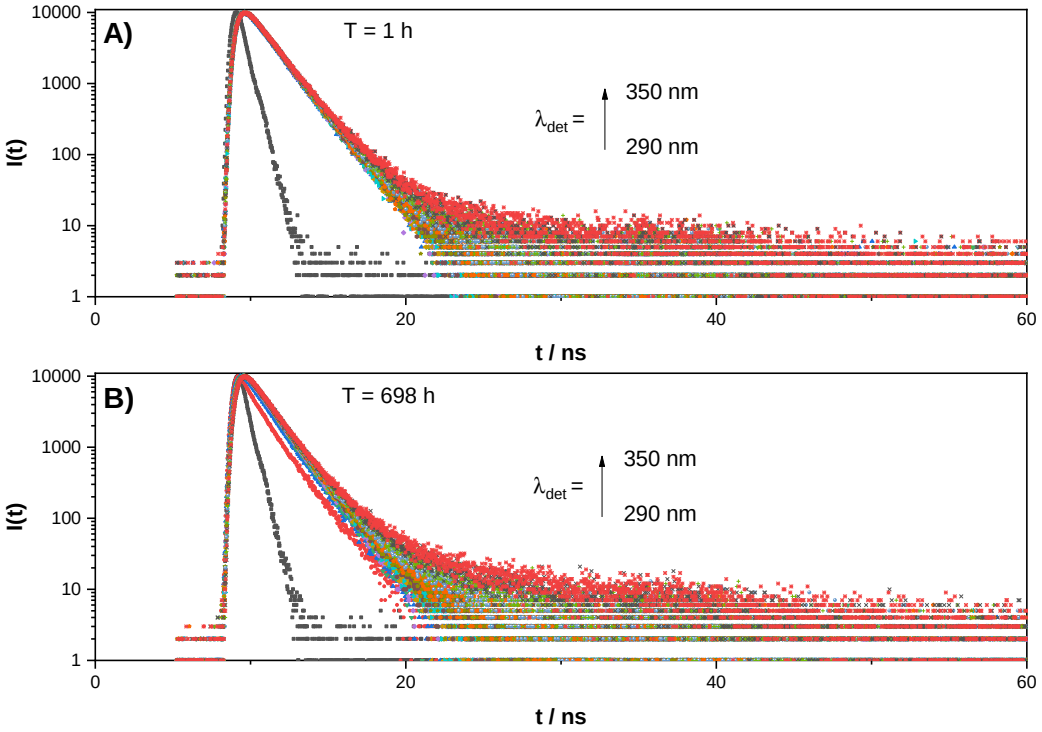

Figure 5.9: The instrumental pulse profile (grey) and fluorescence intensity decays for detection wavelengths of 290, 295, 300, 305, 310, 315, 320, 325, 330, 335, 340, 345, and 350 nm for A) 1 and B) 698 hours after sample preparation of monomeric insulin.

The fluorescence decays were recorded for 1 and 698 hours after the sample preparation of monomeric insulin shown on figure 5.9A and B, respectively. The fluorescence decays were excited at 279 nm and the detection wavelengths ranged from 290-350 nm in increments of 5 nm. In contrast to hexameric insulin, the detection wavelength and the age of the sample does not have a significant influence on the fluorescence decays in the monomeric form. However, there are slight differences which suggests that the protein undergoes spectral relaxation but its conformational change throughout the monitored aggregation time is limited.

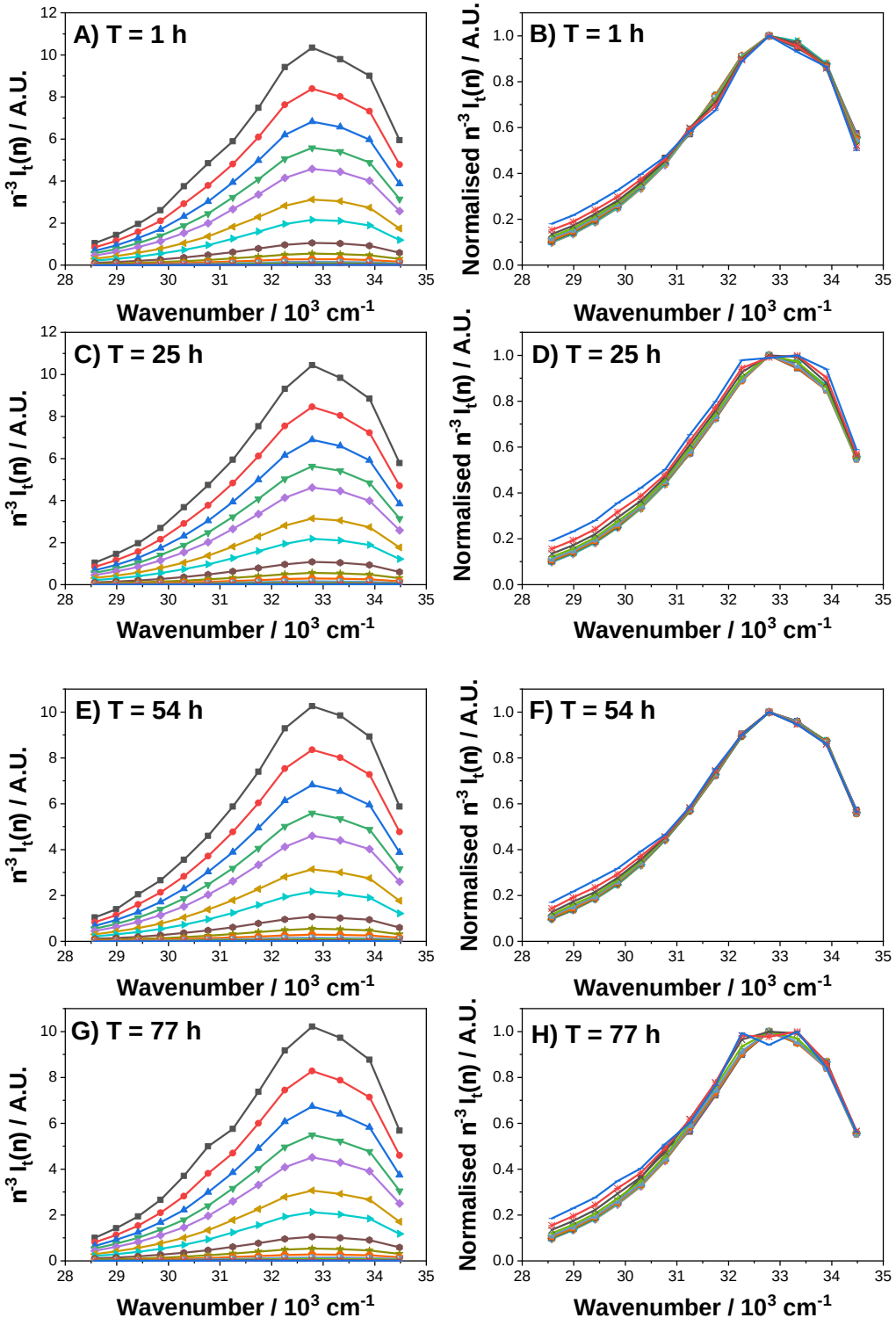
A) T = 1 h
B) T = 1 h
C) T = 25 h
D) T = 25 h
E) T = 54 h
F) T = 54 h
G) T = 77 h
H) T = 77 h
n-3 It(n) / A.U.
Normalised n-3 It(n) / A.U.
Wavenumber / 103 cm-1

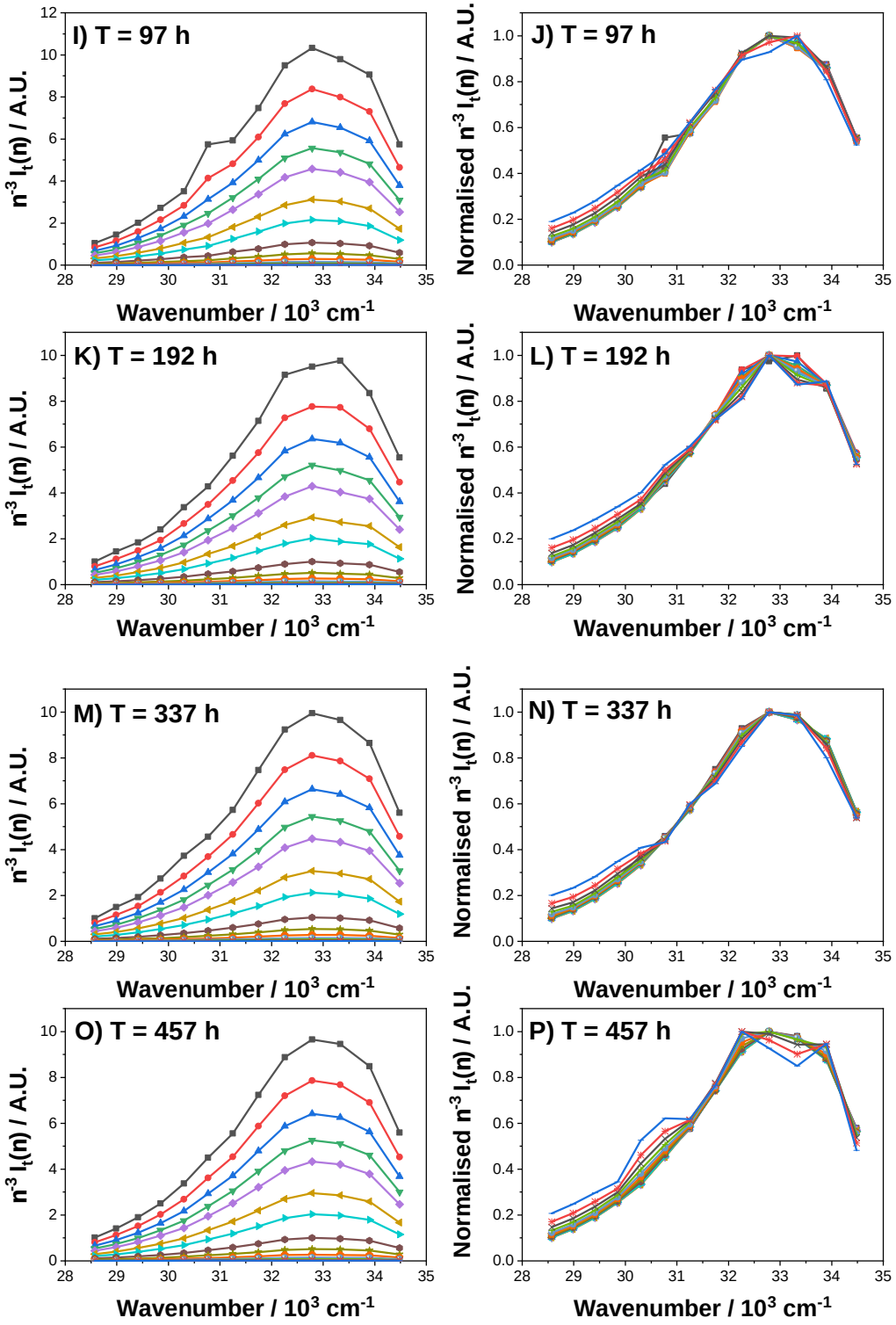
I) T = 97 h
J) T = 97 h
K) T = 192 h
L) T = 192 h
M) T = 337 h
N) T = 337 h
O) T = 457 h
P) T = 457 h
n-3 It(n) / A.U.
Normalised n-3 It(n) / A.U.
Wavenumber / 103 cm-1

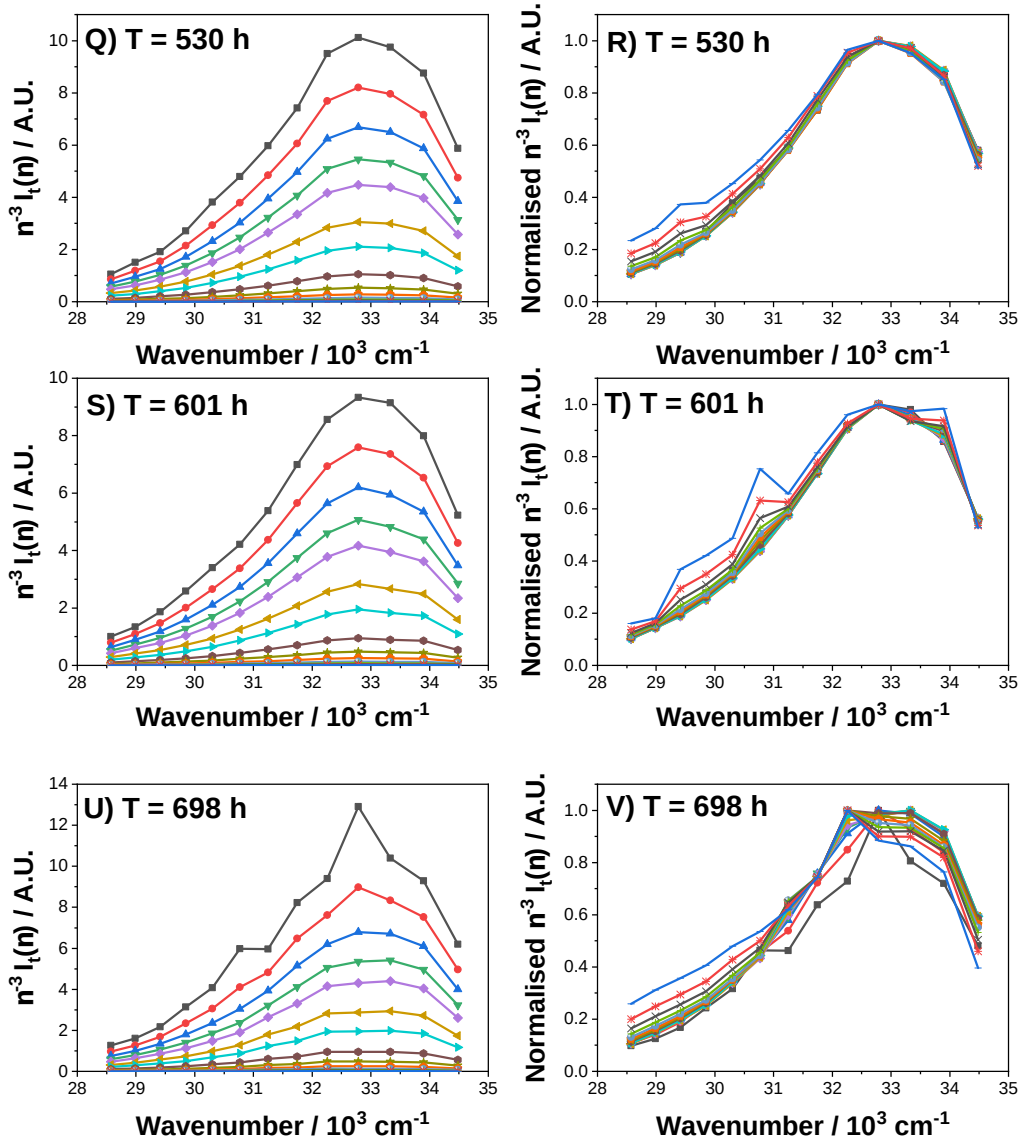

Figure 5.10: The left hand panel show the TRES spectra of monomeric insulin A), C), E), G), I), K), M), O), Q), S), U), and W) for 1, 25, 54, 77, 97, 192, 337, 457, 530, 601, and 698 hours respectively. The right hand panel shows the normalised TRES plots for the free monomeric insulin B), D), F), H), J), L), N), P), R), T), V), and X). The plots were determined at 0, 0.25, 0.5, 0.75, 1, 1.5, 2, 3, 4, 5, 6, 7, 8, 9, and 10 ns after excitation.

The $\nu^{-3}I_t(\nu)$ plots were generated for monomeric insulin at 1, 25, 54, 77, 97, 192, 337, 457, 530, 601, and 698 hours after sample preparation in figure 5.10 (left hand panel). In comparison to the TRES spectra of hexameric insulin, the monomeric insulin does not have scattered light influencing the fluorescence spectra with the exception of 698 hours. The normalised spectra (right hand panel) indicates that there are two fluorescent forms with emission peaks at ~33,000 and 31,000 cm^{-1}. The overall spectral changes are minimal throughout sample ageing.

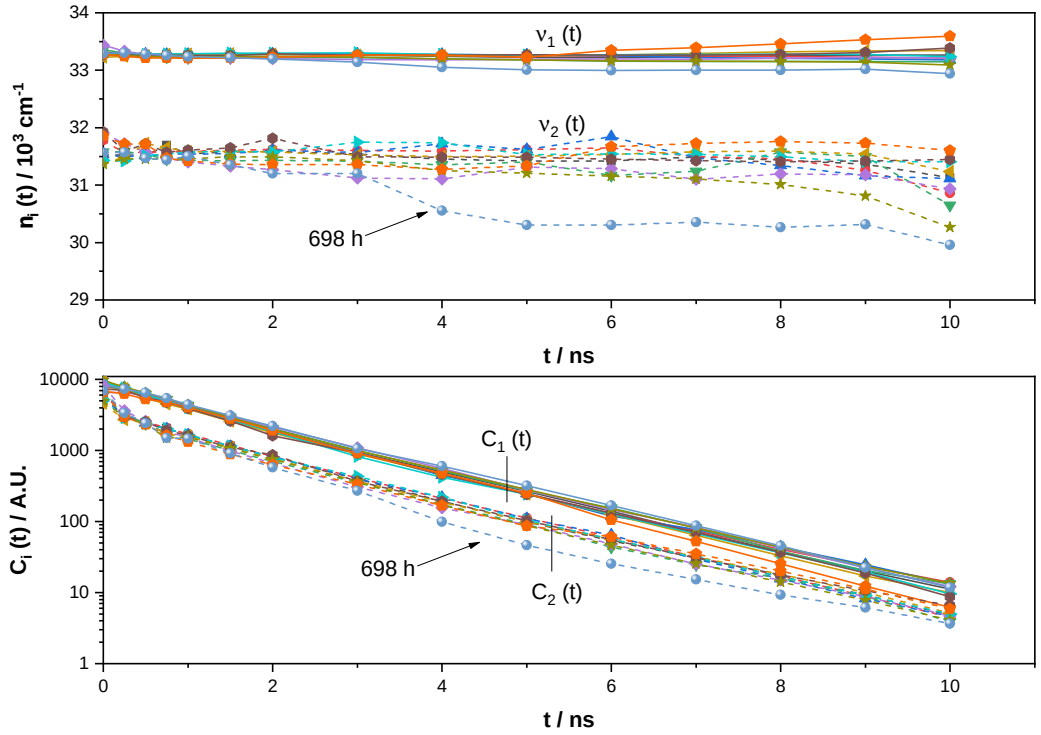

Figure 5.11: Toptygin-based models were used to fit TRES spectra for free insulin and the peak positions were ν_i extracted and plotted for 1 (■), 25 (●), 54 (▲), 77 (▼), 97 (◆), 192 (◄), 337 (►), 457 (⬡), 530 (★), 601 (⬠), and 698 (◕) hours after sample preparation. The components 1, and 2 are represented by grey and red curves, respectively.

To gather more information on the spectral changes for monomeric insulin, all TRES were fitted by the distribution function and the spectral shifts were compared with the hexameric form. As shown on figure 5.11, there are two fluorescence components around 33,500 and 31,000 cm^{-1} where component 1 does not seem to be influenced by sample ageing. The second component all have similar initial peak values throughout

the measured times and undergo slight dielectric relaxation in 10 ns. For 698 hours, the wavenumbers shift from 31,500 to 30,000 cm^{-1} which indicates that conformational changes occurs as structures increase in size. The contributions for the first component is linear and the age of the sample has little to no effect on the lifetime decay. This shows that the there is one fluorescent species present which may not aggregate in 700 hours. The second component shows similar trends but in it experiences a fast decay in the subnanosecond scale. For 698 hours, the second component the curve is no longer linear which suggests that there is more than one fluorescent species present. These results imply that monomeric insulin does not undergo aggregation as quickly as hexameric insulin.

5.3.4 Monitoring the Long-Term Effects of Thioflavin T on Tyrosine when Bound to Monomeric and Hexameric Insulin

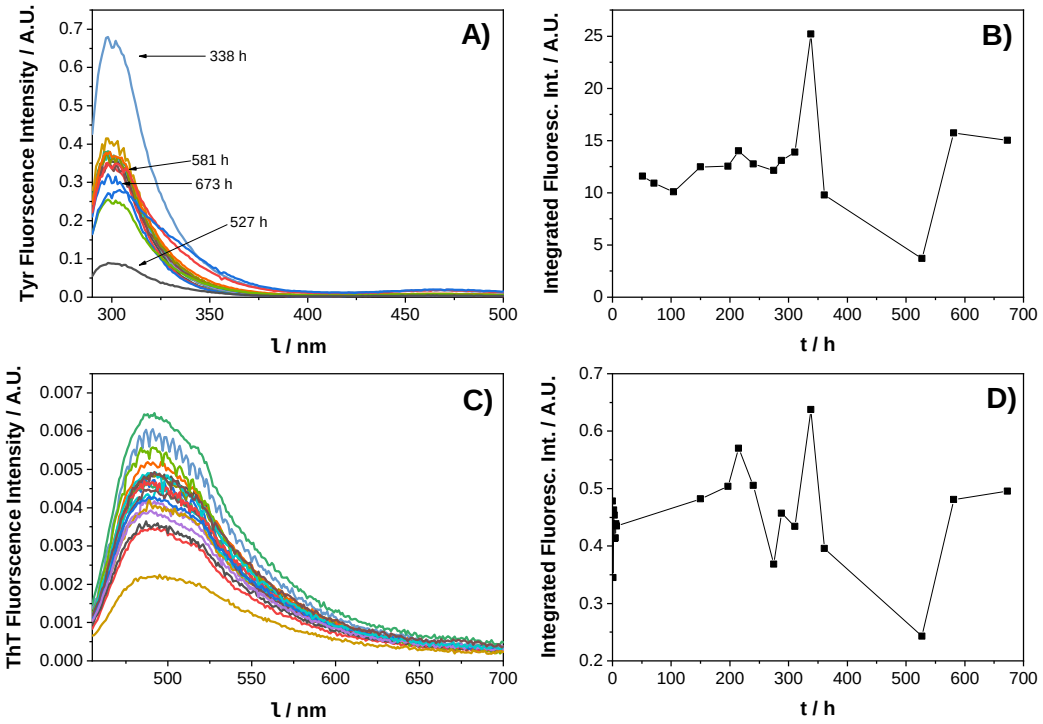

Figure 5.12: Steady state emission measurement of hexameric insulin incubated with Thioflavin T. A) Tyrosine was excited at 279 nm and the fluorescence was collected at 290-500 nm and its B) total fluorescence intensity was calculated by taking the area under the spectrum for 51, 71, 104, 150, 197, 215, 240, 275, 288, 311, 338, 361, 527, 581, and 673 hours after sample preparation. C) Thioflavin T was excited at 440 nm and its fluorescence was collected at 450-700 nm and its D) integrated fluorescence intensity was plotted 0, 1, 2, 3, 4, 5, 6, 7, 150, 197, 215, 240, 275, 288, 311, 338, 361, 527, 581 and 673 hours after sample preparation.

To gather more information on the aggregation kinetics of hexameric insulin, ThT was used to probe β-sheet formation. Steady state emission measurements were carried out where tyrosine and ThT probes were excited at 279 and 440 nm in figure 5.12A and C, respectively. The emission wavelength ranges also differ, where the fluorescence is collected at 290-500 and 450-700 nm for Tyr and ThT, respectively. In contrast to unlabelled hexameric insulin, the overall Tyr fluorescence intensity is lower, and spectral broadening occurs around 673 hours after sample preparation. This suggests that ThT quenches the Tyr fluorescence and inhibits the formation of new fluorescence

species. There are also spikes of high and low intensity at 338 and 527 hours, which are not seen in label free hexameric insulin. Observations from the integrated fluorescence intensity for Tyr and ThT probes exhibit the same trend shown in figure 5.12B and D may suggest that the ThT is attached to the protein. However, due to the lack of β-sheets the probe is unable to form a rigid conformation and therefore, there is no large fluorescence enhancement shown on figure 5.12C. Since the amyloid fibrils predominantly consists of β-sheet structures, the results suggest that long fibrous structures are not formed after 700 hours in physiological conditions. Instead, non-fibrillar aggregates are formed which ThT does not typically bind to [135].

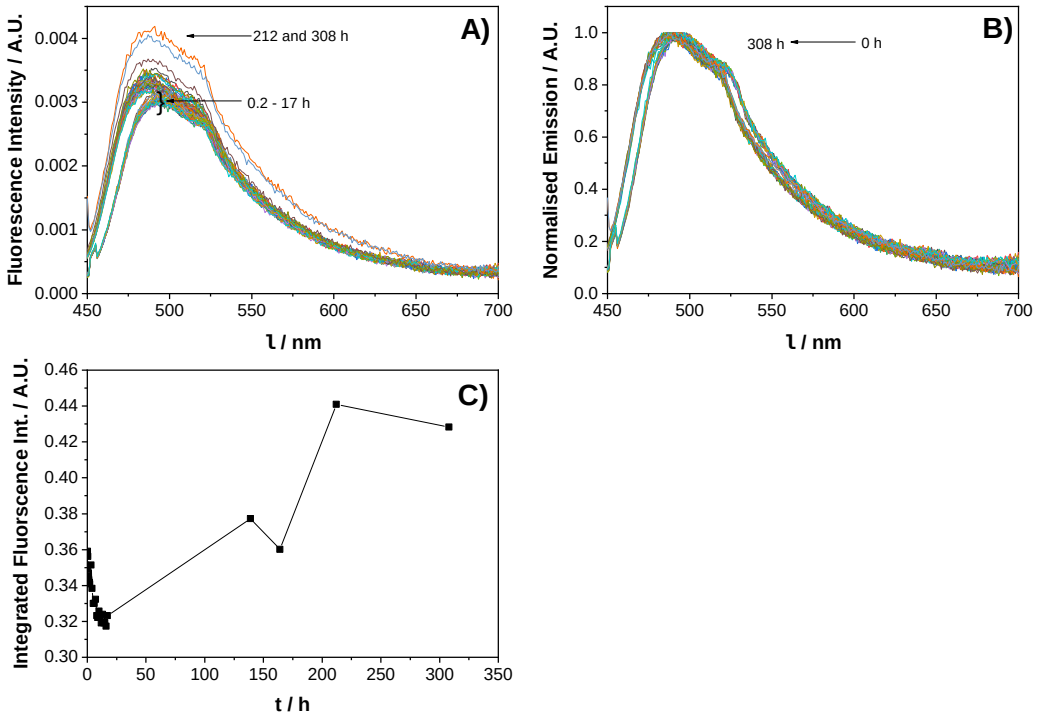

Figure 5.13: Steady state emission measurement of monomeric insulin incubated with Thioflavin T. A) ThT was excited at 440 nm and its fluorescence was collected at 450-700 nm and the B) normalised spectra was plotted for 0.2, 0.5, 0.7, 0.8, 0.9, 1.1, 1.3, 1.4, 1.8, 2, 3, 4, 5, 6, 7, 8, 9, 10, 11, 12, 13, 14, 15, 16, 17, 139, 164, 212, and 308 hours after sample preparation. The spectra for each time point was integrated to show the C) total fluorescence intensity.

For monomeric insulin, the ThT probe was examined up to ~300 hours, shown on figure 5.13. From 0.2-17 hours after sample preparation, the peak position ~500 nm decreases with time. After this time, ThT starts to increase and also experiences a blue

shift (seen more clearly in figure 5.13B). In structures with rich β-sheet formation, the probe exhibits a large intensity enhancement and blue shift (~510 to 480 nm) [136]. The small shift (few nm) and the insignificant enhancement of ~0.12 in the total fluorescence intensity plot, shown on figure 5.13B and C, respectively. This suggests that the monomeric insulin predominately consists of α-helical structures, which is consistent with experiments carried out by Bouchard et al., where insulin prepared in similar conditions prior to heating showed no β-sheet characteristics. However, as insulin was heated to 70 °C, β-sheets start to arise and becomes the abundant structure in mature amyloid fibrils [13]. Observations in figure 5.13 suggests that the monomeric insulin starts to transform into oligomers and β-sheets begins to emerge around 100 hours after sample preparation. This is consistent with Vestergaard et al. where they proposed that insulin oligomers were predominantly α-helical [137].

5.3.5 End Point Assembly for Hexameric and Monomeric Insulin Labelled with Alexa-Fluor 647

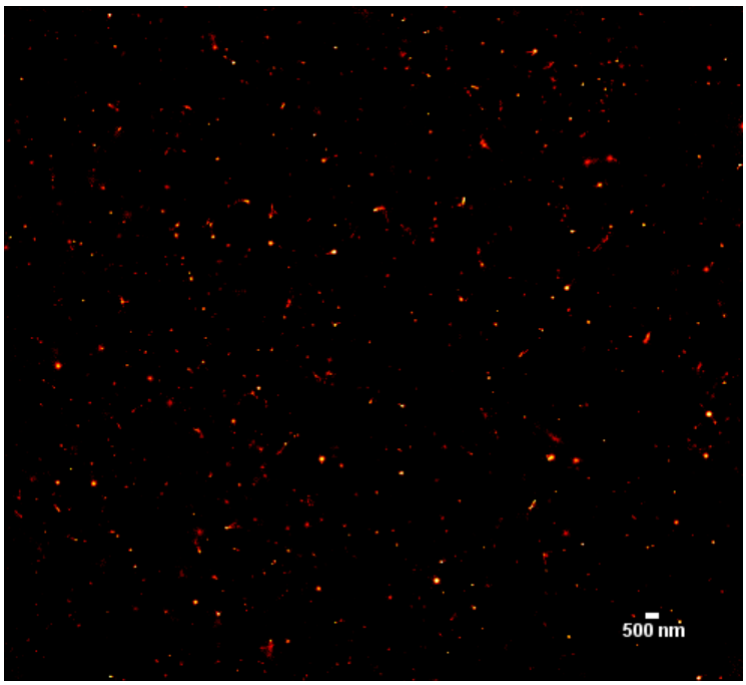

Figure 5.14: dSTORM images for hexameric insulin labelled with Alexa-Fluor 647 incubated at room temperature for 700 hours.

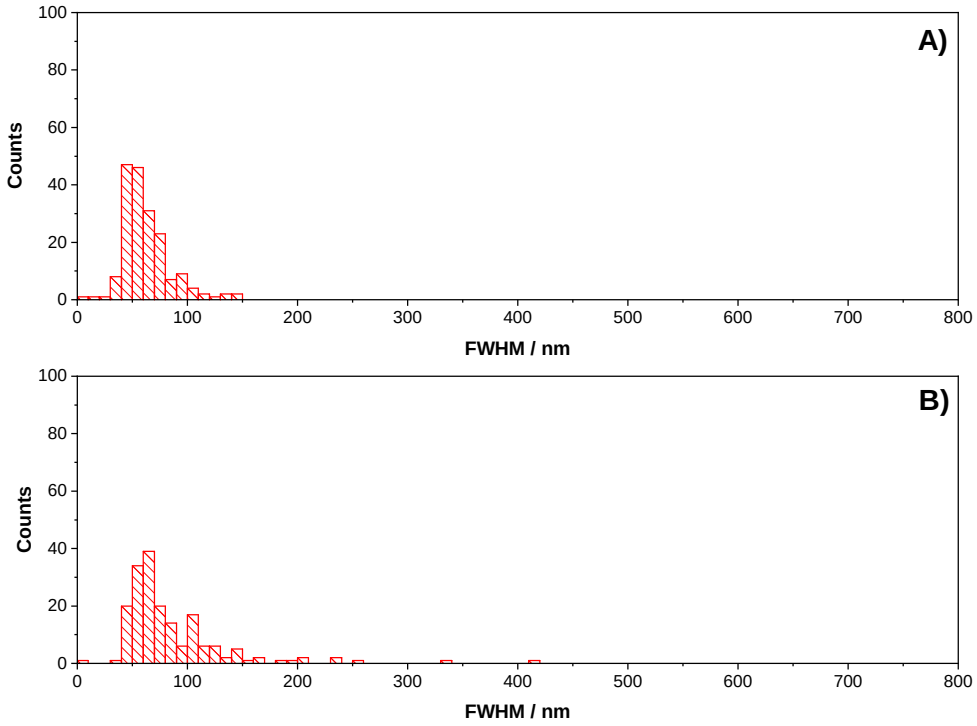

Figure 5.15: Histogram A) width and B) lengths of hexameric insulin analysed from the dSTORM images in figure 5.14.

dSTORM image was used in conjunction with spectroscopy techniques to further understand the self-assembly of hexameric insulin after 700 hours. 10,000 images were taken and to reconstruct this image figure 5.14. There is a large range of different sizes with most of the structures seem to be spherical. The width and length of each structure was measured on Image J and histograms of their full width half maxima were plotted on figure 5.15A and B, respectively. The majority of widths were found to be around 50-70 nm and the dominant lengths were <100 nm. Therefore, this suggests that the structures found at pH 7 after 700 hours have an amorphous structure opposed to a fibrous conformation, this is consistent with the results shown for hexameric insulin labelled with ThT where a lack of fluorescence enhancement demonstrates no β-sheet structure. In addition, Shaban et al. [138] imaged insulin in amyloidal conditions using dSTORM and showed long fibrous structures (~ few μm).

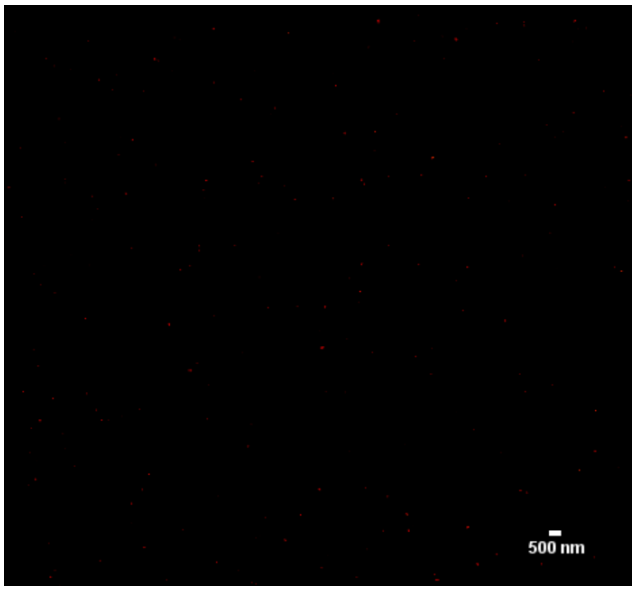

Figure 5.16: dSTORM images for monomeric insulin labelled with Alexa-Fluor 647 incubated at room temperature for 700 hours.

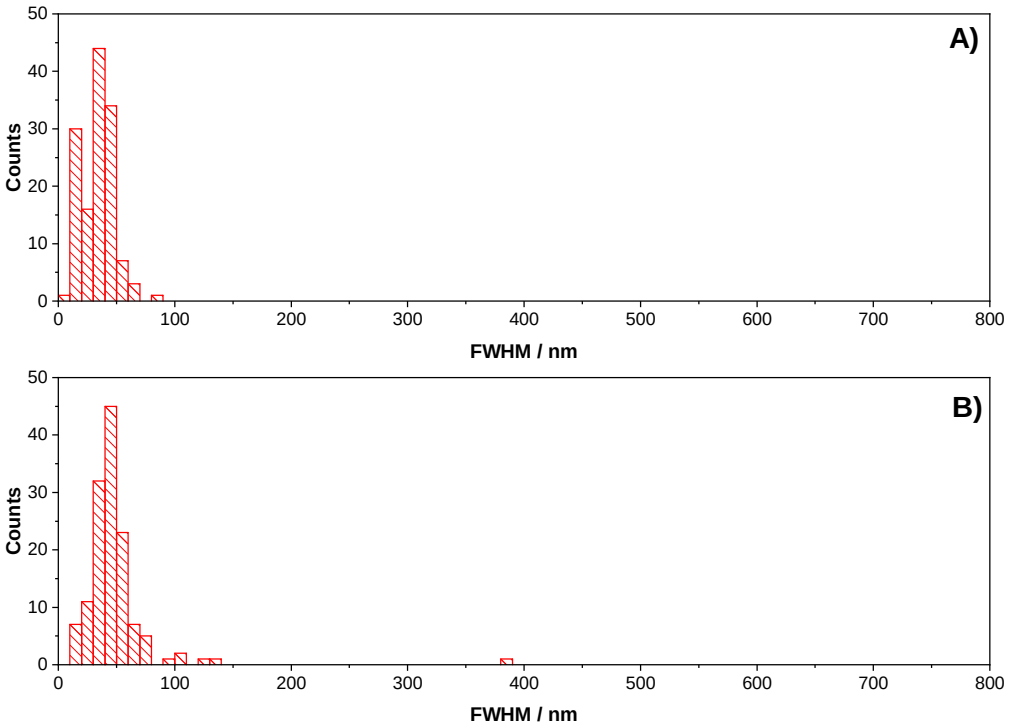

Figure 5.17: Histogram A) width and B) lengths of monomeric insulin analysed from the dSTORM images in figure 5.16

Again, dSTORM images were taken of monomeric insulin incubated for 700 hours at room temperatures. In comparison to hexameric insulin, the structures on figure 5.16 look homogenous and circular. The histogram plotted on figure 5.17A and B show that the lengths and widths of each structure measured is <100 nm, where the majority of structures are around 30-50 nm in size. This indeed shows that there is no fibril formation and may be higher oligomeric structures.

5.4 Conclusion

To gain a deeper understanding of the stability of insulin, the protein was monitored for 700 hours at pH 7 and 2 to produce the hexameric and monomeric forms of insulin, respectively. Insulin has intrinsic fluorophores which were exploited and used as sensitive probes that do not perturb protein self-assembly.

In order to ensure the correct models were used to fit the TRES plots, 2 and 3 Toptygin-based models were compared. It was found that using 3 Toptygin-type models were over parameterized the TRES plots and therefore, one of the components became redundant. This redundancy led to random and misleading kinetics. It can be deduced that hexameric insulin has 2 fluorescent species undergoing conformational changes throughout 700 hours of aggregation.

The steady state emission spectra for hexameric insulin shows a dominant peak around 290 nm which is due to tyrosine fluorescence, however the spectra become broader after 357 hours which suggest complex conformational changes with time. The TRES plots indicate that there are two fluorescent species emitting at 33,000 and 32,000 cm^{-1}. After time, the second component (emitting at 32,000 cm^{-1}) decreases its initial peak wavenumber which is due to larger aggregates being formed. This result is complementary to the steady state emission spectra because it shows a shift to longer wavelengths with respect to aggregation time. Hexameric insulin was incubated with ThT to determine the β-sheet content formed throughout 700 hours. From these experiments, there was no evidence that there were β-sheets present within the structure due to a lack of fluorescent enhancement in the ThT probe. The final structure of hexameric

insulin was further confirmed with the use of dSTORM images, where they showed an absence of long fibrous structures when insulin was incubated for 700 hours at pH 7 in room temperature. This result confirms that at physiological pH and in the presence of zinc ions, the insulin hexamer formation is stable. The stable properties that hexameric insulin in pH 7 provides is exploited in drug product formulations.

The stability of monomeric insulin is also important to study as this form can be more rapidly absorbed into the body compared to bigger structures such as hexamers and dimers. Therefore, it may be exploited in the medicinal field. In contrast to hexameric insulin, the steady state and TRES plots for monomeric insulin display no significant change throughout 700 hours. Furthermore, the initial peak positions show that there are two fluorescent species emitting around 33,500 and 32,000 cm^{-1} which stay constant throughout the measurement. Although there are no dramatic conformational changes, when incubated with ThT, there may be evidence of β-sheets present within the structure. This suggests that the monomeric insulin has formed oligomeric structures as the β-sheet content is relatively low [22]. The dSTORM images have confirmed that there are no fibrous structures present and they are relatively homogenous, this explains the lack of conformational changes seen in the TRES data. The lack of structural change within monomeric insulin suggest that they are more stable than the hexameric form typically used in medicine. However, oligomeric structures are known to be more cytotoxic than fibrils and therefore, it may be more problematic to use monomeric insulin for medicinal purposes.

By using the TRES technique, we have provided a new insight into the tyrosine fluorescence kinetics of bovine insulin during its aggregation. Identification and further characterization of the fluorescent insulin forms will require further TRES studies for the samples at different concentrations, temperatures, and pH conditions. Nevertheless, we have demonstrated that tracking the changes in the intrinsic fluorescence offers a sensitive way of studying unfolding and aggregation of insulin when not modified by extrinsic markers and in the undisturbed clinically relevant environment, for example, inside a plastic delivery cannula or within a storage vial.

Chapter 6

Investigation of Insulin Glycation at Neutral and Acidic pHs

6.1 Introduction

As seen in chapter 5, insulin aggregation still occurs in its monomeric form (at pH 2.5) and its stabilized (hexameric) form at pH 7.4. The result of aggregation, this becomes problematic for long term storage as aggregates are found to be cytotoxic [121] and cause localized amyloidosis at frequent injection sites [8]. Despite insulin aggregation occurring under physiological conditions, a large number of studies were conducted under non-physiological conditions such as constant agitation and at high temperatures to accelerate fibril formation.

Insulin is associated with glycaemia, but reducing sugars are known to interact and modify proteins through a non-enzymatic reaction known as glycation. Glycation occurs when the carbonyl group of the sugar and a free amino group (typically from arginine and lysine residues or N-terminal amino group) form a Schiff's base [139]. Amadori products are produced when the Schiff base rearranges itself into a stable ketoamine. Dehydration reactions and further rearrangements generate advanced glycation end products (AGEs) and play a role in diabetes and cataracts. Glycated proteins are found in Lewy bodies [11] and β-amyloid (Aβ) [12] deposits, which are related to Parkinson's and Alzheimer's disease, respectively. Therefore, it is thought

that reducing sugars could induce protein aggregation, misfolding, and the formation of cross-links with proteins, which increases the stability of protein aggregates [140]. Glycated insulin is unable to transport glucose to cells and inhibits the regulation of blood glucose; therefore, reducing sugars play a key role in insulin resistance [58,59].

It has been reported that free insulin in non-reducing conditions has the tendency to form oligomers, whereas oligomerization in glycated insulin is low [63]; therefore, glucose inhibits amyloid formation [141]. Although, significant glycation occurs over a number of weeks [142], insulin glycation is measured in non-physiological spanning only over a few hours or days.

In previous chapters [107], we have explored the sensitivity of intrinsic tyrosine fluorescence to study insulin alterations and recovered the kinetics of its aggregation with the use of TRES. It has been found that hexameric and monomeric insulin undergoes conformational changes throughout 700 hours. This was further supported by similar assembly kinetics of a model fibrillar protein [143], suggesting a generic mechanism and the sufficient sensitivity of TRES spectra to monitor protein stability for medicinal purposes. Super resolution microscopy was used (dSTORM) in conjunction with spectroscopy to gain a deeper understanding of what type of aggregates have been formed in 700 hours when insulin was incubated with glucose.

In this chapter, we further demonstrate the medical relevance of this methodology and compare its evolution of free insulin and glycated insulin. As there is no tryptophan (Trp) residues in insulin, the fluorescence kinetics are simplified. Understanding these kinetics is likely to provide insights into the mechanism of insulin glycation, which, in turn, may enable the development of better therapeutics to halt or circumvent fibril formation.

6.2 Methodology

6.2.1 Sample Preparation of Hexameric and Monomeric Insulin with Glucose

Bovine insulin, D-(+)-glucose, and phosphate-buffered saline (PBS) pH 7.4 from Sigma Aldrich were used without further purification. Two 50 μM bovine insulin samples were prepared in PBS buffer (0.01 M). One was kept in pH 7.4 (hexameric insulin) and the other (monomeric insulin) was prepared in acetic acid (20%) at pH 2.5. A stock solution of D-(+)-glucose in distilled water was added to both bovine insulin samples, and the final concentration of glucose was 50 mM. The samples were sonicated, stored, and measured at 22 °C.

6.2.2 Fluorescence Measurements of Hexameric and Monomeric Insulin with Glucose

The steady state fluorescence and TRES measurements were carried out in the same manner as described in chapter 5. However, the range of detection wavelengths ranged from 290-340 nm. The fluorescence decay parameters were also recovered the same way as said in the previous chapter.

Modelling TRES

As shown previously in chapter 5, modelling TRES using 3 normalised Guassian distributions overparameterized the spectra. Therefore, in this chapter, only 2 normalised Toptygin-type models were used and their output parameters were examined.

6.2.3 Direct Stochastic Optical Reconstruction Microscopy of Hexameric and Monomeric Insulin Incubated with Glucose and Alexa-Fluor 647

The dSTORM images for hexameric and monomeric insulin with glucose, the same procedure was carried out as described in chapter 5.

6.3 Results and Discussion

6.3.1 Comparison of Long-Term Stability Between Free Hexameric Insulin and Hexameric Insulin with Glucose

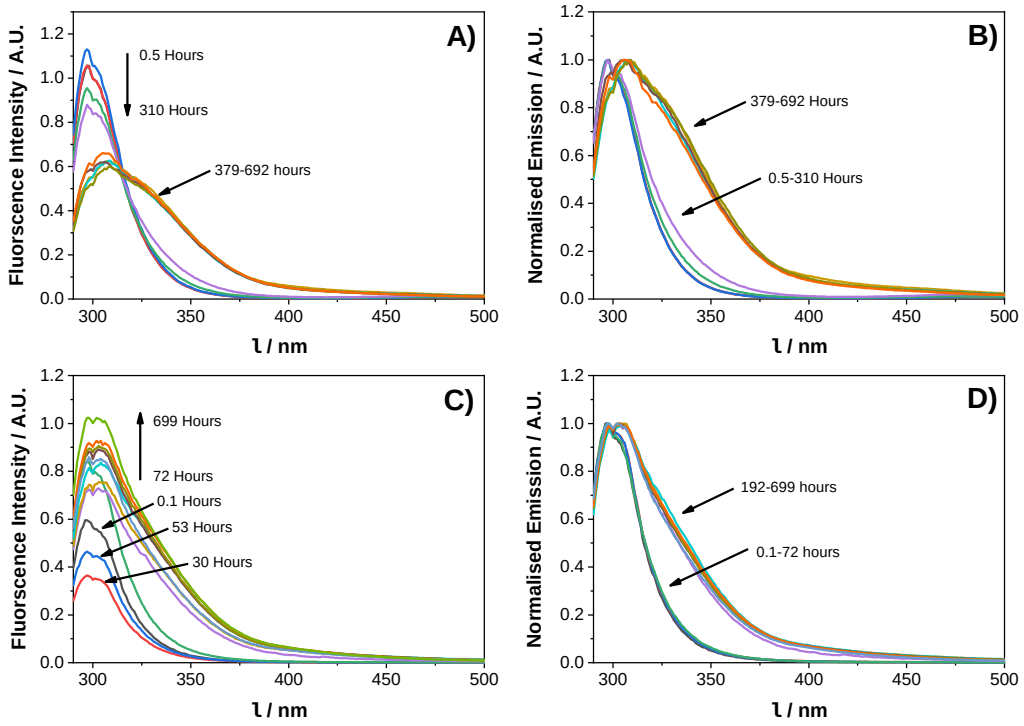

Figure 6.1: Fluorescence intensity of free hexameric insulin A) at 0.5, 26, 44, 196, 310, 379, 459, 528, 605, and 692 hours of preparation and insulin with glucose C) measured at 0.1, 30, 53, 72, 192, 318, 384, 479, 527, 577, 655, and 699 hours after preparation. The corresponding normalised intensities are shown in B) and D), respectively.

The steady-state emission spectra for free insulin (figure 6.1A) show that from 0.5 to 310 hours of incubation time, the fluorescence intensity decreases but the shape of the spectra is maintained. The decrease in tyrosine fluorescence intensity was also observed by Bekard et al. [119], and also an increase in the 1-anilinonaphthalene-8-sulfonic acid (ANS) signal measured in a 22 hours time range. Tyrosine residues (A14), (B16), and (B26) are located in hydrophobic surfaces within insulin [134], and ANS is a probe commonly used to bind in hydrophobic regions. Therefore, due to the conformational changes within the protein, tyrosine residues are increasingly

becoming more exposed to water which explains the decrease in fluorescence intensity. After about 310 hours, the spectra experience a further decrease in intensity and broaden quite significantly. The normalised spectra (figure 6.1B) demonstrate large broadening with a new peak emerging around 330 nm. These effects are likely to be a result of formation of aggregates in a distribution of conformations, which shows fluorescence at longer wavelengths.

When hexameric insulin was incubated with glucose, the fluorescence intensity (shown in figure 6.1C) decreased in the time range of 0.1-30 hours and then started to increase. For the first 30 hours, the trend appeared to be similar to that of free insulin, but it started at a lower level, which can be due to glucose quenching the overall tyrosine fluorescence. At later time periods, glucose inhibits the quenching of tyrosine, which could be caused by glucose acting as a shield around insulin, and tyrosine is no longer exposed to the water, which, in turn, increases tyrosine fluorescence. Barzegar et al. [141] also observed this trend when studying glucose interactions with insulin in similar conditions, they explained that the increase in fluorescence intensity is caused by the rigidity of the protein structure. This is also shown in figure 4.2 where the fluorescence intensity increases in fibrillogenesis model as fibril formation occurs. Figure 6.1D also shows that the normalised spectra start to broaden after 192 hours and there is a second peak around 330 nm, which is not as prominent as seen in free insulin.

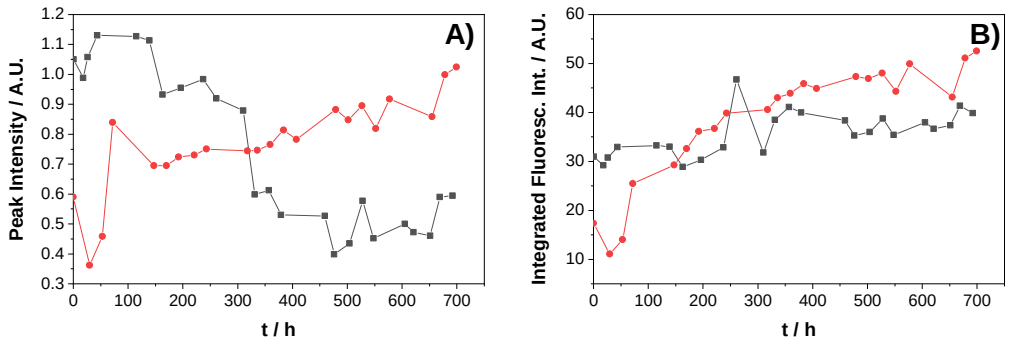

Figure 6.2: A) Peak fluorescence intensity at 298 nm and B) integrated fluorescence spectra taken from 50 μM hexameric insulin (■) in PBS buffer and 50 μM insulin with 50 mM (●) glucose in PBS buffer.

The readings of the fluorescence peak intensities were taken at 298 nm for both free hexameric insulin and hexameric insulin with glucose and are plotted in figure 6.2A. The total fluorescence peak intensities were also calculated by taking the integral of the fluorescence intensity for free insulin decreases, but the integrated fluorescence remains constant. This is consistent with the formation of aggregates of different sizes, each showing varied peak positions on the spectrum.

For glycated hexameric insulin, both the peak intensity and total number of photons emitted increase, which, in turn, suggests not only formation of aggregates (broadening the spectra) but also sugar molecules separating Tyr from the solvent (which increases the quantum yield and thus fluorescence intensity).

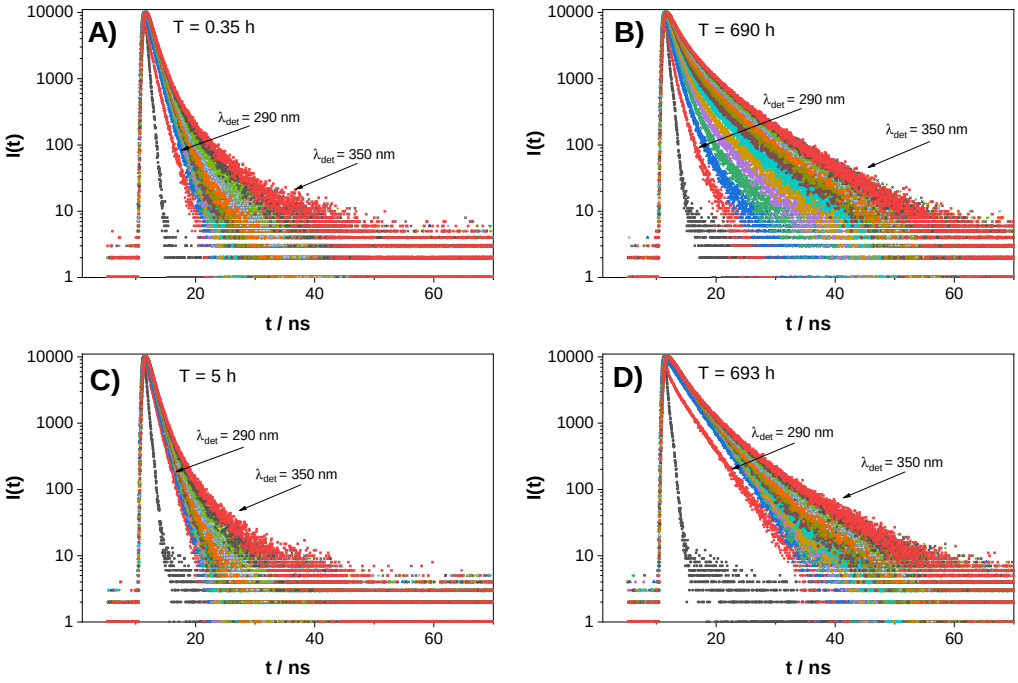

Figure 6.3: Raw fluorescence decays of free hexameric insulin measured at A) 0.35 and B) 690 hours and insulin with glucose measured at C) 5 and D) 693 hours after sample preparation. With an excitation wavelength of 279 nm and detection wavelength range from 290-350 nm.

The fluorescence decays for free and glycated hexameric insulin were measured at several times over the period of about 700 hours of incubation. The emission wavelength detection ranged from 290-350 nm in increments of 5 nm. It can be observed figure 6.3 that the increasing incubation time of both samples results in longer lifetimes and that the spread of decays is more significant in the free hexameric insulin sample. This suggests that the glucose-insulin complex makes tyrosine local environments less heterogenic.

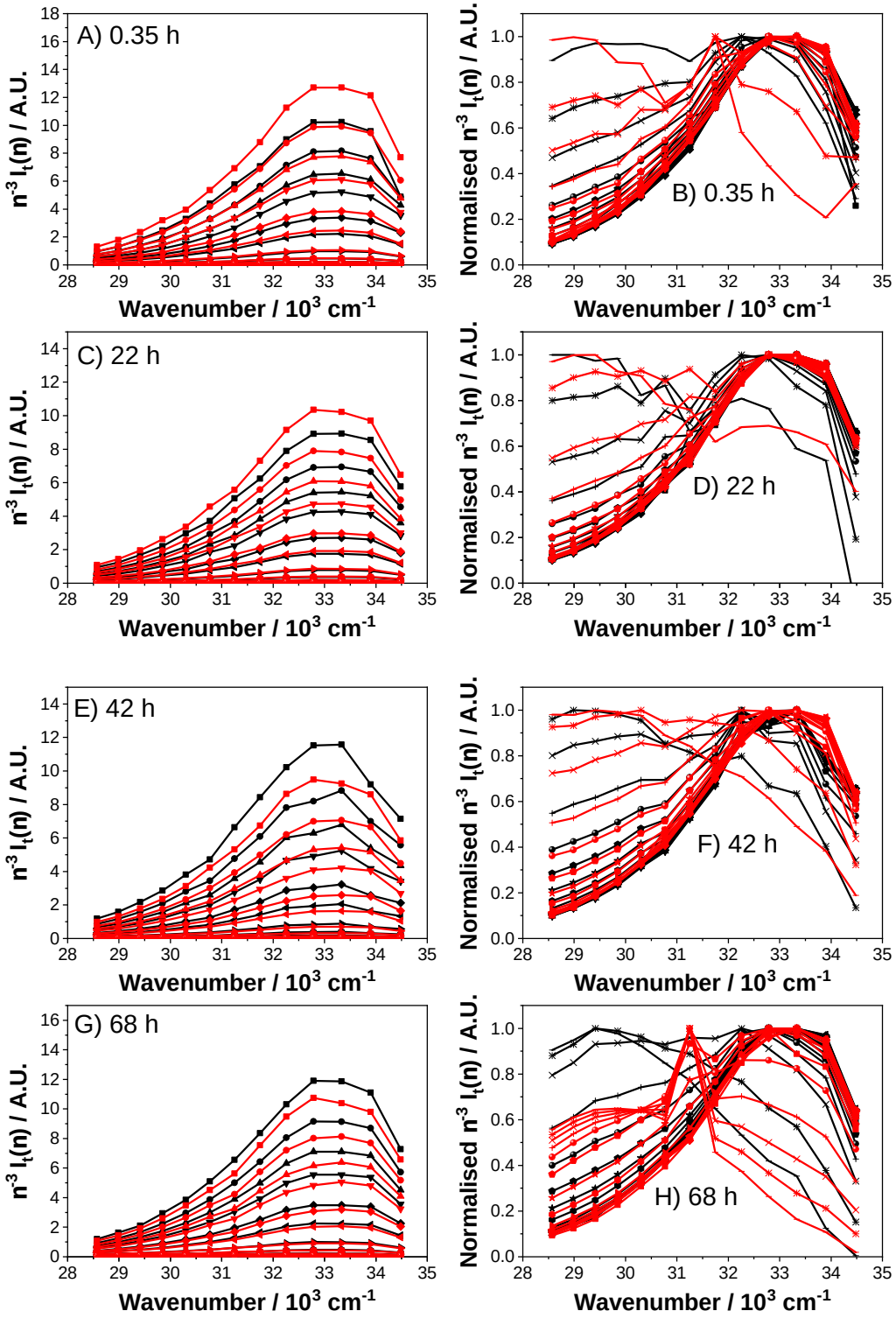
A) 0.35 h
B) 0.35 h
C) 22 h
D) 22 h
E) 42 h
F) 42 h
G) 68 h
H) 68 h
n-3 It(n) / A.U.
Normalised n-3 It(n) / A.U.
Wavenumber / 10^3 cm-1

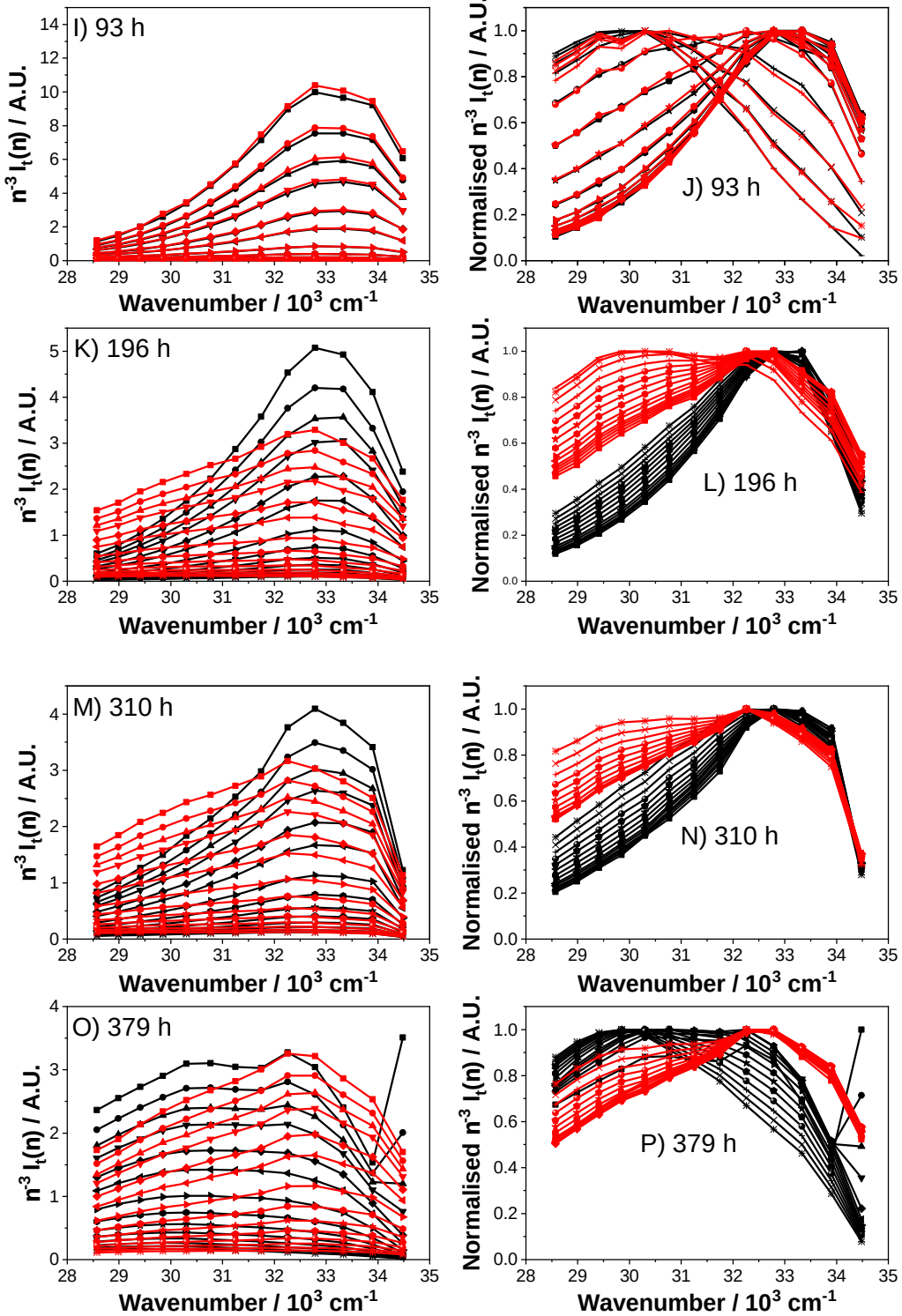
I) 93 h
J) 93 h
K) 196 h
L) 196 h
M) 310 h
N) 310 h
O) 379 h
P) 379 h
n-3 It(n) / A.U.
Normalised n-3 It(n) / A.U.
Wavenumber / 10^3 cm-1

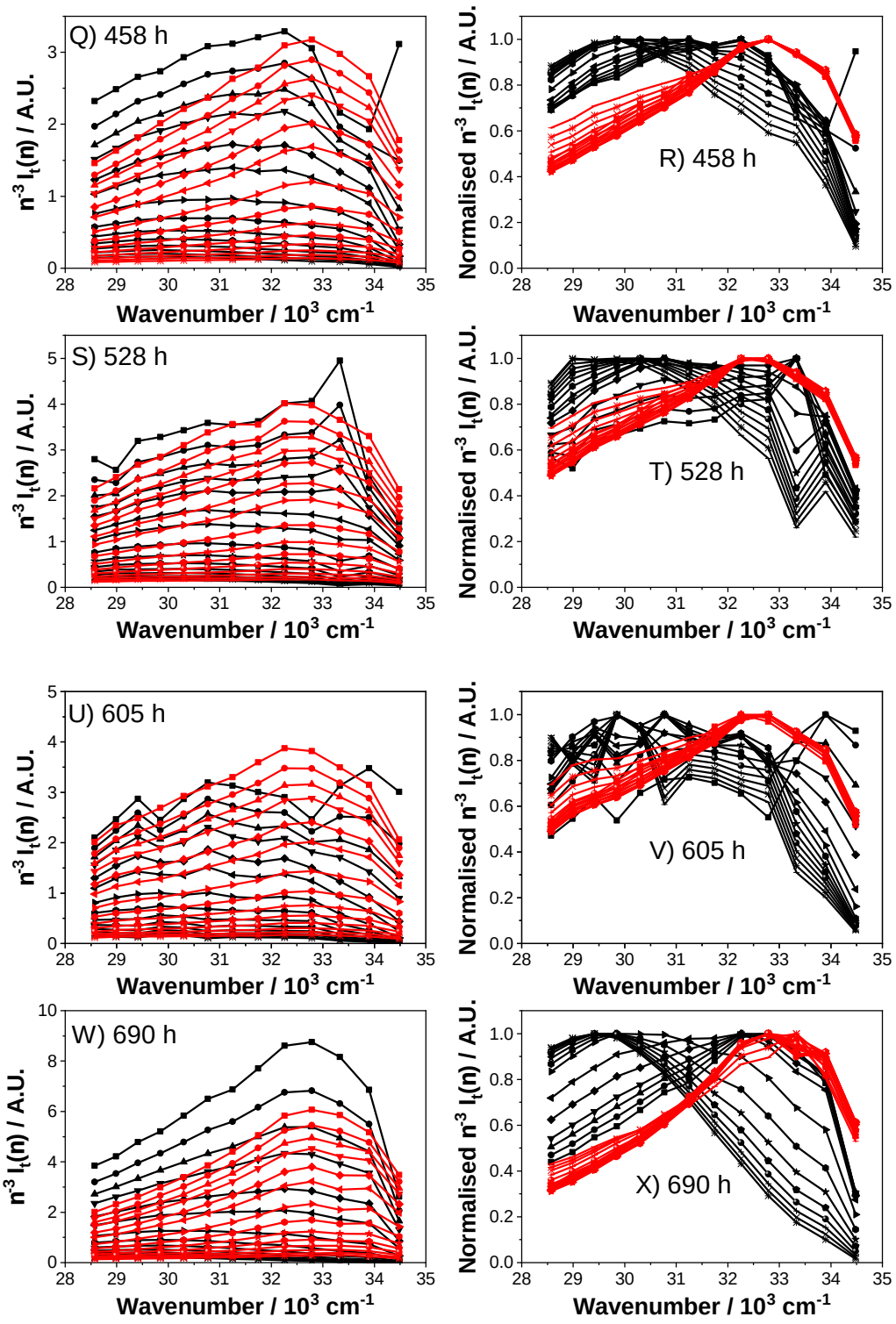

Figure 6.4: TRES spectra of free insulin (black curves) and insulin with glucose (red curves). The left-hand panel demonstrates the evolution of time 0, 0.25, 0.5, 0.75, 1, 1.5, 2, 3, 4, 5, 6, 7, 8, 9, and 10 ns after excitation. Samples were measured at times A) 0.35, C) 22, E) 42, G) 68, I) 93, K) 196, M) 310, O) 458, S) 528, U) 605, and W) 690 hours. The right-hand panel illustrates normalised TRES spectra.

Figure 6.4 shows examples of TRES spectra of the free hexameric insulin and glycated insulin samples after 0.35, 22, 42, 68, 93, 196, 310, 458, 528, 605, and 690 hours of incubation. Initially from 0.35-22 hours (figure 6.4A and C), the fluorescence intensity of free hexameric insulin is lower compared with that of insulin with glucose. In contrast, 42-68 hours (figure 6.4E and G) show that the fluorescence intensity of insulin is higher without glucose. Despite the slight differences in intensity, the spectra from 0.35-93 hours show similar trends. This is better seen from the normalised TRES spectral plots in figure 6.4B, D, F, H, and J. Initially, the slight increase intensity in the sample with glucose could again be explained by glucose shielding insulin from water molecules that would normally quench tyrosine fluorescence. After 196 hours (figure 6.4K and L), glucose influence on tyrosine fluorescence is substantially different: the intensity, as compared to free insulin, decreases faster at higher wavenumbers and slower at smaller wavenumbers. This can be explained in terms of the variety of possible complexes between non-glycated, nonglycated/glycated, and glycated-only insulin molecules. This results in a much broader range of local environments for tyrosine, thus, broadening the fluorescence spectrum. During the initial ~300 hours, we can observe the two dominating bands in the TRES spectra at ~32,500 and ~30,000 cm^{-1}. The 32,500 cm^{-1} which is the tyrosine in glycated insulin shifts to slightly lower energies compared to free insulin because of sugar binding. The other peak is likely to be caused by the fluorescence of the insulin glycation products. The TRES spectral peak at 30,000 cm^{-1} decreases slower than 32,500 cm^{-1} which indicates that the complex molecules have a slower intensity decay compared to noncomplex molecules. For the glycated sample incubated for longer than 350 hours (figure 6.4O-R), the fluorescence peak of the noncomplexes rate of its decay becomes faster. At 500-700 hours (figure 6.4S-X), the TRES spectra do not change their shape. Currently, we explain this by glycated insulin aggregates that are bound together to form fibrils/AGEs, which are more rigid than smaller aggregates. This results in limited orientational freedom for tyrosines (more stable spectra) and quenching by tightly packed complexes (shorter lifetimes). This observation is consistent with the TRES plots for the fibrillogenesis model (shown in figure 4.4), where the peptide shows no conformational changes within the nanosecond

timescale due to the rigidity caused by fibril formation.

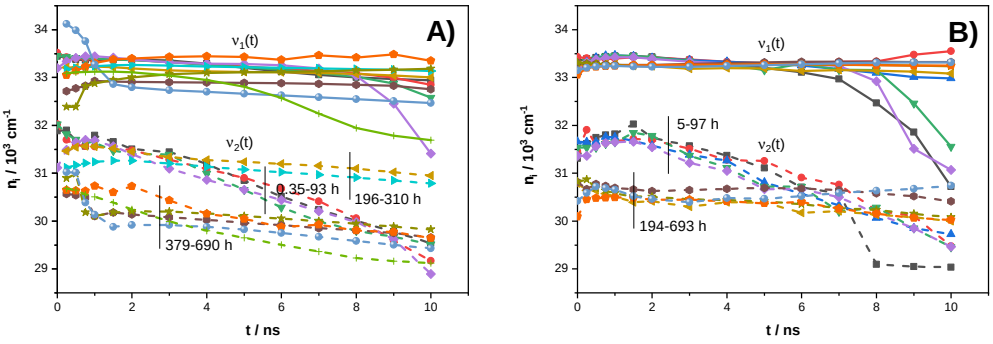

Figure 6.5: Toptygin-type models were used to fit to the TRES spectra of A) free hexameric insulin the peak positions ν_i were extracted and plotted for 0.33 (■), 22 (●), 68 (▼), 93 (◆), 196 (◄), 310 (►), 379 (○), 458 (★), 528 (⬠), 605 (◕), and 690 (|) hours. The TRES parameters for B) insulin with glucose were taken at 5 (■), 28 (●), 72 (▼), 97 (◆), 194 (◄), 454 (○), 530 (★), 607 (⬠), 693 (◕). The components 1 and 2 are represented with solid and dashed curves, respectively.

For quantitative interpretation of the TRES results, the two-component spectrum model equation (3.20) was fitted to the TRES spectra of both samples (free hexameric insulin and hexameric insulin with glucose), and its parameters were recovered. The position of spectral peaks $\nu_i(t)$ are plotted in figure 6.5. The higher energy peaks $\nu_1(t)$ occur for both samples around 33,000 cm^{-1} and remain stable throughout the measured 700 hours. The changes in the second peak positions $\nu_2(t)$ depend substantially on the incubated times of the samples. During the first 190 hours, $\nu_2(t)$ for both samples ~32,000 to ~30,000 cm^{-1} during 10 ns after excitation, however, there is a substantial difference between free and glycated insulin. While $\nu_2(t)$ in a free insulin sample has a decreasing trend in all stages of aging, $\nu_2(t)$ in the glycated sample seems to increase over the first 2 ns after excitation. This is due to the presence of a third fluorescent

glycation product not appearing in a free insulin sample. Its presence increases the complexity of the fluorescence spectrum and the two-component model is no longer adequate and thus the apparent increase in $\nu_2(t)$ in the way the model accommodates the additional fluorescence. At 194 and 310 hours, the lack of shifting to lower energies during 10 ns might be an indication that insulin is in its intermediate stage where their size increases and therefore, their conformation does not change as quickly as smaller aggregates. However, when hexameric insulin is incubated with glucose during this time, it shows that $\nu_2(t)$ decreases to a lower level of ~30,500 cm^{-1} which is also shown for older samples 379 to 690 hours. The initial peak shift is probably caused by tighter aggregation of insulin proteins. The free insulin sample still shows a red shift of ν_2 to around 29,500 cm^{-1}, whereas the glycated sample shows only slight shifts, confirming the formation of more rigid structures. This is consistent with previous studies which have suggested that glycation cross links protein aggregates together [63].

6.3.2 Comparison of Long-Term Stability Between Free Monomeric Insulin and Monomeric Insulin with Glucose

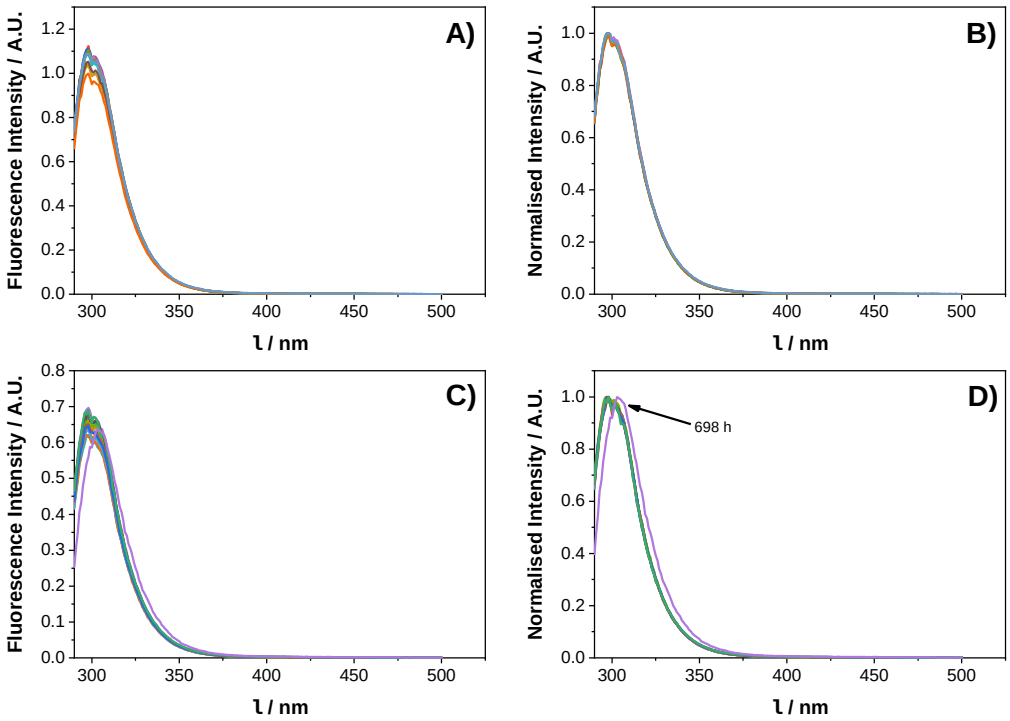

Figure 6.6: Fluorescence intensity of free monomeric insulin A) at 1, 25, 54, 97, 192, 337, 457, 530, 601, and 698 hours of preparation and insulin with glucose C) measured at 0.17, 19, 55, 67, 90, 117, 162, 188, 235, 259, 306, 360, 452, 474, 522, 594, and 698 hours after preparation. The corresponding normalised intensities are shown in B) and D), respectively.

The steady state emission spectra for free monomeric insulin and monomeric insulin with glucose was measured from 0-700 hours to study the effects glycation has on another form of insulin (shown in figure 6.6). The fluorescence spectrum for monomeric insulin with or without glucose show no significant difference with the exception of 698 hours after preparation. The shape of the spectra is maintained but it is shifted towards higher wavelengths, this may indicate that the tyrosine residue is exposed to a more polar environment such as water.

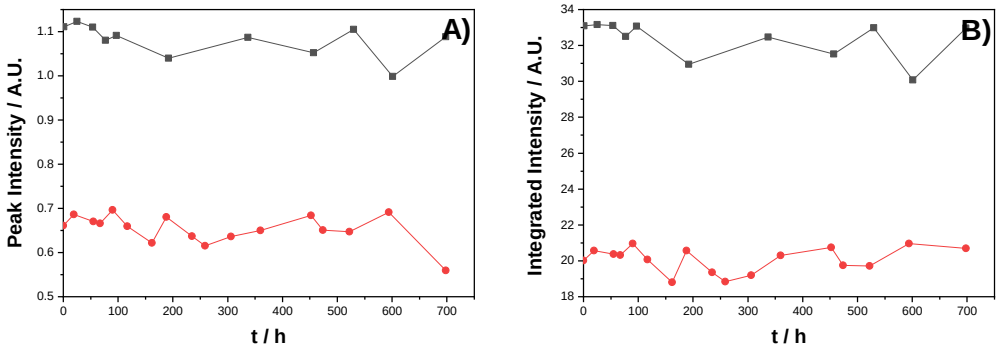

Figure 6.7: Peak fluorescence intensity at 298 nm and B) integrated fluorescence spectra taken from 50 μM monomeric insulin (■) in PBS buffer and 50 μM insulin with 50 mM (●) glucose in PBS buffer.

The peak (298 nm) and integrated intensities were taken and shown on figure 6.7A and B, respectively. There is no significant change between the peak and integrated intensities shown, which is expected because there is very little change in the spectra throughout 700 hours in monomeric insulin and insulin with glucose. However, insulin with glucose shows that the fluorescence has been quenched when comparing the spectra to free insulin and since the spectra does not change. This suggests that glucose creates ground state complexes, thus, reducing the quantum yield of the tyrosine fluorophore.

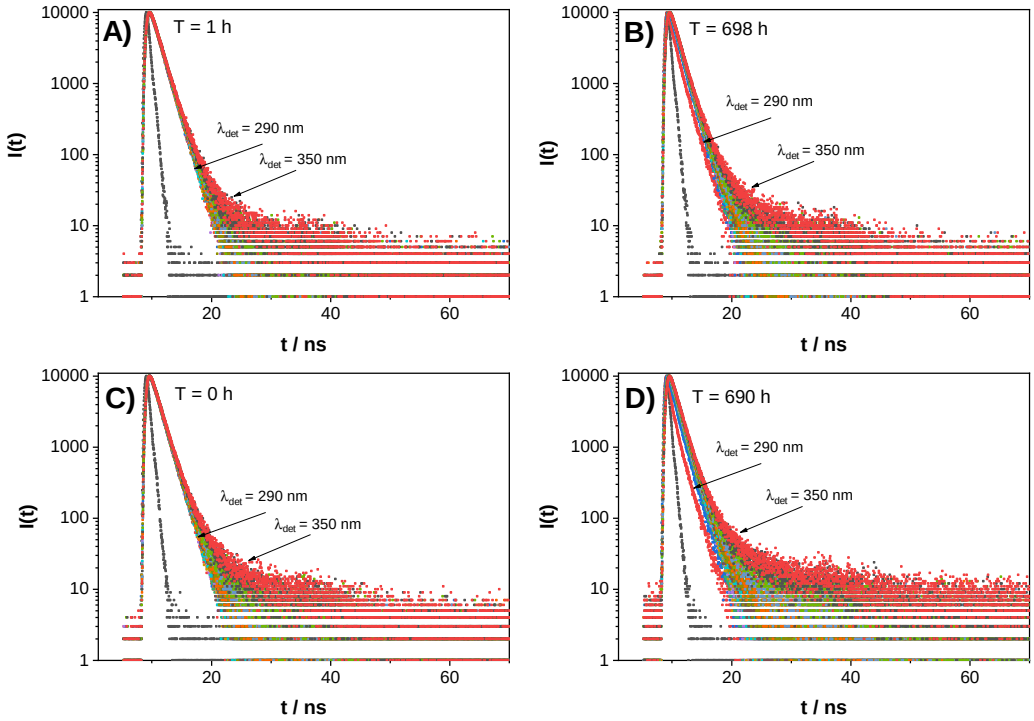

Figure 6.8: Raw fluorescence decays of free monomeric insulin measured at A) 1 and B) 698 hours and insulin with glucose measured at C) 1 and D) 698 hours after sample preparation. With an excitation wavelength of 279 nm and detection wavelength range from 290-350 nm.

We can gather more information upon the interaction of monomeric insulin with glucose by measuring the fluorescence lifetime decays for both samples at 1 and 698 hours after sample preparation and at different detection wavelengths. By comparing both samples (shown on figure 6.8), it can be observed that the spread of fluorescence decays may indicate that monomeric insulin with glucose is more heterogenous than free insulin. Both samples show an increase in lifetime decay for each detection wavelength after 698 hours, this suggests that there is an increase in populations of aggregates. However, it is still more homogenous compared to hexameric insulin shown in figure 6.3.

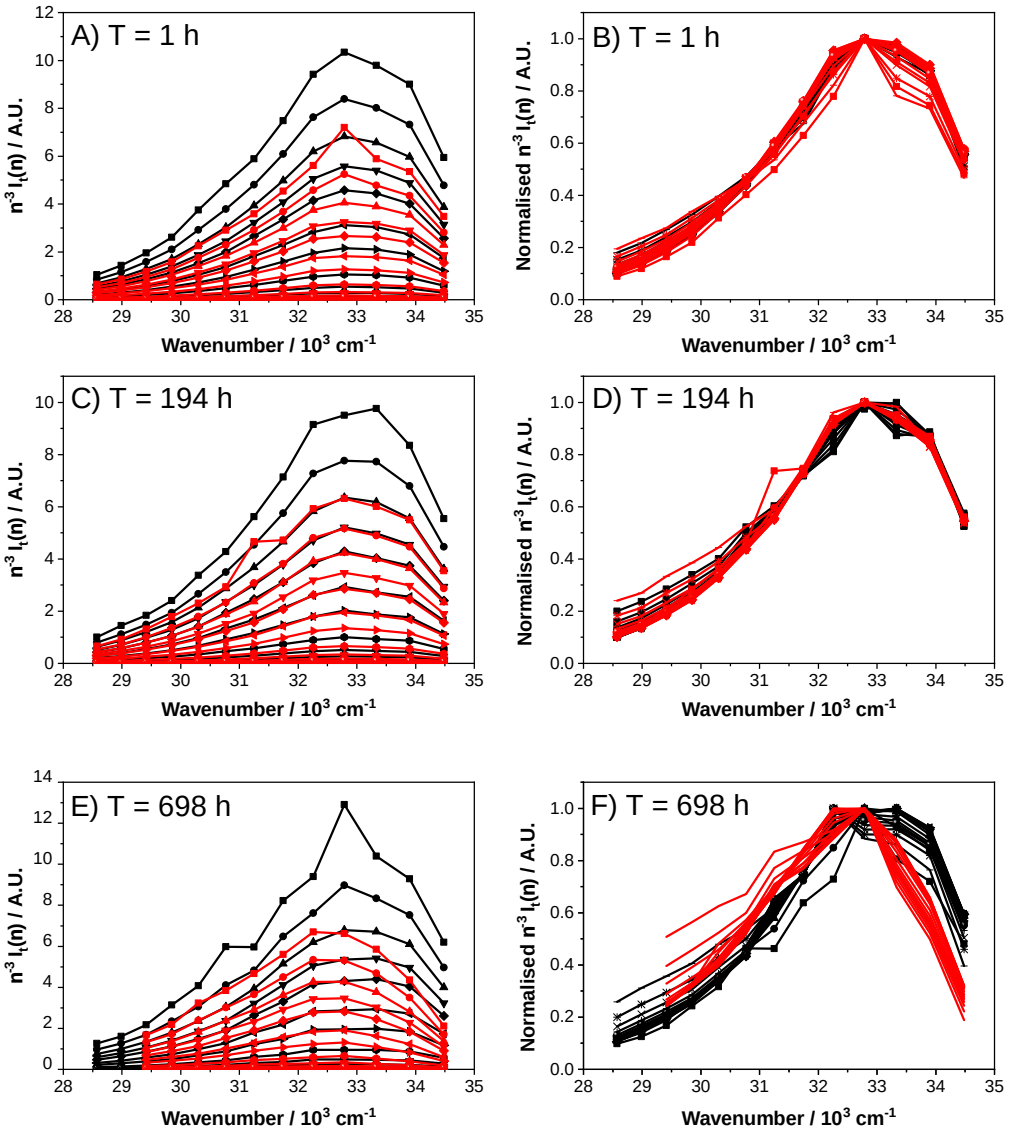

Figure 6.9: TRES spectra of free insulin (black curves) and insulin with glucose (red curves). The left-hand panel demonstrates the evolution of time 0, 0.25, 0.5, 0.75, 1, 1.5, 2, 3, 4, 5, 6, 7, 8, 9, and 10 ns after excitation. Samples were measured at times A) 1, C) 194, and E) 698 hours. The right-hand panel illustrates normalised TRES spectra.

The TRES spectra plots for monomeric insulin and insulin with glucose is shown in figure 6.9. The shape of each TRES spectra from 1-194 hours are similar, however, the intensity of TRES is lower when glucose is incubated with insulin as it quenches the tyrosine fluorescence. Not only does glucose reduce the fluorescence intensity after 698 hours of sample preparation, the spectra also show a spectral shift towards lower energies. This indicates that at long periods of time, glucose can quench and also expose tyrosine residues into polar environments. This means that glucose can have an effect upon monomeric insulin's shape and stability over long periods of time. However, only after 196 hours, glucose has already created dramatic changes upon the structure of hexameric insulin. Which indicates that monomeric insulin is more stable than hexameric insulin.

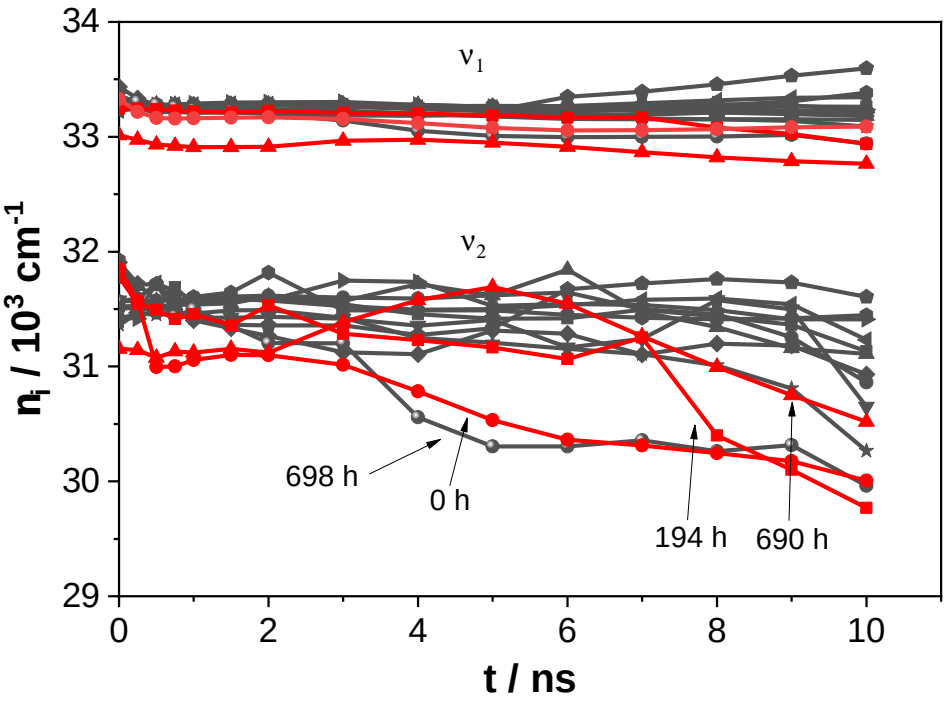

Figure 6.10: Toptygin-type models were used to fit to the TRES spectra of A) free hexameric insulin the peak positions ν_i were extracted and plotted for 1 (■), 25 (●), 77 (▼), 97 (◆), 192 (◄), 337 (►), 457 (⬠), 530 (★), 601 (⬠), and 698 (◕) hours. The TRES parameters for B) insulin with glucose were taken at 1 (■), 194 (●), and 690 (▲). The components 1 and 2 are represented with solid and dashed curves, respectively.

For a more quantitative analysis, peak positions $\nu_i(t)$ of Toptygin-type models were

extracted and shown on figure 6.10. Component 1 for both free monomeric insulin and insulin with glucose appear around 33,500 cm^{-1} apart from insulin with glucose measured at 690 hours of incubation (33,000 cm^{-1}). This may indicate that the aggregate for $\nu_1(t)$ increases in size and/or the tyrosine is exposed to more polar environments. The second component has an initial peak position of around 32,000 cm^{-1} for 0 and 194 hours, their peak positions both shift to 30,000 cm^{-1}. This suggest that their conformation is triggered by excitation light and the structures at this time are relatively small which can undergo fast conformational changes compared to larger aggregates. For 698 hours after sample preparation, $\nu_2(t)$ for glycated insulin has an initial peak of ~31,000 cm^{-1} which indicates that glucose increases the size of insulin through glycation. The peak position increases then decreases throughout 10 ns, which can be explained because $\nu_2(t)$ may need to be fitted with 3 Toptygin-type model to be able to correctly represent the fluorescent species formed during this aggregation time.

6.3.3 End Point Assembly for Hexameric and Monomeric Insulin with Glucose Labelled with Alexa-Fluor 647

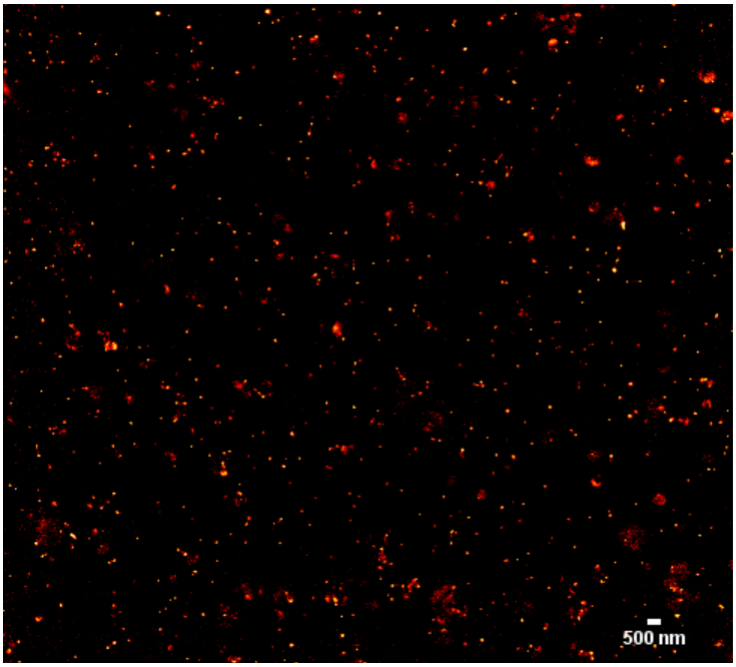

Figure 6.11: dSTORM images of hexameric insulin with glucose labelled with Alexa-Fluor 647 incubated at room temperature for 700 hours.

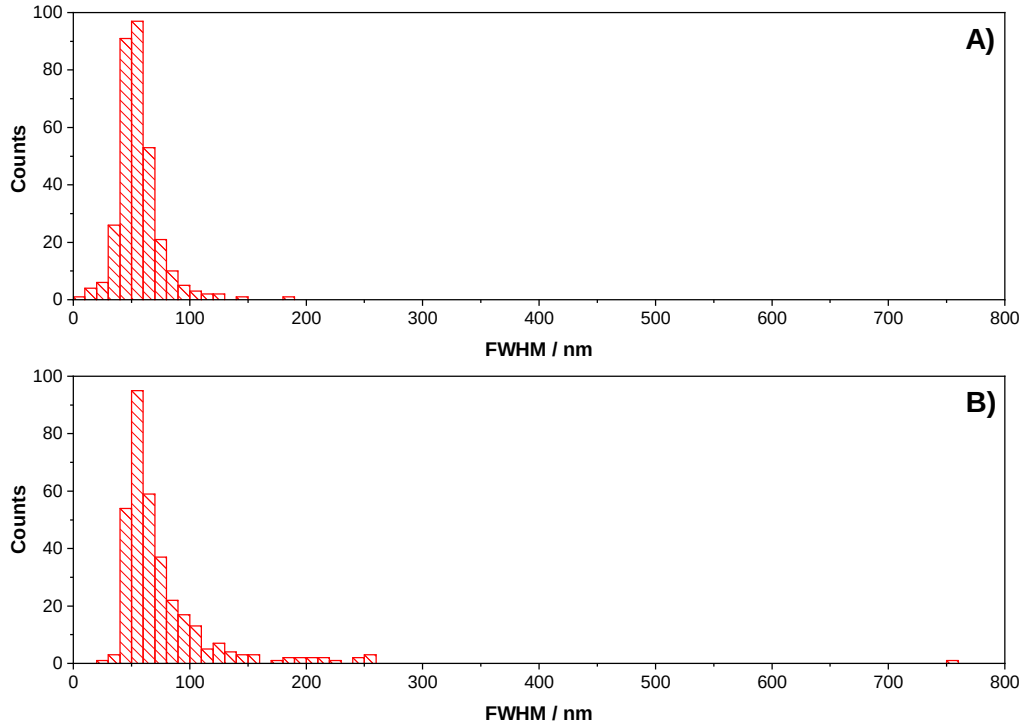

Figure 6.12: Histogram A) width and B) lengths of hexameric insulin with glucose analysed from the dSTORM images in figure 6.11.

dSTORM images were used to further understand the glycation of hexameric insulin and these images were taken after 700 hours of incubation. There is a range of different sizes and there is an abundance of structures compared to free hexameric insulin shown in figure 5.14. The width and length of each structure was measured on Image J and histograms of their full widths were plotted on figure 6.12A and B, respectively. The majority of widths were found to be around 50 nm, which is similar to what was found in free hexameric insulin. However, there is a big distribution of lengths, (from ~30 to 750 nm) and a great abundance of aggregates compared to free hexameric insulin. Therefore, this suggests that hexameric insulin incubated with glucose for 700 hours enhances the formation of aggregates.

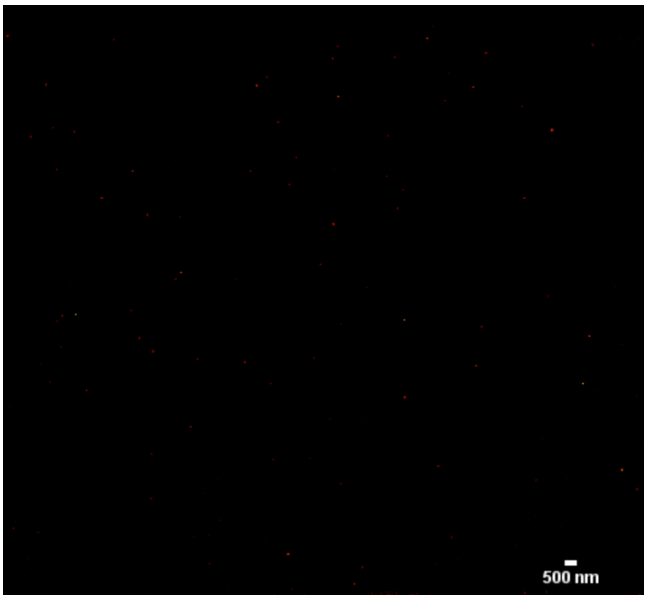

Figure 6.13: dSTORM images of monomeric insulin with glucose labelled with Alexa-Fluor 647 incubated at room temperature for 700 hours.

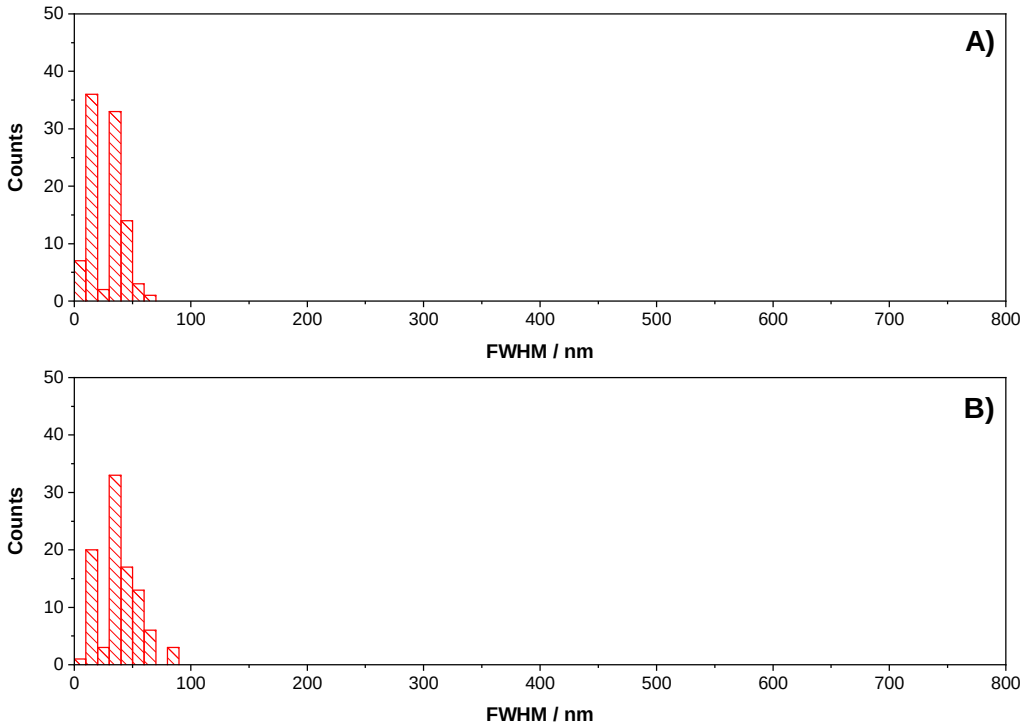

Figure 6.14: Histogram A) width and B) lengths of monomeric insulin with glucose analysed from the dSTORM images in figure 6.13.

Again, dSTORM images were taken of monomeric insulin with glucose incubated for 700 hours at room temperatures. The measurement shows that the lengths and widths are all below 100 nm and there are very few visible structures compared to free monomeric insulin (figure 5.16) and hexameric insulin with glucose (figure 6.11). Since the majority of structures are below 50 nm, this indicates that glucose may inhibit the formation of monomeric insulin aggregates. This is consistent with studies observed in Barzegar et al. [141] which shows that with the presence of glucose, the structural stability of insulin increases and there is a decrease in aggregation.

6.4 Conclusion

To gain a deeper understanding of the effect glucose has on the stability of insulin, the protein was incubated with the sugar and the local environments tyrosine had was monitored for 700 hours when insulin was both in its hexameric and monomeric forms.

The steady state emission spectra for hexameric insulin with glucose shows a dominant peak around 300 nm and the fluorescence intensity decreases for the first 30 hours and then intensity increases up to 700 hours after sample preparation. Around 192-700 hours, spectral broadening occurs at longer wavelengths which may be due to the combination of different fluorescence species formed during this time. In contrast, in free hexameric insulin, the intensity decreased from 0-700 hours and the spectra broadening occurred. This suggests that glucose shields the quenching of tyrosine in the long term and prevent hexameric insulin from creating new fluorescent species. However, looking at the time-resolved emission spectra and dSTORM measurements, evidences suggests that larger and more rigid structures are being formed compared to free hexameric insulin. This indicates that the tyrosine in the new fluorescent species may be quenched by glucose or the nearby complexes.

It is important to study how the glucose affects the stability monomeric insulin at long time periods as this form is known as the bioactive form of insulin because it circulates within the blood stream and attaches to insulin receptors. The steady state

spectra show that there is no spectral shape change with or without the incubation of glucose. There is only a shift towards longer wavelengths at 700 hours which suggests that conformational changes occur and tyrosine residues are exposed to more polar environments. The same can be observed in the TRES spectra for monomeric insulin and insulin with glucose, where both spectra show no significant changes apart from at later stages at 700 hours. This shows that monomeric insulin is less likely to be influenced by glycation.

To summarize, we suggest that observed modifications of TRES spectra offer the opportunity to distinguish forms of protein glycation, thus offering systematic studies of glycation induced by a variety of sugars, environmental conditions, anti-glycation factors, and so forth. However, this aim cannot be achieved by fitting experimental TRES spectra to the more complex models of the spectrum, as this approach is already the subject of several assumptions (a three-exponential representation of the individual fluorescence intensity decays and Toptygin-type profile of the spectrum). Instead, the experimental TRES spectra could be considered as an approximation and used to propose a selection of alternative models of the kinetics, for which the relevant fluorescence intensity decays $I_\lambda(t)$ will be calculated numerically. Confirmation of the specific type of glycation would be achieved in order to find the best-fitting kinetic model and the values of its parameters. Our preliminary attempts to fit the numerical solutions of the kinetic models to the experimental decay data demonstrate full feasibility of this approach.

Chapter 7

Conclusions and Future Work

In this thesis, intrinsic fluorescence (Tyr) has been used as a non-invasive probe to allow the detection of protein aggregation and glycation at the molecular level. In addition to tyrosine residues, extrinsic probes such as Thioflavin T and Alexa-Fluor dyes have been exploited to reveal β-sheet formation and to image end assemblies of the model protein and insulin, respectively.

A de novo peptide that self-assembles from the monomer up and which possesses homogeneous kinetics was synthesised. Two peptides were synthesised, one model was labelled with Alexa-Fluor 488 dye to capture the images at the end of fibril formation using structure illumination microscopy (SIM). The other peptide was created with a slight modification of replacing an extrinsic fluorophore for an intrinsic fluorophore to monitor the self-assembly with minimal interference. SIM images showed that there were long fibrous structures were formed within a few hours. The tyrosine response during aggregation was monitored for 700 hours via time-resolved emission spectroscopy (TRES) which showed no environmental changes after 24 hours. Which suggest that fibril formation occurs within a few hours and remains stable for several few weeks. The fluorescence of ThT did not increase when mixed with the protein model, and therefore there was no β-sheets present in the protein model. The protein model with the interaction with glucose was also studied, the combination of steady state emission and TRES implying that glucose inhibits fibril formation. The simplicity of the fibrillogenesis model and the inclusion of an intrinsic fluorophore makes it an

ideal reference for other natural proteins that contain tyrosine residues.

The natural protein of interest, insulin, also contains tyrosine residues. Insulin has been split up into two oligomeric states through different pH conditions. The tyrosine response for hexameric insulin shows drastic conformational changes throughout 700 hours compared to monomeric insulin. The steady state emission spectra show that intensities of hexameric insulin decrease over time, and after 379 hours, the spectrum broadens significantly. TRES spectra show there is a prominent peak around 33,000 cm^{-1} and around 30,000 cm^{-1} the peak emerges over time in the nanosecond timescale. After 379 hours, the higher wavenumbers decay faster than lower wavenumbers. With the combination of these results, hexameric insulin undergoes partial unfolding, which exposes the tyrosine residues to water and large conformational changes contribute to several species of aggregates occurring in the solution. This is consistent as insulin regularly undergoes polymorphism. With regard to the monomeric form, no change was observed in the steady state or time-resolved emission spectra. This indicates that monomeric insulin does not undergo fibril formation due to the lack of conformational changes detected by tyrosine. Thioflavin T was labelled in insulin and it showed a lack of β-sheet formation in both forms of insulin, which indicates that fibril formation was not formed. Direct stochastic optical reconstruction microscopy (dSTORM) images confirmed this, where insulin formed unstructured aggregates. Insulin which is an important medicine to keep blood glucose levels stable for diabetics. Therefore, the ability to monitor the stability of different forms of insulin in physiological conditions for a period of a few weeks is vital.

In addition to studying insulin aggregation in physiological conditions, both forms were incubated with glucose. The steady state emission spectra show that when hexameric insulin is incubated with glucose, the peak intensity around 300 nm increases and the spectrum broadens with time. The increase in intensity is due to glucose shielding tyrosine residues from water. Broadening occurs but it is not as prominent as seen in free hexameric insulin. For TRES spectra, the tyrosine response is similar to free hexameric insulin until 93 hours of incubation. After 196 hours, begins to show less deviation around 30,000 cm^{-1} in the nanosecond timescale when

incubation time increases. This observation shows that insulin aggregates undergo less conformational changes because advance glycation end products are cross linking aggregates making them more rigid. For monomeric insulin, there are no significant changes seen in either steady state or time resolved emission spectra, which shows that monomeric insulin is less likely to be influenced by glycation.

For future work to further develop the understanding of fibril formation, the tyrosine in the fibrillogenesis model could be replaced by tryptophan. Since tryptophan is known to be a highly sensitive probe to its local environment, it is an ideal probe to monitor protein folding where the emission spectra undergo a blue shift from polar to non-polar environments. Tryptophan also exist in important proteins such as human serum albumin (HSA) which is known to readily aggregate into amyloids and undergo glycation. Monitoring tryptophan would enable us to gather more in-depth information about the folding of the model peptide and it could be used as a reference model for other proteins undergoing aggregation and glycation.

Structural illumination microscopy has the ability to view protein dynamics in real time and it is able to break the diffraction barrier by a factor of 2, which makes it an ideal technique to observe early fibril formation. Direct stochastic optical reconstruction microscopy (dSTORM) are able to resolve objects below 50 nm and it would be more informative if dSTORM images were taken at several time points after sample preparation.

In addition to using steady state and TRES measurements to monitor fibrillogenesis, the fibrillogenesis model could also be probed by means of the time-resolved anisotropy of tyrosine, $r(t) = (r_o - r_\infty)\exp(-t/\tau_r) + r_\infty$, where the rotational time τ_r and the final anisotropy r_∞ are likely to increase due to increasing size of the fibrils. Circular dichroism (CD) is commonly used to determine the secondary structures within protein structures, mass spectrometry is able to characterize small protein aggregates and oligomers (MS), and electron microscopy (EM) is used to obtain high resolution images. All these techniques can be combined with the spectroscopy methods used in this thesis to bring to bear further information while still eliminating any need for

extrinsic fluorophores. The TRES approach has demonstrated that tracking changes in the intrinsic fluorescence offers a sensitive method of studying the stability, aggregation and glycation effects without the use of extrinsic markers. Studying it under physiological conditions is clinically relevant for environments such as inside a plastic delivery cannula or within a storage vial.

Bibliography

[1] F. Chiti and C. M. Dobson, "Protein Misfolding, Functional Amyloid, and Human Disease," *Annual Review of Biochemistry*, vol. 75, no. 1, pp. 333–366, 2006.

[2] L. Nielsen, R. Khurana, A. Coats, S. Frokjaer, J. Brange, S. Vyas, V. N. Uversky, and A. L. Fink, "Effect of Environmental Factors on the Kinetics of Insulin Fibril Formation," *Biochemistry*, vol. 40, no. 20, pp. 6036–6046, 2001.

[3] R. G. Ellis-Behnke, Y.-X. Liang, S.-W. You, D. K. C. Tay, S. Zhang, K.-F. So, and G. E. Schneider, "Nano neuro knitting: Peptide nanofiber scaffold for brain repair and axon regeneration with functional return of vision," *Proceedings of the National Academy of Sciences*, vol. 103, no. 13, pp. 5054–5059, 2006.

[4] B. van den Berg, R. Wain, C. M.Dobson, and R. Ellis, "Macromolecular crowding and protein refolding kinetics," *The EMBO Journal*, vol. 19, no. 15, pp. 3870–3875, 2000.

[5] T. P. J. Knowles, M. Vendruscolo, and C. M. Dobson, "The amyloid state and its association with protein misfolding diseases.," *Nature reviews. Molecular cell biology*, vol. 15, pp. 384–96, 2014.

[6] D. Eisenberg and M. Jucker, "The amyloid state of proteins in human diseases," *Cell*, vol. 148, pp. 1188–1203, 2012.

[7] P. Saeedi, I. Petersohn, P. Salpea, B. Malanda, S. Karuranga, N. Unwin, S. Colagiuri, L. Guariguata, A. A. Motala, K. Ogurtsova, J. E. Shaw, D. Bright, and R. Williams, "Global and regional diabetes prevalence estimates for 2019 and

projections for 2030 and 2045: Results from the International Diabetes Federation Diabetes Atlas, 9th edition," *Diabetes Research and Clinical Practice*, vol. 157, p. 107843, 2019.

[8] F. E. Dische, C. Wernstedt, G. T. Westermark, P. Westermark, M. B. Pepys, J. A. Rennie, S. G. Gilbey, and P. J. Watkins, "Insulin as an amyloid-fibril protein at sites of repeated insulin injections in a diabetic patient," *Diabetologia*, vol. 31, pp. 158–161, 1988.

[9] K. R. Wilhelm, K. Yanamandra, M. A. Gruden, V. Zamotin, M. Malisauskas, V. Casaite, A. Darinskas, L. Forsgren, and L. A. Morozova-Roche, "Immune reactivity towards insulin, its amyloid and protein S100B in blood sera of Parkinson's disease patients," *European Journal of Neurology*, vol. 14, no. 3, pp. 327–334, 2007.

[10] L. Nielsen, S. Frokjaer, J. F. Carpenter, and J. Brange, "Studies of the Structure of Insulin Fibrils by Fourier Transform Infrared (FTIR) Spectroscopy and Electron Microscopy," *Journal of Pharmaceutical Sciences*, vol. 90, no. 1, p. 29–37, 2001.

[11] G. Münch, H. J. Lüth, A. Wong, T. Arendt, E. Hirsch, R. Ravid, and P. Riederer, "Crosslinking of alpha-synuclein by advanced glycation endproducts–an early pathophysiological step in Lewy body formation?," *Journal of chemical neuroanatomy*, vol. 20, pp. 253–257, 2000.

[12] N. Sasaki, R. Fukatsu, K. Tsuzuki, T. Koike, I. Wakayama, R. Yanagihara, and R. Garruto, "Advanced Glycation End Products in Alzheimer's Disease and Other Neurodegenerative Diseases," *The American Journal of Pathology*, vol. 153, pp. 1149–1155, 1998.

[13] M. Bouchard, J. Zurdo, E. J. Nettleton, C. M. Dobson, and C. V. Robinson, "Formation of insulin amyloid fibrils followed by FTIR simultaneously with CD and electron microscopy," *Protein Science*, vol. 9, no. 10, pp. 1960–1967, 2000.

[14] Q. Hua and M. A. Wesss, "Comparative 2D NMR Studies of Human Insulin and Des-pentapeptide Insulin: Sequential Resonance Assignment and Implications

for Protein Dynamics and Receptor Recognition," *Biochemistry*, vol. 30, pp. 5505–5515, 1991.

[15] P. Tito, E. J. Nettleton, and C. V. Robinson, "Dissecting the hydrogen exchange properties of insulin under amyloid fibril forming conditions: A site-specific investigation by mass spectrometry," *Journal of Molecular Biology*, vol. 303, no. 2, pp. 267–278, 2000.

[16] V. Feingold, A. B. Jenkins, and E. W. Kraegen, "Effect of contact material on vibration-induced insulin aggregation," *Diabetologia*, vol. 27, pp. 373–378, 1984.

[17] C. Iannuzzi, M. Borriello, M. Portaccio, and G. Irace, "Insights into Insulin Fibril Assembly at Physiological and Acidic pH and Related Amyloid Intrinsic Fluorescence," *Int. J. Mol. Sci.*, vol. 18, p. 2551, 2017.

[18] M. Amaro, K. Kubiak-Ossowska, D. J. S. Birch, and O. J. Rolinski, "Initial stages of beta-amyloid Aβ 140 and Aβ 142 oligomerization observed using fluorescence decay and molecular dynamics analyses of tyrosine," *Methods and Applications in Fluorescence*, vol. 1, no. 1, p. 015006, 2013.

[19] M. Amiri, K. Jankeje, and J. R. Albani, "Origin of fluorescence lifetimes in human serum albumin. Studies on native and denatured protein," *Journal of Fluorescence*, vol. 20, no. 3, pp. 651–656, 2010.

[20] E. J. Nettleton, P. Tito, M. Sunde, M. Bouchard, C. M. Dobson, and C. V. Robinson, "Characterization of the oligomeric states of insulin in self-assembly and amyloid fibril formation by mass spectrometry.," *Biophysical journal*, vol. 79, no. 2, pp. 1053–1065, 2000.

[21] A. Ahmad, V. N. Uversky, D. Hong, and A. L. Fink, "Early in the fibrillation of monomeric insulin," *Journal of Biological Chemistry*, vol. 280, no. 52, pp. 42669–42675, 2005.

[22] D. P. Hong, A. Ahmad, and A. L. Fink, "Fibrillation of human insulin A and B chains," *Biochemistry*, vol. 45, no. 30, pp. 9342–9353, 2006.

[23] M. F. Dunn, "Zinc – ligand interactions modulate assembly and stability of the insulin hexamer – a review," *BioMetals*, vol. 2, pp. 295–303, 2005.

[24] L. Nielsen, S. Frokjaer, J. Brange, V. N. Uversky, and A. L. Fink, "Probing the mechanism of insulin fibril formation with insulin mutants," *Biochemistry*, vol. 40, no. 28, pp. 8397–8409, 2001.

[25] J. S. Pedersen, C. B. Andersen, and D. E. Otzen, "Amyloid structure - one but not the same: The many levels of fibrillar polymorphism," *FEBS Journal*, vol. 277, no. 22, pp. 4591–4601, 2010.

[26] D. N. Woolfson, "The design of coiled-coil structures and assemblies," *Advances in protein chemistry*, vol. 70, no. 04, pp. 79–112, 2005.

[27] N. Faruqui, A. Bella, J. Ravi, S. Ray, B. Lamarre, and M. G. Ryadnov, "Differentially instructive extracellular protein micro-nets," *Journal of the American Chemical Society*, vol. 136, pp. 7889–7898, 2014.

[28] G. Bhak, S. Lee, J. W. Park, S. Cho, and S. R. Paik s, "Amyloid hydrogel derived from curly protein fibrils of α-synuclein," *Biomaterials*, vol. 31, no. 23, pp. 5986–5995, 2010.

[29] A. Herland, D. Thomsson, O. Mirzov, I. G. Scheblykin, and O. Inganäs, "Decoration of amyloid fibrils with luminescent conjugated polymers," *Journal of Materials Chemistry*, vol. 18, no. 1, pp. 126–132, 2008.

[30] P. Rondeau and E. Bourdon, "The glycation of albumin: Structural and functional impacts," *Biochimie*, vol. 93, no. 4, pp. 645–658, 2011.

[31] M. C. De Rosa, M. T. Sanna, I. Messana, M. Castagnola, A. Galtieri, E. Tellone, R. Scatena, B. Botta, M. Botta, and B. Giardina, "Glycated human hemoglobin (HbA(1c)): Functional characteristics and molecular modeling studies," *Biophysical Chemistry*, vol. 72, no. 3, pp. 323–335, 1998.

[32] J. L. Jiménez, E. J. Nettleton, M. Bouchard, C. V. Robinson, C. M. Dobson, and H. R. Saibil, "The protofilament structure of insulin amyloid fibrils," *Proceedings*

of the National Academy of Sciences of the United States of America, vol. 99, no. 14, pp. 9196–9201, 2002.

[33] J. S. Sharp, J. A. Forrest, and R. A. Jones, "Surface denaturation and amyloid fibril formation of insulin at model lipid-water interfaces," *Biochemistry*, vol. 41, no. 52, pp. 15810–15819, 2002.

[34] M. I. Smith, J. S. Sharp, and C. J. Roberts, "Nucleation and growth of insulin fibrils in bulk solution and at hydrophobic polystyrene surfaces," *Biophysical Journal*, vol. 93, no. 6, pp. 2143–2151, 2007.

[35] V. I. Stsiapura, A. A. Maskevich, S. A. Tikhomirov, and O. V. Buganov, "Charge transfer process determines ultrafast excited state deactivation of thioflavin T in low-viscosity solvents," *Journal of Physical Chemistry A*, vol. 114, no. 32, pp. 8345–8350, 2010.

[36] J. Mohanty, S. Dutta Choudhury, H. Pal, and A. C. Bhasikuttan, "Early detection of insulin fibrillation: a fluorescence lifetime assay to probe the pre-fibrillar regime," *Chemical Communications*, vol. 48, no. 18, p. 2403, 2012.

[37] A. S. Koti, M. M. G. Krishna, and N. Periasamy, "Time-resolved area-normalized emission spectroscopy (TRANES): A novel method for confirming emission from two excited states," *Journal of Physical Chemistry A*, vol. 105, pp. 1767–1771, 2001.

[38] A. Bella, M. Shaw, S. Ray, and M. G. Ryadnov, "Filming protein fibrillogenesis in real time.," *Scientific reports*, vol. 4, p. 7529, 2014.

[39] D. Pinotsi, A. K. Buell, C. Galvagnion, C. M. Dobson, G. S. Kaminski Schierle, and C. F. Kaminski, "Direct observation of heterogeneous amyloid fibril growth kinetics via two-color super-resolution microscopy," *Nano Letters*, vol. 14, no. 1, pp. 339–345, 2014.

[40] K. U. Linderstrøm-Lang, "Proteins and Enzymes," *Lane Medical Lectures*, vol. 6, pp. 52–73, 1952.

[41] J. C. Kendrew, R. E. Dickerson, B. E. Strandberg, R. G. Hart, and D. R. Davies, "Structure of myoglobin: A three-dimensional Fourier synthesis at 2 A. resolution," *Nature*, vol. 185, pp. 422–427, 1960.

[42] B. M. F. Perutz, M. G. Rossmann, A. N. N. F. Cullis, H. Muirhead, G. Will, and A. C. T. North, "Structure of Hæmoglobin: A Three-Dimensional Fourier Synthesis at 5.5-Å. Resolution, Obtained by X-Ray Analysis," *Nature*, vol. 185, pp. 416–422, 1960.

[43] M. Sunde, L. C. Serpell, M. Bartlam, P. E. Fraser, M. B. Pepys, and C. C. F. Blake, "Common Core Structure of Amyloid Fibrils by Synchrotron X-ray Diffraction," *The Journal of Molecular Biology*, vol. 273, pp. 729–739, 1997.

[44] E. Wolf, P. S. Kim, and B. Berger, "Multicoil - a program for predicting 2-stranded and 3-stranded coiled coils," *Protein Sci*, vol. 6, no. 6, pp. 1179–1189, 1997.

[45] F. H. C. Crick, "The packing of alpha-helices: simple coiled-coils," *Acta Cryst.*, vol. 6, pp. 689–697, 1953.

[46] P. B. Harbury, T. Zhang, P. S. Kim, and T. Alber, "A switch between two-, three-, and four-stranded coiled coils in GCN4 leucine zipper mutants," *Science*, vol. 262, no. 5138, pp. 1401–1407, 1993.

[47] P. B. Harbury, P. S. Kim, and T. Alber, "Crystal structure of an isoleucine-zipper trimer," *Nature*, vol. 371, pp. 80–83, 1994.

[48] J. F. Conway and D. A. Parry, "Three-stranded α-fibrous proteins: the heptad repeat and its implications for structure," *International Journal of Biological Macromolecules*, vol. 13, no. 1, pp. 14–16, 1991.

[49] M. J. Pandya, G. M. Spooner, M. Sunde, J. R. Thorpe, A. Rodger, and D. N. Woolfson, "Sticky-end assembly of a designed peptide fiber provides insight into protein fibrillogenesis," *Biochemistry*, vol. 39, no. 30, pp. 8728–8734, 2000.

[50] E. K. O'Shea, J. D. Klemm, P. S. Kim, and T. Alber, "X-ray structure of the GCN4 leucine zipper, a two-stranded, parallel coiled coil," *Science*, vol. 254, no. 5031, pp. 539–544, 1991.

[51] P. P. Nakka, K. Li, and D. Forciniti, "Effect of Differences in the Primary Structure of the A-Chain on the Aggregation of Insulin Fragments," *ACS Omega*, vol. 3, no. 8, pp. 9636–9647, 2018.

[52] J. Brange and L. Langkjaer, "Insulin Structure and Stability," in *Stability and Characterization of Protein and Peptide Drugs: Case Histories* (Y. J. W. Pearlman and Rodney, eds.), ch. 11, pp. 315–348, New York: Springer, Boston, MA, 1993.

[53] G. Dodson and D. Steiner, "The role of assembly in insulin's biosynthesis," *Current Opinion in Structural Biology*, vol. 8, pp. 189–194, 1998.

[54] V. Sluzky, J. A. Tamada, A. M. Klibanov, and R. Langer, "Kinetics of insulin aggregation in aqueous solutions upon agitation in the presence of hydrophobic surfaces.," *Proceedings of the National Academy of Sciences*, vol. 88, pp. 9377–9381, 1991.

[55] M. I. Ivanova, S. A. Sievers, M. R. Sawaya, J. S. Wall, and D. Eisenberg, "Molecular basis for insulin fibril assembly," *Proceedings of the National Academy of Sciences*, vol. 106, no. 45, pp. 18990–18995, 2009.

[56] G. G. Glenner, E. D. Eanes, H. A. Bladen, R. P. Linke, and J. D. Termine, "Beta-pleated sheet fibrils. A comparison of native amyloid with synthetic protein fibrils.," *The Journal of Histochemistry and Cytochemistry*, vol. 22, pp. 1141–1158, 1974.

[57] J. L. Farrant and E. H. Mercer, "Electron microscopical observations of fibrous insulin," *Biochimica et Biophysica Acta*, vol. 8, pp. 335–359, 1952.

[58] Y. H. A. Abdel-Wahab, F. P. M. O'Harte, H. Ratcliff, N. H. McClenaghan, C. R. Barnett, and P. R. Flatt, "Glycation of insulin in the islets of Langerhans of normal and diabetic animals," *Diabetes*, vol. 45, pp. 1489–96, 1996.

[59] Y. H. A. Abdel-Wahab, F. P. M. O'Harte, C. R. Barnett, and P. R. Flatt, "Characterization of insulin glycation in maintained in tissue culture," *Journal of Endocrinology*, vol. 152, pp. 59–67, 1997.

[60] F. P. M. O'Harte, H. Hojrup, C. R. Barnett, and P. R. Flatt, "Identification of the Site of Glycation of Human Insulin," *Peptides*, vol. 17, pp. 1323–1330, 1996.

[61] R. J. Solá and K. A. I. Griebenow, "Effects of Glycosylation on the Stability of Protein Pharmaceuticals," *Biochemistry*, vol. 98, no. 4, pp. 1223–1245, 2010.

[62] S. Guedes, R. Vitorino, M. R. M. Domingues, F. Amado, and P. Domingues, "Mass Spectrometry Characterization of the Glycation Sites of Bovine Insulin by Tandem Mass Spectrometry," *J Am Soc Mass Spectrom*, vol. 20, pp. 1319–1326, 2009.

[63] P. Alavi, R. Yousefi, and S. Amirghofran, "Structural Analysis and Aggregation Propensity of Reduced and Nonreduced Glycated Insulin Adducts," *Appl Biochem Biotechnol*, vol. 170, pp. 623–638, 2013.

[64] M. Falconi, M. Bozzi, M. Paci, A. Raudino, R. Purrello, A. Cambria, M. Sette, and M. T. Cambria, "Spectroscopic and molecular dynamics simulation studies of the interaction of insulin with glucose," *International Journal of Biological Macromolecules*, vol. 29, pp. 161–168, 2001.

[65] V. Zoete, M. Meuwly, and M. Karplus, "Investigation of Glucose Binding Sites on Insulin," *PROTEINS: Structure, Function, and Bioinformatics*, vol. 55, pp. 568–581, 2004.

[66] A. Gautieri, A. Redaelli, M. J. Buehler, and S. Vesentini, "Age- and diabetes-related nonenzymatic crosslinks in collagen fibrils: Candidate amino acids involved in Advanced Glycation End-products," *Matrix Biology*, vol. 34, pp. 89–95, 2014.

[67] M. Kasha, "Characterization of Electronic Transitions in Complex Molecules," *Discussions of the Faraday Society*, vol. 9, pp. 14–19, 1950.

[68] A. Warshel and S. T. Russell, "Calculations of Electrostatic Interactions in Biological Systems and in Solutions," *Quarterly Reviews of Biophysics*, vol. 17, no. 3, pp. 283–422, 1984.

[69] S. D. Figueiró, A. A. Macêdo, M. R. Melo, A. L. Freitas, R. A. Moreira, R. S. De Oliveira, J. C. Góes, and A. S. Sombra, "On the dielectric behaviour of collagen-algal sulfated polysaccharide blends: Effect of glutaraldehyde crosslinking," *Biophysical Chemistry*, vol. 120, no. 2, pp. 154–159, 2006.

[70] A. Ahmad, T. Kurkina, K. Kern, and K. Balasubramanian, "Applications of the static quenching of rhodamine B by carbon nanotubes," *ChemPhysChem*, vol. 10, no. 13, pp. 2251–2255, 2009.

[71] S. Srisantitham, M. Sukwattanasinitt, and S. Unarunotai, "Effect of pH on fluorescence quenching of organic dyes by graphene oxide," *Colloids and Surfaces A: Physicochemical and Engineering Aspects*, vol. 550, no. February, pp. 123–131, 2018.

[72] M. Arik, N. Çelebi, and Y. Onganer, "Fluorescence quenching of fluorescein with molecular oxygen in solution," *Journal of Photochemistry and Photobiology A: Chemistry*, vol. 170, no. 2, pp. 105–111, 2005.

[73] A. Jain, C. Blum, and V. Subramaniam, *Fluorescence Lifetime Spectroscopy and Imaging of Visible Fluorescent Proteins*. Elsevier, first edit ed., 2009.

[74] A. Margineanu, J. J. Chan, D. J. Kelly, S. C. Warren, D. Flatters, S. Kumar, M. Katan, C. W. Dunsby, and P. M. French, "Screening for protein-protein interactions using Förster resonance energy transfer (FRET) and fluorescence lifetime imaging microscopy (FLIM)," *Scientific Reports*, vol. 6, p. 28186, 2016.

[75] H. Stockmann, V. Todorovic, P. L. Richardson, V. Marin, V. Scott, C. Gerstein, M. Lake, L. Wang, R. Sadhukhan, and A. Vasudevan, "Cell-Surface Receptor-Ligand Interaction Analysis with Homogeneous Time-Resolved FRET and Metabolic Glycan Engineering: Application to Transmembrane and GPI-Anchored Receptors," *Journal of the American Chemical Society*, vol. 139, no. 46, pp. 16822–16829, 2017.

[76] A. Kitamura, K. Nagata, and M. Kinjo, "Conformational analysis of misfolded protein aggregation by FRET and live-cell imaging techniques," *International Journal of Molecular Sciences*, vol. 16, no. 3, pp. 6076–6092, 2015.

[77] S. V. Thakkar, K. M. Allegre, S. B. Joshi, D. B. Volkin, and C. R. Middaugh, "An Application of Ultraviolet Spectroscopy to Study Interactions in Proteins Solutions at High Concentrations," *Journal of Pharmaceutical Sciences*, vol. 101, no. 9, pp. 3051–3061, 2012.

[78] A. Gobrecht, R. Bendoula, J. M. Roger, and V. Bellon-Maurel, "Combining linear polarization spectroscopy and the Representative Layer Theory to measure the Beer-Lambert law absorbance of highly scattering materials," *Analytica Chimica Acta*, vol. 853, no. 1, pp. 486–494, 2015.

[79] S. E. Leblanc, M. Atanya, K. Burns, and R. Munger, "Quantitative impact of small angle forward scatter on whole blood oximetry using a Beer-Lambert absorbance model," *Analyst*, vol. 136, no. 8, pp. 1637–1643, 2011.

[80] A. Quaranta, D. J. McGarvey, E. J. Land, M. Brettreich, S. Burghardt, H. Schönberger, A. Hirsch, N. Gharbi, F. Moussa, S. Leach, H. Göttinger, and R. V. Bensasson, "Photophysical properties of a dendritic methano[60]fullerene octadeca acid and its tert-butyl ester: Evidence for aggregation of the acid form in water," *Physical Chemistry Chemical Physics*, vol. 5, no. 5, pp. 843–848, 2003.

[81] D. G. Duff and C. H. Giles, "The Effects of Association on the Beer's Law Behaviour of Dye Solutions," *Journal of the Society of Dyers and Colourists*, vol. 88, no. 5, pp. 181–184, 1972.

[82] S. A. Berger, "The role of metal ion polymerization in beer's law deviations using extractive-colorimetric procedures," *Spectroscopy Letters*, vol. 23, no. 6, pp. 783–790, 1990.

[83] D. Toptygin and L. Brand, "Spectrally- and time-resolved fluorescence emission of indole during solvent relaxation: A quantitative model," *Chemical Physics Letters*, vol. 322, pp. 496–502, 2000.

[84] M. J. Sanderson, I. Smith, I. Parker, and M. D. Bootman, "Fluorescence Microscopy," *Cold Spring Harbor Protocols*, vol. 10, no. 10, pp. 1–36, 2014.

[85] S. W. Hell and J. Wichmann, "Breaking the diffraction resolution limit by stimulated emission : stimulated-emission-depletion fluorescence microscopy," *Optics Letters*, vol. 19, no. 11, pp. 780–782, 1994.

[86] T. A. Klar and S. W. Hell, "Subdiffraction resolution in far-field fluorescence microscopy," *Optics Letters*, vol. 24, no. 14, pp. 954–956, 1999.

[87] E. Betzig, G. H. Patterson, R. Sougrat, O. W. Lindwasser, S. Olenych, J. S. Bonifacino, M. W. Davidson, J. Lippincott-schwartz, and H. F. Hess, "Imaging Intracellular Fluorescent Proteins at Nanometer Resolution," *Science*, vol. 313, no. September, pp. 1642–1646, 2006.

[88] M. G. L. Gustafsson, "Surpassing the lateral resolution limit by a factor of two using structured illumination microscopy.," *Journal of Microscopy*, vol. 198, no. 2, pp. 82–87, 2000.

[89] M. G. L. Gustafsson, D. a. Agard, and J. W. Sedat, "Doubling the lateral resolution of wide-field fluorescence microscopy using structured illumination," *Proc. SPIE Int. Soc. Opt. Eng.*, vol. 3919, p. 141–150, 2000.

[90] M. Heilemann, S. van de Linde, M. Schüttpelz, R. Kasper, B. Seefeldt, A. Mukherjee, P. Tinnefeld, and M. Sauer, "Subdiffraction-resolution fluorescence imaging with conventional fluorescent probes," *Angewandte Chemie - International Edition*, vol. 47, no. 33, pp. 6172–6176, 2008.

[91] M. Heilemann, S. van de Linde, A. Mukherjee, and M. Sauer, "Super-Resolution Imaging with Small Organic Fluorophores **," *Angew. Chem. Int. Ed.*, vol. 48, pp. 6903–6908, 2009.

[92] S. van de Linde, A. Löschberger, T. Klein, M. Heidbreder, S. Wolter, M. Heilemann, and M. Sauer, "Direct stochastic optical reconstruction microscopy with standard fluorescent probes," *Nature Protocols*, vol. 6, no. 7, pp. 34–38, 2011.

[93] M. Shaw, L. Zajiczek, and K. O. Holleran, "High speed structured illumination microscopy in optically thick samples," *Methods*, vol. 88, pp. 11–19, 2015.

[94] M. G. L. Gustafsson, "Nonlinear structured-illumination microscopy : Wide-field fluorescence imaging with theoretically unlimited resolution," *PNAS*, vol. 102, no. 37, pp. 13081–13086, 2005.

[95] Y. Hirano, A. Matsuda, and Y. Hiraoka, "Recent advancements in structured-illumination microscopy toward live-cell imaging," *Microscopy*, vol. 64, no. 4, pp. 237–249, 2015.

[96] G. S. Kaminski Schierle, S. van de Linde, M. Erdelyi, E. K. Esbjörner, T. Klein, E. Rees, C. W. Bertoncini, C. M. Dobson, M. Sauer, and C. F. Kaminski, "In situ measurements of the formation and morphology of intracellular β-amyloid fibrils by super-resolution fluorescence imaging," *Journal of the American Chemical Society*, vol. 133, no. 33, pp. 12902–12905, 2011.

[97] C. H. Michel, S. Kumar, D. Pinotsi, A. Tunnacliffe, P. S. George-Hyslop, E. Mandelkow, E. M. Mandelkow, C. F. Kaminski, and G. S. K. Schierle, "Extracellular monomeric tau protein is sufficient to initiate the spread of tau protein pathology," *Journal of Biological Chemistry*, vol. 289, no. 2, pp. 956–967, 2014.

[98] K. I. Mortensen, L. S. Churchman, J. A. Spudich, and H. Flyvbjerg, "Optimized localization analysis for single-molecule tracking and super-resolution microscopy," *Nature Methods*, vol. 7, no. 5, pp. 377–383, 2010.

[99] R. B. Merrifield, "Solid Phase Peptide Synthesis. I. The Synthesis of a Tetrapeptide," *Journal of the American Chemical Society*, vol. 85, no. 14, pp. 2149–2154, 1963.

[100] A. Isidro-Llobet, M. Álvarez, and F. Albericio, "Amino acid-protecting groups," *Chemical Reviews*, vol. 109, p. 2455–2504, 2009.

[101] M. Karas, D. Bachmann, U. Bahr, and F. Hillenkamp, "Matrix-assisted ultraviolet laser desorption of non-volatile compounds," *International Journal of Mass Spectrometry and Ion Processes*, vol. 78, pp. 53–68, 1987.

[102] M. Karas, M. Glückmann, and J. Schäfer, "Ionization in matrix-assisted laser desorption/ionization: Singly charged molecular ions are the lucky survivors," *Journal of Mass Spectrometry*, vol. 35, no. 1, pp. 1–12, 2000.

[103] R. C. Beavis, T. Chaudhary, and B. T. Chait, "a-Cyano-4hydroxycinnamic Acid as a Matrix for Matrix- assisted Laser Desorption Mass-Spectrometry," *Organic Mass Spectrometry*, vol. 27, pp. 156–158, 1992.

[104] K. Strupat, M. Karas, and F. Hillenkamp, "2,5-Dihydroxybenzoic acid: a new matrix for laser desorption-ionization mass spectrometry," *International Journal of Mass Spectrometry and Ion Processes*, vol. 111, pp. 89–102, 1991.

[105] D. N. Woolfson and M. G. Ryadnov, "Peptide-based fibrous biomaterials: some things old, new and borrowed," *Current Opinion in Chemical Biology*, vol. 10, no. 6, pp. 559–567, 2006.

[106] M. Shaw, A. Bella, and M. G. Ryadnov, "CREIM: Coffee ring effect imaging model for monitoring protein self-assembly in situ," *Journal of Physical Chemistry Letters*, vol. 8, p. 48464851, 2017.

[107] L. H. C. Chung, D. J. S. Birch, V. Vyshemirsky, M. G. Ryadnov, and O. J. Rolinski, "Insulin aggregation tracked by its intrinsic TRES," *Applied Physics Letters*, vol. 111, p. 263701, 2017.

[108] A. Alghamdi, V. Vyshemirsky, D. J. S. Birch, and O. J. Rolinski, "Detecting beta-amyloid aggregation from time-resolved emission spectra," *Methods Appl. Fluoresc*, vol. 6, p. 024002, 2018.

[109] H. Levine, "Thioflavine T interaction with synthetic Alzheimer's disease β-amyloid peptides: Detection of amyloid aggregation in solution," *Protein Science*, vol. 2, no. 3, pp. 404–410, 1993.

[110] V. Foderà, F. Librizzi, M. Groenning, M. Van De Weert, and M. Leone, "Secondary nucleation and accessible surface in insulin amyloid fibril formation," *Journal of Physical Chemistry B*, vol. 112, no. 12, pp. 3853–3858, 2008.

[111] C. McGuiness, K. Sagoo, D. McLoskey, and D. J. Birch, "A new sub-nanosecond LED at 280 nm: application to protein fluorescence," *Measurement Science and Technology*, vol. 15, pp. 19–22, 2004.

[112] J. Pellaud, U. Schote, T. Arvinte, and J. Seelig, "Conformation and Self-association of Human Recombinant Transforming Growth Factor-Beta3 in Aqueous Solutions *," *The Journal of Biological Chemistry*, vol. 274, no. 12, pp. 7699–7704, 1999.

[113] R. McGuire and I. Feldman, "The Quenching of Tyrosine and Tryptophan Fluorescence by H20 and D20," *Photochemistry and Photobiology*, vol. 18, pp. 119–124, 1973.

[114] O. J. Rolinski, D. McLaughlin, D. J. Birch, and V. Vyshemirsky, "Resolving environmental microheterogeneity and dielectric relaxation in fluorescence kinetics of protein," *Methods and Applications in Fluorescence*, vol. 4, p. 024001, 2016.

[115] O. J. Rolinski, T. Wellbrock, D. J. Birch, and V. Vyshemirsky, "Tyrosine Photophysics during the Early Stages of Beta-Amyloid Aggregation Leading to Alzheimer's," *Journal of Physical Chemistry Letters*, vol. 6, pp. 3116–3120, 2015.

[116] R. D. Deegan, O. Bakajin, T. F. Dupont, G. Huber, S. R. Nagel, and T. A. Witten, "Capillary flow as the cause of ring stains from dried liquid drops," *Nature*, vol. 389, no. 6653, pp. 827–829, 1997.

[117] J. Brange, L. Andersen, E. D. Laursen, G. Meyn, and E. Rasmussen, "Toward understanding insulin fibrillation," *Journal of Pharmaceutical Sciences*, vol. 86, no. 5, pp. 517–525, 1997.

[118] S. Störkel, H. M. Schneider, H. Müntefering, and S. Kashiwagi, "Iatrogenic, insulin-dependent, local amyloidosis," *Lab Invest.*, vol. 48, pp. 108–111, 1983.

[119] I. B. Bekard and D. E. Dunstan, "Tyrosine Autofluorescence as a Measure of Bovine Insulin Fibrillation," *Biophysj*, vol. 97, pp. 2521–2531, 2009.

[120] Q. X. Hua and M. A. Weiss, "Mechanism of insulin fibrillation: The structure of insulin under amyloidogenic conditions resembles a protein-folding intermediate," *Journal of Biological Chemistry*, vol. 279, pp. 21449–21460, 2004.

[121] T. Zako, M. Sakono, N. Hashimoto, M. Ihara, and M. Maeda, "Bovine insulin filaments induced by reducing disulfide bonds show a different morphology, secondary structure, and cell toxicity from intact insulin amyloid fibrils," *Biophysical Journal*, vol. 96, no. 8, pp. 3331–3340, 2009.

[122] E. Kachooei, A. A. Moosavi-Movahedi, F. Khodagholi, H. Ramshini, F. Shaerzadeh, and N. Sheibani, "Oligomeric forms of insulin amyloid aggregation disrupt outgrowth and complexity of neuron-like PC12 cells," *PLoS ONE*, 2012.

[123] A. Gladytz, E. Lugovoy, A. Charvat, T. Häupl, K. R. Siefermann, and B. Abel, "Intermediates caught in the act: Tracing insulin amyloid fibril formation in time by combined optical spectroscopy, light scattering, mass spectrometry and microscopy," *Physical Chemistry Chemical Physics*, vol. 17, no. 2, pp. 918–927, 2015.

[124] J. R. Lakowicz, *Principles of fluorescence spectroscopy, 3rd Edition, Joseph R. Lakowicz, editor*. 2006.

[125] M. R. Nilsson, "Techniques to study amyloid fibril formation in vitro," *Methods*, vol. 34, no. 1, pp. 151–160, 2004.

[126] R. Khurana, C. Coleman, C. Ionescu-Zanetti, S. A. Carter, V. Krishna, R. K. Grover, R. Roy, and S. Singh, "Mechanism of thioflavin T binding to amyloid fibrils," *Journal of Structural Biology*, vol. 151, no. 3, pp. 229–238, 2005.

[127] N. H. Mudliar, A. M. Pettiwala, A. A. Awasthi, and P. K. Singh, "On the Molecular Form of Amyloid Marker, Auramine O, in Human Insulin Fibrils," *The Journal of Physical Chemistry B*, vol. 120, no. 49, pp. 12474–12485, 2016.

[128] Y. Hong, L. Meng, S. Chen, C. W. T. Leung, L. T. Da, M. Faisal, D. A. Silva, J. Liu, J. W. Y. Lam, X. Huang, and B. Z. Tang, "Monitoring and inhibition of insulin fibrillation by a small organic fluorogen with aggregation-induced emission characteristics," *Journal of the American Chemical Society*, vol. 134, no. 3, pp. 1680–1689, 2012.

[129] Z. Zhong, A. Pramanik, K. Ekberg, O. T. Jansson, H. Jörnvall, J. Wahren, and R. Rigler, "Insulin binding monitored by fluorescence correlation spectroscopy," *Diabetologia*, vol. 44, pp. 1184–1188, 2001.

[130] Y. Porat, A. Abramowitz, and E. Gazit, "Inhibition of amyloid fibril formation by polyphenols: Structural similarity and aromatic interactions as a common inhibition mechanism," *Chemical Biology and Drug Design*, vol. 67, no. 1, pp. 27–37, 2006.

[131] A. J. Thompson, T. W. Herling, M. Kubánková, A. Vyšniauskas, T. P. Knowles, and M. K. Kuimova, "Molecular Rotors Provide Insights into Microscopic Structural Changes during Protein Aggregation," *Journal of Physical Chemistry B*, vol. 119, no. 32, pp. 10170–10179, 2015.

[132] S. Wolter, A. Loschberger, T. Holm, S. Aufmkolk, M.-C. Dabauvalle, S. van de Linde, and M. Sauer, "rapidSTORM: accurate, fast open-source software for localization microscopy," *2Nature Methods*, vol. 9, pp. 1040–1041, 2012.

[133] J. R. Lakowicz, "On Spectral Relaxation in Proteins," *Photochemistry and Photobiology*, vol. 72, no. 4, pp. 421–437, 2000.

[134] E. H. Strickland and D. Mercola, "Near-ultraviolet tyrosyl circular dichroism of pig insulin monomers, dimers, and hexamers. Dipole-dipole coupling calculations in the monopole approximation.," *Biochemistry*, vol. 15, pp. 3875–3884, 1976.

[135] M. Lindgren, K. Sörgjerd, and P. Hammarström, "Detection and Characterization of Aggregates, Prefibrillar Amyloidogenic Oligomers, and Protofibrils Using

Fluorescence Spectroscopy," *Biophysical Journal*, vol. 88, no. 6, pp. 4200–4212, 2005.

[136] H. Naiki, K. Higuchi, M. Hosokawa, and T. Takeda, "Fluorometric determination of amyloid fibrils in vitro using the fluorescent dye, thioflavine T," *Analytical Biochemistry*, vol. 177, no. 2, pp. 244–249, 1989.

[137] L. M. Oliveira, A. Lages, R. A. Gomes, H. Neves, C. Família, A. V. Coelho, and A. Quintas, "Insulin glycation by methylglyoxal results in native-like aggregation and inhibition of fibril formation," *BMC Biochemistry*, vol. 12, pp. 1–13, 2011.

[138] H. A. Shaban, C. A. V. Cruz, J. Savatier, and S. Brasselet, "Polarized super-resolution structural imaging inside amyloid fibrils using Thioflavine T," *Scientific Reports*, no. June, pp. 1–10, 2017.

[139] C. Iannuzzi, G. Irace, and I. Sirangelo, "Differential effects of glycation on protein aggregation and amyloid formation," *Frontiers in Molecular Biosciences*, vol. 1, pp. 1–8, 2014.

[140] C. Iannuzzi, G. Irace, and I. Sirangelo, "Role of Glycation in Amyloid : Effect on the Aggregation Process and Cytotoxicity," in *Exploring New Findings on Amyloidosis* (A. M. Fernandez-Escamilla, ed.), no. November, ch. 6, pp. 167–185, Rijeka: InTech, 2016.

[141] A. Barzegar, Y. Panahi, and N. Pouladi, "Reduction in aggregation of insulin through conformational stabilization by glucose," *Asian Journal of Chemistry*, vol. 19, pp. 1749–1756, 2007.

[142] V. P. Singh, A. Bali, N. Singh, and A. S. Jaggi, "Advanced Glycation End Products and Diabetic Complications," *Korean J. Physiol Pharmacol*, vol. 18, pp. 1–14, 2014.

[143] L. H. C. Chung, D. J. S. Birch, V. Vyshemirsky, A. Bella, M. G. Ryadnov, and O. J. Rolinski, "Protein fibrillogenesis model tracked by its intrinsic time-resolved emission spectra," *Methods Appl. Fluoresc.*, vol. 7, p. 035003, 2019.

Appendix A

Fluorescence Decay Parameters of Fibrillogenesis Model

The fluorescence decay for each detection wavelength was fitted to a three-exponential function:

$$I_\lambda(t) = \sum_{i=1}^{3} \alpha_i(\lambda) \exp\left(\frac{-t}{\tau_i(\lambda)}\right) \tag{A.1}$$

λ / **nm**	$\tau 1$ / **ns**	**A1 / %**	$\tau 2$ / **ns**	**A2 / %**	$\tau 3$ / **ns**	**A3 / %**	**Sc / %**	χ^2
290	0.02	95.68	1.04	2.78	2.11	1.54	36.82	1.29
295	0.49	39.29	1.51	53.94	2.84	6.77	0.00	1.30
300	0.81	49.78	1.84	49.74	6.68	0.48	4.58	1.14
305	0.39	39.77	1.54	56.74	3.59	3.49	13.39	1.07
310	0.43	40.11	1.57	57.01	3.85	2.88	2.77	1.05
315	0.50	39.43	1.62	58.25	4.20	2.32	4.73	1.19
320	0.45	43.52	1.63	54.77	4.58	1.71	1.15	1.17
325	0.50	40.44	1.64	57.61	4.63	1.95	5.04	1.11
330	0.44	40.98	1.58	56.44	4.24	2.58	6.37	1.39
335	0.56	40.40	1.69	58.06	5.43	1.54	7.00	1.42
340	0.55	43.62	1.70	54.97	5.88	1.40	4.84	1.16

Table A.1: Lifetime data extracted from 0.33 hours of ageing fibrillogenesis model including lifetime values (T1, T2, T3), pre-exponential values (A1, A2, A3), scatter component (Sc), χ^2, and absorbance values for each corresponding wavelength.

λ / **nm**	$\tau 1$ / **ns**	**A1 / %**	$\tau 2$ / **ns**	**A2 / %**	$\tau 3$ / **ns**	**A3 / %**	**Sc / %**	χ^2
290	0.45	43.64	1.57	52.62	3.17	3.74	0.00	1.22
295	0.42	39.16	1.48	54.25	2.90	6.59	0.00	1.24
300	0.53	37.83	1.60	58.34	3.44	3.83	5.93	1.16
305	0.49	38.28	1.60	58.93	3.90	2.79	5.17	1.08
310	0.54	37.84	1.61	59.21	3.91	2.95	5.34	1.18
315	0.54	36.89	1.63	60.59	4.16	2.52	5.48	1.08
320	0.44	43.54	1.64	54.83	4.71	1.63	0.00	1.10
325	0.65	41.89	1.74	56.69	5.23	1.42	6.28	1.09
330	0.55	41.67	1.72	56.81	5.24	1.53	3.49	1.16
335	0.59	42.23	1.72	56.35	5.62	1.42	4.79	1.16
340	0.59	42.14	1.73	56.58	6.32	1.28	5.61	1.19

Table A.2: Lifetime data extracted from 43 hours of ageing fibrillogenesis model including lifetime values (T1, T2, T3), pre-exponential values (A1, A2, A3), scatter component (Sc), χ^2, and absorbance values for each corresponding wavelength.

λ / **nm**	$\tau 1$ / **ns**	**A1 / %**	$\tau 2$ / **ns**	**A2 / %**	$\tau 3$ / **ns**	**A3 / %**	**Sc / %**	χ^2
290	0.44	37.59	1.48	55.24	2.82	7.17	5.90	1.22
295	0.55	38.96	1.62	58.05	3.52	3.00	6.73	1.19
300	0.46	41.88	1.58	54.94	3.52	3.18	0.00	1.03
305	0.56	40.57	1.67	57.51	4.29	1.92	7.10	1.12
310	0.55	37.67	1.63	59.99	4.19	2.34	6.62	1.18
315	0.49	39.75	1.59	57.34	3.94	2.91	4.45	1.16
320	0.56	43.62	1.67	54.61	4.56	1.77	0.44	1.16
325	0.58	42.19	1.69	56.23	5.01	1.58	5.68	1.10
330	0.58	33.06	1.66	64.64	4.87	2.29	16.21	1.22
335	0.63	44.26	1.74	54.38	5.64	1.36	6.77	1.25
340	0.58	43.03	1.71	55.53	5.96	1.44	6.06	1.18

Table A.3: Lifetime data extracted from 312 hours of ageing fibrillogenesis model including lifetime values (T1, T2, T3), pre-exponential values (A1, A2, A3), scatter component (Sc), χ^2, and absorbance values for each corresponding wavelength.

λ / **nm**	$\tau 1$ / **ns**	**A1 / %**	$\tau 2$ / **ns**	**A2 / %**	$\tau 3$ / **ns**	**A3 / %**	**Sc / %**	χ^2
290	0.47	40.64	1.54	54.47	3.11	4.89	3.57	1.21
295	0.56	43.15	1.66	54.87	3.95	1.99	2.97	1.12
300	0.46	42.76	1.57	54.09	3.60	3.15	0.00	1.16
305	0.53	39.45	1.63	58.25	4.17	2.29	4.88	1.09
310	0.48	40.07	1.59	57.24	4.03	2.69	2.52	1.11
315	0.52	41.06	1.63	56.72	4.30	2.22	2.51	1.13
320	0.49	41.44	1.62	56.40	4.41	2.17	2.68	1.07
325	0.54	44.31	1.68	53.94	4.80	1.75	2.52	1.13
330	0.60	44.60	1.72	53.97	5.46	1.44	4.48	1.14
335	0.58	46.76	1.72	51.81	5.65	1.42	2.50	1.10
340	0.62	43.69	1.72	54.80	6.12	1.51	5.43	1.14

Table A.4: Lifetime data extracted from 454 hours of ageing fibrillogenesis model including lifetime values (T1, T2, T3), pre-exponential values (A1, A2, A3), scatter component (Sc), χ^2, and absorbance values for each corresponding wavelength.

λ / **nm**	$\tau 1$ / **ns**	**A1 / %**	$\tau 2$ / **ns**	**A2 / %**	$\tau 3$ / **ns**	**A3 / %**	**Sc / %**	χ^2
290	1.46	82.83	2.77	32.08	3.08	-14.91	70.28	1.26
295	1.57	93.63	3.97	107.85	4.01	-101.48	41.94	1.14
300	1.55	94.35	3.54	5.66	350	-0.01	22.22	1.22
305	1.55	94.35	3.65	5.66	350	-0.01	13.82	1.14
310	0.67	14.41	1.64	81.21	3.73	4.37	9.13	1.04
315	0.62	14.52	1.63	81.58	3.93	3.90	7.19	1.11
320	1.12	42.67	1.90	55.75	4.99	1.59	6.27	1.16
325	0.55	17.96	1.65	79.21	4.49	2.83	5.03	1.12
330	0.55	21.27	1.69	76.58	5.07	2.15	4.74	1.12
335	0.52	23.88	1.70	74.08	5.42	2.05	4.03	1.14
340	0.75	28.20	1.77	69.98	6.23	1.82	5.44	1.15

Table A.5: Lifetime data extracted from 693 hours of ageing fibrillogenesis model including lifetime values (T1, T2, T3), pre-exponential values (A1, A2, A3), scatter component (Sc), χ^2, and absorbance values for each corresponding wavelength.

Appendix B

MALDI-ToF Mass Spectra for Fibrillogenesis Model

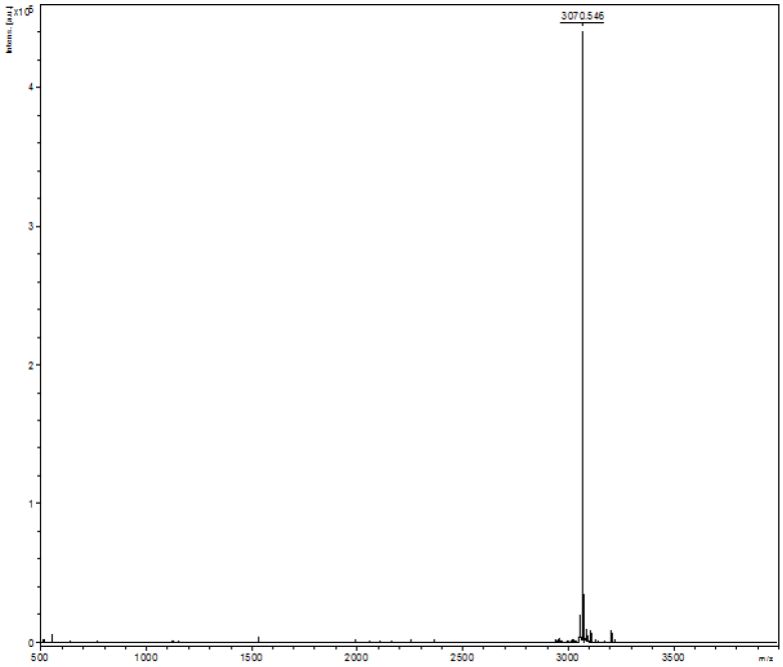

Figure B.1: MALDI-ToF mass spectra for fibrillogenesis model labelled with tyrosine. The dominant peak m/z value matches the theoretical value of the protein model.

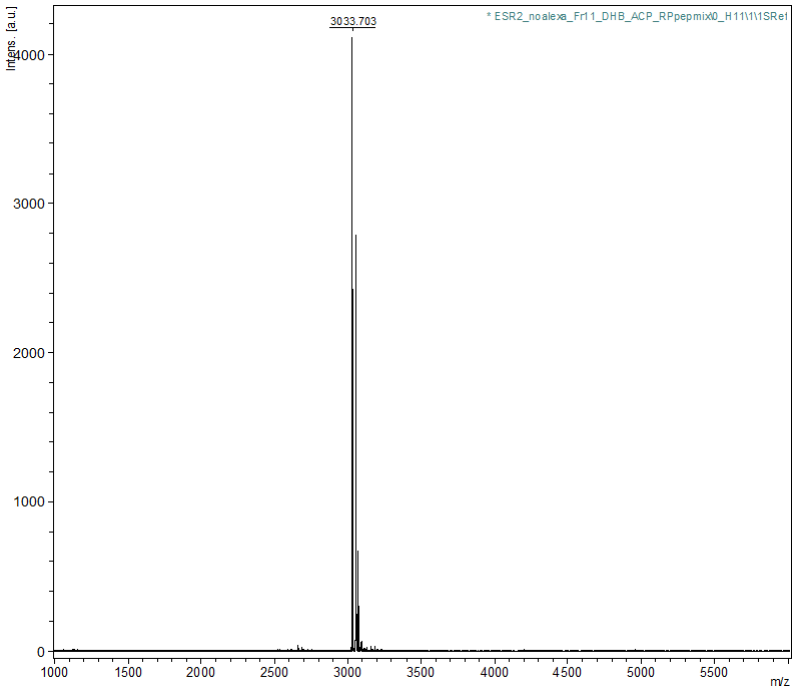

Figure B.2: MALDI-ToF mass spectra for unlabelled fibrillogenesis model. The dominant peak m/z value matches the theoretical value of the protein model.

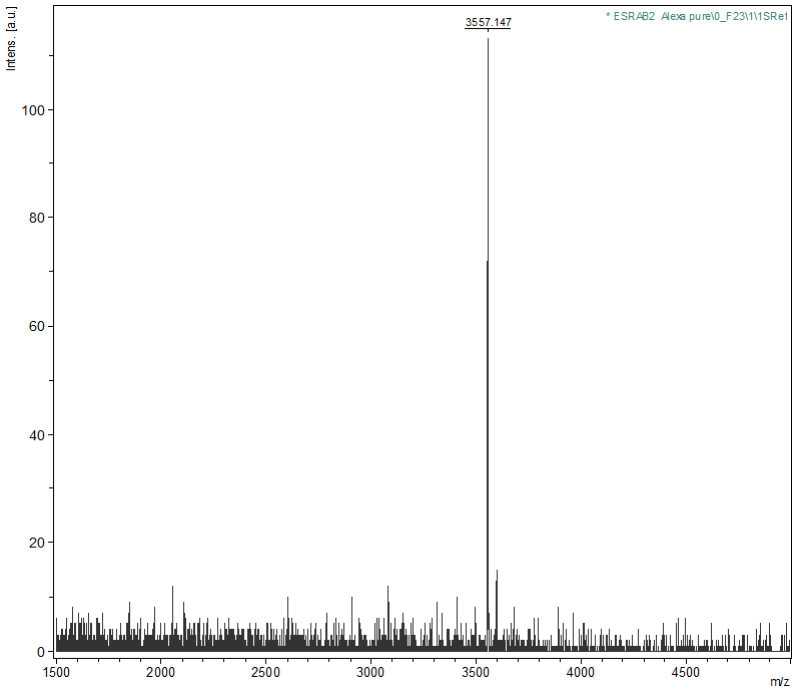

Figure B.3: MALDI-ToF mass spectra for fibrillogenesis model labelled with Alexa-Fluor 488. The dominant peak m/z value matches the theoretical value of the protein model.

Appendix C

RP-HPLC Profile for Fibrillogenesis Model

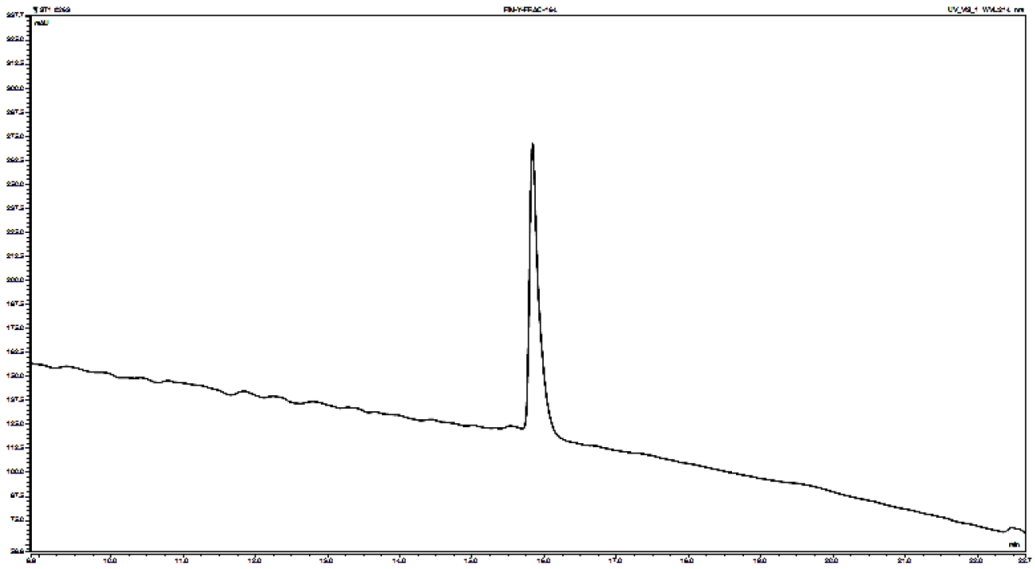

Figure C.1: RP-HPLC profile for fibrillogenesis model labelled with tyrosine residue. Excitation wavelength of 214 nm was used and one peak shows retention time of ~16 minutes.

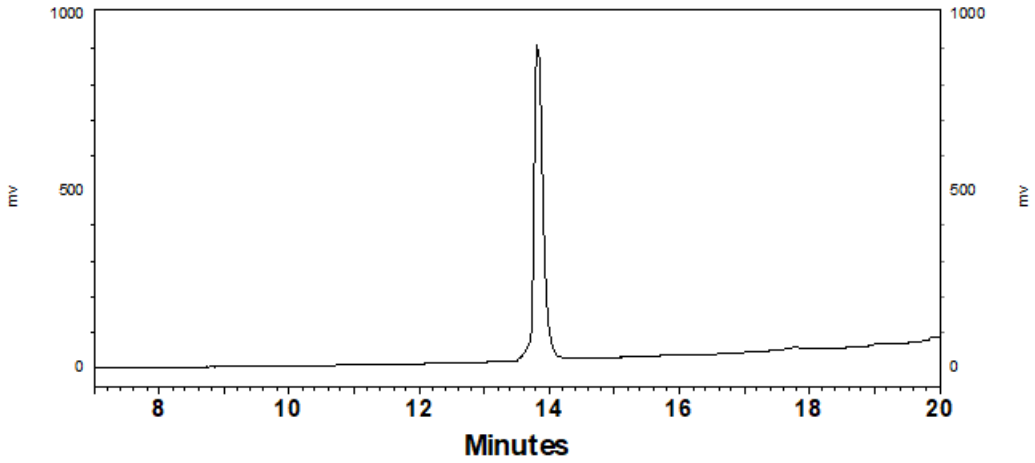

Figure C.2: RP-HPLC profile for a label free fibrillogenesis model. Excitation wavelength of 214 nm was used and one peak shows retention time of ~14 minutes.

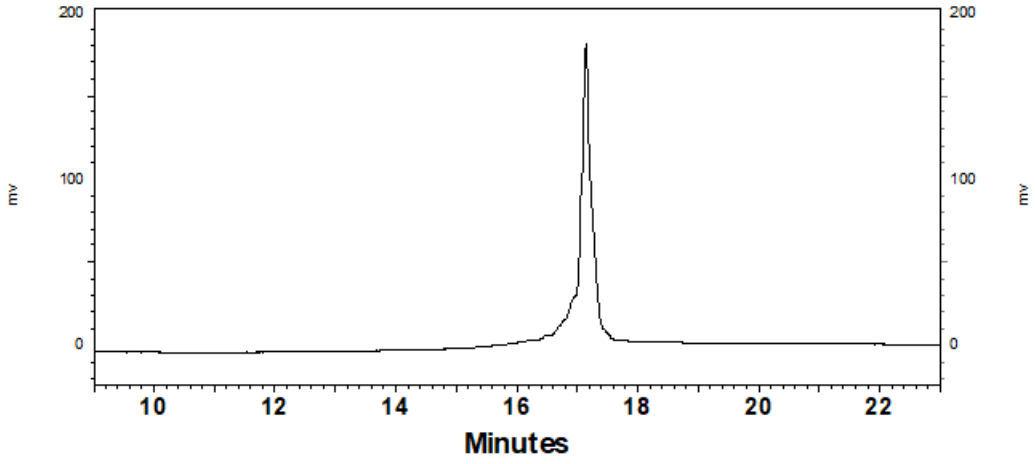

Figure C.3: RP-HPLC profile for fibrillogenesis model labelled with Alexa-Fluor 488. Excitation wavelength of 214 nm was used and one peak shows retention time of ~17 minutes.

Appendix D

Fluorescence Decay Parameters of Hexameric Insulin

*The lifetime >350 ns (350 ns is the high-limit value of the lifetime considered by the software) and a very low and negative value of the associated pre-exponential factor indicate that the third component contributes to the background signal and the fluorescence decay is 2-exponential.

λ / **nm**	$\tau 1$ / **ns**	**A1 / %**	$\tau 2$ / **ns**	**A2 / %**	$\tau 3$ / **ns**	**A3 / %**	χ^2
290	0.43	2382.62	0.50	-2446.26	1.33	163.64	1.22
295	1.15	-4072.63	1.20	2509.76	1.24	1662.87	1.09
300	1.02	-51.80	2.31	85.92	2.40	65.88	0.92
305	0.99	71.38	2.16	28.63	2.30	0.00	1.06
310	0.13	26.12	0.97	73.88	1.75	0.00	1.06
315	0.27	18.51	1.06	81.49	1.98	0.00	1.05
320	0.28	6.69	1.15	30.07	2.36	63.24	1.14
325	0.31	4.32	1.21	66.08	2.89	29.60	1.16
330	0.38	30.25	1.26	66.32	3.46	3.44	1.17
335	0.37	3.18	1.28	33.56	3.95	63.25	1.18
340	0.40	3.38	1.34	60.98	4.39	35.64	1.19
345	0.55	59.25	1.42	4.07	4.79	36.68	1.19
350	0.57	4.46	1.51	53.63	5.15	41.91	1.19

Table D.1: The results of fitting 3 exponential models to the fluorescence intensity decays $I_\lambda(t)$ of hexameric insulin sample recorded at different wavelengths λ and at 0.35 hours after sample preparation.

λ / **nm**	$\tau 1$ / **ns**	**A1 / %**	$\tau 2$ / **ns**	**A2 / %**	$\tau 3$ / **ns**	**A3 / %**	χ^2
290	0.92	-1.69	1.78	77.26	3.52	24.43	1.16
295	0.94	48.07	2.35	51.96	2.40	-0.03	1.13
300	0.90	47.99	2.17	52.03	2.33	-0.02	1.14
305	0.73	49.52	1.46	-0.02	>350*	50.50	1.18
310	0.71	56.03	1.47	-0.02	>350*	43.99	1.27
315	0.87	37.14	2.07	-0.01	2.10	62.87	1.12
320	0.23	46.37	0.90	28.61	1.64	25.02	1.06
325	0.27	81.16	1.07	18.85	2.10	-0.01	1.18
330	0.33	58.09	1.15	35.70	2.50	6.21	1.27
335	0.43	3.65	1.25	35.14	3.39	61.21	1.18
340	0.39	41.36	1.27	55.17	3.75	3.47	1.14
345	0.43	55.10	1.33	41.41	4.32	3.50	1.23
350	0.44	42.95	1.35	52.72	4.47	4.33	1.26

Table D.2: The results of fitting 3 exponential models to the fluorescence intensity decays $I_\lambda(t)$ of hexameric insulin sample recorded at different wavelengths λ and at 22 hours after sample preparation.

λ / **nm**	$\tau 1$ / **ns**	**A1 / %**	$\tau 2$ / **ns**	**A2 / %**	$\tau 3$ / **ns**	**A3 / %**	χ^2
290	0.89	70.99	1.58	-0.24	6.43	29.25	1.18
295	0.92	-98.98	2.37	83.66	2.46	115.32	1.05
300	0.85	42.93	1.61	57.09	>350*	-0.02	1.20
305	0.71	40.95	1.50	-0.01	>350*	59.06	1.07
310	0.73	70.46	1.46	-0.01	>350*	29.54	1.18
315	0.52	6.29	1.17	62.84	2.41	30.87	1.17
320	0.50	62.32	1.23	3.60	3.15	34.08	1.19
325	0.51	57.38	1.31	2.36	4.12	40.26	1.05
330	0.58	2.64	1.38	52.17	4.64	45.19	1.08
335	0.52	53.54	1.37	3.35	4.90	43.11	1.08
340	0.80	62.82	1.68	3.96	5.41	33.22	1.13
345	0.58	4.49	1.55	50.44	5.66	45.07	1.13
350	0.61	5.65	1.63	41.64	5.79	52.71	1.16

Table D.3: The results of fitting 3 exponential models to the fluorescence intensity decays $I_\lambda(t)$ of hexameric insulin sample recorded at different wavelengths λ and at 68 hours after sample preparation.

λ / **nm**	$\tau 1$ / **ns**	**A1 / %**	$\tau 2$ / **ns**	**A2 / %**	$\tau 3$ / **ns**	**A3 / %**	χ^2
290	0.93	82.29	1.8	18.02	6.34	-0.31	1.06
295	0.83	70.82	1.59	-0.02	57.03	29.2	1.18
300	0.22	75.2	0.92	-0.01	1.65	24.81	1.02
305	0.44	64.94	1.14	5.19	2.44	29.86	1.05
310	0.39	63.23	1.17	3.65	3.04	33.11	1.17
315	0.58	44.55	1.33	53.26	4.25	2.19	1.01
320	0.46	57.31	1.28	39.57	4.44	3.12	1.15
325	0.53	52.78	1.36	43.66	4.98	3.56	1.15
330	0.56	45.45	1.43	50.23	5.24	4.33	1.17
335	0.56	43.68	1.51	51.11	5.53	5.22	1.16
340	0.62	38.63	1.69	6.36	5.8	55.01	1.05
345	0.66	7.71	1.82	37.78	6.03	54.5	1.09
350	0.77	32.33	2.1	9.00	6.23	58.66	1.18

Table D.4: The results of fitting 3 exponential models to the fluorescence intensity decays $I_\lambda(t)$ of hexameric insulin sample recorded at different wavelengths λ and at 93 hours after sample preparation.

λ / **nm**	$\tau 1$ / **ns**	**A1 / %**	$\tau 2$ / **ns**	**A2 / %**	$\tau 3$ / **ns**	**A3 / %**	χ^2
290	0.03	96.81	0.86	2.08	1.71	1.11	1.30
295	0.05	87.70	1.03	12.31	2.49	0.00	1.11
300	0.61	52.18	1.35	43.41	3.81	4.41	1.09
305	0.67	44.25	1.54	3.95	4.75	51.80	0.99
310	0.67	4.99	1.64	52.61	5.21	42.39	1.13
315	0.81	5.79	2.01	30.88	5.80	63.32	1.14
320	0.85	31.54	2.24	61.56	6.28	6.90	1.07
325	0.71	37.84	2.07	9.36	6.17	52.80	1.08
330	0.76	53.28	2.32	10.39	6.48	36.33	1.05
335	0.76	12.68	2.34	39.84	6.53	47.48	1.07
340	0.65	15.03	2.27	40.57	6.36	44.40	1.19
345	0.71	15.67	2.43	44.20	6.58	40.12	1.08
350	0.66	44.79	2.47	38.84	6.58	16.37	1.08

Table D.5: The results of fitting 3 exponential models to the fluorescence intensity decays $I_\lambda(t)$ of hexameric insulin sample recorded at different wavelengths λ and at 693 hours after sample preparation.